



MARTIN-LUTHER-UNIVERSITÄT  
HALLE-WITTENBERG

Funktionalisierung von Oberflächenbeschichtungen  
auf Basis von Polyelektrolyt-Multischichtsystemen für  
die Stimulierung der osteogenen  
Stammzellendifferenzierung

## **Kumulative Dissertation**

zur Erlangung des akademischen Grades  
*Doctor rerum naturalium* (Dr. rer. nat.)

vorgelegt der

Naturwissenschaftlichen Fakultät I  
– Biowissenschaften –  
der Martin-Luther-Universität Halle-Wittenberg

von Frau Dipl.-Pharm. Catharina Husteden  
geboren in Nordhorn

1. Gutachter/in: Prof. Dr. Thomas Groth
2. Gutachter/in: Prof. Dr. Sonja Kessler
3. Gutachter/in: Prof. Dr. Emanuel Schneck

Verteidigung am 08.09.2023

*Für meine Familie*

# Inhaltsverzeichnis

<i>Abbildungsverzeichnis</i>	<i>IV</i>
<i>Tabellenverzeichnis</i>	<i>IV</i>
<i>Abkürzungsverzeichnis</i>	<i>V</i>
<b>1) Einleitung</b>	<b>1</b>
<b>1.1) Vielfältige Ursachen komplizierter Frakturen</b>	<b>1</b>
<b>1.2) Knochenstruktur und -remodellierung</b>	<b>2</b>
1.2.1) Beteiligte Zellen und extrazelluläre Mikroumgebung	3
1.2.2) Knochenremodellierung	4
<b>1.3) Derzeitige klinische Behandlungsmöglichkeiten komplizierter Frakturen</b>	<b>6</b>
<b>1.4) Neue Strategien in der Knochenregeneration</b>	<b>7</b>
1.4.1) Biomaterialien für den Knochenersatz	8
1.4.2) Oberflächenmodifizierung	10
1.4.2.1) Layer-by-Layer-Methode für die Oberflächenmodifizierung	10
1.4.3) Oberflächenfunktionalisierung im Bereich der Knochenregeneration	12
1.4.3.1) Arzneimittel	12
1.4.3.2) Liposomen	13
1.4.3.3) Proteintherapie mit Signalmolekülen	14
1.4.3.4) Lokale Gentherapie	16
1.4.3.5) Lipoplexe	17
1.4.4) Interaktion zwischen Biomaterial und mesenchymalen Stammzellen	19
<b>1.5) Zielstellung</b>	<b>22</b>
<b>2) Kumulativer Teil</b>	<b>23</b>
<b>2.1) Allgemeines</b>	<b>25</b>
<b>2.2) Verwendete Polyelektrolyte und Lipide</b>	<b>25</b>
<b>2.3) Publikation I</b>	<b>29</b>
<b>2.4) Publikation II</b>	<b>45</b>
<b>2.5) Publikation III</b>	<b>49</b>
<b>2.6) Publikation IV</b>	<b>66</b>
<b>2.7) Manuskript I</b>	<b>87</b>
<b>3) Generelle Diskussion</b>	<b>120</b>
<b>3.1) Potenzial der Funktionalisierungsstrategien</b>	<b>120</b>
<b>3.2) Generelle Hürden im Tissue Engineering</b>	<b>123</b>
<b>3.3) Regulatorische Herausforderungen für die klinische Translation</b>	<b>124</b>
<b>4) Zusammenfassung und Ausblick</b>	<b>126</b>
<b>5) Literaturverzeichnis</b>	<b>130</b>
<b>6) Anhang</b>	<b>138</b>

## Abbildungsverzeichnis

<i>Abbildung 1</i>	Risikofaktoren für eine beeinträchtigte Knochenheilung	<i>1</i>
<i>Abbildung 2</i>	Hierarchischer Aufbau des Knochengewebes	<i>2</i>
<i>Abbildung 3</i>	Zelluläre und molekulare Mechanismen der Knochenremodellierung	<i>5</i>
<i>Abbildung 4</i>	Schematische Darstellung des Tissue-Engineering-Konzeptes	<i>8</i>
<i>Abbildung 5</i>	Prinzip der Layer-by-Layer-Methode	<i>11</i>
<i>Abbildung 6</i>	Struktureller Aufbau kationischer Lipide am Beispiel von DOTMA und deren Anordnung zu Liposomen in wässriger Umgebung	<i>13</i>
<i>Abbildung 7</i>	Signaltransduktion für die BMP-Familie	<i>15</i>
<i>Abbildung 8</i>	Grundlegender Mechanismus der nicht-viralen Genübertragung mit Lipoplexen	<i>19</i>
<i>Abbildung 9</i>	Differenzierungspotenzial von mesenchymalen Stammzellen	<i>20</i>
<i>Abbildung 10</i>	Der Signalweg bei Adhäsion von Stammzellen an Biomaterialien	<i>21</i>
<i>Abbildung 11</i>	Chemische Struktur von Hyaluronsäure	<i>26</i>
<i>Abbildung 12</i>	Chemische Struktur von Chitosan	<i>26</i>
<i>Abbildung 13</i>	Chemische Struktur von Chondroitinsulfat	<i>27</i>
<i>Abbildung 14</i>	Chemische Struktur von OH4	<i>27</i>
<i>Abbildung 15</i>	Chemische Struktur von OO4	<i>28</i>
<i>Abbildung 16</i>	CLSM-Aufnahmen von co-transfizierten MSCs	<i>122</i>

## Tabellenverzeichnis

<i>Tabelle 1</i>	Unterteilung der nicht-kollagenen Proteine der ECM sowie ihre Vertreter und Funktionen im Knochengewebe	<i>4</i>
<i>Tabelle 2</i>	Knochenersatzmaterialien für die Knochenreparatur und -regeneration	<i>9</i>
<i>Tabelle 3</i>	Vektortypen für die Gentherapie und ihre Vor- und Nachteile	<i>18</i>
<i>Tabelle 4</i>	Allgemeine Informationen zu den Fachzeitschriften	<i>23</i>
<i>Tabelle 5</i>	Darlegung des prozentualen Eigenanteils an den Veröffentlichungen	<i>23</i>
<i>Tabelle 6</i>	Darlegung des prozentualen Eigenanteils an den Manuskripten	<i>24</i>
<i>Tabelle 7</i>	Herausforderungen und Einschränkungen im Knochen-TE	<i>124</i>
<i>Tabelle 8</i>	Aktuell zugelassene Produkte aus Gewebezüchtung	<i>125</i>

## Abkürzungsverzeichnis

BMP	<i>Bone Morphogenetic Protein</i>
BMPR	<i>Bone Morphogenetic Protein Receptor</i>
BSP	<i>Bone Sialoprotein</i>
CHI	Chitosan
CLSM	<i>Confocal Laser Scanning Microscopy</i>
COL	<i>Collagen I</i>
CS	Chondroitinsulfat
DBM	<i>Demineralized Bone Matrix</i>
DEX	Dexamethason
DKK-1	<i>Dickkopf-related Protein 1</i>
DMP1	Dentin-Matrix-Protein-1
DNA	<i>Desoxyribonucleic Acid</i>
DOPE	1,2-dioleoyl-sn-glycero-3-phosphoethanolamin
DOTMA	N-[1-(2,3-Dioleoyloxy)propyl]-N,N,N-trimethylammoniumchlorid
DSPP	Dentin-Sialophosphoprotein
ECM	<i>Extracellular Matrix</i>
EMA	Europäische Arzneimittel-Agentur
ELISA	<i>Enzyme-linked Immunosorbent-Assay</i>
ERK	<i>Extracellular-Signal Regulated Kinase</i>
FAK	Fokale Adhäsionskinase
FGF	<i>Fibroblast Growth Factor</i>
FHL-2	<i>Four and a half LIM Domains Protein 2</i>
GAG	Glykosaminoglykan
GDF	<i>Growth Differentiation Factor</i>
HA	Hyaluronsäure
HAP	Hydroxyapatit
HSC	Hämatopoetische Stammzellen
IGF	<i>Insulin-like Growth Factor</i>
IL	Interleukin
LbL	<i>Layer-by-Layer</i>
LEF	<i>Lymphoid Enhancer-binding Factor</i>
LPX	Lipoplexe
M-CSF	<i>Macrophage Colony-stimulating Factor</i>
MEPE	Matrix-extrazelluläres Phosphoglykoprotein

MKP	<i>Mitogen-activated Protein Kinase</i>
MSC	Mesenchymale Stammzellen
MGP	Matrix-Gla-Protein
mRNA	<i>Messenger Ribonucleic Acid</i>
NSAID	<i>Non-steroidal Anti-inflammatory Drug</i>
OCN	Osteocalcin
OH4	N-{6-amino-1-[N-(9Z)-octadec-9-enylamino]-1-oxohexan-(2S)-2-yl}zs-N'-{2-[N, N-bis(2-aminoethyl)amino]ethyl}-2-hexadecylpropandiamid
OO4	(N-{6-amino-1-[N-(9Z)-octadec-9-enylamino]-1-oxohexan-(2S)-2-yl}-N'-{2-[N,N-bis(2-aminoethyl)amino]ethyl}-2[(9Z)-octadec-9enyl]
OPG	Osteoprotegerin
OPN	Osteopontin
OSX	Osterix
PDGF	<i>Platelet-derived Growth Factor</i>
PEM	Polyelektrolyt-Multilayer
PGE	Prostaglandin-E
PLGA	Polylactid-co-Glycolid
PSA	Pseudoarthrose
RANK	<i>Receptor Activator of NF-κB</i>
RANKL	<i>Receptor Activator of NF-κB Ligand</i>
RIA	Reamer-Irrigator-Aspirator
RNA	<i>Ribonucleic Acid</i>
RUNX2	<i>Run-related Transcription Factor 2</i>
SIBLINGs	<i>Small Integrin-binding N-linked Glycoproteins</i>
SMD	<i>Substrate-mediated Gene-Delivery</i>
SOST	Sclerostin
SLRP	<i>Small Leucin-rich Proteoglycans</i>
SPARC	<i>Secreted Protein Acidic and Rich in Cysteine</i>
TAZ	<i>Transcriptional Co-Activator with PDZ-binding Motif</i>
TCF	T-Zell-spezifischer Transkriptionsfaktor
TE	<i>Tissue Engineering</i>
TGF	<i>Transforming Growth Factor</i>
TNF	Tumornekrosefaktor
TSP	Thrombospondin
VEGF	<i>Vascular Endothelial Growth Factor</i>

## 1) Einleitung

### 1.1) Vielfältige Ursachen komplizierter Frakturen

Der Knochen ist ein komplexes und dynamisches Gewebe, das einer ständigen Resorption und Neubildung unterliegt und dessen einzigartige Remodellierungsfähigkeit in den meisten Fällen die Heilung kleiner Knochenverletzungen ermöglicht.<sup>1,2</sup> Doch trotz der hervorragenden Regenerationsfähigkeit des Knochens stellen große oder instabile Frakturen sowie Fraktur-Pseudarthrosen (PSA) herausfordernde klinische Szenarien ohne eine durchgehend zufriedenstellende Lösung dar. Speziell PSA, die auf Basis einer nicht ausreichend ausgeheilten Bruchstelle nach einer Knochenfraktur entstehen und starke Schmerzen sowie Bewegungseinschränkungen durch die Entstehung eines Falschgelenkes (knöcherne Fehlheilung) hervorrufen können, gehen häufig mit einer erhöhten Patientenmorbidity und erheblichen sozioökonomischen Kosten einher.<sup>3-5</sup> Darüber hinaus können Traumata, Knochentumorresektionen oder Arthritis zu größeren Knochendefekten führen, die eine Heilung beeinträchtigen können.<sup>6</sup> Weitere Risikofaktoren einer unzureichenden Knochenheilung sind in Abbildung 1 dargestellt.



**Abbildung 1:** Risikofaktoren für eine beeinträchtigte Knochenheilung.<sup>7,8</sup>

Epidemiologen schätzen, dass eine verzögerte Heilung oder PSA bei 5–10 % aller Frakturen und bei 20 % der Frakturen mit hohem Aufprall auftreten.<sup>9,10</sup> In den Vereinigten Staaten werden die jährlichen Kosten für die Behandlung von Knochendefekten auf rund 5 Milliarden Dollar geschätzt.<sup>11</sup> Trotz der hohen Ausgaben unterliegt die Knochenregenerationstherapie derzeit noch Einschränkungen, die zu einer gesellschaftlichen und wirtschaftlichen Belastung sowie einer verringerten Lebensqualität der Patienten führen.<sup>9</sup> Es besteht daher ein dringender Bedarf an Therapien zur Knochenregeneration, die

erschwinglich sind und bessere klinische Ergebnisse für die Patienten erzielen. Das Verständnis für die Struktur des Knochens sowie dessen Remodellierungsprozesse ist für die Entwicklung von Therapieoptionen essenziell und soll im folgenden Kapitel genauer erklärt werden.

## 1.2) Knochenstruktur und -remodellierung

Der Knochen ist ein mineralisiertes Bindegewebe, das bedeutsame Funktionen im Körper ausübt: Fortbewegung, Unterstützung und Schutz des Weichgewebes, Calcium- und Phosphatspeicherung und Knochenmarkbeherbergung.<sup>12,13</sup> Die mechanischen Eigenschaften variieren dabei je nach Lokalisation und Funktion.<sup>14</sup> Aufgrund seiner komplexen und hierarchischen Struktur kann Knochen als Nanokomposit definiert werden, das aus anorganischem nanokristallinem Hydroxyapatit (HAP), organischen Bestandteilen (hauptsächlich Kollagenen) und Wasser besteht. Auf makroskopischer Ebene wird Knochen in zwei Kategorien unterteilt: kortikalen Knochen (Knochenrinde) und spongiösen Knochen (Schwammknochen). Die Kortikalis umschließt peripher die Spongiosa und hat eine hohe mechanische Festigkeit, die stabilisierend und stützend wirkt. Im Gegensatz dazu hat die Spongiosa eine geringe mechanische Festigkeit mit einer leichten und porösen Struktur, die eine geeignete Umgebung für den Knochenstoffwechsel und die hämatopoetische Funktion bietet. Darüber hinaus erleichtert die Spongiosa es, multidirektionale Kräfte während der Körperbewegung zu übertragen und zu unterstützen.<sup>15</sup>

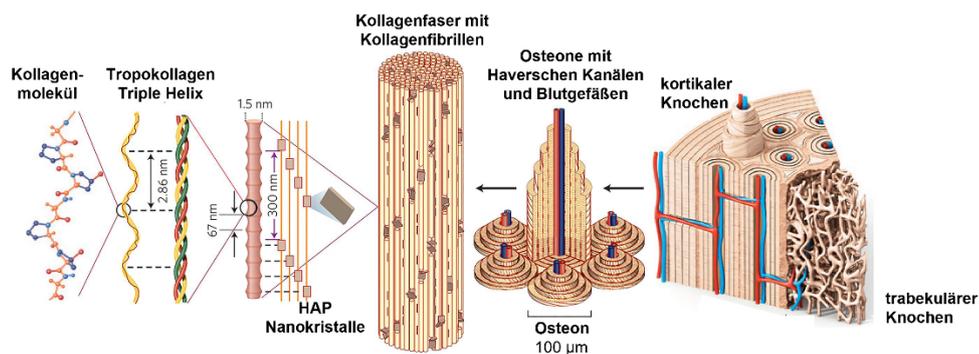


**Abbildung 2:** Hierarchischer Aufbau des Knochengewebes. Abbildung geändert nach Wei et al.<sup>16</sup>

Wie in Abbildung 2 zu erkennen ist, besteht auf der Mikrometerebene (10–500 µm) der kortikale Knochen aus Osteonen, die entlang der Längsachse des Knochens angeordnet sind. Ein Osteon, eine funktionelle Einheit des Knochengewebes, besteht aus dem Lamellenknochen, der in einem konzentrischen Kreis angeordnet ist. Nervenfasern und Blutgefäße verlaufen durch den Knochen und bilden den Haversschen Kanal. Bei der

Spongiosa bilden anisotrop angeordnete stäbchenförmige Trabekelknochen ein wabenartiges Netzwerk neben kleinen, unregelmäßigen Hohlräumen, die rotes Knochenmark enthalten. Der Raum zwischen den Trabekelknochen wird von Blutgefäßen und Knochenmark ausgefüllt, worin sich hämatopoetische Stammzellen (HSCs) und mesenchymale Stammzellen (MSCs) befinden.<sup>17</sup> Im nanomikroskopischen Maßstab erzeugen sowohl kortikale als auch spongiöse Knochen mineralisierte Kollagenfibrillen, die durch abwechselnde Ausrichtung der Kollagenmoleküle und Apatitkristalle entstehen und sich im Mikromaßstab zu Lamellen formieren.<sup>18</sup>

### 1.2.1) Beteiligte Zellen und extrazelluläre Mikroumgebung

Kortikalis und Spongiosa bieten einen unterstützenden und schützenden Raum für das Wachstum von Knochengewebezellen. Von besonderer Bedeutung sind die im Knochenmark befindlichen HSCs und MSCs.<sup>17</sup> Die HSCs sind hauptsächlich für die Bildung von Blutgefäßen und Immunzellen verantwortlich und tragen außerdem zur Bildung von Osteoklasten bei.<sup>19</sup> Die MSCs sind im Wesentlichen für die Bildung mesenchymaler Abstammungszellen verantwortlich, darunter Osteoblasten, Chondroblasten, Adipozyten und andere Stromazellen. Diese Zellen sind essenziell, um die physiologische Homöostase des Knochengewebes aufrechtzuerhalten und Knochendefekte zu regenerieren.<sup>20</sup>

Eine weitere wichtige Komponente des Knochengewebes ist die nanostrukturierte extrazelluläre Matrix (engl. *Extracellular Matrix*, ECM), welche die Adhäsion, Proliferation und Differenzierung von Osteoblasten, Osteozyten und Osteoklasten beeinflusst.<sup>21,22</sup> Knochen-ECM besteht aus zwei Hauptkomponenten: einem mineralischen Teil, bestehend aus HAP (70–90 %), und einem organischen Teil (10–30 %), der sich hauptsächlich aus Kollagen zusammensetzt (ca. 90 % der organischen Matrix), wobei der Rest aus nicht-kollagenen Proteinen besteht (ca. 10 %).<sup>23</sup> Als Kollagen dominiert hauptsächlich Kollagen Typ I (97 %), mit kleineren Mengen an Typ III, V, XI und XIII.<sup>24,25</sup> Die nicht-kollagenen Proteine können in vier Gruppen eingeteilt werden:  $\gamma$ -Carboxyglutamat-haltige Proteine, Proteoglykane, Glykoproteine und *Small Integrin-binding N-linked Glycoproteins* (SIBLINGs).<sup>26</sup> Proteoglykane sind durch das Vorhandensein von Glykosaminoglykan(GAG)-Resten gekennzeichnet, die kovalent an den Proteinkern gebunden sind. Glykoproteine enthalten kovalent an die Proteinkette gebundene Kohlenhydratmoleküle in verschiedenen Kombinationen und Positionen. Die  $\gamma$ -Carboxyglutamat-haltigen Proteine entstehen durch die intrazelluläre Carboxylierung von

Glutaminsäure unter Einfluss von Vitamin K, während SIBLINGs eine Familie Integrin-bindender Glykophosphoproteine darstellen. Die jeweiligen Vertreter und ihre Funktionen im Knochengewebe sind in Tabelle 1 dargestellt.<sup>27</sup>

<b>Klassifizierung nicht-kollagener Proteine</b>	<b>Vertreter</b>	<b>Funktion im Knochengewebe</b>
Proteoglykane	<ul style="list-style-type: none"> <li>➤ Keratansulfat, Chondroitinsulfat, Heparansulfat, Hyaluronsäure, Dermatan-sulfat</li> <li>➤ Familie der <i>Small Leucin-rich Proteoglycans</i> (SLRPs): Biglykan, Decorin, Keratocan, Asporin</li> </ul>	<ul style="list-style-type: none"> <li>➤ Förderung der Kollagenfibrillogenese</li> <li>➤ Förderung der Knochenbildung</li> <li>➤ Förderung der Mineralablagerung</li> </ul>
Glykoproteine	<ul style="list-style-type: none"> <li>➤ Familie der <i>Secreted Protein Acidic and Rich in Cysteine</i> (SPARC): Osteonectin</li> <li>➤ Thrombospondine (TSP)</li> <li>➤ R-Spondine</li> <li>➤ Fibronectin, Vitronectin, Laminin</li> </ul>	<ul style="list-style-type: none"> <li>➤ Förderung des Knochenaufbaus und Mineralisierung</li> <li>➤ Regulierung der Kollagenfibrillogenese</li> <li>➤ Erhaltung der biomechanischen Eigenschaften</li> <li>➤ Regulierung der Wnt/<math>\beta</math>-Catenin-Signalgebung</li> </ul>
$\gamma$ -Carboxy-glutamat-haltige Proteine	<ul style="list-style-type: none"> <li>➤ Osteocalcin (OCN)</li> <li>➤ Matrix-Gla-Protein (MGP)</li> <li>➤ Periostin</li> </ul>	<ul style="list-style-type: none"> <li>➤ Regulierung des Calciumstoffwechsels</li> <li>➤ Inhibierung des Knochenaufbaus und Mineralisierung</li> <li>➤ Erhaltung der Knochenstärke</li> </ul>
SIBLINGs	<ul style="list-style-type: none"> <li>➤ Knochen-Sialoprotein (BSP)</li> <li>➤ Osteopontin (OPN)</li> <li>➤ Dentin-Matrix-Protein-1 (DMP1)</li> <li>➤ Dentin-Sialophosphoprotein (DSPP)</li> <li>➤ Matrix-extrazelluläres Phosphoglykoprotein (MEPE)</li> </ul>	<ul style="list-style-type: none"> <li>➤ Förderung des Knochenaufbaus und Mineralisierung</li> <li>➤ Regulierung des Phosphatstoffwechsels</li> <li>➤ Regulierung der Knochenremodellierung</li> </ul>

**Tabelle 1:** Unterteilung der nicht-kollagenen Proteine der ECM sowie ihre Vertreter und Funktionen im Knochengewebe.<sup>27</sup>

### 1.2.2) Knochenremodellierung

Knochen wird durch den Prozess der Knochenremodellierung kontinuierlich ab- und aufgebaut. Der Ablauf resultiert aus einem regulierten Gleichgewicht zwischen knochenbildenden Osteoblasten, knochenresorbierenden Osteoklasten und den Osteozyten. Die Regulation der Knochenremodellierung kann sowohl parakrin als auch endokrin erfolgen.<sup>28</sup> Wie in Abbildung 3 dargestellt wird, sind an der parakrinen Regulation mehrere Faktoren beteiligt, darunter Zytokine (IL-1, IL-6, TNF-alpha sowie M-CSF aktivierend; IL-4 und Interferon- $\gamma$  inhibierend), PGE2 sowie VEGF.<sup>29-32</sup> Entscheidend für die Differenzierung zu knochenbildenden Osteoblasten aus mesenchymalen Vorläufern ist die Aktivierung von Signalkaskaden durch die Schlüsselproteine BMP und Wnt.<sup>33</sup> Weiterhin können diese zu Osteozyten differenzieren, die in der Lage sind, die Osteoblastogenese durch die Produktion von Inhibitoren (DKK-1 und SOST) der Wnt-Signalübertragung zu

regulieren.<sup>34</sup> Osteoklasten, die an der Knochenresorption beteiligt sind, werden durch RANK-RANKL-OPG-Signalwege aktiviert. Bei erforderlicher Knochenresorption exprimieren Osteoblasten und Osteozyten RANKL auf ihrer Oberfläche, und dieses bindet dann an RANK in Osteoklastenvorläufern, wodurch deren Differenzierung aktiviert wird. OPG wird sezerniert, um die Knochenresorptionsbindung an RANKL zu stoppen, wodurch die Möglichkeit einer RANK-RANKL-Bindung blockiert und eine Knochenresorption verhindert wird.<sup>35</sup> Einmal aktiviert, binden reife Osteoklasten an die Knochenmatrix und werden polarisiert.

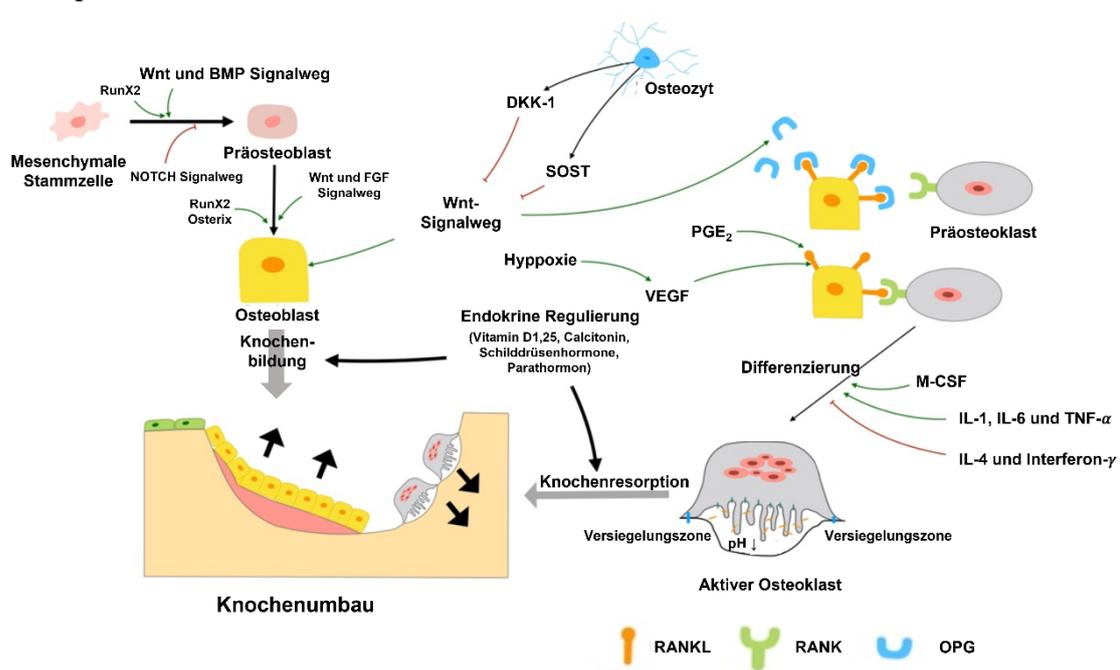


**Abbildung 3:** Zelluläre und molekulare Mechanismen der Knochenremodellierung.  
Abbildung geändert nach NOVAIS et al.<sup>36</sup>

Ihr Zytoskelett organisiert sich in Aktinringen, die eine Versiegelungszone für eine isolierte saure Mikroumgebung bilden, um Mineralien aufzulösen und die Knochenmatrix zu verdauen.<sup>37</sup> Nach der Resorption endozytieren die Osteoklasten die abgebauten Kollagenfragmente, und das freigesetzte Calcium und Phosphat werden nach Transport durch die Zelle an der funktionellen sekretorischen Domäne freigesetzt, bevor sie in den Blutkreislauf gelangen.<sup>38</sup> Auch endokrine Faktoren wie Parathormon, Vitamin D, Calcitonin und Schilddrüsenhormone beeinflussen die Knochenbildung und -resorption.<sup>39</sup> Für eine detailliertere Betrachtung der einzelnen parakrinen und endokrinen Faktoren, die am Knochenumbau beteiligt sind, soll auf weiterführende Lektüre verwiesen werden.<sup>28,40</sup>

### 1.3) Derzeitige klinische Behandlungsmöglichkeiten komplizierter Frakturen

Die klinische Methode der Wahl zur Knochenregeneration ist nach wie vor die Autotransplantation (oder auch Autograft-Technik).<sup>41</sup> Hier dient das eigene Skelett als Ressource für das Spendermaterial. Dabei wird Knochen chirurgisch von einer Spenderstelle, typischerweise dem Beckenkamm, entnommen und an der defekten Stelle platziert. Die Überlegenheit dieses Therapiekonzeptes resultiert aus der hohen biologischen Leistungsfähigkeit des Transplantats, die sich aus der Realisierung wichtiger Anforderungen wie Osteokonduktion (Unterstützung des natürlichen Knochenwachstums), Osteoinduktion (Stimulierung der Knochenneubildung/Osteoneogenese) und Osteogenese (Knochenentwicklung) ergeben.<sup>42</sup> Obwohl diese Technik effektiv ist, sind die Mengen an autologem Knochen begrenzt, und sie kann zu einer beträchtlichen Morbidität an der Entnahmestelle und anhaltenden postoperativen Schmerzen führen.<sup>43</sup>

Bei Allotransplantaten wird das Knochentransplantat einem Spender entnommen und kann im Vergleich zum Autotransplantat in größeren Mengen gewonnen werden. Das Transplantat kann dabei von einer lebenden Person oder einer Leiche entnommen werden. Durch die strengen Verarbeitungsverfahren, denen das Spendermaterial unterzogen wird, wird sichergestellt, dass das Allotransplantat keine lebenden Zellen enthält. Es dient somit als inerte Füllstoff für den Knochendefekt, jedoch ohne intrinsische osteogene Aktivität. Durch das geringe osteogene Potenzial haben Allotransplantate eine schlechte Transplantat-Wirt-Integration, die zu zahlreichen Knochenregenerationsausfällen führt und eine hohe Spätversagensrate aufweist. Zusätzlich besteht ein Infektionsrisiko durch einen Erregertransfer vom Spender auf den Empfänger.<sup>44,45</sup> Dennoch ist Knochen nach Blut das am zweithäufigsten allograftierte Gewebe, was die hohe Nachfrage nach Materialien zur Unterstützung der Knochenheilung widerspiegelt.<sup>46</sup>

Demineralisierte Knochenmatrix (engl. *Demineralized Bone Matrix*, DBM) ist eine Form von Allotransplantat, bei der eine saure Lösung zur Entfernung mineralischer Komponenten verwendet wird, während ein Großteil der proteinhaltigen Komponenten nativ im Knochenimplantat verbleibt, zusammen mit geringen Mengen an calciumbasierten Feststoffen, anorganischen Phosphaten und Spuren von Zelltrümmern. Somit hat DBM den theoretischen Vorteil, sowohl osteokonduktive als auch osteoinduktive Eigenschaften zu besitzen.<sup>47</sup> Neben einer beträchtlichen Variabilität von Charge zu Charge liegen jedoch

zusätzlich nur wenige qualitativ hochwertige Studien vor und seine inhärente osteoinduktive Aktivität beim Menschen ist unklar.<sup>48,49</sup>

Andere Behandlungsoptionen für die Knochenreparatur umfassen die Distraktionsosteogenese mit externen ILIZAROV-Fixatoren, die auf der Fähigkeit basiert, das Knochenwachstum durch langsames Auseinanderziehen zweier abgeschnittener Knochenenden zu stimulieren. Weiterhin besteht eine Therapieoption mit der MASQUELET-induzierten Membrantechnik, einem zweistufigen Verfahren, bei dem der Chirurg einen Abstandshalter aus Polymethylmethacrylat (Spacer) in den Knochendefekt einsetzt und nach Bildung einer hochgradig osteogenen Membran um den Spacer diesen wieder entfernt. Mit dem Reamer-Irrigator-Aspirator (RIA) kann autogenes spongiöses Knochentransplantatmaterial aus dem intramedullären Kanal des Femurs mithilfe eines spezifischen Bohrsystems entnommen werden.<sup>50-52</sup> Während sich gezeigt hat, dass diese Techniken Knochendefekte verbessern können, sind die Ergebnisse widersprüchlich und mit hohen Kosten und erhöhter Morbidität verbunden. Im Speziellen treten bei den ILIZAROV- und MASQUELET-Techniken zahlreiche Komplikationen auf, einschließlich hoher Raten von *Pin-Tract*-Infektion (Infektion um Nägel, Stifte oder Drähte bei externer Fixation) und Gelenksteifheit. Zudem erfordern diese Methoden längere Behandlungszeiten, die eine hervorragende Patienten-Compliance voraussetzen.<sup>53-56</sup> Die RIA-Knochentransplantations-technik wurde darüber hinaus in Verbindung mit iatrogenen Femurfraktur und kortikaler Perforation gebracht.<sup>57</sup>

Angetrieben von der dringenden klinischen Notwendigkeit, alternative Behandlungstherapien zu entwickeln, sind in den letzten Jahrzehnten neue Forschungsgebiete und interdisziplinäre Ansätze entstanden. Diese sollen die gleichen Ergebnisse wie Knochenautotransplantate und Alлотransplantate erzielen, jedoch die damit verbundenen Nachteile umgehen.

#### **1.4) Neue Strategien in der Knochenregeneration**

Das erfolgreiche Management von Knochenverlustszenarien erfordert nach GIANNOUDIS et al. vier notwendige biologische Komponenten: (1) ansprechende osteogene Zellen, (2) osteoinduktive Wachstumsfaktoren, (3) eine osteokonduktive Matrix und (4) eine optimale mechanische Umgebung.<sup>58</sup> In den vergangenen Jahrzehnten haben sich *Tissue Engineering* (deutsch Gewebekonstruktion, TE) und regenerative Medizin als vielversprechende Strategien für die Knochenrekonstitution herauskristallisiert, mit dem Ziel, die mit

traditionellen Techniken verbundenen Komplikationen zu umgehen und die oben genannten Anforderungen zu erfüllen.<sup>59</sup> Als interdisziplinäres Gebiet beinhaltet TE die kombinierte Verwendung von Stamm- bzw. Vorläuferzellen, Signalmolekülen und Biomaterialien, um die Regeneration von Geweben und Organen zu unterstützen, denen das Selbstregenerationspotenzial fehlt.<sup>60,61</sup> Das Konzept ist schematisch in Abbildung 4 dargestellt. Dieser Trend umfasst sowohl TE-Projekte, die darauf abzielen, Organe für Transplantationen unter Laborbedingungen zu gewinnen, als auch die Forschung an Stammzellen, die unter physiologischen Bedingungen eine Schlüsselrolle bei der Geweberegeneration spielen, sowie Gentechnik, *Drug Delivery* und Materialwissenschaften.<sup>62</sup>

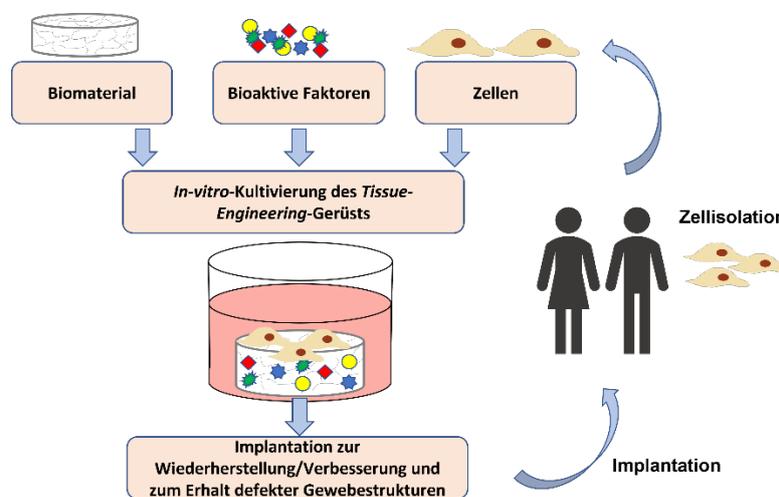


**Abbildung 4:** Schematische Darstellung des Tissue-Engineering-Konzeptes.

#### 1.4.1) Biomaterialien für den Knochenersatz

Knochenersatzstoffe können definiert werden als ein synthetisches, anorganisches oder biologisch organisches Biomaterial, das zur Behandlung eines Knochendefekts anstelle von autogenem oder allogenen Knochen eingesetzt werden kann.<sup>63</sup> Als Biomaterial wird dabei jede Substanz oder Kombinationen von Substanzen definiert, die Gewebe, Organe oder Funktionen des Körpers teilweise oder vollständig ergänzt oder ersetzt.<sup>64</sup> Idealerweise sollten diese Knochenersatzmaterialien für den Einsatz als Implantat im TE mehrere Kriterien erfüllen. Sie sollten biokompatibel, bioresorbierbar, osteokonduktiv, osteoinduktiv, strukturähnlich zum Knochen, porös, mechanisch widerstandsfähig, einfach zu handhaben, sicher und kostengünstig sein.<sup>65</sup> Eine Reihe von Gerüsten, hergestellt aus verschiedenen Arten von Materialien, wurde im Laufe der Zeit entwickelt und für die Gewebezüchtung des Knochengewebes verwendet und untersucht. Die verwendeten

Materialien können dabei in folgende Gruppen unterteilt werden: Polymere (synthetische und natürliche), Keramik, Metalle und Komposite, die Kombinationsprodukte aus den zuvor genannten Biomaterialien sind. In Tabelle 2 sind Beispiele für die jeweiligen Gruppen sowie deren Vor- und Nachteile aufgelistet.<sup>66</sup> Derzeit gibt es mehrere Technologien, die eine Herstellung poröser Gerüste ermöglichen (z. B. 3D-Druck, Elektrosponnen, Stereolithographie, *Fused Deposition Modeling*, selektives Lasersintern, Gefriertrocknung, Gasschäumen, Lösungsmittelguss bzw. Partikellaugung und Phasentrennung).<sup>67</sup> Trotz der schnellen Entwicklung von Technologien für die Herstellung von Biomaterialien stehen Forscher/-innen immer noch vor der Herausforderung, vollständig biokompatible Materialien mit geeigneten physikalisch-chemischen und mechanischen Eigenschaften zu entwickeln.<sup>68</sup> Ein häufiges Problem bei der Verwendung von Biomaterialien ist die langsame Implantatintegration. Eine erfolgreiche Osteointegration beruht nämlich nicht nur auf der mechanischen Verzahnung zwischen Implantat und Gewebe, sondern auch auf zellulären Interaktionen auf der Oberflächenebene, um die Osteokonduktion, Osteoinduktion und Heilung während der frühen Phase der Implantation zu fördern.<sup>69</sup> Neuartige Methoden zur Verbesserung der Biomaterialintegration sind daher ein aktuelles Forschungsziel.<sup>70,71</sup> Insbesondere Modifikationen der Oberflächen- oder Masseneigenschaften der oben genannten Materialien bieten eine hervorragende Alternative zur Optimierung der Gesamtleistung des Implantats.

Material	Beispiele	Vorteile	Nachteile
Polymere (natürliche)	<ul style="list-style-type: none"> <li>➤ Proteine: Kollagen, Fibrin, Gelatine, Seidenfibroin</li> <li>➤ Polysaccharide: Hyaluronsäure, Chondroitinsulfat, Cellulose, Stärke, Alginat, Agarose, Chitosan, Dextran</li> </ul>	<ul style="list-style-type: none"> <li>+ biologisch abbaubar</li> <li>+ Biokompatibilität</li> <li>+ Bioaktivität</li> <li>+unbegrenzte Quelle</li> </ul>	<ul style="list-style-type: none"> <li>- geringe mechanische Festigkeit</li> <li>- hohe Abbauraten</li> </ul>
Polymere (synthetische)	<ul style="list-style-type: none"> <li>➤ Polyglykolsäure</li> <li>➤ Polymilchsäure</li> <li>➤ Poly-(ε-caprolacton)</li> <li>➤ Poly-(laktid-co-glykolid)</li> <li>➤ Polyhydroxyethylmethacrylat</li> </ul>	<ul style="list-style-type: none"> <li>+ Bioabbaubarkeit</li> <li>+ Biokompatibilität</li> <li>+ Vielseitigkeit</li> </ul>	<ul style="list-style-type: none"> <li>- geringe mechanische Festigkeit</li> <li>- hohe lokale Konzentration an sauren Abbauprodukten</li> </ul>
Keramik	<ul style="list-style-type: none"> <li>➤ Calciumphosphat: korallener oder synthetischer Hydroxyapatit (HAP), Silikat-substituiertes HAP, β-Tricalciumphosphat, Dicalciumphosphat-Dehydrat</li> <li>➤ Biogläser und Glaskeramik: bioaktive Gläser aus Silikat oder Borat/Borosilikat</li> <li>➤ Aluminiumoxid-Keramik</li> </ul>	<ul style="list-style-type: none"> <li>+ Biokompatibilität</li> <li>+ Bioabbaubarkeit</li> <li>+ Bioaktivität</li> <li>+ Osteokonduktivität</li> </ul>	<ul style="list-style-type: none"> <li>- Sprödigkeit</li> <li>- geringe Bruchfestigkeit</li> <li>- Abbauraten schwer vorhersagbar</li> </ul>
Metalle	<ul style="list-style-type: none"> <li>➤ Titan und seine Legierungen</li> <li>➤ Tantal</li> <li>➤ Edelstahl</li> <li>➤ Magnesium und seine Legierungen</li> </ul>	<ul style="list-style-type: none"> <li>+ hervorragende mechanische Eigenschaften</li> <li>+ hohe Festigkeit</li> <li>+ Biokompatibilität</li> </ul>	<ul style="list-style-type: none"> <li>- mangelnde Gewebefesthaftung</li> <li>- Korrosion</li> <li>- Toxizitätsgefahr durch Freisetzung von Metallionen</li> </ul>

**Tabelle 2:** Knochenersatzmaterialien für die Knochenreparatur und -regeneration: Beispiele, Vor- und Nachteile. Tabelle geändert nach GARCÍA-GARETA et al.<sup>66</sup>

### 1.4.2) Oberflächenmodifizierung

Die Modifizierung der Oberfläche von Biomaterialien ermöglicht es, durch spezifische chemische oder physikalische Behandlung eine günstigere Umgebung für Zellen zu schaffen, welche die Zelladhäsion, -proliferation und -migration verbessert.<sup>72</sup> Insbesondere die Anwendung von nanoskaligen Oberflächenmodifizierungen kann die Leistung der Gerüste und die zellulären Reaktionen auf die Gewebereparatur optimieren.<sup>68</sup> Die biologischen und mechanischen Eigenschaften sowie der Abbau von Knochengerüsten können verbessert werden, indem Beschichtungen im Nano- und Mikromaßstab unter Verwendung verschiedener Abscheidungsverfahren aufgebracht werden; Beispiele für diese Verfahren sind Atomlagenabscheidung, Schicht-für-Schicht (engl. *Layer-by-Layer*, LbL)-Technik, *Plasma Spraying*, elektrophoretische Abscheidung oder Sol-Gel-Prozesse.<sup>73-75</sup> Insbesondere die LbL-Technik ist vielversprechend bei der Bereitstellung einer Umgebung, die dem nativen Knochen ähnelt, indem sie die Strukturen und Funktionen der nativen ECM nachahmt und die Zelladhäsion, -proliferation und -migration fördert.<sup>76-78</sup>

#### 1.4.2.1) *Layer-by-Layer-Methode für die Oberflächenmodifizierung*

Die LbL-Technik wurde 1992 von DECHER und Mitarbeitern entwickelt und ist eine einfache und effektive Strategie zur Oberflächenmodifizierung. Die Technik basiert ursprünglich auf elektrostatischer Anziehung zur Bildung von Polyelektrolytkomplexen. Dabei kommt es zur Adsorption von entgegengesetzt geladenen Polyelektrolyten auf einem Substrat, was in einer Abscheidung von idealerweise einheitlichen Einzelschichten der Polyelektrolyte resultiert. Die Wiederholung dieses Vorgangs mit entgegengesetzt geladenen Polyelektrolyten führt letztlich zur Bildung mehrschichtiger Polyelektrolytfilme, die auch als Polyelektrolyt-Mehrschichtsysteme (PEM) bezeichnet werden. Neben der elektrostatischen Anziehung kann die Bildung von Mehrschichtsystemen auch durch kovalente Bindung, Van-der-Waals-Kräfte, Wasserstoffbrückenbindungen und hydrophobe Wechselwirkungen oder eine Kombination dieser Kräfte erzeugt werden.<sup>79</sup> Die Eigenschaften der nanostrukturierten Mehrschichtsysteme werden durch die verwendeten Makromoleküle beeinflusst. Unter den verschiedenen Methoden der LbL-Beschichtung ist die traditionelle immersive Methode die am weitesten verbreitete Technologie. Aufgrund der Einfachheit des Tauchprozesses zum Beschichten von Substraten nahezu jeder Geometrie oder Größe ist dieser Ansatz leicht zugänglich.<sup>80</sup> In Abbildung 5 ist dieser Prozess schematisch dargestellt. Um nicht anhaftende oder schwach anhaftende Polyelektrolyte zu entfernen, wird das Substrat üblicherweise zwischen den Abscheidungsschritten mit Wasser oder einem geeigneten

Lösungsmittel gespült. Wie in Abbildung 5 gezeigt wird, führt die Abscheidung von Elektrolyten auf der Oberfläche nicht zur Bildung von stöchiometrischen 1:1-Komplexen, sondern zu einer Überkompensation der Ladung an der Oberfläche, wodurch die Abscheidung weiterer Schichten durch elektrostatische Wechselwirkungen ermöglicht wird.<sup>81</sup> Dieser Vorgang kann wiederholt werden, bis die gewünschte Dicke der Materialbeschichtung erreicht ist.

Um den LbL-Abscheidungsprozess zu beschleunigen, haben SCHLENOFF et al. das Sprüh-LbL-Verfahren eingeführt, bei dem Polyelektrolytlösungen auf ein vertikales Substrat gesprüht werden und die Schicht nach Entwässerung und Trocknung gebildet wird.<sup>82</sup> Daher hängt die Zeit für die Bildung der Monoschicht nicht von der Diffusion der molekularen Spezies ab.

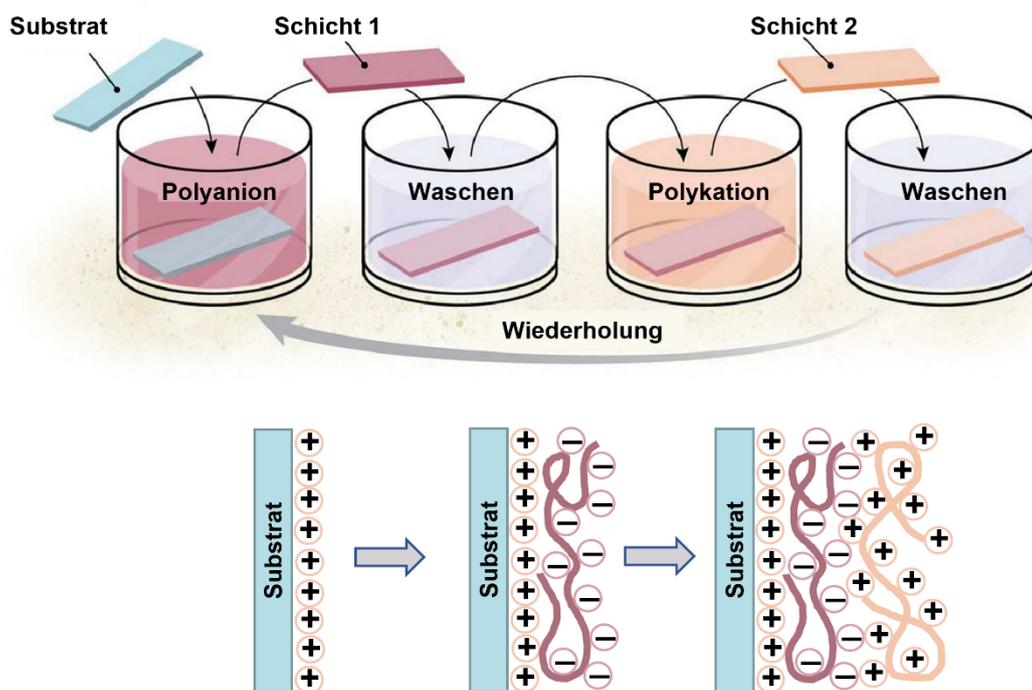


**Abbildung 5:** Prinzip der Layer-by-Layer-Methode. Abbildung geändert nach FERREIRA et al.<sup>83</sup>

Eine weitere LbL-Technik mit kurzer Abscheidungszeit ist die Spin-LbL-Methode. Bei dieser Technik werden die Lösungen oder Suspensionen auf einem Substrat abgeschieden, das an einem Schleuderbeschichter befestigt ist. Die Rotationsgeschwindigkeit erzeugt eine hohe Zentrifugalkraft und einen Luftstrom an der Oberfläche, der ein schnelles Verdünnen und Trocknen der Flüssigkeit ermöglicht, was eine hohe Gleichmäßigkeit der Schicht fördert.<sup>84,85</sup>

Insgesamt hat sich die LbL-Technik als einfache, effiziente und vielseitige Methode zur Oberflächenmodifikation bei der Herstellung von TE-Gerüsten erwiesen.<sup>86</sup> Darüber hinaus können die physikalisch-chemischen Eigenschaften von Mehrschichtfilmen wie Topographie, Elastizität und Festigkeit sowie Hydrophobie bzw. Hydrophilie optimiert werden, indem die Beschichtungszusammensetzung und die Verarbeitungsparameter geändert werden, was wiederum die Kontrolle über biologische Zellreaktionen ermöglicht.<sup>83</sup> Weiterhin erlauben die milden, wässrigen Montagebedingungen die Einarbeitung kleiner Moleküle und biologischer Wirkstoffe unter Vermeidung von Lösungsmitteln, Temperaturen, pH-Werten und Ionenstärken, die diese Verbindungen destabilisieren können. In zahlreichen Studien wurde über die Verwendung der LbL-Technik berichtet, um Proteine, Wachstumsfaktoren, Polysaccharide, Nukleinsäuren und funktionelle Peptide in Biomaterialien einzubauen und Beschichtungen mit kontrollierten Abbauraten herzustellen.<sup>87-90</sup> Eine Vielzahl von Komponenten wurde bisher in LbL-Beschichtungen eingesetzt. Zu den am häufigsten verwendeten Polyelektrolyten zählen biokompatible Polyelektrolyte wie Chitosan (CHI), Hyaluronsäure (HA), Chondroitinsulfat (CS), Kollagen Typ I (COL), Heparin und Alginat.<sup>91</sup>

### **1.4.3) Oberflächenfunktionalisierung im Bereich der Knochenregeneration**

Innovative Ansätze im Knochen-TE streben die Verwendung von Biomaterialien an, die zusätzlich zur Biokompatibilität ein inhärentes osteoinduktives Potenzial aufweisen, indem sie über direkte Wechselwirkungen zwischen Zellen und Biomaterial *in situ* Regenerationsmechanismen induzieren. Diese Funktionalisierung von Knochengerüstmaterialien kann durch Beladen mit Biomolekülen (z. B. Wachstumsfaktoren und/oder Arzneimitteln) erzielt werden, um Knochenerkrankungen zu behandeln oder die Knochenregeneration durch Stimulation von Zelladhäsion, -proliferation und -differenzierung zu fördern. Nachfolgend soll auf verschiedene Strategien für die Funktionalisierung von PEMs eingegangen werden.

#### *1.4.3.1) Arzneimittel*

Im Implantat eingebaute Arzneimittel sollen am gewünschten Ort, in angemessener Konzentration und über einen bestimmten Zeitraum wirken. Zusammengesetzte LbL-Filme können dazu beitragen, diese Anforderungen zu erfüllen, indem sie den Freisetzungsräum des Arzneimittels begrenzen, eine lokale Abgabe an das Gewebe ermöglichen, die Toxizität reduzieren und Schutz vor dem Kontakt mit physiologischen Medien bieten. Eine Vielzahl von Arzneimitteln wurde angewendet, von denen bekannt ist, dass sie die Knochenbildung

fördern, z. B. Dexamethason (DEX) und Simvastatin.<sup>92,93</sup> Von diesen Arzneimitteln hat sich DEX, ein synthetisches Glucocorticoid, aufgrund seiner guten Stabilität und geringen Kosten als bevorzugter Arzneimittelkandidat für die Knochenbildung etabliert. Es ist bekannt, dass DEX die Knochenbildung verstärkt, indem es die Proliferation und Differenzierung von mesenchymalen Stammzellen zu Osteoblasten induziert. Es wurde gezeigt, dass DEX *in vitro* die osteogene Differenzierung von Stammzellen induziert, indem es die Transkription von FHL-2 erhöht. Die Bindung von FHL-2 an  $\beta$ -Catenin potenziert den Transport von  $\beta$ -Catenin zum Zellkern, wo es TCF/LEF-1 bindet und zur Transkription von RUNX2 führt. Zudem trägt DEX zur osteogenen Differenzierung bei, indem es die Expression des RUNX2-Co-Aktivators TAZ erhöht. Darüber hinaus stimuliert die DEX-Behandlung die Expression des Gens, das für MKP-1 kodiert, das den Schlüsseltranskriptionsfaktor RUNX2 über die Signalübertragung der ERK dephosphoryliert und dadurch aktiviert.<sup>94</sup> Hohe Konzentrationen von DEX würden jedoch die Proliferation von Osteoblasten unterdrücken und toxische Nebenwirkungen verursachen.<sup>95</sup> Daher ist eine anhaltende Freisetzung von DEX aus dem Depot von Vorteil, um die Wirksamkeit zu verbessern und seine Nebenwirkung auf die Knochenregeneration zu minimieren.<sup>96</sup>

#### 1.4.3.2) Liposomen

Um die zelluläre Aufnahme und die Bioverfügbarkeit von Arzneimitteln zu verbessern sowie deren unerwünschte Effekte zu reduzieren, werden liposomale Nanopartikel eingesetzt, die diese Arzneimittel verkapseln. Darüber hinaus können Liposomen aufgrund ihrer inhärenten Ladung als Komponente für die Bildung von Multischichtsystemen durch LbL verwendet werden. PEMS können als Reservoir für die lokale Freisetzung von Arzneimitteln aus Liposomen dienen. Liposomen werden in mehr als 20 % der zugelassenen klinischen Studien zur kontrollierten Arzneimittelabgabe als Arzneistoffträger verwendet.<sup>97</sup> MONTEIRO et al. konnten in einer Studie bereits demonstrieren, dass eine Verkapselung von DEX in Liposomen die Osteogenese von MSCs fördern kann.<sup>98</sup>

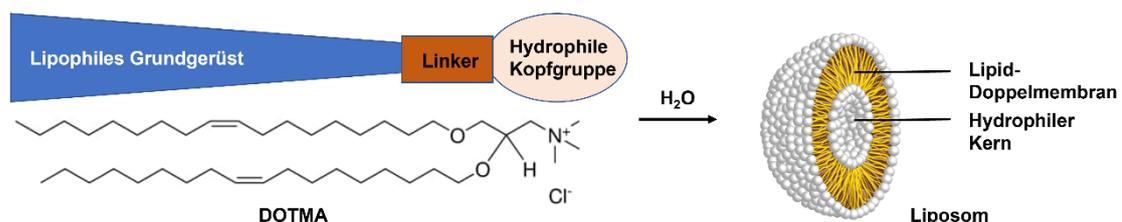


**Abbildung 6:** Struktureller Aufbau kationischer Lipide am Beispiel von DOTMA und deren Anordnung zu Liposomen in wässriger Umgebung

Liposomale Formulierungen, die erstmals 1965 von BANGHAM beschrieben wurden, bestehen aus einer oder mehreren Lipiddoppelschichten, die das wässrige Vesikelinnere von der äußeren wässrigen Phase abgrenzen (siehe Abbildung 6). Sie sind als kugelförmige Vesikel mit Partikelgrößen im Bereich von 30 nm bis zu mehreren Mikrometern definiert. Die Nanovesikel auf Lipidbasis können durch Dispergieren amphiphiler Lipide wie Phospholipide und Cholesterol in der wässrigen Phase gebildet werden. Die treibende Kraft dafür ist der hydrophobe Effekt, der von den Alkylketten ausgeht. Bei diesem Phänomen assoziieren unpolare Moleküle in Wasser zu größeren Aggregaten. Beeinflussen lassen sich die Aggregationsstrukturen durch ionische, hydrophile oder sterische Abstoßung der Kopfgruppen.<sup>99</sup>

Für die Herstellung von Liposomen kommen neben amphiphilen Phospholipiden auch kationische Lipide zum Einsatz, die durch ein lipophiles Grundgerüst gekennzeichnet sind, das über eine Linkerstruktur mit einer kationischen Kopfgruppe verbunden ist. Das erste kationische Lipid DOTMA (siehe Abbildung 6) nutzen FELGNER et al. in ihrer Formulierung mit dem Helferlipid DOPE für die Verkapselung bzw. Komplexierung von Nukleinsäuren.<sup>100</sup> Seither wurde eine Vielzahl von kationischen Lipiden synthetisiert, wobei die Grundstruktur aus einem hydrophoben Lipidbereich und einem hydrophilen Kopfbereich unangetastet blieb, was die kationischen Lipide zu klassischen Amphiphilen macht. Zur Verbesserung der Liposomen-Eigenschaften werden häufig sogenannte Helferlipide eingesetzt, zu denen z. B. DOPE oder Cholesterol gehören. Ihnen wird eine Liposomenstabilisierende Wirkung zugeschrieben.<sup>101,102</sup> PONTI et al. zeigen in einem Überblicksartikel die Entwicklungen der letzten Jahre im Bereich der kationischen Lipide.<sup>103</sup>

#### *1.4.3.3) Proteintherapie mit Signalmolekülen*

Mit dem verbesserten Verständnis der Frakturheilung und der Knochenregeneration auf molekularer Ebene wurde eine Reihe von Schlüsselmolekülen identifiziert, die diesen komplexen physiologischen Prozess regulieren. Dabei ist die Heilung von Knochenbrüchen ein mehrstufiger Prozess, der von einer komplexen räumlich-zeitlichen Zytokinkaskade orchestriert wird und die Kombination verschiedener Zelltypen erfordert, darunter Entzündungszellen, Endothelzellen, mesenchymale Stammzellen sowie Chondrozyten und Osteozyten.<sup>104</sup> *Tissue-Engineering*-Ansätze zielen daher darauf ab, Zellen und Knochenersatzmaterialien mit diesen Signal-Biomolekülen zu kombinieren, die für eine effektive Gewebereparatur entscheidend sind. Die Hauptfamilien der Wachstumsfaktoren, die an der Knochenregeneration beteiligt sind, umfassen VEGF, FGF, TGF, BMP, PDGF,

TNF-alpha und IGF.<sup>105</sup> Besondere Aufmerksamkeit wurde jedoch auf die Verwendung der BMPs gerichtet, die mit TGF- $\beta$  verwandt sind und die Fähigkeit besitzen, eine *de-novo*-Knochenbildung zu induzieren.<sup>106</sup> Sie sind potente osteoinduktive Faktoren und induzieren sowohl die Mitogenese von MSCs und anderen Osteoprogenitoren als auch deren Differenzierung zu Osteoblasten. Ihre osteogene Wirkung üben BMPs durch ihre Wechselwirkung mit mesenchymalen Stammzellen aus, indem sie an die Oberflächenrezeptoren BMPR-1 und BMPR-2 binden und anschließend intrazelluläre kanonische und nicht-kanonische Wege auslösen, wobei der relevanteste der Smad-Transkriptionsfaktorweg ist (siehe Abbildung 7).<sup>107</sup> Die Rezeptor-regulierten Smads bilden nach BMP-Rezeptorbindung und Phosphorylierung des Typ-I-Rezeptors einen Komplex mit Smad 4, der weiterhin in den Zellkern transloziert. Die Aktivierung dieses Signalwegs führt zur Hochregulierung von Transkriptionsfaktoren, die stark mit der osteoblastischen Differenzierung assoziiert sind, wie RUNX2 und OSX (siehe Abbildung 3).<sup>108</sup> Durch die Aktivierung dieser Transkriptionsfaktoren werden weitere osteogene Marker induziert, die für die Differenzierung von Osteoblasten spezifisch sind, einschließlich typischer ECM-Komponenten wie OCN und OPN.

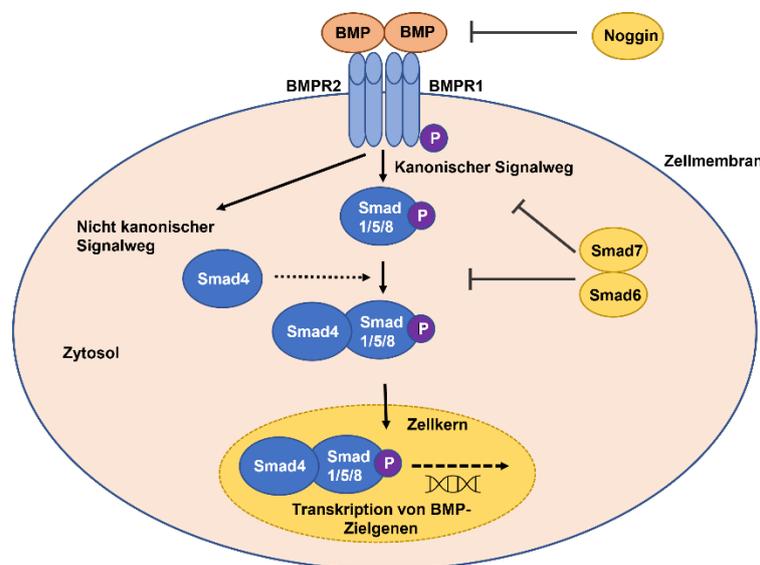


**Abbildung 7:** Signaltransduktion für die BMP-Familie. Die BMP-Signalgebung wird durch die Bindung von BMP-Liganden an BMPR1 und BMPR2 initiiert. Im kanonischen Weg phosphorylieren BMP-Rezeptoren Smad 1/5/8, die an Co-Smad4 binden können und in den Zellkern transloziert werden, um die Expression von Zielgenen zu regulieren. In den nicht-kanonischen Signalwegen aktivieren BMP-Rezeptoren Nicht-Smad-Signalwege. Die Antagonisierung erfolgt durch Noggin, Smad 6 und/oder Smad 7. BMP: Knochenmorphogenetisches Protein, BMPR: BMP-Rezeptor, P: Phosphat. Abbildung geändert nach AL-SAMMARRAIE et al.<sup>109</sup>

Unter Verwendung rekombinanter Desoxyribonukleinsäure (DNA)-Technologie ist BMP-2 als rekombinantes Protein seit 2008 für die klinische Verwendung von der Europäischen

Arzneimittel-Agentur (EMA) zugelassen (InductOs<sup>®</sup> von Medtronic BioPharma B.V., BMP-2 beladener Kollagenschwamm).<sup>110,111</sup> Rekombinantes knochen-morphogenetisches Protein-2 (rhBMP-2) konnte jedoch die klinischen Erwartungen weitgehend nicht erfüllen: Die Wirksamkeit von rhBMP-2 ist durch seine schnelle Freisetzung aus dem Gerüst begrenzt und daher sind klinisch supraphysiologische Mengen an rhBMP-2 erforderlich, um eine ausreichende Knochenbildung zu induzieren.<sup>112</sup> Dies erhöht nicht nur die Kosten der Proteintherapie, sondern wurde auch mit Komplikationen wie ektopischer Knochenbildung und Weichteilschwellung in Verbindung gebracht.<sup>113,114</sup>

#### *1.4.3.4) Lokale Gentherapie*

Die zuvor genannten Nachteile (supraphysiologische Mengen, hohe Kosten, ektopische Knochenbildung), die mit der Proteintherapie verbunden sind, haben Forscher/-innen dazu veranlasst, neue Strategien zu entwickeln, um den Mangel an Knochenregeneration an Stellen mit Knochenschwund zu überwinden. Die Gentherapie ist eine alternative Methode und beschreibt den Prozess des Einführens exogener DNA oder Boten-Ribonukleinsäure (mRNA), die für spezifische Zielproteine kodiert, in Zellen verschiedener Gewebe und deren Umwandlung in deren proteinsynthetisierende Einheiten.

Zu den Hauptvorteilen der Gentherapie gehört die Möglichkeit, die Dauer der Genexpression zu kontrollieren und auf spezifische Organe abzielen, in denen das Gen auf physiologische Weise exprimiert werden kann. So kann im Falle einer BMP-Gentherapie eine zeitlich begrenzte Sekretion des Proteins ermöglicht werden. Idealerweise ist die durch Transfektion erzielte Genexpression auf die Frakturstelle begrenzt. Dadurch ahmt die Transgenexpression natürliche Genexpressionsprozesse während der Knochenheilung nach, ohne dass hohe Dosen eines Wachstumsfaktors erforderlich sind. In Studien wurde gezeigt, dass eine BMP-Gentherapie die Sekretion des Proteins im Pikogramm-Bereich induziert und damit die Osteogenese stimulieren kann.<sup>115,116</sup> Verglichen mit der Anwendung von rhBMP-2 im Mikrogrammbereich spiegelt dies natürliche Mengen wider. Darüber hinaus wurde in Tiermodellen gezeigt, dass nur eine kurze BMP-2- oder 6-Expression erforderlich ist, um eine Knochenregeneration und Frakturheilung zu erreichen.<sup>116,117</sup> Eine systemische Distribution der Nukleinsäure und damit auch das Risiko einer Genabgabe an unerwünschte Zelltypen können zudem durch eine lokale Applikation verhindert werden. Weiterhin bietet die Einarbeitung von Nukleinsäureträgersystemen in Substraten die Möglichkeit, diese besser vor äußeren Einflüssen zu schützen, ihre

Freisetzung aus dem Trägermaterial zu kontrollieren und die Zelladhäsion zu beeinflussen, um die Zytotoxizität zu verbessern.<sup>118</sup>

Durch Immobilisierung von Genvektoren in natürlichen oder synthetischen Substraten mittels kovalenter Bindung oder unspezifischer Adsorption entstehen genaktivierte Materialien, deren Gentransfer als Substrat-vermittelte Genabgabe (engl. *Substrate-mediated Gene-Delivery*, SMD) oder Reverse Transfektion bzw. Festphasen-Abgabe (engl. *Solid-Phase Gene-Delivery*) bezeichnet wird. Dabei hat sich die Strategie der SMD nicht nur *in vitro* als erfolgreich erwiesen, sondern auch *in vivo* bei der oberflächenvermittelten Genabgabe implantierbarer Stents. LEVY et al. formulierten dafür eine PLGA-Beschichtung für implantierbare Koronarstents, in die sie DNA integrierten. Die Nukleinsäure wurde dabei über einen Zeitraum von mindestens zehn Tagen in funktioneller Form aus dem Stent freigesetzt und ergab eine signifikante Genabgabe *in vivo*.<sup>119</sup> Daher könnte die SMD die Therapieoptionen für den Einsatz in der regenerativen Medizin erheblich bereichern.

#### 1.4.3.5) Lipoplexe

Um die Aufnahme der DNA durch Zellen zu fördern, ist es üblich, DNA mit einem Träger oder Vektor zu komplexieren. Obwohl die Abgabe von unverpackter Nukleinsäure die sicherste Art der Genabgabe darstellt, ist ein solches Verfahren eher ineffektiv, da Nukleinsäuren bei physiologischem pH-Wert anionisch sind, sodass sie nicht passiv in Zellen eindringen können. Darüber hinaus sind sie in dieser Form anfällig für einen Nuklease-vermittelten Abbau.<sup>120</sup> Daher stehen sowohl virale als auch nicht-virale Verfahren für den Gentransfer zur Verfügung. Ihre Vor- und Nachteile sind in Tabelle 3 dargestellt. Viren haben die intrinsische Fähigkeit, Zellen zu infizieren, und die virale Gentherapie macht sich diese effiziente Fähigkeit von Viren zunutze, um die Ziel-DNA (durch einen als ‚Transduktion‘ bezeichneten Prozess) in Zellen einzuführen. Sequenzen des viralen Genoms, die mit Virulenz und Pathogenität assoziiert sind, werden im Allgemeinen eliminiert und mit Zielgenen und ihren regulatorischen Sequenzen modifiziert, um einen rekombinanten viralen Vektor herzustellen. Virale Vektoren sind jedoch mit zahlreichen Nachteilen verbunden, z. B. Immunogenität und Kanzerogenität, die Wissenschaftler/-innen dazu veranlasst haben, nach neuen Möglichkeiten für den Gentransfer zu forschen. FELGNER et al. prägten 1987 erstmals den Begriff der Lipofektion, der den Gentransfer mittels kationischer Lipid/DNA-Komplexe, der sogenannten Lipoplexe (LPX), beschreibt.<sup>100</sup> Diese können die Nachteile umgehen, die mit einer Genabgabe mittels viraler Vektoren auftreten.<sup>121</sup> Der als Transfektion benannte nicht-virale Gentransfer ist preiswerter,

einfacher in der Herstellung, in größeren Maßstäben produzierbar und in der Lage, Risiken wie Immunogenität und Kanzerogenität zu minimieren.<sup>122</sup>

Vektortyp	Vorteile	Nachteile
Virale Vektoren	+ hohe Transduktionseffizienz + Transgen-Expression kann durch Virus kontrolliert werden (transient oder persistent) + Transduktion spezieller Zelltypen möglich	- hohe Immunogenität - begrenzte Beladungskapazität - Sicherheitsbedenken - Risiko einer Tumorentstehung durch Insertionsmutagenesen - Schwierigkeit des Scale-ups - teure und komplexe Produktion - Risiko einer übermäßigen Proteinsekretion durch stabile Integration
Nicht-virale Vektoren	+ einfache Herstellung + geringe Kosten + geringe Immunogenität + hohe Beladungskapazität	- geringe <i>In-vivo</i> -Transfektionseffizienz - material- und konzentrationsabhängige Toxizität - transiente Genexpression

**Tabelle 3:** Vektortypen für die Gentherapie und ihre Vor- und Nachteile.<sup>123</sup>

Zuletzt wurden mit den COVID-19-mRNA-Impfstoffen Comirnaty® (Pfizer/BioNTech) und Spikevax® (Moderna) erstmals auf Lipofektion basierende Arzneimittel, genauer Vakzine, auf dem europäischen Markt zugelassen. Dies veranschaulicht die Erfolge, die mit dieser Art von Genabgabe erzielt wurden, um genetisches Material zu stabilisieren und erfolgreich in Zellen zu transportieren.<sup>124</sup>

Als Schlüsselkomponente für die Lipofektion kondensiert und komplexiert die kationische Lipidformulierung die negative Nukleinsäure. Beteiligte Prozesse sind unter anderem die COULOMB-Wechselwirkung zwischen den positiven Ladungen der Lipide und den negativen Ladungen der DNA-Phosphatgruppen sowie die Freisetzung von Gegenionen und der daraus resultierende Entropiegewinn.<sup>125</sup> Die Komplexbildung zwischen Nukleinsäure und kationischer Lipidformulierung ergibt sich dabei aus einer spontanen Organisation von thermodynamisch quasi-stabilen Strukturen, die als LPX bezeichnet werden.<sup>126</sup> Ein nur teilweise verstandener Prozess sind dabei die Kinetik und Thermodynamik dieser Komplexierung, die von den relativen Konzentrationen der Komponenten, der Geschwindigkeit und Reihenfolge des Mischens sowie von Temperatur, Salzkonzentrationen und Ionenstärke abhängen. Die Lipide können DNA zu chemisch und physikalisch unterschiedlichen Aggregaten kondensieren, deren Struktur und/oder Transfektionsaktivität von den zuvor genannten Variablen abhängen.<sup>127</sup> Für eine detaillierte Auseinandersetzung mit den unterschiedlichen LPX-Strukturen soll auf zusammenfassende Literatur verwiesen werden.<sup>128</sup> Typischerweise werden Komplexe zwischen kationischen Lipiden und Nukleinsäuren durch einfaches Mischen von vorgeformten kationischen Liposomen und DNA in einer wässrigen Lösung hergestellt. In den letzten Jahren hat auch

die Mikrofluidik als Herstellungsmethode an Bedeutung gewonnen, da dieses Verfahren es erlaubt, Prozessparameter einzustellen.<sup>129</sup> Je nach Menge der eingesetzten Nukleinsäure können bei der Komplexbildung neutral, negativ oder positiv geladene LPX entstehen. Das Ladungsverhältnis zwischen kationischen Amino-Funktionen der Lipidformulierung (N) zu Phosphatgruppen der DNA (P) wirkt sich hierbei ebenfalls auf die Transfektion aus und wird als N/P-Verhältnis ausgedrückt.<sup>130</sup> Für die effiziente Transfektion werden meist LPX mit positiver Gesamtladung verwendet, da diese über elektrostatische Wechselwirkungen mit der negativ geladenen Zellmembran interagieren können und somit eine Membraninteraktion und eine Endozytose antreiben.<sup>131</sup> Die Wege der zellulären Aufnahme von LPX und die intrazelluläre Freisetzung des genetischen Materials werden bis zum jetzigen Zeitpunkt nicht im Detail verstanden. Die grundlegenden Mechanismen der Genübertragung mittels LPX sind in Abbildung 8 dargestellt. Für eine detailliertere Auseinandersetzung soll auf einen Übersichtsartikel verwiesen werden.<sup>131</sup>

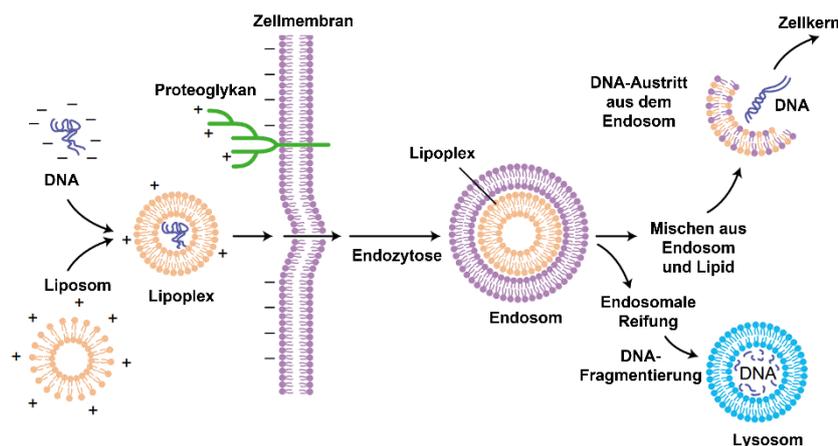


**Abbildung 8:** Grundlegender Mechanismus der nicht-viralen Genübertragung mit Lipoplexen. DNA wird durch Wechselwirkung mit einem kationischen Lipid kondensiert, um einen Lipoplex zu bilden. Durch Wechselwirkung mit der Zellmembran verschmelzen die Strukturen mit der Zellmembran. Die Komplexe werden durch Endozytose internalisiert, was zur Bildung eines doppelschichtigen invertierten Vesikels führt. Während der Reifung des Endosoms zu einem Lysosom kann die endosomale Wand aufbrechen und die enthaltene DNA in das Zytoplasma oder auch die perinukleäre Region freigesetzt werden. In den Zellkern transportierte DNA kann zur Genexpression führen. Alternativ könnte DNA innerhalb des Lysosoms abgebaut werden. Abbildung geändert nach PARKER et al.<sup>132</sup>

#### 1.4.4) Interaktion zwischen Biomaterial und mesenchymalen Stammzellen

Neben den Biomaterialien ist ein weiteres Element des TE die Interaktion mit ansprechenden Zellen. Da ausdifferenzierte Zellen gewöhnlich eine niedrige Proliferationsaktivität aufweisen und ihre Isolation teilweise problematisch ist, werden im Knochen-TE insbesondere MSCs benutzt.<sup>133</sup> Ihre einfache Isolierung, ausgeprägte Proliferationsaktivität und die Fähigkeit, zu Adipozyten, Chondrozyten, Myoblasten, Osteoblasten oder Tenozyten zu differenzieren, macht sie zu optimalem Zellmaterial im TE.<sup>134</sup> Ob und in welchen

Phänotyp sich eine Stammzelle differenziert, wird hauptsächlich durch den intrinsischen Zustand oder die Mikroumgebung bestimmt, in dem sich die Stammzelle befindet.<sup>135</sup> Viele der Kultivierungs-Stimuli, von denen bekannt ist, dass sie die MSC-Differenzierung beeinflussen, wurden identifiziert und sind in Abbildung 9 dargestellt. Zusammen mit Faktoren, die das Schicksal von Stammzellen induzieren, ist die Wechselwirkung zwischen Stammzelle und Biomaterial ein bedeutsamer Parameter, der die Eigenschaften von Stammzellen sowohl in Kultur als auch *in vivo* beeinflusst.

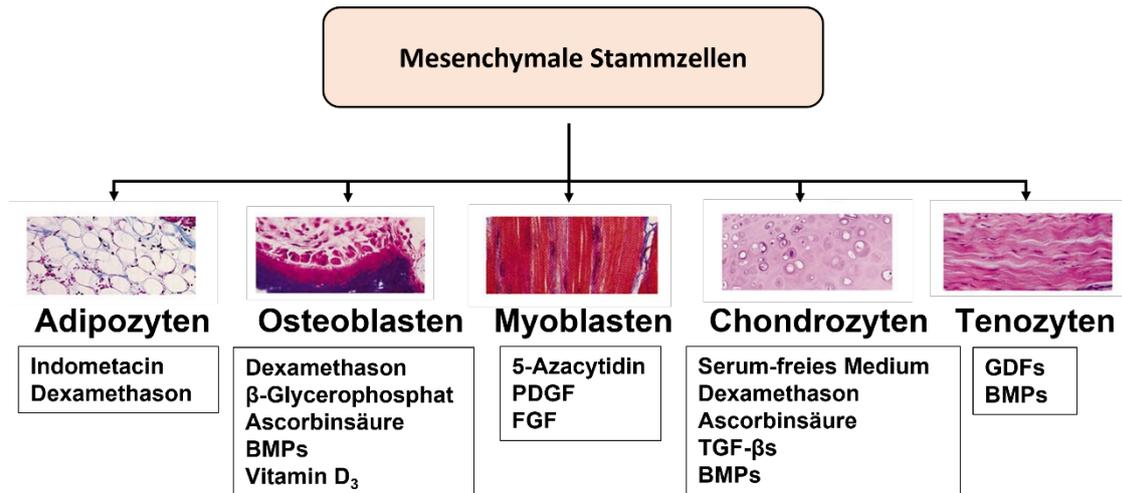


**Abbildung 9:** Differenzierungspotenzial von mesenchymalen Stammzellen. Diese Abbildung zeigt einige der In-vitro-Kulturbedingungen (eingerahmt), die den jeweiligen Prozess der Differenzierung in eine bestimmte Linie fördern können.

Diese Wechselwirkungen und damit die zellulären Aktivitäten sind von einer Vielzahl von Materialeigenschaften abhängig. Es ist bekannt, dass Benetzbarkeit, Elastizität, chemische Zusammensetzung und Topographie eines Biomaterials das Verhalten von Zellen beeinflussen.<sup>136-138</sup> LI et al. diskutieren in einem Überblicksartikel umfassend physikalische und chemische Parameter eines Biomaterials hinsichtlich ihres Einflusses auf MSCs.<sup>139</sup>

Zellen, einschließlich Stammzellen, können mehrere extrazelluläre Signale aus ihrer Mikroumgebung wahrnehmen und sie gleichzeitig in kohärente Umweltsignale konvertieren, um das Zellverhalten zu regulieren. Unspezifische Adhäsion tritt im Allgemeinen durch Van-der-Waals-, ionische und elektrostatische Kräfte auf. Im Vergleich dazu wird die spezifische Adhäsion durch die ECM vermittelt, einschließlich Kollagen I, Fibronectin, Laminin, Vitronectin, Peptide, Wachstumsfaktoren, Glucosamin und anderer aktiver Moleküle. Durch die Aktivierung von Rezeptoren auf der Oberfläche der Zellmembran und die Übertragung des chemischen Signals wird eine Reihe biologischer Zellaktivitäten moduliert.<sup>140</sup> Eine wesentliche Technik im TE zielt daher auf die

Verwendung von ECM-Komponenten ab, um die ECM-Struktur zu imitieren und dadurch besser mit Stammzellen zu interagieren.

Der Zelladhäsionsprozess besteht aus einer Reihe von kaskadierten Reaktionen, die in vier Schritte unterteilt werden können: Zelladhäsion, Zellausbreitung, Organisation des Zytoskeletts und die Bildung fokaler Adhäsionen.<sup>141</sup> Die anfängliche Adhäsion spielt eine entscheidende Rolle bei der Zelldifferenzierung und Langzeitstabilität und wird durch Ionenbindung oder Van-der-Waals-Kräfte vermittelt.<sup>142</sup> Die Adhäsion fördert die Wechselwirkung zwischen der ECM und dem Integrin oder Transmembranrezeptor, was zur Bildung von fokalen Adhäsionskomplexen führt. Dabei bindet die zytoplasmatische Domäne des Integrinrezeptors an Adapterproteine (z. B. Talin, Vinculin, Tensin und Paxillin), die weiter an Aktinfilamente binden.

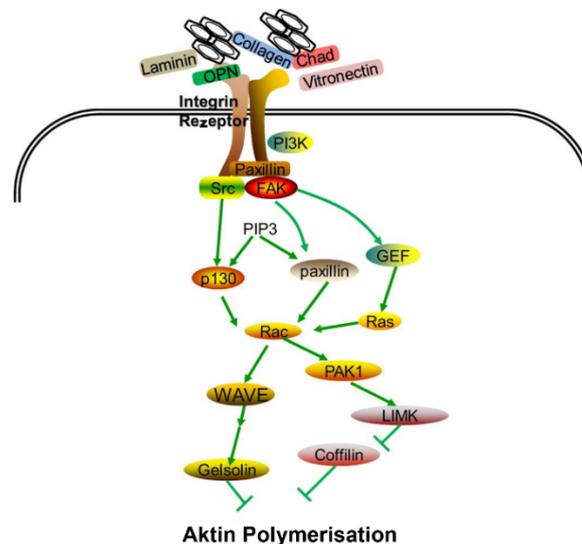


**Abbildung 10:** Der Signalweg bei Adhäsion von Stammzellen an Biomaterialien. Geändert nach GAO et al.<sup>144</sup>

Die ECM-Integrin-Zytoskelett-Achse vermittelt den Adhäsionsprozess, der nicht nur die Zell-Biomaterial-Adhäsion reguliert, sondern auch für die Signalübertragung in die Zellmembran verantwortlich ist (siehe Abbildung 10). Integrine verbinden die ECM mit dem Zytoskelett durch fokale Adhäsionskomponenten und aktivieren die fokale Adhäsionskinase (FAK) und die Src-Kinase. Die FAK phosphoryliert zwei weitere Gruppen, Paxillin und Crk-assoziertes Substrat (p130cas), welche die Bindung des Signaladapterproteins mit der fokalen Adhäsion ermöglichen.<sup>143</sup> Dieser Prozess ist von einem Aktin-Aufbau und einer dynamischen FAK-Änderung begleitet, die weiterhin in Zelladhäsion, -ausbreitung, -invasion, -proliferation und -apoptose involviert sind.<sup>144</sup>

## 1.5) Zielstellung

Das Ziel der vorliegenden Arbeit war es, ausgehend von Polyelektrolyt-Multischichtsystemen neue Konzepte für die Therapie von Knochendefekten zu entwickeln. Dafür sollten nanostrukturierte Oberflächenbeschichtungen von Knochen

ersatzmaterialien unter Verwendung der *Layer-by-Layer*-Technik entwickelt werden, denen durch gezielte Funktionalisierung das intrinsische Potenzial verliehen wird, *in situ* zelluläre Regenerationsmechanismen zu stimulieren. Hierfür sollten zwei Konzepte untersucht werden:

- 1) Es sollten Lipid/DNA-Komplexe (Lipoplexe) für die Funktionalisierung von Polyelektrolyt-Multischichtsystemen eingesetzt werden, die für das osteoinduktive Protein BMP-2 kodieren und dieses *in situ* an humanen mesenchymalen Stammzellen exprimieren können.
- 2) Weiterhin sollte eine Funktionalisierung mit Liposomen erfolgen, die das osteoinduktive Arzneimittel Dexamethason enthalten und in der Lage sind, die Differenzierung von mesenchymalen Stammzellen zu Osteoblasten zu stimulieren.

Als kationische Lipide wurden die Verbindungen OH4 und OO4 zur Verfügung gestellt, die in Publikationen bereits umfassend charakterisiert wurden und sich in Kombination mit dem Helferlipid DOPE als effiziente Transportvesikel herauskristallisiert haben.<sup>145-151</sup> Die Konjugation der Vesikel sollte mit einem osteokonduktiven Polyelektrolyt-Multischichtsystem erfolgen, für deren Herstellung die Polyelektrolyte Hyaluronsäure, Chitosan, Chondroitinsulfat und Kollagen verwendet wurden. Diese Polyelektrolyte zeichnen sich durch hervorragende Biokompatibilität und -abbaubarkeit aus und eignen sich somit als Gerüstmaterial für den Einsatz in der regenerativen Medizin.<sup>152-155</sup>

Der Schwerpunkt dieser Arbeit lag sowohl auf der physikalisch-chemischen Charakterisierung dieser Systeme als auch auf *In-vitro*-Experimenten an Modellzelllinien sowie an humanen mesenchymalen Stammzellen.

## 2) Kumulativer Teil

Allgemeine Information zu den Fachzeitschriften				
Titel	BIOspektrum	ACS Applied Materials & Interfaces	Material Science and Engineering: C	Advanced Healthcare Materials
Impact Factor 2021	0,051	10,383	8,457	11,092
5-Year Impact	0,051	8,985	6,341	8,054
Herausgeber	Springer	American Chemical Society	Elsevier	Wiley-VCH Verlag

**Tabelle 4:** Allgemeine Informationen zu den Fachzeitschriften

Darlegung des prozentualen Eigenanteils an den nachfolgenden <b>Veröffentlichungen</b>	
Publikation I	C. Husteden, F. Doberenz, N. Goergen, S. R. Pinnapireddy, C. Janich, A. Langner, F. Syrowatka, A. Repanas, F. Erdmann, J. Jedelská, U. Bakowsky, T. Groth, C. Wölk. <i>Contact-Triggered Lipofection from Multilayer Films Designed as Surfaces for In Situ Transfection Strategies in Tissue Engineering</i> . ACS Appl. Mater. Interfaces 2020 <b>Eigenanteil: A = 70 %, B = 60 %</b>
Publikation II	C. Husteden, T. Groth, C. Wölk <i>Implantatüberzüge für die in-situ Transfektion in der regenerativen Medizin</i> . BIOspektrum, Volume 20, Issue 4, 2021 <b>Eigenanteil: A = 90 %, B = 50 %</b>
Publikation III	Y.A. Brito Barrera, C. Husteden, J. Alherz, B. Fuhrmann, C. Wölk, T. Groth <i>Extracellular matrix-inspired surface coatings functionalized with dexamethasone-loaded liposomes to induce osteo- and chondrogenic differentiation of multipotent stem cells</i> . Materials Science & Engineering C 2021 <b>Eigenanteil: A = 30 %, B = 30 %</b>
Publikation IV	C. Husteden, Y. A. Brito Barrera, S. Tegtmeyer, J. Borges, J. Giselbrecht, M. Menzel, A. Langner, J. F. Mano, C.E.H. Schmelzer, C. Wölk, T. Groth <i>Lipoplex-functionalized thin-film surface coating based on extracellular matrix components as local gene delivery system to control osteogenic stem cell differentiation</i> , Advanced Healthcare Materials 2022 <b>Eigenanteil: A = 40 %, B = 35 %</b>

**Tabelle 5:** Darlegung des prozentualen Eigenanteils an den Veröffentlichungen. Der Eigenanteil setzt sich wie folgt zusammen:

A: eigener Anteil an der Planung, der Durchführung, der Auswertung der Experimente und der Anfertigung der dazugehörigen Abbildungen

B: eigener Anteil an der Anfertigung des Manuskripts.

Darlegung des prozentualen Eigenanteils an den nachfolgenden <b>Manuskripten</b>	
Manuskript I	C. Husteden, S. Tegtmeyer, J. Weber, R. Eckenstaler, F. Erdmann, F. Seifert, R. A. Benndorf, A. Langner, T. Groth, C. Wölk <i>Osteogenic Stem Cell Differentiation Induced by Contact            Triggered In Situ BMP-2 Transfection from DNA-lipid            Nanoparticle Loaded Multilayer Films</i> Eingereicht am: <b>Eigenanteil: A = 70 %, B = 70 %</b>

**Tabelle 6:** Darlegung des prozentualen Eigenanteils an den Manuskripten. Der Eigenanteil setzt sich wie folgt zusammen:

A: eigener Anteil an der Planung, der Durchführung, der Auswertung der Experimente und der Anfertigung der dazugehörigen Abbildungen

B: eigener Anteil an der Anfertigung des Manuskripts.

## 2.1) Allgemeines

Der folgende Abschnitt beinhaltet drei Publikationen, die als *Research*-Artikel in internationalen Fachzeitschriften unter Anwendung des *Peer-Review*-Verfahrens veröffentlicht wurden. Hinzu kommt ein *Perspektiven*-Artikel in einem Magazin für Biowissenschaften. Der *Perspektiven*-Artikel führt noch einmal in das angestrebte Konzept der oberflächenvermittelten Transfektion in der regenerativen Medizin ein. Weiterhin wird ein Manuskript, das zukünftig in einer internationalen Fachzeitschrift eingereicht werden soll, mit in diese Arbeit aufgenommen. Diese Artikel und das Manuskript bilden die Grundlage der vorliegenden Arbeit und fassen die experimentellen Ergebnisse zusammen. Alle Artikel thematisieren Funktionalisierungsmöglichkeiten von Oberflächenbeschichtungen auf Basis von Polyelektrolyt-Multischichtsystemen. In Artikel I und Manuskript I wird ein aus HA und CHI hergestelltes Multischichtsystem unter Verwendung der Lipidformulierung OH4:DOPE charakterisiert. Die komplexierte Nukleinsäure exprimiert *in vitro* zum einen ein Reporter-gen (pCMV-GFP) und zum anderen das therapeutisch aktive BMP-2. In den Artikeln III und IV wird die kationische Lipidformulierung OO4 verwendet. Dieses wird einerseits als Liposom eingesetzt, welches das Arzneimittel DEX verkapselt und in einem PEM-System aus COL und HA konjugiert ist (Publikation III). Andererseits wird es als LPX-formulierung angewendet und eingebettet in ein Multischichtsystem aus COL und CS. Die komplexierte Nukleinsäure exprimiert *in vitro* das Protein BMP-2 (Publikation IV).

## 2.2) Verwendete Polyelektrolyte und Lipide

**Hyaluronsäure:** HA ist ein GAG, das im gesamten menschlichen Körper vorkommt. Es ist weitverbreitet im Bindegewebe der Dermis, in der Synovialflüssigkeit, im Glaskörper und in der Zahnpulpamatrix. HA ist ein lineares Polyanion mit wiederholenden Disaccharid-Einheiten aus D-Glucuronsäure und N-Acetyl-D-Glucosamin. Die Glucuronsäure wird im Disaccharid glycosidisch  $\beta(1\rightarrow3)$  an das N-Acetyl-D-Glucosamin geknüpft, das an die nächste Glucuronsäure in der polymeren Kette glycosidisch  $\beta(1\rightarrow4)$  gebunden ist. Als ECM-Komponente hält es das Gewebe hydratisiert und erhält die physikalische Form der ECM.<sup>156</sup> HA wirkt als Signalmolekül, indem es mit Zelloberflächenrezeptoren interagiert und die Zellproliferation, -migration und -differenzierung reguliert. Weiterhin gilt es weder als zytotoxisch<sup>157</sup> noch als antigen oder immunogen.<sup>158</sup>

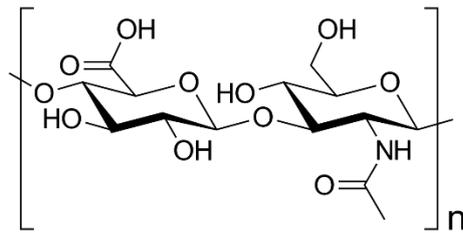


**Abbildung 11:** Chemische Struktur von Hyaluronsäure.

**Chitosan:** CHI ist die deacetylierte Form von Chitin. Chitin ist die Strukturkomponente, die im Außenskelett von Krebstieren vorkommt. Seine linearen Ketten bestehen hauptsächlich aus  $\beta$ -1,4-verknüpften N-Acetyl-D-Glucosamin- und D-Glucosamin-Einheiten, die biologisch abbaubar sind. Im Gegensatz zu seiner Quelle Chitin ist CHI in verdünnten sauren Lösungen mit einem pH-Wert unter 6,5 gut löslich, wobei der Deacetylierungsgrad und das Molekulargewicht die Löslichkeit stark beeinflussen.<sup>159</sup> Die verwendeten Deacetylierungsbedingungen sowie das Molekulargewicht des CHI beeinflussen auch eine Vielzahl physikalisch-chemischer und biologischer Eigenschaften des Polykations. CHI ist bioaktiv, biologisch abbaubar, antibakteriell sowie biokompatibel und besitzt eine hydrophile Oberfläche.<sup>160-162</sup> Ebenfalls wurde berichtet, CHI besitze das Potenzial einer verbesserten Zelladhäsion, Proliferation sowie Osteoblastendifferenzierung und -mineralisierung.<sup>163</sup>

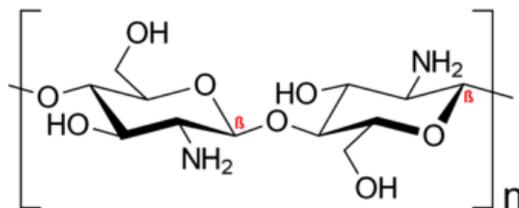


**Abbildung 12:** Chemische Struktur von Chitosan.

**Chondroitinsulfat:** CS wird in der extrazellulären Matrix von Knorpel, Knochen und anderen Geweben gefunden. CS sind O-verknüpfte GAG, die aus sich wiederholenden Glucuronsäure- und N-Acetylgalactosamin-Disacchariden bestehen. Für die Knochenentwicklung sind CS-GAGs bedeutsam, da sie die Osteogenese unterstützen und die Knochenresorption unterdrücken können.<sup>164, 165</sup>

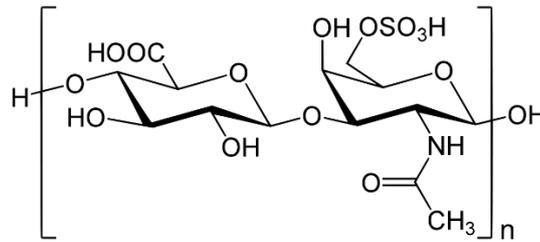


Abbildung 13: Chemische Struktur von Chondroitinsulfat.

**Kollagen Typ-I:** Kollagene werden auf natürliche Weise von verschiedenen Zellen synthetisiert, darunter Myoblasten, Osteoblasten, Fibroblasten und Chondrozyten. Gebildetes Kollagen wird basierend auf die Strukturen, die es ausbildet, in Kollagen I, II, III, V und XI eingeteilt. Kollagen I gilt als der dominanteste Kollagentyp im Körpergewebe.<sup>166</sup> Es ist das am häufigsten vorkommende ECM-Protein, das an der Regulation von Zellausbreitung, Wachstum und Differenzierung beteiligt ist. Es hat zudem Eigenschaften wie biologische Abbaubarkeit, geringe Antigenität und Bioaktivität gegenüber verschiedenen Zelltypen.<sup>167</sup>

**OH4:** Das Lipid besteht aus einer Malonsäurediamidstruktur als Grundgerüst. Der erste Teil der Kopfgruppe hat eine Tris(2-aminoethyl)amin-Einheit, die über eine Amidbindung an die Carboxylgruppe des Malonsäurebausteins geknüpft ist. Den zweiten Teil der Kopfgruppe bildet das L-Lysin, das durch eine weitere Amidbindung mit der zweiten Carboxylgruppe des Malonsäurebausteins verbunden ist. Zudem besitzt OH4 zwei Alkylketten, eine Oleylkette und eine Hexadecylkette. In vorangegangenen Arbeiten konnte demonstriert werden, dass OH4 in einer equimolaren Mischung mit DOPE ein effizientes Trägersystem für den Transfer von DNA in Zellen darstellt.<sup>145-148</sup>

Die chemische Bezeichnung ist (N-{6-amino-1-[N-(9Z)-octadec-9-enylamino]-1-oxohexan-(2S)-2-yl}-N'-{2-[N,N-bis(2-aminoethyl)amino]ethyl}-2-hexadecylpropandiamid).

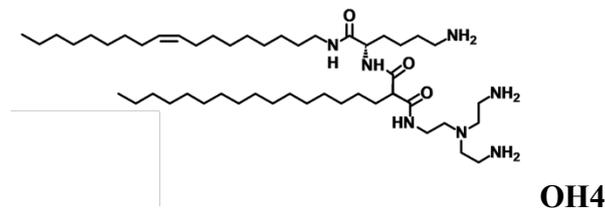
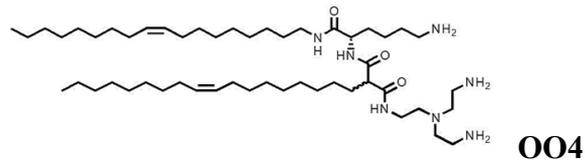


Abbildung 14: Chemische Struktur von OH4.

**OO4:** Das Lipid OO4 unterscheidet sich von OH4 nur durch das Vorhandensein einer weiteren Oleylkette anstelle der Hexadecylkette. In vorangegangenen Arbeiten konnte gezeigt werden, dass OO4 in einer molaren Mischung mit DOPE von 1:3 stabile Liposomen bildet und effektiv seine Fracht in Zielzellen transportieren kann.<sup>150, 151</sup>

Die chemische Bezeichnung ist (N-{6-amino-1-[N-(9Z)-octadec-9-enylamino]-1-oxohexan-(2S)-2-yl}N'-{2-[N,N-bis(2-aminoethyl)amino]ethyl}-2[(9Z)-octadec-9enyl]).



**Abbildung 15:** Chemische Struktur von OO4.

### 2.3) Publikation I

## **Contact-Triggered Lipofection from Multilayer Films Designed as Surfaces for in Situ Transfection Strategies in Tissue Engineering**

C. Husteden, F. Doberenz, N. Goergen, S. R. Pinnapireddy, C. Janich, A. Langner, F. Syrowatka, A. Repanas, F. Erdmann, J. Jedelská, U. Bakowsky, T. Groth, C. Wölk.

ACS Applied Materials & Interfaces 2020

<https://doi.org/10.1021/acsami.9b18968>

*Supporting Information* ist dem Anhang beigelegt.

## Contact-Triggered Lipofection from Multilayer Films Designed as Surfaces for in Situ Transfection Strategies in Tissue Engineering

Catharina Husteden, Falko Doberenz, Nathalie Goergen, Shashank Reddy Pinnapireddy, Christopher Janich, Andreas Langner, Frank Syrowatka, Alexandros Repanas, Frank Erdmann, Jarmila Jedelská, Udo Bakowsky, Thomas Groth, and Christian Wölk\*

Cite This: *ACS Appl. Mater. Interfaces* 2020, 12, 8963–8977

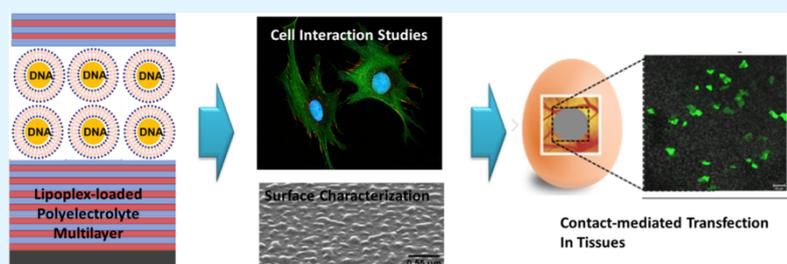
Read Online

ACCESS |

Metrics & More

Article Recommendations

Supporting Information



**ABSTRACT:** Biomaterials, which release active compounds after implantation, are an essential tool for targeted regenerative medicine. In this study, thin multilayer films loaded with lipid/DNA complexes (lipoplexes) were designed as surface coatings for in situ transfection applicable in tissue engineering and regenerative medicine. The film production and embedding of lipoplexes were based on the layer-by-layer (LbL) deposition technique. Hyaluronic acid (HA) and chitosan (CHI) were used as the polyelectrolyte components. The embedded plasmid DNA was complexed using a new designed cationic lipid formulation, namely, OH4/DOPE 1/1, the advantageous characteristics of which have been proven already. Three different methods were tested regarding its efficiency of lipid and DNA deposition. Therefore, several surface specific analytics were used to characterize the LbL formation, the lipid DNA embedding, and the surface characteristics of the multilayer films, such as fluorescence microscopy, surface plasmon resonance spectroscopy, ellipsometry, zeta potential measurements, atomic force microscopy, and scanning electron microscopy. Interaction studies were conducted for optimized lipoplex-loaded polyelectrolyte multilayers (PEMs) that showed an efficient attachment of C2C12 cells on the surface. Furthermore, no acute toxic effects were found in cell culture studies, demonstrating biocompatibility. Cell culture experiments with C2C12 cells, a cell line which is hard to transfect, demonstrated efficient transfection of the reporter gene encoding for green fluorescent protein. In vivo experiments using the chicken embryo chorion allantois membrane animal replacement model showed efficient gene-transferring rates in living complex tissues, although the DNA-loaded films were stored over 6 days under wet and dried conditions. Based on these findings, it can be concluded that OH4/DOPE 1/1 lipoplex-loaded PEMs composed of HA and CHI can be an efficient tool for in situ transfection in regenerative medicine.

**KEYWORDS:** C2C12 myoblasts, chorion allantois membrane, in situ transfection, layer-by layer technique, lipofection, lipoplex, polyelectrolyte multilayer

### INTRODUCTION

In recent decades, the development of therapeutic strategies in which the drug is a nucleic acid has become an important research focus, which is called as gene therapy.<sup>1–3</sup> A major challenge for the establishment of gene therapy is, in addition to the development of therapeutic nucleic acid, the overcoming of biological barriers by means of suitable delivery systems. Currently, virus-based vehicles are the most effective method for nucleic acid transfer.<sup>4–6</sup> Viral systems, however, have some disadvantages in which the oncogenic and immunogenic potentials are the most serious ones.<sup>7,8</sup> As a result, nonviral nucleic acid delivery systems, such as lipoplexes (cationic

lipid–nucleic acid complexes) or polyplexes (cationic polymer–nucleic acid complexes) are a topic of increasing interest. Such delivery systems mimic functions of viral cell entry and avoid the problems and risks associated with viral vectors.<sup>9–13</sup> Nanosized nonviral delivery systems are often employed for systemic administration.<sup>14</sup> Nevertheless, several hurdles have

Received: October 23, 2019

Accepted: January 31, 2020

Published: January 31, 2020

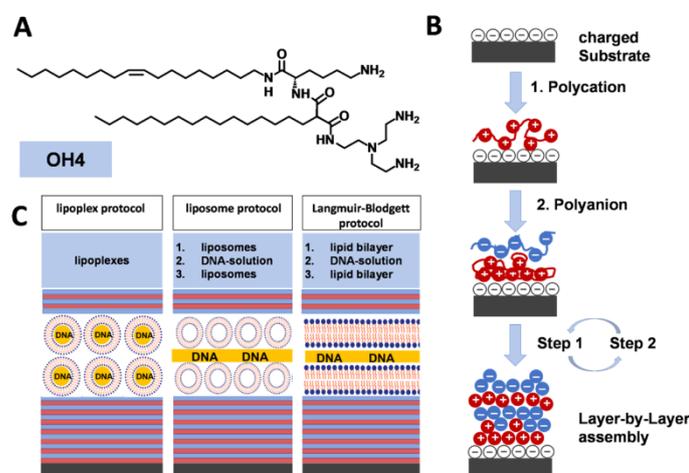


**Figure 1.** (A) Structure of the cationic lipid OH4 used in this study. (B) Principle of the LbL assembly technique. An alternate adsorption of a polyanion and a polycation on a charged substrate leads to the construction of PEMs. (C) Schematic representation of the three used protocols for incorporating lipid and DNA into the PEM film. Lipoplex protocol: LPXs are embedded in the PEM film. Liposome protocol: following charged materials were successively adsorbed to the PEM film: (1) CLs; (2) pDNA; (3) CLs. LB protocol: (1) LB formed cationic lipid bilayer; (2) pDNA; (3) LB formed cationic lipid bilayer. After loading with DNA using the three protocols, cover layers composed of polyelectrolytes were adsorbed.

to be overcome: the interaction with serum proteins which can induce vigorous immune responses, clearance by the mononuclear phagocytic system, and the lack of specific cell targeting which is connected with not only less efficiency but also risk of side effects.<sup>15–17</sup> An alternative to the systemic route is the so-called “substrate-mediated gene delivery”, which includes the encapsulation or immobilization of either nonviral or viral gene vectors on or within a biomaterial. This allows the nucleic acid delivery system to be positioned in a cellular microenvironment to achieve localized and efficient gene delivery to cells and tissues.<sup>18</sup> For instance, a biomaterial-triggered transfection to access osteoneogenesis and achieve bone regeneration reduces the risk of ectopic osteogenic differentiation in other tissues.<sup>19</sup> Furthermore, DNA-loaded biomaterials may result in a prolonged transfection because of the depot effect. Such systems are used for the induction of blood vessel formation.<sup>20</sup>

There are several approaches which associate a gene carrier with biomaterials for substrate immobilization of the nucleic acid vector. The immobilization on covalently modified biomaterials using the specific binding of avidin with biotin is one strategy.<sup>21–23</sup> Among all strategies, the layer-by-layer technique (LbL-technique) has become established as a simple, inexpensive procedure for multilayer formation and allows a broad range of structural variations.<sup>24</sup> The LbL-technique was developed by Decher et al. in the early 1990s and describes the alternating coating of materials with cationic and anionic polyelectrolytes, which results in a thin nanostructured polyelectrolyte-multilayer film (PEM-film) (Figure 1B).<sup>25,26</sup> Biological materials and functionalized nanoparticles can be incorporated into the PEM-film to produce a delivery system for functionalization nanoparticles.<sup>27–29</sup> In addition to this, PEMs were discovered to be effective vectors for the delivery of DNA and capable of successful transfection.<sup>30</sup> However, in these systems, the naked DNA is exposed to the extracellular environment upon release from the delivery system, resulting in rapid enzymatic degradation in vivo. A

system which releases nucleic acids encapsulated in a protecting delivery vehicle would be more beneficial. Therefore, more complex systems are described in which nucleic acid-loaded vehicles (protection of the nucleic acid and improvement of cellular uptake) are embedded in PEM films: systems are described using chitosan (CHI)-polyplexes and hyaluronic acid (HA) to build an LbL system for sustained release.<sup>31,32</sup> Other LbL systems use only Lipofectamine 2000 lipoplexes and DNA as the components.<sup>33</sup> Nevertheless, these systems are loaded with high amounts of polynucleotides (multiple nucleic acid layers inside the LbL system). This may be a disadvantage if delivery systems are loaded with DNA encoding for highly active cytokines. One example is the bone morphogenetic protein, for example, BMP-2, which can induce ectopic bone formation.<sup>19</sup> A reduced amount of DNA, resulting in local restricted production of small amounts BMP-2, would be more appropriate for this application. The ideal system allows a controlled position of the nucleic acid inside the PEM film, in order to control release kinetics. First approaches were made to incorporate only one layer with DNA-loaded nanoparticles (polyethylene imine polyplexes,<sup>34</sup> adeno viruses,<sup>35</sup> and Lipofectamine 2000 lipoplexes<sup>36</sup>). Nevertheless, these three studies emphasize the biological proof of concept instead of the efficiency of engineering (DNA loading capacity, homogeneity of loading). More systematic studies are required to give information about the efficiencies of loading procedures and surface characteristics.

HA and CHI are excellent candidates for LbL coating of implants. Biopolymer properties like biodegradability, biocompatibility, and no immunogenicity make HA and CHI a suitable material for tissue-engineered scaffolds.<sup>37–41</sup> HA is a negatively charged glycosaminoglycan composed of D-glucuronic acid and N-acetyl-D-glucosamine [linked via alternating  $\beta$ -(1  $\rightarrow$  4) and  $\beta$ -(1  $\rightarrow$  3) glycosidic bonds] and a component of the extracellular matrix. CHI, a cationic polysaccharide composed of randomly distributed  $\beta$ -(1  $\rightarrow$  4)-linked D-glucosamine and N-acetyl-D-glucosamine, is originated from

chitin. Another advantage is that there are monographs for sodium hyaluronate and CHI in the European Pharmacopeia and the United States Pharmacopeia, which facilitates a possible clinical translation and production according to the Good Manufacturing Practices (GMP) guidelines.

In this study, we present a novel approach toward surface contact-triggered DNA delivery that uses lipoplexes (lipid DNA complexes) as nanoscaled delivery system for embedding DNA in PEM films. The customized cationic lipid OH4 (Figure 1A) is the main component of the lipoplexes. Earlier works demonstrated that OH4 in an equimolar ratio with the colipid 1,2-dioleoyl-*sn*-glycero-3-phosphoethanolamine (DOPE) is an efficient delivery system for plasmid DNA (pDNA) with superior transfection efficiency compared to other lipid compositions.<sup>42–45</sup> The OH4/DOPE 1/1 lipoplexes are embedded in PEMs composed of HA and CHI. This strategy provides a protection of DNA against enzymatic degradation<sup>43</sup> and triggers the cellular internalization and intracellular trafficking.<sup>43,44,46,47</sup> Only one layer of OH4/DOPE 1/1 lipoplexes will be incorporated in the LbL system while the loading process will be studied. Different loading protocols for loading lipid/DNA layers into the film will be evaluated regarding their efficiency of lipid and DNA deposition to establish the most effective way of film modification (Figure 1C). Surface-sensitive analytical methods, more precisely, surface plasmon resonance spectroscopy (SPR), fluorescence microscopy, ellipsometry, and zeta potential measurements, in combination with gel electrophoretic analysis, were used to evaluate the DNA loading capability. Morphological studies of the lipoplex-loaded films were performed using atomic force microscopy (AFM) and scanning electron microscopy (SEM). Because of future applications in bone regenerative medicine, we screened the system with the most effective DNA loading regarding interactions with C2C12 cells. The focus of these studies was set on cell attachment, viability, and transfection efficiency. The work generates a system which is biocompatible and has high transfection rates also in an *in vivo* animal replacement model.

## MATERIALS AND METHODS

**Materials.** If not stated otherwise, all chemicals were purchased from Sigma-Aldrich (Taufkirchen, Germany). HA sodium salt with an average molecular weight of 1.3 MDa was provided from Kraeber & Co GmbH (Ellerbek, Germany) and native low-molecular weight CHI ( $M_w \approx 62$  kDa, 85% degree of deacetylation) from Hepe Medical Chitosan GmbH (Halle, Germany). Both polysaccharides were used as polyelectrolytes for multilayer formation. Polyethyleneimine (PEI,  $M_w \approx 750$  kDa) was used as a priming layer in multilayer formation. pDNA pCMV-GFP was acquired from Plasmid Factory (Bielefeld, Germany). The synthesis and characterization of the used cationic lipid OH4 (*N*-{6-amino-1-[*N*-(9Z)-octadec-9-enylamino]-1-oxohexan-(2S)-2-yl]-*N'*-{2-[*N,N*-bis(2-aminoethyl)amino]ethyl}-2-hexadecylpropanamide) were described in our previous work.<sup>42</sup> The phospholipids DOPE and 1,2-dioleoyl-*sn*-glycero-3-phosphoethanolamine-*N*-(lissamine rhodamine B sulfonyl) (ammonium salt) (Rhod-DOPE) were acquired from Avanti Polar Lipid, Inc. (Al, USA).

**Preparation of Cationic Liposomes.** Liposomes were prepared by the film hydration procedure.<sup>48</sup> A thin lipid film was prepared from the cationic lipid OH4 and the colipid DOPE by dissolving them separately in chloroform/methanol (8:2 v/v) and combining both stock solutions to a molar OH4/DOPE ratio of 1:1. Subsequently, the organic solvent was removed by evaporation at room temperature for 30 min at 500 mbar and for further 2 h at <15 mbar. After formation of the dry lipid films, sterile-filtered 10 mM MES buffer solution (pH

6.5) or 10 mM MES buffer solution containing 0.15 M NaCl (pH 4.0) were added to the lipid film depending on the DNA-loading method, to achieve a final lipid concentration of 1 mg/mL. Afterward, the lipid dispersions were incubated at 50 °C while shaking them at 1400 rpm for 30 min (Eppendorf Thermomixer 5436) followed by sonication at 37 kHz for 5 min at 30 °C.

**Lipoplex Formation.** Lipoplexes were prepared by combining pDNA with the OH4/DOPE 1:1 (n/n) lipid dispersion to an N/P ratio of 4 (ratio of primary amines of the cationic lipids—N—to phosphate groups of the nucleic acid—P) in sterile-filtered 10 mM MES buffer solution (pH 6.5). The pDNA was added to the lipid dispersion in one step followed by gentle mixing. The samples were incubated for 15 min at room temperature. The amount of pDNA added depends on the kind of experiment, which is indicated in the Results and Discussion section.

**Surface Cleaning.** Silicon wafers (Si-Mat, Germany) with a size of  $10 \times 10$  mm<sup>2</sup> and round glass coverslips with a diameter of 12 mm (Menzel, Germany) were cleaned according to the RCA-1 protocol for the removal of organic residues.<sup>49</sup> The procedure uses a mixture of ultrapure water (Milli-Q-plus system, Millipore), ammonium hydroxide (25%, Carl Roth GmbH & Co. KG, Karlsruhe, Germany), and hydrogen peroxide (35%, Carl Roth GmbH & Co. KG, Karlsruhe, Germany) at a ratio of 5:1:1. Initially, ultrapure water and ammonium solution were heated up to 70 °C, and hydrogen peroxide was added to the mixture. The silicon samples were immersed in this solution for 15 min, then excessively washed with ultrapure water, and dried with a stream of compressed air. New gold-coated sensors, used for SPR measurements, were purchased from IBIS Technologies B.V. (Enschede, Netherlands), cleaned with 99.8% ethanol, and rinsed with ultrapure water. Sensors were immediately incubated in an ethanol solution of 2 mM mercaptoundecanoic acid (MUDA, 95%, Sigma, Germany) at room temperature overnight to generate a negatively charged surface by the formation of a self-assembled monolayer exposing carboxyl groups.<sup>50</sup>

**Basal PEM Assembly Using the LbL Method.** The PEM assembly was performed on glass, gold, and silicon, depending on the requirements of the methods. All solutions were prepared using ultrapure water (Milli-Q-plus system, Millipore). Both CHI as well as HA and PEI polyelectrolyte solutions were prepared at a concentration of 2 mg/mL in 0.15 M NaCl buffer, adjusted to pH 4.0 and filtered through a 0.22  $\mu$ m filter (VWR, Germany).<sup>51</sup> The washing steps were always carried out with 0.15 M NaCl, adjusted to pH 4.0, and filtered through a 0.22  $\mu$ m filter (VWR, Germany). LbL build up was achieved using the pipet approach, wherein 300  $\mu$ L of each polymer solution was deposited directly onto the cleaned substrate in a 24 well plate. PEI was used as a primary layer to obtain a positive surface charge. After the polyelectrolyte was allowed to adsorb for 15 min at room temperature whilst simultaneous shaking, the samples were rinsed three times. Then, substrates were alternately incubated with HA solution for 15 min, washed with 0.15 M NaCl solution for 5 min, followed by incubation with CHI solution for 15 min. Multilayer coating was performed at room temperature under gentle shaking. The LbL deposition was repeated until five HA/CHI bilayers were formed, with an additional negatively charged layer of HA named [HA/CHI]<sub>5</sub>HA. Subsequently, the basal PEM was used for loading with lipid and DNA.

**Loading of PEMs with Lipid/DNA Layers.** Three different loading protocols were used to find the most effective method for lipid/DNA loading (summary, Figure 1C).

**Lipoplex Protocol.** Preformed lipoplexes (LPX), characterized by efficient DNA encapsulation and positive zeta potential,<sup>42,43</sup> were directly loaded on the basal PEM according to the LbL pipet approach. LPX solution (140  $\mu$ L) was made up to 300  $\mu$ L with 0.15 M NaCl and transferred to the basal PEM film for adsorption as the terminal layer, shaken gently for 2 h, and then rinsed three times with 0.15 M NaCl (pH 4.0).

**Liposome Protocol.** Three hundred microliters of cationic liposome (CL) formulation OH4/DOPE 1:1 (n/n) with a concentration of 1 mg/mL in sterile-filtered 10 mM MES buffer solution containing 0.15 M NaCl pH 4 were added to the basal PEM

film and incubated for 1 h with gentle shaking. Afterward, three washing steps (0.15 M NaCl, pH 4) were performed. Subsequently, different amounts of pDNA pCMV-GFP (depending on the type of experiment) in 0.15 M NaCl buffer pH 4 were applied to the film and incubated for 30 min. After a triple washing step, a second 1 h incubation with 300  $\mu$ L of the liposome formulation OH4/DOPE 1:1 (n/n) in 10 mM MES buffer containing 0.15 M NaCl at pH 4 ( $c = 1$  mg/mL) was performed, followed by a three-fold rinse.

**Langmuir–Blodgett Protocol.** Langmuir–Blodgett (LB) was used for lipid deposition. An OH4/DOPE 1:1 (n/n) solution with a concentration of 1 mg/mL in chloroform/methanol 1:1 (v/v) was spread using a microsyringe onto the air/water interface in a LB trough (NIMA, Coventry, UK). NaCl (0.15 M), adjusted to pH 4.0, was used as the subphase. At least 10 min were allowed for solvent evaporation, and then, the monolayer was compressed at a rate of 1.0 cm/min to a surface pressure of 30 mN/m. After film stabilization, the monolayer was transferred to a [HA/CHI]<sub>3</sub>HA-coated glass plate using the blotting device of the trough with a speed of 1.0 mm/min (1) up and (2) down by the LB technique, forming a lipid bilayer on the [HA/CHI]<sub>3</sub>HA film. All lipid membrane depositions were performed at  $\sim 25$  °C. After a three-fold wash step, the lipid-coated [HA/CHI]<sub>3</sub>HA substrates were immersed in a solution containing different amounts of DNA (depending on the type of experiment) in 0.15 M NaCl and incubated for 30 min. Subsequently, the sample was washed three times, and the lipid coating using the LB technique was carried out with the LB trough again as described above.

After lipid DNA embedding using one of the three loading protocols, the LbL method was used to deposit an additional layer of HA and a terminal CHI layer using the methods mentioned above. This step was used to protect the lipid/DNA layer and reduce desorption of both components. In some cases, a final film modification with fibronectin (FN) was performed using an incubation step with a 20  $\mu$ g/mL FN solution in sterile-filtered phosphate buffered saline (PBS) at 37 °C for 4 h followed by rinsing three times. The final PEM was immersed in PBS to prepare for biological experiments.

**SPR to Study Multilayer Growth.** The SPR experiments were performed using an IBIS-iSPR imaging device (IBIS Technologies B.V.). SPR is based on the detection of changes in the refractive index at the gold/liquid interface of the gold sensor surface caused by the adsorption of molecules. The resulting change in the SPR angle shift ( $m^\circ$ ) is proportional to the mass ( $\Gamma_{\text{SPR}}$ ) of adsorbed molecules on the surface. The MUDA-modified gold sensors were placed into the flow chamber and equilibrated with degassed 0.15 M NaCl (pH 4.0) to obtain a stable baseline. Thereafter, each polyelectrolyte was injected with a flow rate of 3  $\mu$ L/s for 15 min. After each polyelectrolyte adsorption, the flow chamber was rinsed three times with 0.15 M NaCl solution pH 4.0 for 5 min each to remove unbound molecules. The measurements were carried out at 10 different regions of interest on the sensor surfaces predefined by software.

**Confocal Laser Scanning Microscopy to Study Lipid and DNA Deposition on PEMs.** Rhodamine-labeled lipid formulation of OH4/DOPE/Rhod-DOPE 1:1:0.002 (n/n) ( $\lambda_{\text{ex}}^{\text{max}} = 560$  nm;  $\lambda_{\text{em}}^{\text{max}} = 583$  nm) was used for screening lipid loading in the PEM. Covalently TM-rhodamine-labeled pDNA ( $\lambda_{\text{ex}}^{\text{max}} = 546$  nm;  $\lambda_{\text{em}}^{\text{max}} = 576$  nm) (single staining) or covalently Cy5-labeled pDNA ( $\lambda_{\text{ex}}^{\text{max}} = 649$  nm;  $\lambda_{\text{em}}^{\text{max}} = 670$  nm) (costaining in the presence of labeled lipid) were taken for screening DNA loading in the PEMs. The covalent DNA labeling was performed using the Label IT Nucleic Acid Labeling Kit from Mirus (WI, USA), according to the manufacturer's instructions. After production of the lipid/DNA-loaded PEM using the tagged lipid mixture and/or tagged DNA, the labeled PEM was washed three times and then fixed on a slide with Aquatex mounting medium (Merck, Darmstadt, Germany). The films were stored overnight at 7 °C to cure the mounting medium and then examined by confocal laser scanning microscopy (CLSM) (LSM 710, Carl Zeiss, Oberkochen, Germany).

**Thickness Measurements.** A spectroscopic ellipsometer (M-2000 V; J.A. Woollam Company, Lincoln, NE) equipped with WVase32 software was used for measuring the thickness of PEMs at

different stages of the production under dry and wet conditions. The initial substrate was a silicon wafer. In these experiments, PEMs were loaded with 1.5  $\mu$ g of DNA. Using a Cauchy model for the optical properties of the polymer film:  $n(\lambda) = A_n + B_n/\lambda^2 + C_n/\lambda^4$ , the refractive index ( $A_n$ ) of films was fitted under dry and wet conditions from ellipsometric parameters  $\Delta$  and  $\psi$ . Here, negligible  $B_n$  and  $C_n$  were considered zero. Ellipsometric measurements under dry conditions were performed at incident angles of 55–70° within a wavelength range of  $\lambda = 375$ –1000 nm. Data were obtained from 15 different points on each sample using samples in duplicate. Measurements in the wet condition were done in a fluid cell (0.5 mL liquid cell, Woollam) at a fixed angle of incidence of 70°. The used solution for measurement in a liquid cell was 0.15 M NaCl (pH 4). The  $\Delta$  offset, generated by the glass windows of the cell, was first determined and later subtracted from the raw ellipsometric data in WVase32 software. Data were obtained from five different points on each sample using samples in duplicate.

**Zeta-Potential Measurements.** The surface zeta-potential was determined using the SurPASS electrokinetic analyzer (Anton Paar, Graz, Austria). Therefore, PEM-films prepared with the lipoplex protocol or the liposome protocol ( $c_{\text{DNA}} = 1.5$   $\mu$ g) were prepared on special glass cover slips (10  $\times$  20 mm<sup>2</sup>). The flow of electrolyte (1 mM KCl in water) was adjusted to a distance to maintain 300 mbar as a maximum pressure. Hydrochloric acid (HCl) at concentration 0.1 M was used for pH titration. In addition to this, the pH value was adjusted to pH 10.5 using 1 M sodium hydroxide (NaOH) before starting a measurement. Finally, the measurements were carried out with an automated titration ranging from pH 10.5 to pH 2.25, which was adjusted by two titration steps: 0.25 mL from pH 3.0 to 5.0 and 0.03 mL from pH 5.0 to 10.5. The zeta potential was calculated by the provided software. Each test was done in triplicate.

**Atomic Force Microscopy.** AFM was performed with a NanoWizard II (JPK Instruments, Berlin, Germany) using PEMs prepared on silicon wafers in duplicate ( $c_{\text{DNA}} = 1.5$   $\mu$ g). All samples were imaged in dry conditions (dried with compressed air). Topographical images were recorded using silicon nitride cantilevers (Bruker Nano Inc., Santa Barbara, CA) in the intermittent contact mode in a standard liquid cell (JPK Instruments) with 0.15 M NaCl. JPK Data Processing V5.0.85 and Gwyddion V2.49 software were utilized for data postprocessing. Roughness parameters  $R_a$  and  $R_q$  were determined according to DIN EN ISO 4287/4288.

**Scanning Electron Microscopy.** SEM was performed with an ESEM XL 30 FEG, (Philips, Netherlands). The PEMs were prepared on silicon wafers in duplicate ( $c_{\text{DNA}} = 1.5$   $\mu$ g). SEM was used in the high vacuum mode ( $p = 10^{-6}$  mbar) to determine nanostructure dimensions. Before observation, specimens were coated with 20 nm chromium using a sputter coater and then broken. The observation was then carried out at the generated break edge. The samples were tilted at 60°. Images were generated at 12 kV acceleration voltage typically with the secondary electron signal and analyzed using the software Gwyddion (version 2.40).

**Particle Size Measurements.** Size distributions were measured by dynamic light scattering (DLS) with a Zetasizer Nano ZS ZEN3600 (Malvern Instruments, Worcestershire, UK). The scattering angle was 173°. Three measurements consisting of 15 runs with a time duration of 20 s for each run were performed at 25 °C. For the calculations, a viscosity  $\eta = 0.8872$  mPa·s and a refractive index of 1.33 were assumed. The autocorrelation function was evaluated by Zetasizer Software 7.12 (Malvern Instruments, Worcestershire, UK) 3.0 using the CONTIN analysis to generate intensity- and number-weighted size distribution curves.

**pDNA Loading Efficiency on the PEM Film.** The DNA loading efficiency was determined indirectly by agarose gel electrophoresis. After PEM film construction on the coverslips in 24-well plates, the coverslips were rinsed with 0.15 M NaCl (pH 4) and then transferred into a new 24-well plate before being treated with lipoplexes. Various OH4/DOPE 1:1 N/P 4 lipoplex concentrations (0.5, 1, 2, 3, 4, 5, 6, and 7  $\mu$ g pDNA) were loaded using the lipoplex protocol to the basal PEM ([HA/CHI]<sub>3</sub>HA) and incubated under gentle shaking for 2 h. Subsequently, the supernatant of each well was transferred into tubes

for DNA quantification, and the films were then washed twice with 0.15 M NaCl solution (pH 4). The rinsing solutions were also transferred into tubes. DNA quantification was performed by gel electrophoresis. Different lipoplex dispersion supernatants (50  $\mu$ L) and the rinsing solutions were used for gel electrophoresis and briefly mixed with 10  $\mu$ L of blue/orange 6 $\times$  loading dye (G190A) and 4  $\mu$ L 1% heparin (v/w), or sodium dodecyl sulfate (SDS) (0.15 M). Heparin or SDS was used to release DNA from lipoplexes. All samples were electrophoresed on 1% agarose gel containing 0.308  $\mu$ g/mL EtBr in 1% TAE buffer (pH 8) for 1 h at 90 V. Additionally, a 1 kb DNA ladder (G571A) (Promega, Madison, WI, USA) and a pDNA standard dilution series (0.01, 0.1, 0.2, 0.3, 0.5, and 0.8  $\mu$ g pDNA) were applied. The fluorescent DNA bands were visualized and photographed with an UVP UVsolo touch (Analytik Jena AG, Jena, Germany). The gels were analyzed with the software VisionWorks LS Analysis Software from Analytik Jena AG.

**Cell Culture.** C2C12 mouse myoblast cell line was obtained from DSMZ (Deutsche Sammlung von Mikroorganismen und Zellkulturen, Braunschweig, Germany). C2C12 myoblasts were maintained in Dulbecco's modified Eagle's medium (DMEM) supplemented with 10% fetal bovine serum (FBS), 2 mM L-glutamine, and 50  $\mu$ g/mL gentamicin. Cultured cells were grown at 37  $^{\circ}$ C in a humidified 5% CO<sub>2</sub>/95% air atmosphere. For splitting, cells of almost confluent cultures were washed twice with sterile PBS (Gibco, Thermo Fisher Scientific, Germany), followed by treatment with 0.05% trypsin/0.02% ethylenediaminetetraacetic acid (EDTA) solution at 37  $^{\circ}$ C for 2 min. With a subsequent addition of serum-containing DMEM, trypsin was inactivated. Finally, the cells were seeded in new culture flasks at a density of 25,000 cells/mL.

**Cell Adhesion Studies.** The PEMs were built on cleaned and sterilized round glass coverslips, and lipoplexes were incorporated using the lipoplex protocol ( $m_{\text{DNA}} = 1.5 \mu\text{g}$ ) and stored in PBS. The coverslips were washed briefly with Milli-Q water to prevent salt crystallization and transferred into 24 well plates. Cell adhesion was assayed in DMEM in the presence of 10% FBS through seeding at a density of 25,000 cells/mL. Using fluorescence staining and CLSM, filamentous actin, nucleus, and vinculin were visualized. After 24 h of incubation, the medium was carefully removed and samples were rinsed with PBS once. Using 4% paraformaldehyde in PBS solution, the adherent cells were fixed at room temperature for 15 min, then washed three times with PBS each for 5 min. Permeabilization was then conducted by applying 0.5% (v/v) Triton X-100 for 10 min, followed by PBS rinsing (3 times, each 5 min). The nonspecific binding sites were further blocked using 1% (w/v) bovine serum albumin (BSA) solution in PBS at room temperature for 1 h. The order of staining was designed as follows: (a) monoclonal anti-vinculin clone hVIN-1 mouse acites fluid antibody (1:200, Sigma-Aldrich, Germany); (b) goat anti-mouse IgG secondary antibody, Alexa Fluor 647 (1:1000, Thermo Fisher Scientific, Germany) for detection of the target primary antibody; (c) phalloidin-Atto 488 (1:50, Sigma-Aldrich, Germany) for staining filamentous actin; and (d) BOBO-1 (1:200, Invitrogen, Darmstadt, Germany) for staining the nucleus. All antibodies and dyes were diluted in 1% (w/v) BSA in PBS, and cells were incubated in each solution for 30 min at room temperature. PBS washing (3 times, each 5 min) was performed after each staining step. Afterward, all samples were briefly dipped in ultrapure water and mounted to object holders employing Mowiol 4-88 containing 25 mg/mL 1,4-diazabicyclo[2.2.2]-octane (Carl Roth GmbH & Co. KG, Karlsruhe, Germany). We applied 10 $\times$  (cell count) and oil immersion 40 $\times$  (cell morphology) objectives to explore the samples with CLSM (LSM 710, Carl Zeiss, Oberkochen, Germany). The Zeiss efficient navigation (ZEN 2011) software and Fiji<sup>52</sup> were used for qualitative image analysis and quantitative cell count, respectively, where results represent three replicates per sample.

**Microscopic Cell Viability Studies.** C2C12 cells with a density of  $1 \times 10^5$  cells/mL were seeded on the different substrates for 24 h. Subsequently, cells were stained with the Live/Dead Cell Imaging Kit (488/570) according to the manufacturer's instructions. The negative control used in this experiment was a cleaned coverslip without PEMs, which was treated with 20  $\mu$ g/mL FN to have a nontoxic

surface of high biocompatibility.<sup>53,54</sup> As a positive control, cells were stained after incubation at 60  $^{\circ}$ C for 30 min to have a sample with nonviable cells. All samples were examined with CLSM (LSM 710, Carl Zeiss, Oberkochen, Germany).

**In Vitro Cell Viability and Transfection Efficiency Studies.** Cells with a cell density of  $1 \times 10^5$  cells/mL were seeded on PEM-films. After an incubation period of 24 h at 37  $^{\circ}$ C and 5% CO<sub>2</sub>, the green fluorescent protein (GFP) expression was measured by fluorescence-activated cell sorting (FACS) analysis. Therefore, cells were detached with 0.05% trypsin/0.02% EDTA solution from the DNA-loaded PEM-film and centrifuged at 220g for 5 min. After washing, the cells were resuspended in 500  $\mu$ L of PBS containing 1% BSA. Cell viability was determined by propidium iodide (PI) staining with a concentration of 50  $\mu$ g/mL. The relative fluorescence units were measured with a BD Accuri C6 Plus flow cytometer (BD Bioscience, USA). Per measurement 10,000 cells were analyzed in each sample (GFP:  $\lambda_{\text{exc}}$ : 488 nm,  $\lambda_{\text{em}}$ : 510 nm; PI:  $\lambda_{\text{exc}}$ : 488 nm,  $\lambda_{\text{em}}$ : 617 nm). Single cells were gated by the size (FSC-H) and granularity (SSC) with the associated device software. The calculated single cell population was gated to detect GFP-expressing and PI positive cells by calculating the relative amount of transfected cells and dead cells. All samples were tested in triplicate.

**Chorion Allantois Membrane Transfection Assay.** Fertilized eggs were purchased from VALO BioMedia (Osterholz-Scharmbeck, Germany). Upon delivery, fertilized chicken eggs were cleaned with 70% (v/v) ethanol and incubated in an egg-hatching incubator equipped with an automatic rotator at a temperature of 37  $^{\circ}$ C and a relative humidity of 60–70%. On egg development day (EDD) 4 a window of 30 mm diameter was made into an egg shell using a pneumatic egg opener (schuett-biotec, Germany), to expose the CAM surface. The exposed part of the egg was then covered with a small Petri dish and placed back into the incubator. On EDD 10 lipoplex-loaded PEMs were topically applied to the CAM surface with the coated side of the coverslips (area of 1.13 cm<sup>2</sup>) and incubated for 24 h. In these experiments, PEMs that were dried under air stream and stored under dry conditions, as well as PEMs which were stored in PBS were tested. As a negative control, uncoated coverslips were used and incubated for 24 h as well. Afterward, the CAM area with the coverslips was cut out and placed on a microscope slide, including the coverslips. Immediately thereafter, it was examined by CLSM (Zeiss, LSM 700).

## RESULTS AND DISCUSSION

**Characterization of Formation of Lipoplex-Loaded PEM.** The formation of multilayer fabricated by an alternating adsorption of HA and CHI with a priming layer of PEI was monitored with SPR (Figure 2A). The measured angle shifts correspond to the increase of adsorbed mass during LbL formation. It is evident that every incubation step with a charged polymer solution results in a mass deposition. Consequently, the basal PEM formation, consisting of the deposition of 6 HA layers and 5 CHI layers, named [HA,CHI]<sub>5</sub>HA, was successful. The ability to form multilayers from HA and CHI which promote cell attachment has been described previously.<sup>55</sup> Because of the terminal HA layer of the basal PEM, the LbL procedure was able to proceed with positively charged components. This allowed us to test three lipid/DNA deposition methods (schematic illustration in Figure 1C, for details, see the Materials and Methods section) with regard to their efficiency to load the PEM with lipid and pDNA, respectively. With the lipoplex protocol, a layer of positively charged lipoplexes<sup>43</sup> is incorporated in the PEM. The liposome protocol proceeds the LbL technique with a layer of positively charged liposomes,<sup>42</sup> followed by a layer of DNA (polyanion) and an additional layer of positively charged liposomes. For the LB protocol, the DNA will be electrostatically complexed between two positively charged lipid bilayers

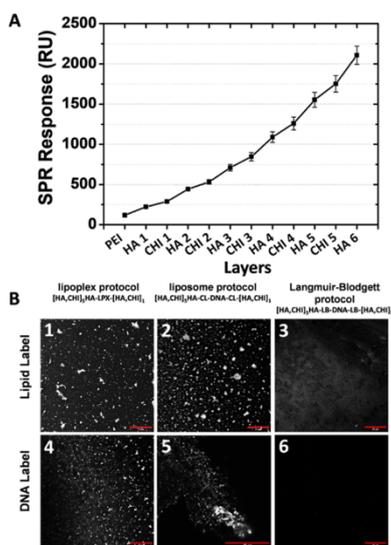


**Figure 2.** (A) Angle shifts during multilayer formation obtained with SPR indicating increased mass deposition. PEI was used as the priming layer followed by alternating deposition of HA and CHI. Results are means  $\pm$  SD of 10 different spots on a sample. The resulting sequence [HA,CHI]<sub>5</sub>HA is the basal layer as the starting material for lipid/DNA embedding. (B) CLSM images of PEMs after treatment with three different lipid/DNA loading protocols. Image 1–3: PEM films with rhodamine-DOPE-labeled lipid formulation OH4/DOPE 1:1 N/P 4. Image 4–6 PEM-films with covalently labeled TM-rhodamine-DNA after incubation with  $m_{DNA} = 0.5 \mu\text{g}/\text{PEM}$ . The scale corresponds to 25  $\mu\text{m}$ .

created by the LB technique. The idea of the different loading protocols is to compare a strategy where the lipid/DNA complex is formed a priori (lipoplex protocol) with two methods where the lipid/DNA complex is formed on the film during the PEM manufacturing process (liposome and LB protocol). The success of the three lipid/DNA deposition methods was screened by confocal microscopy using either lipid compositions or the DNA with a covalent rhodamine label. Figure 2B demonstrates that the utilization of the lipoplex protocol results in a successful lipid (Figure 2B, image 1) and DNA (Figure 2B, image 4) embedding. The final PEM sequence [HA,CHI]<sub>5</sub>HA-LPX-[HA,CHI]<sub>1</sub> successfully incorporated the preformed positively charged lipoplexes. The lipid/DNA loading with the liposome protocol, resulting in the final PEM sequence [HA,CHI]<sub>5</sub>HA-CL-DNA-CL-[HA,CHI]<sub>1</sub>, shows efficient lipid deposition (Figure 2B, image 2). However, DNA deposition was less efficient (Figure 2B, image 5) compared to the lipoplex protocol. The LB protocol results in a very homogeneous lipid deposition (Figure 2B, image 3). An increase in the water contact angle demonstrates successful lipid transfer (Supporting Information, Figure S1A). Nevertheless, the resulting PEM with the sequence [HA,CHI]<sub>5</sub>HA-LB-DNA-LB-[HA,CHI]<sub>1</sub> did not appear to have incorporated DNA according to the CLSM results (Figure 2B, image 6). The investigation of the LB protocol by ellipsometry with hydrated samples shows no significant increase in layer thickness after treating a OH4/DOPE coated basal-layer (PEM sequence: [HA,CHI]<sub>5</sub>HA-LB) with DNA (Supporting Information, Figure S1B). This also indicates a rather neglectable

DNA deposition. An explanation of the lacking DNA incorporation after using the LB protocol cannot be made from the presented experiments. However, future research will focus on the optimization of this protocol.

Because of the differing efficiencies of the three lipid/DNA loading protocols, ongoing research focused only on the lipoplex and the liposome protocol, as the LB protocol was inefficient according to DNA adsorption under the used experimental conditions. The film thickness gives further insights into deposition of material during the utilization of the lipoplex and liposome protocol. Ellipsometry, which gives averaged thickness values, was the method of choice for this purpose (Figure 3). Figure 3A represents the ellipsometry measurements of dried specimens. It has to be mentioned that the thickness values do not represent the dimensions of the sample under hydrated conditions. Figure 3A demonstrates that every incubation step was associated with a significant increase in film thickness for either the lipoplex protocol or the liposome protocol. The thickness increase indicates material deposition, which is also supported by the CLSM images (Figure 2B).

Ellipsometry measurements were also performed using a fluid cell in order to gain insights into the dimensions of the hydrated LbL films. The results are presented in Figure 3B. The basal PEM had a thickness of roughly 35 nm. The addition of lipoplexes (lipoplex protocol) yielded a thickness increase of about 38 nm. The addition of the cover layer results in a final film thickness of  $\approx 82$  nm. From the dimensions of the lipoplexes (100–200 nm, see following paragraphs), we expected higher values. In conclusion, the determined thickness values indicate a deformation of the lipoplexes (soft matter particles, positively overall charge<sup>43</sup>) on the negatively charged surface (Figure 3C). In contrast, the DNA loading according to the liposome protocol indicates a different behavior. Adsorption of the first liposome layer to the basal PEM results in a thickness increase by approximately 137 nm (Figure 3B). This size fits better to the size of the liposomes (z-average diameter 114 nm with a polydispersity index of 0.370 determined by DLS, corresponding correlation curve and cumulant fit are presented in Figure S2), which may show a certain extent of deformation after attachment (see Figure 3D). The addition of DNA results in a thickness decrease by 53 nm (see Figure 2D). The polyanionic DNA results in a rupture and rearrangement of the CLs during the complex formation. As a consequence, the encapsulated aqueous core of the liposomes get lost, and a decrease in the particle volume occurs (Figure 3D). Similar observations were made for the lamellar lipoplex formation process in bulk systems,<sup>56,57</sup> also for OH4/DOPE 1/1 (n/n).<sup>45</sup> The addition of a second liposome layer increases the film thickness by 69 nm. Finally, the addition of the cover layer (first HA, again a polyanion which induces the rupture of CLs, followed by CHI) results in a total PEM film thickness of about 152 nm. Consequently, the film thickness of [HA,CHI]<sub>5</sub>HA-LPX-[HA,CHI]<sub>1</sub> (lipoplex protocol) was significantly smaller with 82 nm than the thickness reached after utilization of the liposome protocol to produce [HA,CHI]<sub>5</sub>HA-CL-DNA-CL-[HA,CHI]<sub>1</sub> (152 nm).

In order to examine the surface charge in dependence on the DNA immobilization procedure, zeta potential measurements were performed using a pH titration technique (Figure 4). The basal PEM ([HA,CHI]<sub>5</sub>HA) showed a negative zeta potential at pH values higher than pH 3, which is related to the presence

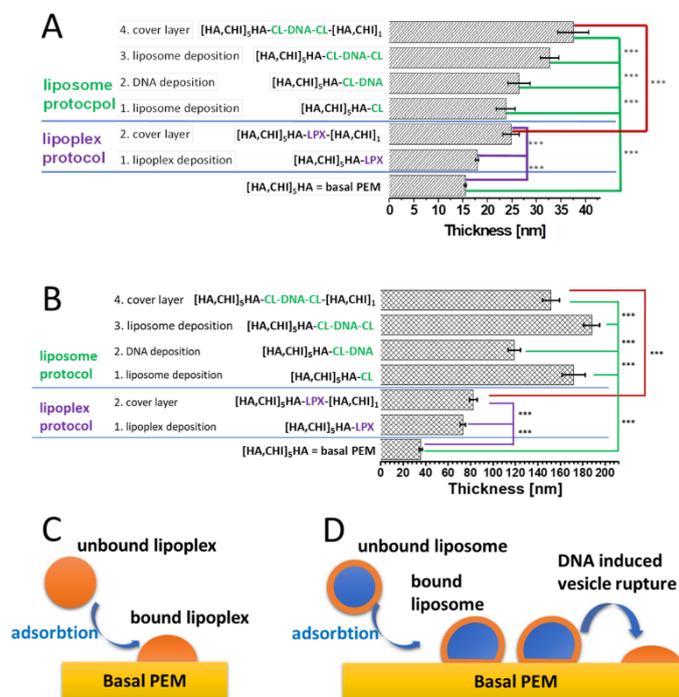


**Figure 3.** (A,B) Ellipsometry with dried samples (A) and hydrated samples (B): calculated thickness of the basal PEM  $[\text{HA}, \text{CHI}]_5 \text{HA}$  followed by the lipoplex loading processes using the lipoplex and the liposome protocol studied with ellipsometry. (C) Schematic illustration of the proposed mechanism of lipoplex adsorption. (D) Schematic illustration of the proposed mechanism of liposome adsorption and the followed thickness decrease because of DNA-induced vesicle rupture and rearrangement. The values in (A,B) show mean and corresponding standard deviation (error bars) [ $n(\text{A}) = 30$ ,  $n(\text{B}) = 10$ ]. The three stars (\*\*\*) indicate significant differences in the measured thickness values determined by one-way ANOVA ( $\alpha = 0.05$ ).

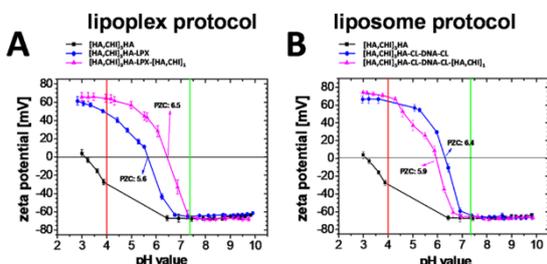


**Figure 4.** pH-dependent (acid-to-base pH titration) zeta potential measurements of the LbL film at different stages of assembly. (A) Comparison of the basal PEM  $[\text{HA}, \text{CHI}]_5 \text{HA}$ , the film after loading with lipoplexes according to the lipoplex protocol ( $[\text{HA}, \text{CHI}]_5 \text{HA-LPX}$ ), and the full-assembled DNA-loaded film using the lipoplex protocol with the cover layer  $[\text{HA}, \text{CHI}]_5 \text{HA-LPX-}[\text{HA}, \text{CHI}]_1$ . (B) Comparison of the basal PEM  $[\text{HA}, \text{CHI}]_5 \text{HA}$ , the film after loading with the sequence liposomes–DNA–liposomes according to the liposome protocol ( $[\text{HA}, \text{CHI}]_5 \text{HA-CL-DNA-CL}$ ), and the full assembled DNA loaded film using the liposome protocol with cover layer ( $[\text{HA}, \text{CHI}]_5 \text{HA-CL-DNA-CL-}[\text{HA}, \text{CHI}]_1$ ). The additional lines highlight pH 4 [red line in (A,B)], the working pH during multilayer assembling, and the physiological pH 7.4 [green line in (A,B)], the pH to which the final film is adjusted. PZC = point of zero charge.

of deprotonated carboxylic groups of HA that have a  $\text{p}K_a$  value of around 3.<sup>58</sup> As a consequence, the film surface charge is

dominated by the terminal HA layer, which covers the surface. This is also a necessary prerequisite for adsorption of CLs or positively charged lipoplexes according to the different loading protocols. The direct loading of positively charged lipoplexes (lipoplex protocol, LbL sequence  $[\text{HA}, \text{CHI}]_5 \text{HA-LPX}$ ) resulted in a sigmoidal zeta potential curve. The point of zero charge (PZC) was at pH 5.6. This demonstrates that the surface is not completely covered by the lipoplexes. Otherwise, the surface charge would be dominated by the primary amino functions of OH4 ( $\text{p}K_a \approx 8-9$ ), resulting in a higher PZC. On the other hand, the intermingling of liposomes and HA can also result in such sigmoidal potential during pH titration, as shown for other PEM systems by other groups.<sup>59</sup> The switch to negative charges above pH 5.6 and the negative plateau between  $-60$  and  $-70$  mV, which is exactly the value of the HA-dominated basal PEM, indicates that also HA is partially present at the surface (Figure 4A). The CLSM images confirm that the lipoplexes bind in patches on the surface of the basal PEM (Figure 2B, image 1). The addition of the cover layer (consisting of a layer HA followed by a final layer of CHI, LbL sequence  $[\text{HA}, \text{CHI}]_5 \text{HA-LPX-}[\text{HA}, \text{CHI}]_1$ ) shifts the sigmoidal zeta potential curve to higher pH values, resulting in a PZC of 6.5. The surface is more dominated by the primary amino functions of CHI resulting in this shift. An effect of HA is also visible which yields in the high negative zeta potential values at basic pH values. Subsequently, the different layers penetrate partially into each other.<sup>60,61</sup> While examining the values at pH

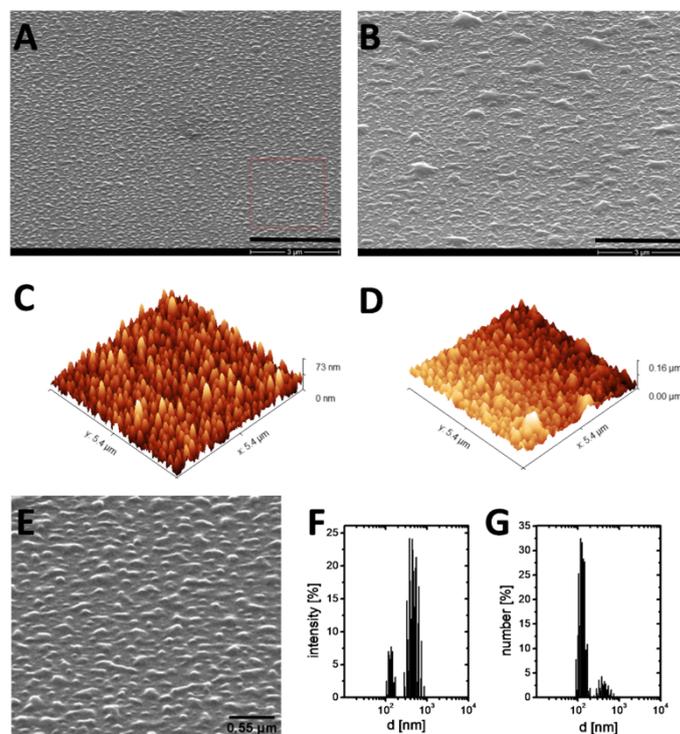


**Figure 5.** (A–E) SEM (A,B) and AFM (C,D) analysis of lipid/DNA loaded PEMs using the lipoplex protocol, film sequence  $[\text{HA,CHI}]_5\text{HA-LPX-}[\text{HA,CHI}]_1$  (A,C) and the liposome protocol, film sequence  $[\text{HA,CHI}]_5\text{HA-CL-DNA-CL-}[\text{HA,CHI}]_1$  (B,D). Scale of SEM images (A,B) corresponds to  $3\ \mu\text{m}$ . (E) shows a detail of (A) which is indicated by the red square. (F,G) Intensity-weighted (F) and number-weighted (G) size distribution curves of the lipoplex formulation before loading onto PEMs.

**Table 1.** Roughness Parameters  $R_a$  (Roughness Average) and  $R_q$  (Root-Mean-Square Roughness) Were Determined Using the Software Gwyddion V2.49<sup>a</sup>

roughness parameter (nm)	lipoplex protocol $[\text{HA,CHI}]_5\text{HA-LPX-}[\text{HA,CHI}]_1$	liposome protocol $[\text{HA,CHI}]_5\text{HA-CL-DNA-CL-}[\text{HA,CHI}]_1$
$R_a$	$6.67 \pm 1.25$	$9.13 \pm 1.59$
$R_q$	$9.10 \pm 1.79$	$11.75 \pm 2.26$

<sup>a</sup>Results are the mean  $\pm$  SD of 10 areas per samples in duplicate.

4, the pH of the film built-up, a charge switch from negative to positive after lipoplex adsorption was observed ( $\zeta$   $[\text{HA,CHI}]_5\text{HA} = -30\ \text{mV} \rightarrow \zeta$   $[\text{HA,CHI}]_5\text{HA-LPX} = +47\ \text{mV}$ ; Figure 4A, red line). This demonstrates the effective charge-driven LbL assembly.

Comparable surface properties were observed for the construction of the LbL system with the liposome protocol. The single layers are not strictly separated; PZC values below 7 imply that they partially interpenetrate, although a cationic component is a terminal layer (Figure 4B).

Regardless of the protocol used to load the DNA, the zeta potential of the final PEM under neutral conditions is  $-65\ \text{mV}$  (pH 7.3, green line, Figure 4A,B). The PEM has a negative surface charge, although the last layer is composed of CHI. This demonstrates the intermingling of both polyelectrolytes.

The surface topography of multilayers is visualized by SEM and AFM under dry conditions. Both methods demonstrated that the surface of PEMs loaded with the lipoplex protocol ( $[\text{HA,CHI}]_5\text{HA-LPX-}[\text{HA,CHI}]_1$ , Figure 5A,C) show smaller and more regularly distributed elevations on the surface

compared to PEMs loaded with the liposome protocol ( $[\text{HA,CHI}]_5\text{HA-CL-DNA-CL-}[\text{HA,CHI}]_1$ , Figure 5B,D). The lateral dimensions of the elevations on the  $[\text{HA,CHI}]_5\text{HA-LPX-}[\text{HA,CHI}]_1$  coating ranges between 100 and 500 nm, a size which is in alignment with the size determined by DLS for lipoplexes (compare Figure 5E with F,G). The DLS measurements show a bimodal size distribution for the lipoplex formulation with one size species between 100 and 200 nm and a second one between 300 and 1000 nm. The number-weighted distribution (Figure 5G) demonstrates that the smaller particles dominate in the lipoplex formulation. In summary, the AFM and SEM images of the  $[\text{HA,CHI}]_5\text{HA-LPX-}[\text{HA,CHI}]_1$  PEM indicate that lipoplexes are incorporated in the film  $[\text{HA,CHI}]_5\text{HA-LPX-}[\text{HA,CHI}]_1$  without aggregation in comparison of the size of the LPXs. AFM and the SEM images of the PEM loaded with the liposome protocol ( $[\text{HA,CHI}]_5\text{HA-CL-DNA-CL-}[\text{HA,CHI}]_1$ , Figure 5B,D) show patches (elevations with an increasing height) with lateral dimensions in the micrometer scale on the surface surrounded by smaller ones in the nanometer scale. If we

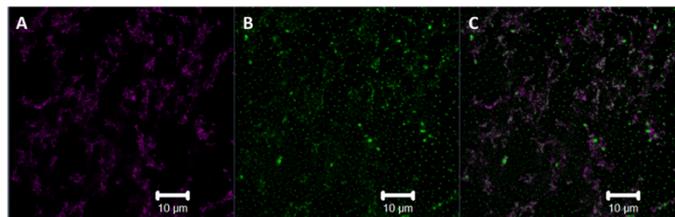


**Figure 6.** CLSM micrograph of a lipoplex-loaded PEM (lipoplex protocol,  $[\text{HA,CHI}]_3\text{HA-LPX-}[\text{HA,CHI}]_1$ ). The lipoplexes are visualized by a co-staining of (A) Cy-5 labeled DNA (magenta) and (B) rhodamine-DOPE labeled liposomes OH4/DOPE 1:1 (green). (C) Merge of (A,B). The scale bar corresponds to 10  $\mu\text{m}$ .

assume that the elevations are incorporated into lipid/DNA complexes, they have a broad size distribution.

Along with the topographical images of AFM (Figure 5C,D), two roughness parameters  $R_a$  and  $R_q$  were assessed to indicate quantitatively the possible differences in the surface roughness (Table 1). Both parameters demonstrate that the surface of PEMs loaded with the liposome protocol have a higher roughness.

For subsequent investigations, the focus of our research was set on PEMs loaded with the lipoplex protocol because of the fact that surface deposition of lipid/DNA complexes was more uniform and the DNA loading efficiency higher.

A costaining of the lipid component and the DNA component was performed to compare the distribution of DNA and lipid in lipoplex-loaded films of the sequence  $[\text{HA,CHI}]_3\text{HA-LPX-}[\text{HA,CHI}]_1$ , manufactured with the lipoplex protocol (Figure 6). Comparing the fluorescence pattern of the DNA (Figure 6A) with the pattern of the cationic lipid (Figure 6B), differences became apparent. The evaluation of the merged image (Figure 6C) shows that areas exist where costaining of DNA label and lipid label occurs. Further to this, other areas exist where only the fluorescence of the lipid label was detected. This fact can be explained with the used N/P ratio of the lipoplex formulation. At N/P 4, an excess of lipid formulation is present and therewith free CLs which also can be incorporated in the film.<sup>45</sup> Consequently, it is not surprising that DNA-free regions on the PEM exist.

The DNA loading efficiency using lipoplex incorporation according to the lipoplex protocol was determined indirectly by measuring the DNA content in the supernatant. The reason for the choice of this procedure was that the DNA compaction in lipoplexes hinders a reproducible fluorescence-based DNA quantification in the film because of quenching.<sup>62</sup> Furthermore, the presence of colloids after film disassembly prevents a reproducible fluorescence-based DNA quantification because of light-scattering effects. The results of DNA loading in  $[\text{HA,CHI}]_3\text{HA-LPX-}[\text{HA,CHI}]_1$  are shown in Figure 7. The incorporation of different amounts of DNA, from 0.5 to 7  $\mu\text{g}$  on a film-coated area of 1.13  $\text{cm}^2$  (corresponds to 0.44–6.19  $\mu\text{g}/\text{cm}^2$ ), was evaluated. Up to a loading amount of approximately 3  $\mu\text{g}/\text{cm}^2$ , the lipoplexes can be efficiently incorporated into the LbL system (loading efficiency of 100%). The test to load the films with concentrations above 3  $\mu\text{g}/\text{cm}^2$  results in loading efficiencies below 100% (Figure 7). In order to evaluate whether DNA is desorbed from the PEM in subsequent rinsing steps, the washing solutions were also studied for DNA content, showing no burst release of adsorbed DNA from the PEM (see Supporting Information Figure S7). Furthermore, a release experiment of films loaded with 0.88

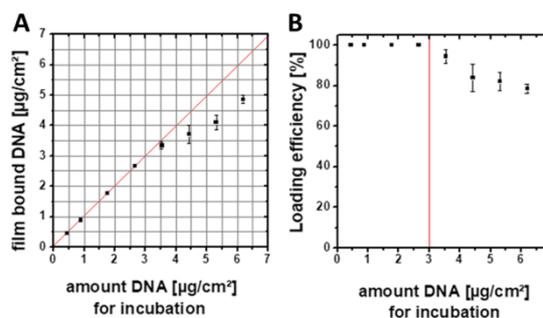


**Figure 7.** (A) Film-bound DNA amounts in  $\mu\text{g}/\text{cm}^2$  in  $[\text{HA,CHI}]_3\text{HA-LPX-}[\text{HA,CHI}]_1$  films loaded according to the lipoplex protocol. DNA concentrations of 0.5–7  $\mu\text{g}$  total DNA in 300  $\mu\text{L}$  medium were examined which corresponds to 0.44–6.19  $\mu\text{g}$  total DNA per  $\text{cm}^2$  LbL substrate (scale of x-axis). The calculation was based on the determination of the area fluorescence density of bands in agarose gel experiments presented in the Supporting Information Figures S4–S6 ( $n = 3$ ). The red line shows the theoretical values of 100% binding efficiency. (B) Calculated DNA loading efficiency from (A). Above an incubation amount of 3  $\mu\text{g}$  DNA per  $\text{cm}^2$  LbL substrate (indicated by the red line), the loading efficiency decreases below 100%.

$\mu\text{g}/\text{cm}^2$  DNA was performed. After 7 days, no released DNA was detected in the supernatant after incubating the PEM film in PBS (Supporting Information Figure S3). This indicates that the DNA is incorporated stably inside the PEM over this investigated time period.

**Cell Interaction Studies.** Because of the planned future applications of lipoplex-loaded thin films in bone tissue engineering, the interaction of C2C12 cells with lipoplex loaded PEMs was investigated. C2C12 mouse myoblasts are an excellent cell line to study osteogenic differentiation *in vitro*.<sup>63</sup> The quantification of the cell area and aspect ratio are indicators for cell spreading on surfaces, which is a strong regulator of cell differentiation.<sup>64</sup> Figure 8A,B shows both parameters on different surfaces (glass or PEM coatings in absence or presence of FN). The cell area and the aspect ratio of C2C12 cells plated on the PEM (empty  $[\text{HA,CHI}]_6$  or DNA-loaded  $[\text{HA,CHI}]_3\text{HA-LPX-}[\text{HA,CHI}]_1$ ) were smaller than those on the glass control. Nevertheless, both parameters increase significantly for all surfaces after FN pre-adsorption, which demonstrates that FN is also efficiently adsorbed on all surfaces. It should be noted that PEMs with adsorbed lipoplexes as terminal layer  $[\text{HA,CHI}]_3\text{HA-LPX}$  (without terminal HA,CHI layer) showed larger cell areas and aspect ratio values compared to the PEM  $[\text{HA,CHI}]_6$  or finished

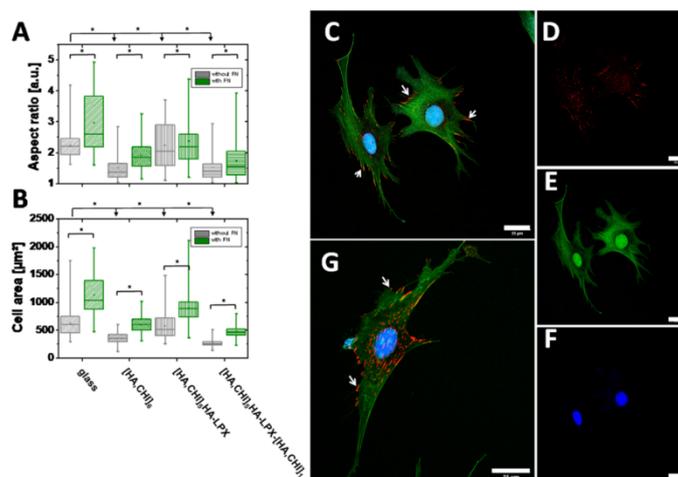


**Figure 8.** Quantification of (A) cell area and (B) aspect ratio of C2C12 cells cultured on different surfaces after 12 h incubation. Image analysis was performed using Fiji software<sup>52</sup> with investigation of at least 10 images per condition. As surface-unmodified glass and glass with different coatings was tested: 12 alternating layers of HA and CHI = [HA,CHI]<sub>6</sub>; 10 alternating layers of HA and CHI followed by a final coating with HA and lipoplexes (intermediate process step of lipoplex embedding according to the lipoplex protocol) = [HA,CHI]<sub>6</sub>HA-LPX; and LbL coatings with embedded lipoplexes using the lipoplex protocol = [HA,CHI]<sub>6</sub>HA-LPX-[HA,CHI]<sub>1</sub>. Further, a secondary modification with FN was studied (green data). The box corresponds to the range in which the middle 50% of the data lie and the band inside the box is the median. The stars indicate significant differences determined by a two-way-ANOVA test ( $\alpha = 0.05$ ). (C) Merged CLSM image of adherent C2C12 cultured on [HA,CHI]<sub>6</sub>HA-LPX-[HA,CHI]<sub>1</sub> after 6 h incubation; the cells were stained for vinculin (red) (D), filamentous actin (green) (E), and the nucleus (blue) (F). (G) Positive control on FN-treated glass. White arrows show focal adhesions positive for vinculin. Scale bar in (C–G) is representative for 25  $\mu\text{m}$ .

DNA-loaded PEM [HA,CHI]<sub>3</sub>HA-LPX-[HA,CHI]<sub>1</sub>. When comparing the surface charge of [HA,CHI]<sub>3</sub>HA-LPX and [HA,CHI]<sub>3</sub>HA-LPX-[HA,CHI]<sub>1</sub> at 7.3, both have a comparable high negative zeta potential (Figure 4A) and it is, most probably, an effect of the NH<sub>2</sub> group density of the lipoplexes compared to CHI.<sup>65</sup> However, this system was not used for subsequent experiments because the lipoplexes are not protected by the cover polyelectrolyte layers. Further to this, the focus was on the DNA-loaded PEM with a terminal FN pre-adsorption, characterized by the sequence [HA,CHI]<sub>3</sub>HA-LPX-[HA,CHI]<sub>1</sub>-FN. This was the DNA-loaded film with the highest cell attachment and spreading.

Further screening for focal adhesions of C2C12 cells growing on PEM [HA,CHI]<sub>3</sub>HA-LPX-[HA,CHI]<sub>1</sub>-FN was conducted using immune histochemical staining. This method was applied to study cell adhesion and spreading through staining of vinculin in focal adhesion and actin filaments. Cells on both substrates, either on [HA,CHI]<sub>3</sub>HA-LPX-[HA,CHI]<sub>1</sub>-FN (Figure 8C–F) or FN-coated glass (Figure 8G), demonstrate strong organization of actin filaments which were longitudinally distributed (green channel) and positioning of vinculin at the end of the actin filaments (red channel, indicated using white arrows). This observation confirms significant interaction of C2C12 through formation of focal adhesions with the surface substrate.

Another important characteristic is the biocompatibility of the DNA-loaded PEM. Hence, the [HA,CHI]<sub>3</sub>HA-LPX-[HA,CHI]<sub>1</sub>-FN multilayer was screened for cell viability 24 h after cell seeding. Microscopic viability tests were performed to get additional information about the distribution of the cells across the film. Figure 9A shows a well (0.34 cm<sup>2</sup>) where the bottom is coated with the DNA-loaded PEM [HA,CHI]<sub>6</sub>HA-LPX-[HA,CHI]<sub>1</sub>. The film is covered with viable cells. The

higher magnification (Figure 9B, live and dead control in Figure 9C,D, respectively) shows that the largest population are viable cells (green fluorescence) which have an elongated shape. Only a few cells are dead (red colour) with a round shape. In addition to this, the FACS analysis demonstrate cell viability of 98.9% for cells growing on the [HA,CHI]<sub>3</sub>HA-LPX-[HA,CHI]<sub>1</sub>-FN multilayer, a value which is in the range of two controls (Figure 9E–G).

Flow cytometry was applied to determine the transfection efficiency for C2C12 cells. Cells seeded on [HA,CHI]<sub>3</sub>HA-LPX-[HA,CHI]<sub>1</sub>-FN thin films loaded with a pDNA encoding for GFP were compared with adherent cells growing on an unloaded [HA,CHI]<sub>6</sub> PEM which were transfected with OH4/DOPE 1/1 lipoplexes in the supernatant containing the same amount of pDNA. The results are presented in Table 2 and Figure 9H–J as representative dot plots. The transfection rate ranges between 5 and 9%, which is a reasonable value for the hard-to-transfect cell line C2C12.<sup>66</sup> In general, the films are more effective in transfecting C2C12 cells compared to the suspension. The contact-triggered transfection is obviously more advantageous compared to the suspension-based transfection with lipoplexes. The incorporation of DNA into the PEM film in the absence of OH4/DOPE 1/1 results in no efficient transfection (Supporting Information, Figure S8).

**In Vivo Studies.** A further step is to investigate the efficacy of the transfection system [HA,CHI]<sub>3</sub>HA-LPX-[HA,CHI]<sub>1</sub>-FN under in vivo conditions. The chorion allantois membrane (CAM) of the chicken embryo was chosen for this purpose. Previous research demonstrates that the CAM is an appropriate animal replacement in vivo model for biomaterial and transfection tests.<sup>67</sup> The experimental design is displayed in Figure 10A. The experiment explores the possibility to have in situ transfection in a complex tissue with lipoplexes loaded

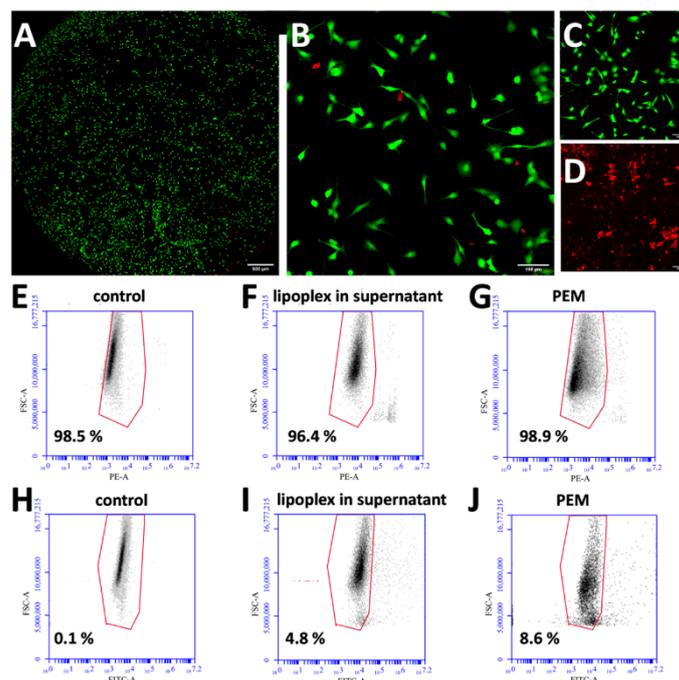


**Figure 9.** (A–D) CLSM viability test of C2C12 cells using the dual Live/Dead cell imaging kit. Cells 24 h after seeding on (A,B) DNA-loaded FN-modified PEMs ( $[\text{HA,CHI}]_6\text{HA-LPX-}[\text{HA,CHI}]_1\text{-FN}$ ),  $5\times$  magnification (A)  $10\times$  magnification (B); (C) FN-coated glass (positive control); (D) FN-coated glass treated at  $60^\circ$  for inducing cell death (dead control). Living cells (green) were differentiated from dead cells (red). Scale bar in (A) corresponds to  $500\ \mu\text{m}$  and in (B–D)  $100\ \mu\text{m}$ . (E–G) Representative FACS viability profiles of (E) untreated C2C12 cells as a live control, (F) C2C12 cells growing on a  $[\text{HA,CHI}]_6$  PEM which were incubated with lipoplexes in solution ( $c_{\text{DNA}} = 0.4\ \mu\text{g}$ ) and (G) C2C12 on  $[\text{HA,CHI}]_3\text{HA-LPX-}[\text{HA,CHI}]_1\text{-FN}$  multilayers ( $c_{\text{DNA}} = 0.4\ \mu\text{g}$ ). Viability of C2C12 cells was determined by the addition of  $50\ \mu\text{g/mL}$  propidium iodide (PI) and gating on cells on FSC-A versus PE-A (propidium iodide). (H–J) Representative transfection efficiency determined by FACS as % GFP positive cells. The results compare (H) untreated C2C12 cells, (I) C2C12 cells growing on a  $[\text{HA,CHI}]_6$  PEM which were incubated with lipoplexes in solution ( $c_{\text{DNA}} = 0.4\ \mu\text{g}$ ), and (J) C2C12 on  $[\text{HA,CHI}]_3\text{HA-LPX-}[\text{HA,CHI}]_1\text{-FN}$  multilayers ( $c_{\text{DNA}} = 0.4\ \mu\text{g}$ ).

**Table 2. Transfection Efficiency Determined by Measuring GFP Fluorescence 24 h after Cells Were Seeded on DNA-Loaded  $[\text{HA,CHI}]_3\text{HA-LPX-}[\text{HA,CHI}]_1\text{-FN}$  PEMs or on  $[\text{HA,CHI}]_6$  PEMs with Lipoplexes in the Supernatant Determined by FACS<sup>a</sup>**

sample	GFP positive cells in %	
	experiment 1	experiment 2
$[\text{HA,CHI}]_6$ PEMs with lipoplexes in supernatant	6.4	4.8
$[\text{HA,CHI}]_3\text{HA-LPX-}[\text{HA,CHI}]_1\text{-FN}$	8.6	6.0

<sup>a</sup>The amount of DNA (immobilized or in solution) was  $0.4\ \mu\text{g}$  per experiment.

in multilayer films. It also investigates if the system can be stored for several days before application. Figure 10B demonstrates GFP expression in the CAM, which had been exposed for 24 h in direct contact with the  $[\text{HA,CHI}]_3\text{HA-LPX-}[\text{HA,CHI}]_1\text{-FN}$  thin film loaded with pDNA encoding for GFP. On another note, different transfection efficiencies were observed depending on the storage condition of the glass plates covered with multilayer films. “Dry storage” was performed with DNA-loaded PEMs, dried directly after preparation, and then stored for 6 days under sterile conditions. “Wet storage” CAM samples were transfected with DNA-loaded PEMs stored

for 6 days in  $0.15\ \text{M}$  NaCl. The latter storage condition yielded in a higher expression of GFP (Figure 10B).

## DISCUSSION

This research provides a proof-of-concept study to develop lipoplex-loaded PEM films for in situ transfection. From an engineering point of view, a method is required to efficiently load defined lipoplex layers into a PEM. Such a defined deposition should be considered for physiological highly active nucleic acid sequences (e.g., cytokine-encoding DNA) to engineer a time-controlled in situ transfection. This can be realized by changing the lipoplex position inside a PEM. This study complements previous research in trying to deposit a single lipoplex layer into PEMs. The work of Holmes and Tabrizian describes the deposition of Lipofectamine 2000 lipoplexes with a negative surface charge into PEMs consisting of glycol-CHI and HA.<sup>36</sup> They could demonstrate efficient DNA transfer out of the lipoplex-loaded surface coating. In addition to that, the authors described an irregular lipoplex distribution in the film and fusion/agglomeration processes of the Lipofectamine 2000 lipoplexes. The present research screens different strategies (lipoplex protocol, liposome protocol, and LB protocol) for embedding DNA compacted in lipoplexes into PEMs composed of HA and CHI. Systematic screening results in an efficient strategy (lipoplex protocol) to

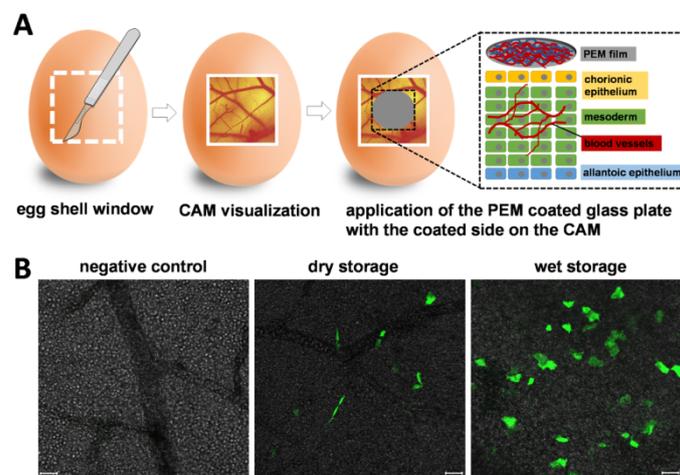


**Figure 10.** (A) Schematic representation of the CAM in vivo trial. On EDD 4, a window of 30 mm diameter was made into an egg shell to expose the CAM surface. On EDD 10, a coverslip coated with lipoplex-loaded PEM's (pCMV-GFP  $c_{DNA} = 1.6 \mu\text{g}$ ) was placed onto the CAM with the coated side and incubated for 24 h. (B) CLSM images of the CAM with GFP-expressing cells in green. "Negative control" denotes CAM treated with an empty glass cover slide. "Dry storage" means the dried PEM-coated coverslips were stored under dry condition 6 days before being applied to the CAM. "Wet storage" means the PEM-coated cover slip was stored in 0.15 M NaCl for 6 days and then applied to the CAM.

absorb positively charged lipoplexes as the single layer into PEMs, while the distribution of the lipoplexes in the system is relatively uniform. Structural investigations using AFM and SEM in comparison with size measurements of lipoplexes indicate that no pronounced fusion or aggregation occurs for the lipoplex protocol contrary to the situation described for the liposome protocol in the paper or the protocol from Holmes and Tabrizian for negatively charged lipoplexes.<sup>36</sup> In conclusion, the PEM system  $[\text{HA,CHI}]_5\text{HA-LPX-}[\text{HA,CHI}]_1$  is in focus of the ongoing research. Although the LB protocol could not achieve sufficient DNA deposition (Figure 2B image 6), it should not get out of focus of future research. The homogeneous lipid deposition covering the whole system is one benefit (Figure 2B image 3), which could not have been achieved either with the lipoplex protocol or with the liposome protocol. There are several parameters which may get adjusted (e.g., pH, ionic strength, time, polyelectrolyte species, and lipid species) in further research to increase the ability to incorporate nucleic acids.

To demonstrate the limits of the functionalized PEM, the loading capacity was determined, demonstrating that it is possible to load up to  $3 \mu\text{g}$  DNA per  $\text{cm}^2$  on the PEM with a loading capacity of 100%. Our work demonstrated that the system  $[\text{HA,CHI}]_5\text{HA-LPX-}[\text{HA,CHI}]_1$  is characterized by a negative surface potential at neutral pH values, surface charge which can inhibit the cell surface interaction.<sup>68</sup> The cell surface interaction studies (cell area, cell aspect ratio, staining of focal adhesions, see Figure 8) result in a FN modified film,  $[\text{HA,CHI}]_5\text{HA-LPX-}[\text{HA,CHI}]_1\text{-FN}$ , with excellent biocompatibility characteristics regarding the viability of C2C12 cells and suitable DNA transfer efficacy. For the transfer to in vivo experiments, the CAM model was selected, an efficient animal replacement model for biocompatibility and efficiency studies of biomaterials.<sup>67,69</sup> The model system is an efficient and time-saving intermediate step between experiments in cell culture and mammalian animal models that does not require approval as an animal experiment when using the correct time frame. In

the present study, we could find evidence for efficient transfer of the model plasmid encoding for GFP to the CAM tissue only triggered by the direct contact between the tissue and a  $[\text{HA,CHI}]_5\text{HA-LPX-}[\text{HA,CHI}]_1\text{-FN}$ -functionalized glass plate. The experiments also confirm that it is possible to store  $[\text{HA,CHI}]_5\text{HA-LPX-}[\text{HA,CHI}]_1\text{-FN}$ -coated implants for 6 days before application without losing the ability for in situ transfection. To what extent storage leads to the reduction in transfection efficiency and which maximum storage time is required for the loss of transfection efficacy must be assessed in future research. Release experiments demonstrated that no lipoplexes or DNA were released after 7 d storage in PBS. Overall, the system seems to work because of a direct contact-triggered transfection of cells, a characteristic which can be used to avoid ectopic effects in later in vivo situations. Zhao et al. demonstrated that cells can enzymatically remodel LbL coatings of chondroitin sulfate and collagen, which means that also structures located inside multilayers are accessible to cells.<sup>70</sup> In the current paper, an enzymatic remodeling by hyaluronidase can explain a contact-triggered uptake of lipoplexes from the PEM into attached cells.

## CONCLUSIONS

This study investigated the development of an in situ transfection system-based LbL technique for immobilization of lipoplexes for future applications in tissue engineering. In particular, three methods for loading HA/CHI-based PEMs with lipid-complexed pDNA were investigated: (i) the adsorption of LPXs (lipoplex protocol), (ii) the separate adsorption of CLs and pDNA, which results in a lipoplex formation on PEM (liposome protocol), (iii) the deposition of separated lipid bilayers using LB techniques and a pDNA layer between in a sandwich-like setting (LB protocol). The studies confirmed that the lipoplex protocol was most effective regarding DNA immobilization and uniformity of the film. The film  $[\text{HA,CHI}]_5\text{HA-LPX-}[\text{HA,CHI}]_1\text{-FN}$  is biocompatible with C2C12 cells and shows efficient in vitro and in vivo

transfection. Additional studies demonstrated the stability of the system and the capability of DNA incorporation. Although this work is not focused on the kinetic aspect of the contact-triggered transfection and the mechanism of DNA transfer, this research is a proof-of-concept study to establish novel surface coatings for contact-triggered in situ transfection. In conclusion, OH4/DOPE 1/1 lipoplex-loaded PEMs composed of HA and CHI have a promising transfection potential and can be adopted as the surface coating of implants to induce in situ transfection in regenerative medicine.

### ■ ASSOCIATED CONTENT

#### SI Supporting Information

The Supporting Information is available free of charge at <https://pubs.acs.org/doi/10.1021/acsami.9b18968>.

Water contact angle measurements, additional ellipsometry measurements, DLS measurements of liposomes, agarose gel images, and additional transfection experiments (PDF)

### ■ AUTHOR INFORMATION

#### Corresponding Author

**Christian Wölk** – Institute of Pharmacy, Department of Medicinal Chemistry, Martin Luther University Halle-Wittenberg, 06120 Halle (Saale), Germany; Institute of Pharmacy, Pharmaceutical Technology, Faculty of Medicine, Leipzig University, 04317 Leipzig, Germany; [orcid.org/0000-0002-8067-7307](https://orcid.org/0000-0002-8067-7307); Email: [christian.woelk@pharmazie.uni-halle.de](mailto:christian.woelk@pharmazie.uni-halle.de), [christian.woelk@medizin.uni-leipzig.de](mailto:christian.woelk@medizin.uni-leipzig.de)

#### Authors

**Catharina Husteden** – Institute of Pharmacy, Department of Medicinal Chemistry, Martin Luther University Halle-Wittenberg, 06120 Halle (Saale), Germany

**Falko Doberenz** – Institute of Pharmacy, Department of Biomedical Materials, Martin Luther University Halle-Wittenberg, 06120 Halle (Saale), Germany

**Nathalie Goergen** – Department of Pharmaceutics and Biopharmaceutics, University of Marburg, 35037 Marburg, Germany

**Shashank Reddy Pinnapireddy** – Department of Pharmaceutics and Biopharmaceutics, University of Marburg, 35037 Marburg, Germany

**Christopher Janich** – Institute of Pharmacy, Department of Medicinal Chemistry, Martin Luther University Halle-Wittenberg, 06120 Halle (Saale), Germany

**Andreas Langner** – Institute of Pharmacy, Department of Medicinal Chemistry, Martin Luther University Halle-Wittenberg, 06120 Halle (Saale), Germany

**Frank Syrowatka** – Interdisciplinary Center of Materials Science, Martin-Luther-University Halle-Wittenberg, 06120 Halle (Saale), Germany

**Alexandros Repanas** – Institute of Pharmacy, Department of Biomedical Materials, Martin Luther University Halle-Wittenberg, 06120 Halle (Saale), Germany

**Frank Erdmann** – Institute of Pharmacy, Department of Pharmacology, Martin Luther University Halle-Wittenberg, 06120 Halle (Saale), Germany

**Jarmila Jedelská** – Department of Pharmaceutics and Biopharmaceutics, University of Marburg, 35037 Marburg, Germany

**Udo Bakowsky** – Department of Pharmaceutics and Biopharmaceutics, University of Marburg, 35037 Marburg, Germany; [orcid.org/0000-0002-3895-0453](https://orcid.org/0000-0002-3895-0453)

**Thomas Groth** – Institute of Pharmacy, Department Biomedical Materials, Martin Luther University Halle-Wittenberg, 06120 Halle (Saale), Germany; Interdisciplinary Center of Materials Science, Martin-Luther-University Halle-Wittenberg, 06120 Halle (Saale), Germany; Laboratory of Biomedical Nanotechnologies, Institute of Bionic Technologies and Engineering, I.M. Sechenov First Moscow State University, 119991 Moscow, Russian Federation; [orcid.org/0000-0001-6647-9657](https://orcid.org/0000-0001-6647-9657)

Complete contact information is available at: <https://pubs.acs.org/10.1021/acsami.9b18968>

#### Notes

The authors declare no competing financial interest.

### ■ ACKNOWLEDGMENTS

This work was supported by the Deutsche Forschungsgemeinschaft (DFG) project-ID 396823779 (C.H. and C.W.) and by grants from the Freundeskreis für Pharmazie e.V. (to C.H.). The authors thank Christin Husteden for proof reading.

### ■ REFERENCES

- (1) O'Connor, T. P.; Crystal, R. G. Genetic Medicines: Treatment Strategies for Hereditary Disorders. *Nat. Rev. Genet.* **2006**, *7*, 261–276.
- (2) Ginn, S. L.; Alexander, I. E.; Edelstein, M. L.; Abedi, M. R.; Wixon, J. Gene Therapy Clinical Trials Worldwide to 2012 - an update. *J. Gene Med.* **2013**, *15*, 65–77.
- (3) Maeder, M. L.; Gersbach, C. A. Genome-editing Technologies for Gene and Cell Therapy. *Mol. Ther.* **2016**, *24*, 430–446.
- (4) Kotterman, M. A.; Schaffer, D. V. Engineering Adeno-associated Viruses for Clinical Gene Therapy. *Nat. Rev. Genet.* **2014**, *15*, 445–451.
- (5) Davidson, B. L.; McCray, P. B., Jr. Current Prospects for RNA Interference-based Therapies. *Nat. Rev. Genet.* **2011**, *12*, 329–340.
- (6) Giacca, M.; Zacchigna, S. Virus-mediated Gene Delivery for Human Gene Therapy. *J. Controlled Release* **2012**, *161*, 377–388.
- (7) Nayak, S.; Herzog, R. W. Progress and Prospects: Immune Responses to Viral Vectors. *Gene Ther.* **2010**, *17*, 295–304.
- (8) Marshall, E. What to Do When Clear Success Comes With an Unclear Risk? *Science* **2002**, *298*, 510–511.
- (9) Yin, H.; Kanasty, R. L.; Eltoukhy, A. A.; Vegas, A. J.; Dorkin, J. R.; Anderson, D. G. Non-viral Vectors for Gene-based Therapy. *Nat. Rev. Genet.* **2014**, *15*, 541–555.
- (10) Glover, D. J.; Lipps, H. J.; Jans, D. A. Towards Safe, Non-viral Therapeutic Gene expression in Humans. *Nat. Rev. Genet.* **2005**, *6*, 299–310.
- (11) Guo, P.; Coban, O.; Snead, N. M.; Trebley, J.; Hoeprich, S.; Guo, S.; Shu, Y. Engineering RNA for Targeted siRNA Delivery and Medical Application. *Adv. Drug Delivery Rev.* **2010**, *62*, 650–666.
- (12) Mundargi, R. C.; Babu, V. R.; Rangaswamy, V.; Patel, P.; Aminabhavi, T. M. Nano/micro technologies for Delivering Macromolecular Therapeutics Using Poly(D,L-lactide-co-glycolide) and its Derivatives. *J. Controlled Release* **2008**, *125*, 193–209.
- (13) Wiethoff, C. M.; Middaugh, C. R. Barriers to Nonviral Gene Delivery. *J. Pharm. Sci.* **2003**, *92*, 203–217.
- (14) Mintzer, M. A.; Simanek, E. E. Nonviral Vectors for Gene Delivery. *Chem. Rev.* **2009**, *109*, 259–302.
- (15) Chen, J.; Wang, K.; Wu, J.; Tian, H.; Chen, X. Polycations for Gene Delivery: Dilemmas and Solutions. *Bioconjugate Chem.* **2019**, *30*, 338–349.

- (16) Scholz, C.; Wagner, E. Therapeutic Plasmid DNA Versus siRNA Delivery: Common and Different Tasks for Synthetic Carriers. *J. Controlled Release* **2012**, *161*, 554–565.
- (17) Wang, T.; Upponi, J. R.; Torchilin, V. P. Design of Multifunctional Non-viral Gene Vectors to Overcome Physiological Barriers: Dilemmas and Strategies. *Int. J. Pharm.* **2012**, *427*, 3–20.
- (18) Kasputis, T.; Farris, E.; Guerreiro, G.; Taylor, J.; Pannier, A. K. Substrate-Mediated Gene Delivery. *The World Scientific Encyclopedia of Nanomedicine and Bioengineering I*; World Scientific, 2016; Vol. 5, pp 219–260.
- (19) Huang, Y.-C.; Simmons, C.; Kaigler, D.; Rice, K. G.; Mooney, D. J. Bone Regeneration in a Rat Cranial Defect with Delivery of PEI-condensed Plasmid DNA Encoding for Bone Morphogenetic Protein-4 (BMP-4). *Gene Ther.* **2005**, *12*, 418–426.
- (20) Shea, L. D.; Smiley, E.; Bonadio, J.; Mooney, D. J. DNA Delivery from Polymer Matrices for Tissue Engineering. *Nat. Biotechnol.* **1999**, *17*, 551–554.
- (21) Bengali, Z.; Shea, L. D. Gene Delivery by Immobilization to Cell-Adhesive Substrates. *MRS Bull.* **2005**, *30*, 659–662.
- (22) Segura, T.; Shea, L. D. Surface-tethered DNA Complexes for Enhanced Gene Delivery. *Bioconjugate Chem.* **2002**, *13*, 621–629.
- (23) Levy, R. J.; Song, C.; Tallapragada, S.; DeFelice, S.; Hinson, J. T.; Vyavahare, N.; Connolly, J.; Ryan, K.; Li, Q. Localized Adenovirus Gene Delivery Using Antiviral IgG Complexation. *Gene Ther.* **2001**, *8*, 659–667.
- (24) Ariga, K.; Hill, J. P.; Ji, Q. Layer-by-layer Assembly as a Versatile Bottom-up Nanofabrication Technique for Exploratory Research and Realistic Application. *Phys. Chem. Chem. Phys.* **2007**, *9*, 2319–2340.
- (25) Decher, G.; Hong, J. D.; Schmitt, J. Buildup of Ultrathin Multilayer Films by a Self-assembly Process: III. Consecutively Alternating Adsorption of Anionic and Cationic Polyelectrolytes on Charged Surfaces. *Thin Solid Films* **1992**, *210–211*, 831–835.
- (26) Decher, G. Fuzzy Nanoassemblies: Toward Layered Polymeric Multicomposites. *Science* **1997**, *277*, 1232–1237.
- (27) Chluba, J.; Voegel, J.-C.; Decher, G.; Erbacher, P.; Schaaf, P.; Ogier, J. Peptide Hormone Covalently Bound to Polyelectrolytes and Embedded into Multilayer Architectures Conserving Full Biological Activity. *Biomacromolecules* **2001**, *2*, 800–805.
- (28) Jessel, N.; Atalar, F.; Lavalle, P.; Mutterer, J.; Decher, G.; Schaaf, P.; Voegel, J.-C.; Ogier, J. Bioactive Coatings Based on a Polyelectrolyte Multilayer Architecture Functionalized by Embedded Proteins. *Adv. Mater.* **2003**, *15*, 692–695.
- (29) Xiao, F.-X.; Pagliaro, M.; Xu, Y.-J.; Liu, B. Layer-by-layer Assembly of Versatile Nanoarchitectures with Diverse Dimensionality: a New Perspective for Rational Construction of Multilayer Assemblies. *Chem. Soc. Rev.* **2016**, *45*, 3088–3121.
- (30) Zhang, J.; Chua, L. S.; Lynn, D. M. Multilayered Thin Films that Sustain the Release of Functional DNA under Physiological Conditions. *Langmuir* **2004**, *20*, 8015–8021.
- (31) Lin, Q.-K.; Ren, K.-F.; Ji, J. Hyaluronic Acid and Chitosan-DNA Complex Multilayered Thin Film as Surface-mediated Nonviral Gene Delivery System. *Colloids Surf., B* **2009**, *74*, 298–303.
- (32) Hartmann, H.; Hossfeld, S.; Schlosshauer, B.; Mitnacht, U.; Pego, A. P.; Dauner, M.; Doser, M.; Stoll, D.; Krastev, R. Hyaluronic Acid/Chitosan Multilayer Coatings on Neuronal Implants for Localized Delivery of siRNA Nanoplexes. *J. Controlled Release* **2013**, *168*, 289–297.
- (33) Yamauchi, F.; Koyamatsu, Y.; Kato, K.; Iwata, H. Layer-by-layer Assembly of Cationic Lipid and Plasmid DNA onto Gold Surface for Stent-assisted Gene Transfer. *Biomaterials* **2006**, *27*, 3497–3504.
- (34) Meyer, F.; Ball, V.; Schaaf, P.; Voegel, J. C.; Ogier, J. Polyplex-embedding in Polyelectrolyte Multilayers for Gene Delivery. *Biochim. Biophys. Acta, Biomembr.* **2006**, *1758*, 419–422.
- (35) Dimitrova, M.; Armtz, Y.; Lavalle, P.; Meyer, F.; Wolf, M.; Schuster, C.; Haikel, Y.; Voegel, J.-C.; Ogier, J. Adenoviral Gene Delivery from Multilayered Polyelectrolyte Architectures. *Adv. Funct. Mater.* **2007**, *17*, 233–245.
- (36) Holmes, C. A.; Tabrizian, M. Substrate-Mediated Gene Delivery from Glycol-Chitosan/Hyaluronic Acid Polyelectrolyte Multilayer Films. *ACS Appl. Mater. Interfaces* **2013**, *5*, 524–531.
- (37) Knopf-Marques, H.; Pravda, M.; Wolfova, L.; Velebny, V.; Schaaf, P.; Vrana, N. E.; Lavalle, P. Hyaluronic Acid and Its Derivatives in Coating and Delivery Systems: Applications in Tissue Engineering, Regenerative Medicine and Immunomodulation. *Adv. Healthcare Mater.* **2016**, *5*, 2841–2855.
- (38) Voigt, J.; Driver, V. R. Hyaluronic Acid Derivatives and Their Healing Effect on Burns, Epithelial Surgical Wounds, and Chronic Wounds: A Systematic Review and Meta-analysis of Randomized Controlled Trials. *Wound Repair Regen.* **2012**, *20*, 317–331.
- (39) Collins, M. N.; Birkinshaw, C. Hyaluronic Acid Based Scaffolds for Tissue Engineering—a Review. *Carbohydr. Polym.* **2013**, *92*, 1262–1279.
- (40) Bernkop-Schnürch, A.; Dünnhaupt, S. Chitosan-based Drug Delivery Systems. *Eur. J. Pharm. Biopharm.* **2012**, *81*, 463–469.
- (41) Rabea, E. I.; Badawy, M. E.-T.; Stevens, C. V.; Smaghe, G.; Steurbaut, W. Chitosan as Antimicrobial Agent: Applications and Mode of Action. *Biomacromolecules* **2003**, *4*, 1457–1465.
- (42) Janich, C.; Wölk, C.; Taßler, S.; Drescher, S.; Meister, A.; Brezesinski, G.; Dobner, B.; Langner, A. Composites of Malonic Acid Diamides and Phospholipids – Structural Parameters for Optimal Transfection Efficiency in A549 cells. *Eur. J. Lipid Sci. Technol.* **2014**, *116*, 1184–1194.
- (43) Janich, C.; Wölk, C.; Erdmann, F.; Groth, T.; Brezesinski, G.; Dobner, B.; Langner, A. Composites of Malonic Acid Diamides and Phospholipids—Impact of Lipoplex Stability on Transfection Efficiency. *J. Controlled Release* **2015**, *220*, 295–307.
- (44) Janich, C.; Pinnapireddy, S. R.; Erdmann, F.; Groth, T.; Langner, A.; Bakowsky, U.; Wölk, C. Fast therapeutic DNA Internalization – A High Potential Transfection System Based on a Peptide Mimicking Cationic Lipid. *Eur. J. Pharm. Biopharm.* **2017**, *118*, 38–47.
- (45) Janich, C.; Taßler, S.; Meister, A.; Hause, G.; Schäfer, J.; Bakowsky, U.; Brezesinski, G.; Wölk, C. Structures of Malonic Acid Diamide/Phospholipid Composites and their Lipoplexes. *Soft Matter* **2016**, *12*, 5854–5866.
- (46) Saffari, M.; Moghimi, H. R.; Dass, C. R. Barriers to Liposomal Gene Delivery: from Application Site to the Target. *Iran. J. Pharm. Res.* **2016**, *15*, 3–17.
- (47) Elouahabi, A.; Ruyschaert, J.-M. Formation and Intracellular Trafficking of Lipoplexes and Polyplexes. *Mol. Ther.* **2005**, *11*, 336–347.
- (48) Szoka, F.; Papahadjopoulos, D. Comparative Properties and Methods of Preparation of Lipid Vesicles (Liposomes). *Annu. Rev. Biophys. Bioeng.* **1980**, *9*, 467–508.
- (49) Gale, G. W.; Small, R. J.; Reinhardt, K. A. Aqueous Cleaning and Surface Conditioning Processes. In *Handbook of Silicon Wafer Cleaning Technology*, 2nd ed.; Reinhardt, K. A., Kern, W., Eds.; William Andrew Publishing: Norwich, NY, 2008; Chapter 4, pp 201–265.
- (50) Ekambaram, B. K.; Niepel, M. S.; Fuhrmann, B.; Schmidt, G.; Groth, T. Introduction of Laser Interference Lithography to Make Nanopatterned Surfaces for Fundamental Studies on Stem Cell Response. *ACS Biomater. Sci. Eng.* **2018**, *4*, 1820–1832.
- (51) Zhao, M.; Li, L.; Zhou, C.; Heyroth, F.; Fuhrmann, B.; Maeder, K.; Groth, T. Improved Stability and Cell Response by Intrinsic Cross-Linking of Multilayers from Collagen I and Oxidized Glycosaminoglycans. *Biomacromolecules* **2014**, *15*, 4272–4280.
- (52) Schindelin, J.; Arganda-Carreras, I.; Frise, E.; Kaynig, V.; Longair, M.; Pietzsch, T.; Preibisch, S.; Rueden, C.; Saalfeld, S.; Schmid, B.; Tinevez, J.-Y.; White, D. J.; Hartenstein, V.; Eliceiri, K.; Tomancak, P.; Cardona, A. Fiji: an Open-source Platform for Biological-image Analysis. *Nat. Methods* **2012**, *9*, 676–682.
- (53) Klein, S.; Prantl, L.; Vykoukal, J.; Loibl, M.; Felthaus, O. Differential Effects of Coating Materials on Viability and Migration of Schwann Cells. *Materials* **2016**, *9*, 150.

- (54) Altankov, G.; Grinnell, F.; Groth, T. Studies on the Biocompatibility of Materials: Fibroblast Reorganization of Substratum-bound Fibronectin on Surfaces Varying in Wettability. *J. Biomed. Mater. Res.* **1996**, *30*, 385–391.
- (55) Liu, Z.-M.; Gu, Q.; Xu, Z.-K.; Groth, T. Synergistic Effect of Polyelectrolyte Multilayers and Osteogenic Growth Medium on Differentiation of Human Mesenchymal Stem Cells. *Macromol. Biosci.* **2010**, *10*, 1043–1054.
- (56) Koynova, R.; Tenchov, B. Cationic Phospholipids: Structure–transfection Activity Relationships. *Soft Matter* **2009**, *5*, 3187–3200.
- (57) Dan, N. Lipid–Nucleic Acid Supramolecular Complexes: Lipoplex Structure and the Kinetics of Formation. *AIMS Biophys.* **2015**, *2*, 163–183.
- (58) Liao, Y.-H.; Jones, S. A.; Forbes, B.; Martin, G. P.; Brown, M. B. Hyaluronan: Pharmaceutical Characterization and Drug Delivery. *Drug Delivery* **2005**, *12*, 327–342.
- (59) Duval, J. F. L.; Werner, C.; Zimmermann, R. Electrokinetics of Soft Polymeric Interphases with Layered Distribution of Anionic and Cationic Charges. *Curr. Opin. Colloid Interface Sci.* **2016**, *24*, 1–12.
- (60) Duval, J. F. L.; Küttner, D.; Nitschke, M.; Werner, C.; Zimmermann, R. Interrelations Between Charging, Structure and Electrokinetics of Nanometric Polyelectrolyte Films. *J. Colloid Interface Sci.* **2011**, *362*, 439–449.
- (61) Guduru, D.; Niepel, M. S.; Gonzalez-Garcia, C.; Salmeron-Sanchez, M.; Groth, T. Comparative Study of Osteogenic Activity of Multilayers Made of Synthetic and Biogenic Polyelectrolytes. *Macromol. Biosci.* **2017**, *17*, 1700078.
- (62) Caruso, F.; Lichtenfeld, H.; Donath, E.; Möhwald, H. Investigation of Electrostatic Interactions in Polyelectrolyte Multilayer Films: Binding of Anionic Fluorescent Probes to Layers Assembled onto Colloids. *Macromolecules* **1999**, *32*, 2317–2328.
- (63) Peschel, D.; Zhang, K.; Fischer, S.; Groth, T. Modulation of Osteogenic Activity of BMP-2 by Cellulose and Chitosan Derivatives. *Acta Biomater.* **2012**, *8*, 183–193.
- (64) McBeath, R.; Pirone, D. M.; Nelson, C. M.; Bhadriraju, K.; Chen, C. S. Cell Shape, Cytoskeletal Tension, and RhoA Regulate Stem Cell Lineage Commitment. *Dev. Cell* **2004**, *6*, 483–495.
- (65) Altankov, G.; Richau, K.; Groth, T. The Role of Surface Zeta Potential and Substratum Chemistry for Regulation of Dermal Fibroblasts Interaction. *Materialwiss. Werkstofftech.* **2003**, *34*, 1120–1128.
- (66) Sork, H.; Nordin, J. Z.; Turunen, J. J.; Wiklander, O. P.; Bestas, B.; Zaghloul, E. M.; Margus, H.; Padari, K.; Duru, A. D.; Corso, G.; Bost, J.; Vader, P.; Pooga, M.; Smith, C. E.; Wood, M. J.; Schiffelers, R. M.; Hällbrink, M.; Andaloussi, S. E. Lipid-based Transfection Reagents Exhibit Cryo-induced Increase in Transfection Efficiency. *Mol. Ther.—Nucleic Acids* **2016**, *5*, No. e290.
- (67) Lei, Y.; Rahim, M.; Ng, Q.; Segura, T. Hyaluronic Acid and Fibrin Hydrogels with Concentrated DNA/PEI Polyplexes for Local Gene Delivery. *J. Controlled Release* **2011**, *153*, 255–261.
- (68) Xu, L.-P.; Meng, J.; Zhang, S.; Ma, X.; Wang, S. Amplified Effect of Surface Charge on Cell Adhesion by Nanostructures. *Nanoscale* **2016**, *8*, 12540–12543.
- (69) Moreno-Jiménez, L.; Kanczler, J. M.; Hulsart-Billstrom, G.; Inglis, S.; Oreffo, R. O. C. The Chorioallantoic Membrane Assay for Biomaterial Testing in Tissue Engineering: A Short-Term In Vivo Preclinical Model. *Tissue Eng., Part C* **2017**, *23*, 938–952.
- (70) Zhao, M.; Altankov, G.; Grabiec, U.; Bennett, M.; Salmeron-Sanchez, M.; Dehghani, F.; Groth, T. Molecular Composition of GAG–collagen I Multilayers Affects Remodeling of Terminal Layers and Osteogenic Differentiation of Adipose-derived Stem Cells. *Acta Biomater.* **2016**, *41*, 86–99.

## 2.4) Publikation II

### **Implantatüberzüge für die in situ Transfektion in der regenerativen Medizin**

C. Husteden, T. Groth, C. Wölk.

BIOspektrum, Volume 20, Issue 4, 2021

<https://doi.org/10.1007/s12268-021-1594-4>

## Regenerative Medizin

# Implantatüberzüge für die *in situ*-Transfektion in der regenerativen Medizin

CATHARINA HUSTEDEN<sup>1</sup>, THOMAS GROTH<sup>2</sup>, CHRISTIAN WÖLK<sup>3</sup>

<sup>1</sup> ABTEILUNG BIOCHEMISCHE PHARMAZIE, INSTITUT FÜR PHARMAZIE, UNIVERSITÄT HALLE-WITTENBERG

<sup>2</sup> AG BIOMEDIZINISCHE MATERIALIEN, INSTITUT FÜR PHARMAZIE, UNIVERSITÄT HALLE-WITTENBERG

<sup>3</sup> PHARMAZEUTISCHE TECHNOLOGIE, INSTITUT FÜR PHARMAZIE, MEDIZINISCHE FAKULTÄT, UNIVERSITÄT LEIPZIG

**A promising approach in regenerative medicine is to modify cell behaviour with growth factors. However, the side of action has to be in spatial control. We present a new strategy in the field of regenerative medicine based on the combination of implant coatings with nano-scaled gene vectors. This enables the local restricted *in situ* transfection of cells to induce the production of cytokines. Therewith, the migration and differentiation of cells can be controlled to support tissue regeneration.**

DOI: 10.1007/s12268-021-1594-4  
© Die Autoren 2021

Das biomedizinische Gebiet der Gewebekonstruktion und Regenerativen Medizin (*tissue engineering and regenerative medicine*, TERM) eröffnet eine Vielzahl an Perspektiven in der Behandlung von Organ- und Gewebdefekten [1, 2]. Durch Innovationen im Bereich der biotechnologischen Methoden hat sich das Spektrum der Therapieoptionen auf diesem Gebiet erheblich erweitert. Der Einsatz von Zytokinen und Wachstumsfaktoren bietet neue Möglichkeiten, das Einwandern und die Differenzierung von Zellen zu beeinflussen. Weiterhin kommen immer häufiger therapeutische Ansätze aus dem Gebiet der Arzneimittel für neuartige Therapien zum Einsatz (*advanced therapy medicinal products*, ATMPs). ATMPs sind Therapeutika, die in mindestens eine der folgenden Kategorien eingeordnet werden können (EU-Richtlinie 2001/83/EG):

- Gentherapeutika
- somatische Zelltherapeutika
- biotechnologisch bearbeitete Gewebeprodukte

ATMPs bieten neue Ansatzpunkte für die Behandlung von angeborenen oder erworbenen Erkrankungen. In den letzten zwei Dekaden haben Therapiestrategien mit ATMPs

den Bereich der klinischen Forschung verlassen und den Arzneimittelmarkt betreten [3].

### Regenerative Medizin durch *in situ*-Transfektion

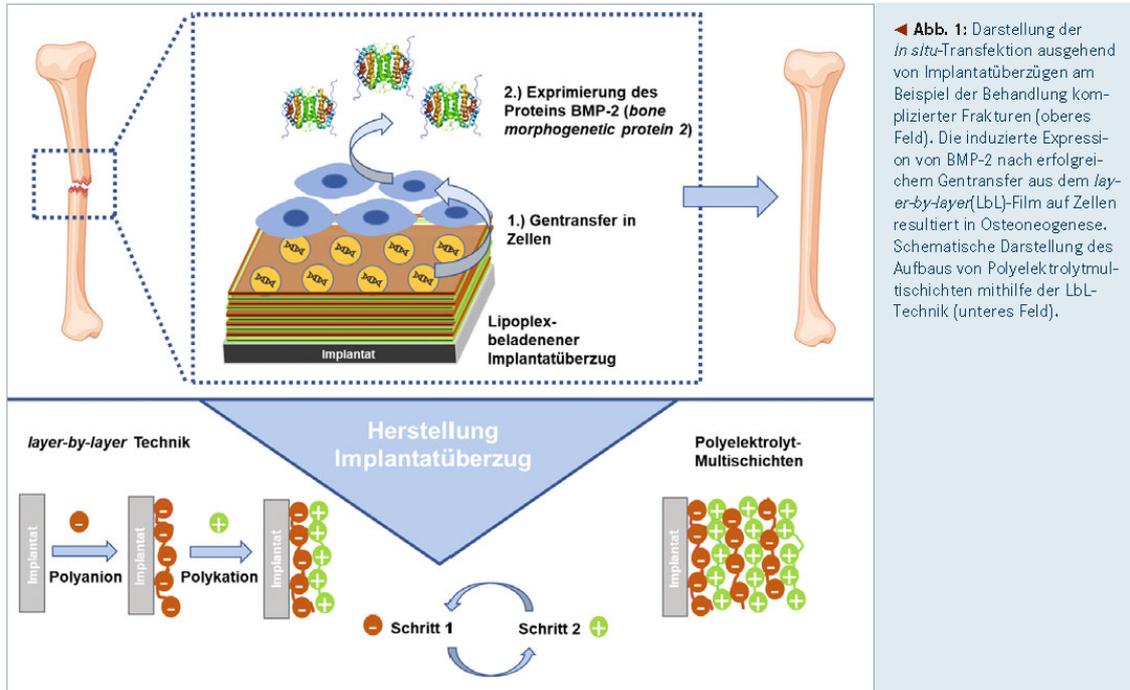
Der von uns gewählte Ansatzpunkt kombiniert materialwissenschaftliche Aspekte und gentherapeutische Ansätze, um funktionalisierte Überzüge für Implantate zu entwickeln, welche im Bereich der regenerativen Medizin eingesetzt werden sollen. Die Schlüsselstrategie beinhaltet eine *in situ*-Transfektion (artifizieller Nukleinsäuretransfer im Organismus) an Körperzellen ausgehend von den eingesetzten Implantaten. Dieser Prozess soll die Produktion von Zytokinen anregen, welche die gezielte Zelldifferenzierung für die Geweberegeneration auslösen. Das Pilotprojekt fokussiert sich auf die Regeneration komplizierter Knochenbrüche. Eine vom Implantat ausgehende *in situ*-Transfektion kann dabei genutzt werden, um körpereigene Zellen zur Produktion von knochenmorphogenetischen Proteinen (*bone morphogenetic proteins*, BMPs) anzuregen und damit die Knochenregeneration zu stimulieren (Abb. 1). Der Vorteil dieser Strategie besteht darin, dass die hochaktiven Zyto-

kine so nur am gewünschten Knochendefekt gebildet werden. Somit werden systemische unerwünschte Effekte verhindert, wie z. B. eine ektopische Ossifikation (Verknöcherung von Muskulatur).

### Herstellung Lipoplex-beladener Implantatüberzüge mittels *layer-by-layer*-Technik

Um Überzüge von einer Stärke im Submikrometerbereich für Implantate zu generieren, sind hohe Anforderungen an den Herstellungsprozess zu stellen. Die Biokompatibilität der Materialien steht dabei im Vordergrund. Der Überzug muss aber auch flexibel auf Implantate mit unterschiedlichsten Formen und Poren übertragbar sein. Der Aufbau von Polyelektrolytmultischichten ist aufgrund der Flexibilität des Prozesses besonders geeignet. Bei dieser Methode werden Lagen komplementärer multivalenter Moleküle Schicht für Schicht aufgebaut (*layer-by-layer technique*, LbL). Beruht der Prozess auf Interaktionen mehrfach geladener Moleküle, ist auch von Polyelektrolytmultischichten die Rede (Abb. 1). Die Flexibilität der LbL-Methode resultiert aus der variablen Verwendung der Grundkomponenten (z. B. geladene Polymere, organische Verbindungen, anorganische Nanopartikel, Biomoleküle). Damit lässt sich die vertikale Struktur des Filmüberzugs, bezogen auf die Oberfläche, sehr leicht variieren. Weiterhin ist der Herstellungsprozess sehr flexibel. Verschiedene Verfahren, wie die Tauch- oder Spray-Methoden bis hin zu Druckverfahren, ermöglichen den Überzug komplexer Geometrien mit Polyelektrolytmultischichten. Ein weiterer Vorteil ist die unkomplizierte Verwendung von wässrigen Lösungsmitteln für den LbL-Prozess unter milden pH-Werten bei Raumtemperatur. Somit kann auch eine hohe Kompatibilität mit biologischen Materialien gewährleistet werden [4].

Unsere Herangehensweise beruht auf einem LbL-basierten Aufbau von Überzügen mit einer Stärke im Submikrometerbereich unter Verwendung von geladenen Biopolymeren. Die Funktionalisierung für die *in situ*-



◀ **Abb. 1:** Darstellung der *in situ*-Transfektion ausgehend von Implantatüberzügen am Beispiel der Behandlung komplizierter Frakturen (oberes Feld). Die induzierte Expression von BMP-2 nach erfolgreichem Gentransfer aus dem *layer-by-layer* (LbL)-Film auf Zellen resultiert in Osteoneogenese. Schematische Darstellung des Aufbaus von Polyelektrolytmultischichten mithilfe der LbL-Technik (unteres Feld).

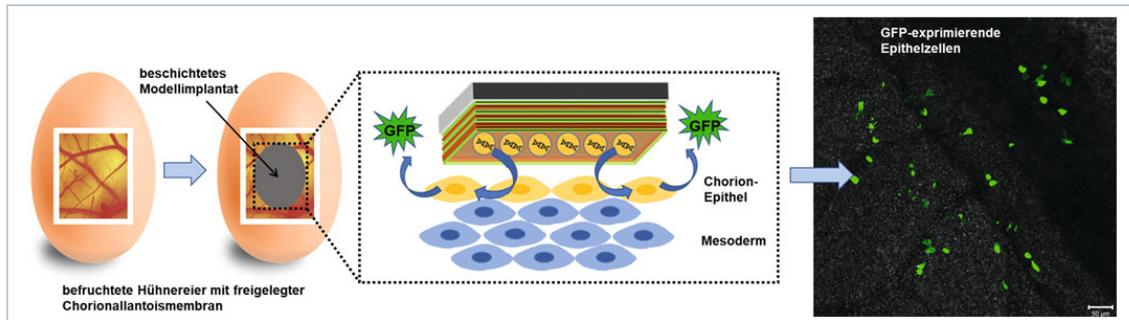
Transfektion beruht auf der Einbettung DNA-beladener Lipidnanopartikel, die Lipoplexe, in die Polyelektrolytmultischichten (Abb. 1). Die dabei verwendeten Materialien haben einen erheblichen Einfluss auf die mechanischen Eigenschaften und die Stabilität des Überzugs. Weiterhin beeinflussen die Eigenschaften des Films wesentlich die Interaktion mit Zellen und Proteinen. Besonders interessant sind LbL-Filme, die auf Komponenten der humanen extrazellulären Matrix beruhen – eine Strategie, die auch in unseren Arbeiten Anwendung findet [5]. Über solche Systeme können gezielt Wachstumsfaktoren aus der interstitiellen Flüssigkeit über die natürlichen Bindungsmotive gebunden werden. Dadurch kann ein Mikromilieu geschaffen werden, welches dem natürlichen Gewebe entspricht. Des Weiteren besitzen Komponenten der extrazellulären Matrix Bindungsmotive für Rezeptoren auf der Zelloberfläche, über die Zelladhäsivität und Differenzierung beeinflusst werden können [6].

Die *in situ*-Transfektion ausgehend vom LbL-Film kann für die lokale Produktion von Wachstumsfaktoren durch transfizierte Zellen genutzt werden, wodurch man einen autokrinen oder parakrinen Effekt erzielen kann. Erste Polyelektrolytmultischichtbasierte Transfektionssysteme nutzten DNA

als Polyanion für den LbL-Aufbau in Kombination mit einem Polykation [7]. Ein Problem besteht aber in der Freisetzung von unkomplexierter DNA. Diese wird schnell von Nucleasen abgebaut und sehr ineffizient von Zellen aufgenommen. Diese Nachteile können umgangen werden, indem man Nucleinsäure-beladene Nanopartikel in die Polyelektrolytmultischichten einbaut. Die Nanopartikelformulierung hat einen schützenden Effekt auf die Nucleinsäure und fördert die zelluläre Aufnahme. Lipoplexe ermöglichen die Umsetzung dieser Strategie.

In einer kürzlich veröffentlichten Arbeit stellen wir einen vielversprechenden Kandidaten für Lipoplex-beladene Implantatüberzüge vor [8]. Als Komponenten für den Schichtaufbau wurden Chitosan und Hyaluronsäure verwendet. Chitosan ist ein kationisches Biopolymer, das durch Deacetylierung von Chitin gewonnen wird. Seine antimikrobiellen Eigenschaften machen es zu einem interessanten Material für Implantatüberzüge [9]. Hyaluronsäure ist ein natürlicher Bestandteil der extrazellulären Matrix im menschlichen Organismus. Weiterhin existieren für beide Biopolymere Qualitätsanforderungen im Europäischen Arzneibuch und der United States Pharmacopeia. Dies erleichtert eine mögliche Marktzulassung.

Als aktive Komponente für die Transfektion wurden selbstentwickelte Lipidformulierungen für den Lipoplexaufbau verwendet, welche herausragende Eigenschaften als Transfektionsreagenz aufweisen [10]. Der kationische Charakter der Lipoplexe erlaubt außerdem eine effiziente Einbettung in die Polyelektrolytmultischicht aus Hyaluronsäure und Chitosan. Um eine effiziente Interaktion von Zellen mit dem Filmüberzug zu gewährleisten, wurde eine finale Funktionalisierung mit Fibronectin, einem wichtigen Bestandteil der extrazellulären Matrix, durchgeführt. Zellen interagieren über Integrine mit Fibronectin und werden in ihrer Adhäsivität und Funktionalität beeinflusst [11]. Die veröffentlichten Studien demonstrieren den effektiven Aufbau des funktionalisierten Überzugs auf Oberflächen. Die Nucleinsäure war dabei fest in den Lipoplexen eingebettet und somit im Überzug verankert. Dies ist eine wesentliche Voraussetzung der Strategie der *in situ*-Transfektion. Eine sofortige Freisetzung der DNA-beladenen Lipoplexe würde das Risiko einer Transfektion ferner Gewebe durch systemische Zirkulation erhöhen. Die lokale Wirkung wäre nicht gegeben. Unsere Strategie sieht vor, dass lediglich solche Zellen transfiziert werden, die direkt im Kontakt mit dem Implantat stehen. Der Lipoplex-



▲ **Abb. 2:** Proof-of-concept-Experiment der *in situ*-Transfektion an der Chorionallantoismembran im Hühnerei. Der Überzug auf dem Modellimplantat besteht aus Chitosan und Hyaluronsäure. Die eingebetteten Lipoplexe sind mit GFP-codierender DNA beladen. Experimentelle Details sind in [8] beschrieben.

beladene Überzug aus Chitosan und Hyaluronsäure wurde effizient von Zellen besiedelt, wobei eine hohe Zytokompatibilität beobachtet wurde. Die auf dem Film wachsenden Zellen konnten die Nukleinsäure aus der Polyelektrolytmultischicht effektiv aufnehmen und das codierte Gen, in diesem Fall das *GFP*-Reportergen (grün fluoreszierendes Protein) effizient exprimieren. Auch komplexe Gewebe, wie die Chorioallantoismembran des befruchteten Hühnereis als *in vivo*-Modell, konnten durch direkten Kontakt mit dem Lipoplex-beladenen Filmüberzug transfiziert werden (Abb. 2). Diese Pilotstudie demonstriert das große Potenzial des von uns entwickelten Systems für die *in situ*-Transfektion. Aktuelle Arbeiten beschäftigen sich mit der Anwendung von Genen für spezielle Wachstumsfaktoren und deren Wirkung auf Stammzellen, welche den Polymerüberzug besiedeln.

**Danksagung**

Dieses Projekt wird von der Deutschen Forschungsgemeinschaft (DFG), Projektnummer 396823779, finanziell unterstützt. Wir danken der Arbeitsgruppe von Prof. Udo Bakows-

ky, Institut für Pharmazeutische Technologie und Biopharmazie, Philipps Universität Marburg, für die CAM-Experimente.

**Literatur**

[1] Vacanti JP, Langer R (1999) Tissue engineering: the design and fabrication of living replacement devices for surgical reconstruction and transplantation. *Lancet* 354: 32–34  
 [2] Vacanti JP (2010) Tissue engineering and regenerative medicine: from first principles to state of the art. *Journal of pediatric surgery* 45: 291–294  
 [3] Paul-Ehrlich-Institut. <https://www.pei.de>  
 [4] Borges J, Mano JF (2014) Molecular interactions driving the layer-by-layer assembly of multilayers. *Chem Rev* 114: 8883–8942  
 [5] Brito Barrera YA, Hause G, Menzel M et al. (2020) Engineering osteogenic microenvironments by combination of multilayers from collagen type I and chondroitin sulfate with novel cationic liposomes. *Materials Today Bio* 7: 100071  
 [6] Zhao M, Altankov G, Grabiec U et al. (2016) Molecular composition of GAG-collagen I multilayers affects remodeling of terminal layers and osteogenic differentiation of adipose-derived stem cells. *Acta Biomaterialia* 41: 86–99  
 [7] Zhang J, Chua LS, Lynn MD (2004) Multilayered thin films that sustain the release of functional DNA under physiological conditions. *Langmuir* 20: 8015–8021  
 [8] Husteden C, Doberenz F, Goergen N et al. (2020) Contact-triggered lipofection from multilayer films designed as surfaces for *in situ* transfection strategies in tissue engineering. *ACS Appl Mater Interfaces* 12: 8963–8977  
 [9] Zheng L, Zhu J (2003) Study on antimicrobial activity of chitosan with different molecular weights. *Carbohydrate Polymers* 54: 527–530  
 [10] Janich C, Wölk C, Erdmann F et al. (2015) Composites of malonic acid diamides and phospholipids – Impact of lipoplex stability on transfection efficiency. *J Control Release* 220: 295–307

[11] Altankov G, Grinell F, Growth T (1996) Studies on the biocompatibility of materials: fibroblast reorganization of substratum bound fibronectin on surfaces varying in wettability. *J Biomed Mater Res* 30: 385–391

Funding note: Open Access funding enabled and organized by Projekt DEAL. Open Access: Dieser Artikel wird unter der Creative Commons Namensnennung 4.0 International Lizenz veröffentlicht, welche die Nutzung, Vervielfältigung, Bearbeitung, Verbreitung und Wiedergabe in jeglichem Medium und Format erlaubt, sofern Sie den/die ursprünglichen Autor(en) und die Quelle ordnungsgemäß nennen, einen Link zur Creative Commons Lizenz beifügen und angeben, ob Änderungen vorgenommen wurden. Die in diesem Artikel enthaltenen Bilder und sonstiges Drittmaterial unterliegen ebenfalls der genannten Creative Commons Lizenz, sofern sich aus der Abbildung legendende nichts anderes ergibt. Sofern das betreffende Material nicht unter der genannten Creative Commons Lizenz steht und die betreffende Handlung nicht nach gesetzlichen Vorschriften erlaubt ist, ist für die oben aufgeführten Weiterverwendungen des Materials die Einwilligung des jeweiligen Rechteinhabers einzuholen. Weitere Details zur Lizenz entnehmen Sie bitte der Lizenzinformation auf <http://creativecommons.org/licenses/by/4.0/deed.de>.



Catharina Husteden, Thomas Groth und Christian Wölk (v.l.n.r.)

**Korrespondenzadresse:**

Dr. Christian Wölk  
 Institut für Pharmazie  
 Universität Leipzig  
 Eilenburger Straße 15a  
 D-04317 Leipzig  
[christian.woelk@medizin.uni-leipzig.de](mailto:christian.woelk@medizin.uni-leipzig.de)

## 2.5) Publikation III

### **Extracellular matrix-inspired surface coatings functionalized with dexamethasone-loaded liposomes to induce osteo- and chondrogenic differentiation of multipotent stem cells**

Y.A. Brito Barrera, C. Husteden, J. Alherz, B. Fuhrmann, C. Wölk, T. Groth

Materials Science & Engineering C, 2021

<https://doi.org/10.1016/j.msec.2021.112516>

*Supporting Information* ist dem Anhang beigelegt.



Contents lists available at ScienceDirect

## Materials Science &amp; Engineering C

journal homepage: [www.elsevier.com/locate/msec](http://www.elsevier.com/locate/msec)

## Extracellular matrix-inspired surface coatings functionalized with dexamethasone-loaded liposomes to induce osteo- and chondrogenic differentiation of multipotent stem cells

Yazmin A. Brito Barrera<sup>a</sup>, Catharina Husteden<sup>b</sup>, Jumanah Alherz<sup>a</sup>, Bodo Fuhrmann<sup>c</sup>, Christian Wölk<sup>d</sup>, Thomas Groth<sup>a,c,e,\*</sup>

<sup>a</sup> Department Biomedical Materials, Institute of Pharmacy, Martin Luther University Halle–Wittenberg, Heinrich-Damerow-Strasse 4, 06120 Halle (Saale), Germany

<sup>b</sup> Medicinal Chemistry Department, Institute of Pharmacy, Martin Luther University Halle-Wittenberg, 06120 Halle (Saale), Germany

<sup>c</sup> Interdisciplinary Center of Materials Science, Martin Luther University Halle-Wittenberg, D-06099 Halle (Saale), Germany

<sup>d</sup> Pharmaceutical Technology, Institute of Pharmacy, Faculty of Medicine, Leipzig University, 04317 Leipzig, Germany

<sup>e</sup> Laboratory of Biomedical Nanotechnologies, Institute of Bionic Technologies and Engineering, I.M. Sechenov First Moscow State University, 119991, Trubetskaya street 8, Moscow, Russian Federation

## ARTICLE INFO

## Keywords:

C3H10T1/2 cells  
Cationic lipids  
Hyaluronic acid  
Collagen I  
Dexamethasone  
Osteogenic/chondrogenic differentiation  
Polyelectrolyte multilayer system

## ABSTRACT

Biomimetic surface coatings can be combined with conventional implants to mimic the extracellular matrix (ECM) of the surrounding tissue to make them more biocompatible. Layer-by-layer technique (LbL) can be used for making surface coatings by alternating adsorption of polyanions and polycations from aqueous solutions without need of chemical reactions. Here, polyelectrolyte multilayer (PEM) systems is made of hyaluronic acid (HA) as polyanion and Collagen I (Col) as polycation to mimic the ECM of connective tissue. The PEM are combined with dexamethasone (Dex)-loaded liposomes to achieve a local delivery and protection of this drug for stimulation of osteo- and chondrogenic differentiation of multipotent stem cells. The liposomes possess a positive surface charge that is required for immobilization on the PEM. The surface properties of PEM system show a positive zeta potential after liposome adsorption and a decrease in wettability, both promoting cell adhesion and spreading of C3H10T1/2 multipotent embryonic mouse fibroblasts. Differentiation of C3H10T1/2 was more prominent on the PEM system with embedded Dex-loaded liposomes compared to the basal PEM system and the use of free Dex-loaded liposomes in the supernatant. This was evident by immunohistochemical staining and an upregulation of the expression of genes, which play a key role in osteogenesis (RunX2, ALP, Osteocalcin (OCN)) and chondrogenesis (Sox9, aggrecan (ACAN), collagen type II), determined by quantitative Real-time polymerase chain reaction (qRT-PCR) after 21 days. These findings indicate that the designed liposome-loaded PEM system have high potential for use as drug delivery systems for implant coatings that can induce bone and cartilage differentiation needed for example in osteochondral implants.

**Abbreviations:** ALP, Alkaline Phosphatase; ACAN, aggrecan; AFM, Atomic force microscopy; ASC, ascorbic acid; BMP, bone morphogenetic proteins; CLSM, Confocal Laser Scanning Microscopy; Col, Collagen I; Dex, Dexamethasone; DMEM, Dulbecco's modified Eagle's medium; DOPE, dioleoylphosphatidylethanolamine; ECM, Extracellular matrix; FCS, Fetal calf serum; GAG, Glycosaminoglycan;  $\beta$ -Gly,  $\beta$ -Glycerophosphate; HA, Hyaluronic acid; RHAMM, hyaluronan-mediated motility; LbL, Layer-by-Layer; (MKP-1), Mitogen-activated protein kinase phosphatase 1; PBS, Phosphate-buffered saline; PEI, Polyethylenimine; PEM, polyelectrolyte multilayer system; qRT-PCR, Quantitative Real-time polymerase chain reaction; OO4, *N*-{6-amino-1-[*N*-(9*Z*)-octadec-9-enylamino]-1-oxohexan-(2*S*)-2-yl]-*N'*-[2-[*N,N*-bis(2-aminoethyl)amino] ethyl]-2-hexadecylpropanoamide; OCD, osteochondral defect; OCN, Osteocalcin; SN, supernatant; SPR, Surface plasmon resonance; TAZ, (transcriptional co-activator with PDZ-binding motif); WCA, Water contact angle.

\* Corresponding author at: Department Biomedical Materials, Institute of Pharmacy, Martin-Luther-University Halle-Wittenberg, Heinrich-Damerow-Strasse 4, 06120 Halle (Saale), Germany.

E-mail address: [thomas.groth@pharmazie.uni-halle.de](mailto:thomas.groth@pharmazie.uni-halle.de) (T. Groth).

<https://doi.org/10.1016/j.msec.2021.112516>

Received 27 August 2021; Received in revised form 19 October 2021; Accepted 22 October 2021

Available online 29 October 2021

0928-4931/© 2021 The Authors. Published by Elsevier B.V. This is an open access article under the CC BY license (<http://creativecommons.org/licenses/by/4.0/>).

Reprinted with permission from Journal of Materials Science & Engineering C, Brito Barrera et al., Extracellular matrix-inspired surface coatings functionalized with dexamethasone-loaded liposomes to induce osteo- and chondrogenic differentiation of multipotent stem cells, Mater. Sci. & En, C, 2021, Volume 131, 112516.

© 2021 Elsevier, DOI: 10.1016/j.msec.2021.112516

## 1. Introduction

Bone and cartilages defects are common disorders affecting people of all ages. These defects are caused by trauma, tumors, infections, and congenital diseases [1,2]. One example are osteochondral defects (OCD) that affect both articular cartilage and subchondral bone as important components of joints in the body [2,3]. The articular cartilage protects the subchondral bone from contact pressure and permits low friction movements of the joint [3]. Commonly, the cartilage and subchondral bone undergo degeneration as the result of osteoarthritis, which requires often surgical interventions [2]. The more recent management of OC lesions does not only aim to relieving patients from pain and repairing damaged tissue but also restoring functionality of the joint [4]. Conventional therapies include drilling techniques, abrasion, micro fracture as well as transplantation of OC allografts and autologous chondrocyte implantation [5,6]. Unfortunately, severe OC defects often require total joint replacement implanting artificial joints made of metals, ceramics and durable polymers [4]. However, these materials are not bioactive, which may cause delayed healing or induction of inflammation as undesired effects [4]. Therefore, coating the implant surface – particularly the metallic parts that are inserted in the bone – with materials that promote engrafting like bioactive calcium phosphates or polymers has been suggested [4].

One of the techniques for surface coating of implants is the Layer-by-Layer technique (LbL) [7]. This surface coating method was established by Decher and coworkers [8] and is based on cycles of alternating adsorption of polyanions and polycations from aqueous solutions onto charged surfaces [8]. LbL has been widely used for various biomedical applications including tissue engineering, medical implants, regenerative medicines, and drug delivery [9–12]. For instance, multilayers made of biogenic polyelectrolytes such as collagen and glycosaminoglycans have been found to guide cell adhesion and function because they mimic partly the composition of extracellular matrix (ECM) of connective tissue [13].

Surface coatings based on LbL can be used to improve biocompatibility of implants but also to deliver a drug locally [14]. A limitation of pharmaceutical treatment of OC defects is that the systemic delivery of drugs is not leading to the desired local effect and it may have systemic side effects [15]. Hence, the advantages of a local delivery are to bring the agent to the target, reducing the drug amount, toxicity and other harmful local and systemic side effects [16,17]. Options to deliver a drug with an orthopedic implant or scaffold can be based on coating the drug on the implant surface or blending the drug with the biomaterials during production [15]. Nowadays, bone regeneration after complicated fractures or larger bone defects is achieved by use of growth factors like bone morphogenetic proteins (BMP), transforming growth factors, and growth hormones [15] to promote cell adhesion, proliferation, and differentiation [18]. However, a limitation of the current clinical use of growth factors like BMP-2, is the high cost and dosage used because of their fast degradation. Particularly the high dosage of growth factors like BMP-2 in mg scale in some clinical applications can have negative local and systemic side effects [19,20]. Therefore, local delivery of small quantities in microgram scale as suggested by Salmeron-Sanchez and coworkers [20] may provide a better solution for regeneration of bone.

On the other hand, nano-sized materials can be applied as systems for release of bioactive agents that can be used in regenerative medicine and treatment of cancer. Liposomes are interesting since they can carry different types of drugs because of their aqueous inner compartment and the hydrophobic part of the lipid bilayer. For example, liposomes have been applied for the delivery of dexamethasone (Dex) to regenerate bone [5,21]. They can be also applied for transfection of cells by the delivery of nucleic acids [22], since positively charged liposomes and lipoplexes can be efficiently internalized into cells. We could show recently that liposomes composed of dioleoylphosphatidylethanolamine (DOPE) and the ionizable lipid *N*-(6-amino-1-[*N*-(9*Z*)-octadec-9-enylamino]-1-oxohexan-(2*S*)-2-yl)-*N'*-(2-[*N,N*-bis(2-aminoethyl)amino]

ethyl)-2[(9*Z*)-octadec-9-enyl]propandiamide (OO4) represent an excellent carrier for drug delivery in cells [23–25]. Overall, liposomes possess a very wide spectrum of application as drug-delivery systems for charged molecules [26], of anti-microbial agents [27], as vaccine carriers [28], transfection agents [29], and delivery of growth and differentiation factors such as BMP-2, TGF, and Dex [21,30]. In addition, liposomes can be used as component for formation of multilayers by LbL due to their inherent charge, which permits localized delivery of drugs avoiding systemic effects [31].

Previous studies combining vesicular structures with polyelectrolytes to fabricate multilayers (PEM) were made using phosphatidylcholine (PC) liposomes, doped with phosphatidylserine (PS) or phosphatidylglycerol (PG) and stabilized with poly-L-lysine (PLL) into PEMs composed of synthetic polymers [32,33]. However, these studies were focussed predominantly on the material science aspects. There are also previous investigations using PC liposomes embedded in different PEM systems to study their interactions with cells. For example, Graf et al. described efficient encapsulation of calcein-loaded PS-containing liposomes into PEMs fabricated from synthetic polymers and their delivery into cells [34]. Demuth et al. described an PEM based systems with embedded liposomes to deliver antigens into the skin via deposition on microneedles [35]. Further approaches created backpacks for cells loaded with echogenic liposomes which encapsulate doxorubicin as potential cancer therapy [36]. A very recent work describes the embedding of liposomes in multilayers as model for exosomes by LbL but used a dye for the evidence of transfer into cells [37]. However so far, no studies reported about the combination of liposomes with LbL for controlled release to engineer connective tissue have been reported.

In tissue engineering, mesenchymal stem cells (MSC) have been used for several years due to their potential to differentiate into various tissues such as muscle, fat, bone, and cartilage and others [38]. C3H10T1/2 is a mesenchymal stem cell line that was obtained from a mouse embryo and can differentiate into various phenotypic lineages such as adipocytes, chondrocytes and osteoblasts by different inductive mediators [39,40]. The phenotypic features and differentiation of MSC to bone and cartilage cells include markers, such as alkaline phosphatase, deposition of calcium phosphate, and the expression of various ECM proteins such as collagen type I (Col) and II, osteocalcin (OCN), proteoglycans like aggrecan (ACAN), and glycosaminoglycans (GAG), etc. [41]. Moreover, it involves the detection of specific transcription factors, which are known to control mesenchymal cell differentiation towards chondrogenic or osteogenic lineages [41]. The transcription factors, Runx2, Osterix, and  $\beta$ -catenin, regulate osteoblast differentiation. Sox family transcription factors like Sox9 regulate chondrocyte differentiation [42]. Further, mesenchymal progenitors are initially marked by expression of Sox9, followed by Runx2 leading to the development of osteoblast [36]. However, cells with Sox9 expression are bipotential and can also differentiate into chondrocytes [42]. The addition of an inductive mediator like Dex can influence both osteogenic and chondrogenic differentiation. [19,38]. Dex can activate  $\beta$ -catenin mediated transcription and this activation induces Runx2 expression and upregulates TAZ and MKP1 that also promote Runx2 activity [43,44]. For chondrogenesis, Dex enhance the expression of Sox9 and activates the gene expression of type II procollagen (Col2a1) and ACAN [45].

OC defects require repair of bone and cartilage together, which means that implant materials or scaffolds should induce osteogenesis in the bone and chondrogenesis in the cartilage part of the defect. Hence, we were interested in elucidating the potential of Dex-loaded cationic liposomes to induce both osteo- and chondrogenic differentiation in C3H10T1/2 cells. Two approaches were combined to develop a functionalized surface coating: (i) an LbL surface coating that mimics the natural ECM of connective tissue by combination of Col and HA in PEM system and (ii) the immobilization of Dex-loaded liposomes for potential local delivery at the defect site. This research presents the physicochemical characteristics of the multilayer films, such as surface zeta potential, thickness, layer growth, and wettability. Cell studies with

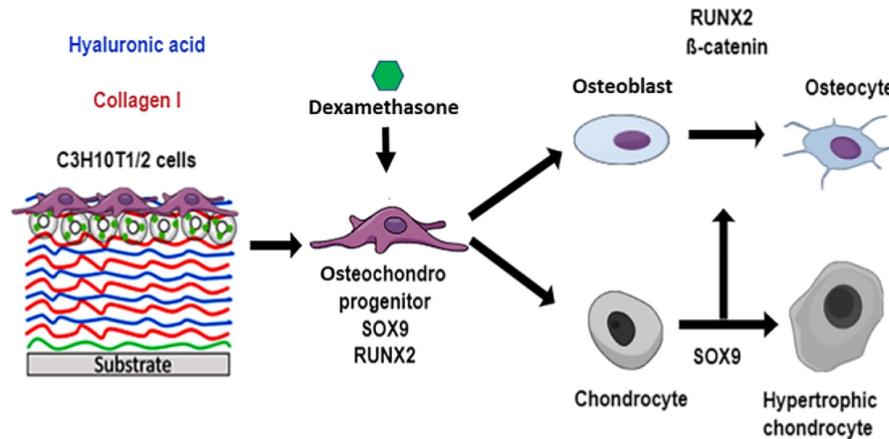


Fig. 1. Schematic illustration of the influence of the Dex in combination with polyelectrolyte multilayer in the regulation of osteoblast and chondrocyte differentiation by Sox9 and Runx2. During the process of osteoblast differentiation, Dex is an important compound for induction of mesenchymal stem cells to osteoblast lineage and clearly influences early stages of osteoblast differentiation as well as for chondrogenesis. Dex begins to play a key role in osteoblast differentiation by activating the Runx2-mediated and  $\beta$ -catenin pathways. For the period of chondrocyte differentiation initiated by Sox9-mediated mesenchymal condensation.

multipotent murine C3H10T1/2 cells evaluated the advantage of using liposomes loaded with Dex immobilized in PEMs to induce both osteogenic and chondrogenic differentiation (Fig. 1).

## 2. Materials and methods

### 2.1. Preparation of cationic liposomes

The lipid film hydration procedure was applied for the preparation of liposomes. Briefly, OO4 and DOPE lipids were separately dissolved in chloroform/methanol (8:2, v/v) to get stock solutions of  $2 \text{ mg mL}^{-1}$ . The stocks were mixed in the molar ratio 1:3 OO4/DOPE ( $M_{OO4} = 860.39 \text{ g mol}^{-1}$ ,  $M_{DOPE} = 744.03 \text{ g mol}^{-1}$ ). The solvent was evaporated, and the obtained thin lipid film was dissolved in water containing 0.15 M of sodium chloride (Carl Roth GmbH, Karlsruhe, Germany) and (0.1 M, final pH 4) acetic acid (Carl Roth GmbH, Karlsruhe, Germany) to obtain a lipid concentration of  $1 \text{ mg mL}^{-1}$ . For the film hydration at  $50^\circ \text{C}$  at 1400 rpm, an Eppendorf Thermomixer 5436 was used for 30 min followed by sonication using a bath sonicator at 37 kHz, 6 cycles for 3 min, while the last cycle was at  $70^\circ \text{C}$  for 4 min. The liposomes were prepared in batch sizes of 1 to 10 mL.

#### 2.1.1. Loading of cationic liposomes with dexamethasone

The liposomes were prepared with a concentration of  $1 \text{ mg mL}^{-1}$  total lipid ( $50 \mu\text{g mL}^{-1}$  Dex) following the liposome preparation protocol explained in previous studies [46] using chloroform/methanol (8:2, v/v) stock solutions of OO4, DOPE and Dex combined to a molar ratio of 1:3:0.2 ( $n_{OO4}:n_{DOPE}:n_{Dex}$ ).

#### 2.1.2. Characterization of liposomes

The size of liposomes was determined by dynamic light scattering (DLS) and zeta potential by laser Doppler velocimetry (LDV) using a Zetasizer Nano ZS ZEN3600 (Malvern Panalytical). DLS measurements were performed in half-volume cuvettes in three independent measurements consisting of 15 runs with a duration time of 20 s for each run at  $25^\circ \text{C}$ . The scattering angle was  $173^\circ$ . For the calculations, a viscosity  $\eta = 0.8872 \text{ mPa s}$  and a refractive index of 1.33 were assumed and the autocorrelation function was evaluated by Zetasizer Software 7.13 (Malvern Panalytical). LDV was performed in a clear disposable folded capillary cell (DTS1060, Malvern Panalytical). Three independent measurements involving 30 runs with a voltage of 60 V were performed

at  $25^\circ \text{C}$ . For the calculations, the viscosity ( $\eta = 0.8872 \text{ mPa s}$ ), dielectric constant ( $\epsilon = 78.5 \text{ F m}^{-1}$ ) and refractive index ( $n = 1.33$ ) of water were assumed. The mobility  $\mu$  of the diffusing aggregates was converted into the  $\zeta$  potential using the Smoluchowski relationship  $\zeta = \mu \eta / \epsilon$  (Zetasizer Software 7.13).

### 2.2. Preparation of substrata

Before the deposition of polyelectrolyte multilayers on glass coverslips ( $\varnothing 12 \text{ mm}$ , VWR, Germany) and silicon wafers (Silicon materials, Kaufering, Germany), organic residues were eliminated after the RCA-1 method. This method suggests mixing the following solutions: ultra-pure water, ammonium hydroxide (Carl Roth GmbH, Karlsruhe, Germany), and hydrogen peroxide (Carl Roth GmbH, Karlsruhe, Germany) in the ratio of 5:1:1, respectively. The gold-coated glass sensor for surface plasmon resonance (SPR, IBIS Technologies BV, Enschede, Netherlands,  $10 \times 10 \text{ mm}^2$ ) were treated by dipping into 0.5 M NaOH in 96% ethanol and followed by rinsing with ethanol (99%) and one last rinsing step with micro pure water followed by drying with nitrogen.

### 2.3. Glycosaminoglycan and collagen I solution preparation

The first solution required in the polyelectrolyte multilayer system was polyethylenimine (PEI). PEI ( $M_w \sim 750 \text{ kDa}$ ) provided from Sigma-Aldrich (Steinheim, Germany) was dissolved in 0.15 M sodium chloride (Carl Roth GmbH, Karlsruhe, Germany) solution at a concentration of  $2 \text{ mg mL}^{-1}$ . A solution of sodium hyaluronate (HA) was used as a negatively charged polyelectrolyte for the multilayer assembly. Therefore, hyaluronic acid sodium salt ( $M_w \sim 1.2 \text{ MDa}$ ) Kraeber & Co GmbH (Ellerbeck, Germany) was dissolved in 0.15 M sodium chloride solution at a concentration of  $0.5 \text{ mg mL}^{-1}$ . The positively charged Col was used as third solution. Col from porcine skin ( $M_w \sim 100 \text{ kDa}$ ) was provided by Sichuan Mingrang Bio-Tech (Sichuan, China) and was dissolved in 0.2 M acetic acid (Carl Roth GmbH, Karlsruhe, Germany) in a concentration of  $2 \text{ mg mL}^{-1}$  as a stock solution and stored in a temperature of  $4^\circ \text{C}$ . Then, it was diluted with sodium chloride solution (0.15 M) to obtain a final concentration of  $0.5 \text{ mg mL}^{-1}$ . The pH value of all solutions was adjusted to pH 4.

#### 2.4. Preparation of polyelectrolyte multilayers

PEM were fabricated on cleaned glass coverslips, gold sensor, and silicon substrates, respectively, depending on the method used afterwards. PEM were fabricated in 24 well plates with 500  $\mu\text{L}$  volume of each solution. PEI was applied as the initial layer by incubation of 15 min to get a positively charged surface. The first layer was formed by the application of polyanion solution (HA solution) for 15 min. The second layer was the polycation solution (Col solution) incubated for 20 min. Each deposition step was followed by washing with 0.15 M sodium chloride for five minutes, *trice*. The application of HA and Col solutions alternated until the ninth layer for liposomes was added. Twelve layers were used for unloaded PEM system [HA/Col]<sub>6</sub> in experiments with liposome-free PEMs. For LbL coatings with embedded liposomes, PEMs with the sequence [HA/Col]<sub>4</sub> were built like described above, followed by a HA layer to get the negative surface for adsorption of the positively charged Dex-loaded liposomes. For liposome deposition, the incubation time was 150 min. This layer was followed by deposition of an additional HA and Col layer to reach the final sequence [HA/Col]<sub>4</sub>HA/Lip [HA/Col].

#### 2.5. Characterization of polyelectrolyte multilayers and surface properties

##### 2.5.1. Ellipsometry

The PEM systems were prepared on silicon wafers. The thickness of PEMs was estimated by the use of ellipsometry (M-2000 V scanning ellipsometer, J.A. Woollam Co. Inc., Lincoln, NE, USA) at room temperature. The measurements were taken at incident angles of 60, 65, 70, and 75 of linear polarized light to the normal surface. The data were analyzed using the software WVase32.

##### 2.5.2. Surface plasmon resonance

The measurements were conducted with an IBIS-iSPR device (IBIS Technologies BV, Enschede, Netherlands). The gold sensor was coated with 11-mercaptoundecanoic acid (MUDA) (Steinheim, Germany), mounted in a flow chamber, and equilibrated with sodium chloride to obtain a stable baseline. Then, the polyelectrolyte solution was injected at a flow rate of 3  $\mu\text{L s}^{-1}$  followed by rinsing with sodium chloride for 15 min. PEI was added for 15 min, HA for 15 min, Col for 20 min and liposomes solution for 150 min until 13 layers were formed. The average of the shift values ( $m^\circ$ ) of each rinsing step was used for plotting the graphs and removing any unbound molecules.

##### 2.5.3. $\zeta$ -Potential measurements

SurPASS electrokinetic (Anton Paar, Graz, Austria) was used to estimate the zeta-potential of PEM-coated glass substrates (10  $\times$  20 mm<sup>2</sup>). The samples were mounted on the gap cell with double-sided tape. The used model electrolyte was 1 mmol·L<sup>-1</sup> KCl in water (Carl Roth GmbH, Karlsruhe, Germany) solution. The pH titration solution from pH 3.0 to 10 (acid-based pH) was 0.1 mol·L<sup>-1</sup> sodium hydroxide (Carl Roth GmbH, Karlsruhe, Germany). The analyzer was adjusted during the measurement process to a flow rate of 100–150 mL·min<sup>-1</sup> at a maximum pressure of 300 mbar.

##### 2.5.4. Water contact angle measurements

The wettability of the PEM was measured by static WCA using an OCA15+ device from Dataphysics (Filderstadt, Germany). The PEMs were prepared using glass cover slips. The sessile drop method was applied using 1  $\mu\text{L}$  of water with the Ellipse-fitting method. The experiments were run in duplicates with five droplets per sample. Means and standard deviations were calculated.

##### 2.5.5. Fluorescence microscopy of PEMs

PEMs were prepared according to the description in Section 2.4 using FITC-labeled HA and Rhodamine-DOPE labeled OO4/DOPE liposomes. The FITC-labelling of HA was done according to protocol published

[47]. The micrographs were taken with confocal laser scanning microscopy (CLSM 701, Carl Zeiss Micro-Imaging GmbH, Jena, Germany) using a 63 $\times$  oil immersion objective. Images were processed with the ZEN2012 software (Carl Zeiss).

#### 2.6. Cell culture conditions

Cryopreserved C3H10T1/2 murine cell line (ATCC; LGC Promochem, Molsheim, France) were thawed and grown in DMEM low glucose medium supplemented with 10% heat-inactivated fetal calf serum and 1% antibiotic solution (penicillin/streptomycin) solution all provided by Biochrom AG (Berlin, Germany). Cultured cells were grown at 37 °C in a humidified 5% CO<sub>2</sub>/95% air atmosphere using a NUAIRE DH Autoflow incubator (NuAire Corp., Plymouth, Minnesota, USA). Cells of almost confluent cultures were washed once with sterile PBS, followed by treatment with 0.25% trypsin/0.02% EDTA (Biochrom) at 37 °C for 3 min. Trypsin was neutralized with DMEM with 10% FCS, and cells were re-suspended in DMEM after centrifugation at 250g for 5 min. Finally, the cells were seeded on PEM coated glass coverslips at different concentrations depending on the assay.

#### 2.7. Cell adhesion and growth

##### 2.7.1. Cell adhesion studies

C3H10T1/2 cells were seeded on glass coverslips coated with PEM that were placed into 24 well plates at a density of 20.000 cell·mL<sup>-1</sup> in DMEM supplemented with 10% FCS. After incubation at 37 °C for 4 h, cells attached to PEM were fixed with 4% paraformaldehyde solution (RotiHistofix, Carl Roth GmbH, Karlsruhe, Germany) for 10 min. After rinsing with PBS twice, the cells were permeabilized with 0.1% Triton X-100 in PBS (v/v) Sigma-Aldrich Chemie GmbH (Taufkirchen, Germany) for 10 min. After rinsing with PBS, nonspecific binding sites were blocked by incubation with 1% (w/v) bovine serum albumin (BSA, Merck, Darmstadt, Germany) in PBS at room temperature for 1 h. The vinculin was stained using primary mouse antibody (1:100, Sigma) and secondary Cy2- conjugated goat anti-mouse antibody (1:100, Dianova). Actin cytoskeleton was visualized by incubating the samples with Phalloidin CruzFluor 555 (1:1000, Santa Cruz Biotechnology, Heidelberg, Germany) at room temperature for 30 min. Cell nuclei were visualized by TO-PRO3 staining (1:500, Invitrogen, Darmstadt, Germany) incubating for 30 min. The samples were washed with PBS and mounted with Roti-Mount FluorCare (Carl Roth GmbH, Karlsruhe, Germany) and examined with confocal laser scanning microscopy (CLSM 701, Carl Zeiss Micro-Imaging GmbH, Jena, Germany) using 10 $\times$  objective for cell counting, 20 $\times$  objective for measurements of cell area and 63 $\times$  oil immersion objective for visualization of focal adhesions, actin and nuclei. Images were processed with the ZEN2012 software (Carl Zeiss). The image analysis, such as cell count and cell area was performed with Image J. The quantification of vinculin-positive focal adhesions was done according to a protocol published previously [48].

##### 2.7.2. Cell growth assay

Qblue assay was used as an indicator of cellular viability and cell growth. Cells were seeded at a density of 20.000 cell·mL<sup>-1</sup> in DMEM 10% FCS and incubated at 37°C/ 5% CO<sub>2</sub> for 24, 48, and 72 h for the first, second and third well-plate, respectively. QBlue reagent was mixed with colorless DMEM to produce a 10% (v/v) solution. The DMEM was removed from cells well-plate and the 10% solution of QBlue assay was added. The cells were incubated with 300  $\mu\text{L}$  of the solution at 37 °C/ 5% CO<sub>2</sub> for 3 h. After incubation, 100  $\mu\text{L}$  was collected from each sample and transferred to 96 well-plates *trice*. The samples were analyzed using the microplate reader (FLUOstar OPTIMA, BMG LabTech, Germany) which was adjusted to a wavelength of 544 nm for excitation and 590 nm for emission.

**Table 1**  
Primers of target and housekeeping genes.

Symbol	Name	Assay ID
<b>Osteoblast</b>		
ALP	Alkaline phosphatase	qMmuCEP0027961
RUNX2	Runt-related transcription factor-2	qMmuCEP0057696
NOG	Noggin	qMmuCEP0058332
SP7	Osterix	qMmuCED0039982
<b>Chondrocyte</b>		
SOX9	Transcription factor SOX-9	qMmuCEP0053111
ACAN	Aggrecan	qMmuCEP0055269
COL1A1	Collagen type 1 alpha 1	qMmuCEP0052648
COL2A1	Collagen type 2 alpha 1	qMmuCEP0055155
Housekeeping gene	60S acidic ribosomal protein P0	qMmuCEP0042968
RPLP0		

## 2.8. Differentiation studies: osteogenesis

### 2.8.1. Alizarin red-S staining

C3H10T1/2 cells were seeded on PEM modified glass coverslips in 24 well plates at a density of  $4 \times 10^4 \text{ mL}^{-1}$ . The cells were cultured on glass in presence of **osteogenic medium** as a positive control (DMEM 10% FCS, 100 nM Dex,  $50 \mu\text{g mL}^{-1}$  ascorbic acid, and 10 mM  $\beta$ -Glycerophosphate), while the **basal medium** was DMEM with 10% FCS (negative control). The medium for the sample group was osteogenic medium without Dex. The Alizarin red (Carl Roth GmbH, Karlsruhe, Germany) staining was performed after 21 days as reported previously [46].

## 2.9. Differentiation studies: chondrogenesis

### 2.9.1. Safranin O staining

C3H10T1/2 cells were seeded on the samples placed into 24 well plates at high density of  $1 \times 10^5 \text{ mL}^{-1}$ . Here, the chondrogenesis requires high density to induce cell-cell interactions similar to the precartilaginous condensation [49]. The cells were incubated in presence of a **chondrogenic medium** as a positive control (DMEM 10% FCS, 100 nM Dex,  $5 \mu\text{g mL}^{-1}$  ascorbic acid) while **basal medium** was DMEM with 10% FCS (negative control). The medium for the samples group was chondrogenic medium in the absence of Dex.

The cells were prepared and fixed as described in Section 2.8. After

removing paraformaldehyde, samples were washed twice with distilled water and incubated in 1% acetic acid for 15 s. Subsequently, the samples were incubated for 15 min with 0.1% safranin O solution (Sigma-Aldrich, Steinheim, Germany). After the incubation time, the samples were washed with PBS and studied with a microscope equipped with a camera (Axiovert 100, Carl Zeiss, Oberkochen, Germany).

## 2.10. RNA extraction and quantitative real-time PCR

C3H10T1/2 cells were seeded on glass coverslips coated with PEM coatings as in the previous section. The re-suspend cells were seeded on the samples in DMEM supplemented with 10% FCS at a density of  $5 \times 10^5 \text{ mL}^{-1}$  for osteogenic and  $1 \times 10^6 \text{ mL}^{-1}$  for chondrogenic differentiation. The composition of media was the same as described above. To evaluate the osteogenic and chondrogenic differentiation, the cells were incubated for 14 days.

The RNA was extracted from samples using TRIzol method (Invitrogen, Darmstadt, Germany) according to the manufacturer's recommended procedure. First, cDNA was synthesized using an iScript Advanced cDNA Synthesis Kit for RT-qPCR (Biorad, Hercules, CA, USA) in 20  $\mu\text{L}$  reactions, according to the manufacturer's instructions.

qRT-PCR was performed under standard enzyme and cycling conditions on a CFX Connect real-time PCR Detection System (Biorad, Hercules, CA, USA). Primer sets were pre-validated by PrimePCR Probe Assays from Biorad (Hercules, CA, USA) for osteogenic genes (ALP, RUNX2, Noggin, and Osterix) and chondrogenic genes (SOX-9, ACAN, collagen alpha 1, and collagen type 2 alpha 1). The housekeeping gene RPLP0 was also used in this study (Table 1). Data analysis was performed using the BioRad CFX Manager Software 3.0 (Hercules, CA, USA). The conditions of qRT-PCR were as follows: 95 °C for 30 s followed by 39 cycles at 95 °C for 15 s and 60 °C for 30 s. The relative expression levels for each gene were calculated and normalized to the housekeeping gene RPLP0 by the DDCT method ( $2^{-\Delta\Delta C_t}$ ) [50].

## 2.11. Immunohistochemical staining

C3H10T1/2 cells were seeded on glass coverslips coated with PEM coatings as described in the previous section of differentiation studies. To study the osteogenic and chondrogenic differentiation, the cells were incubated for 21 days. After the incubation time, cells were fixed using 4% paraformaldehyde (Sigma-Aldrich) solution at room temperature for

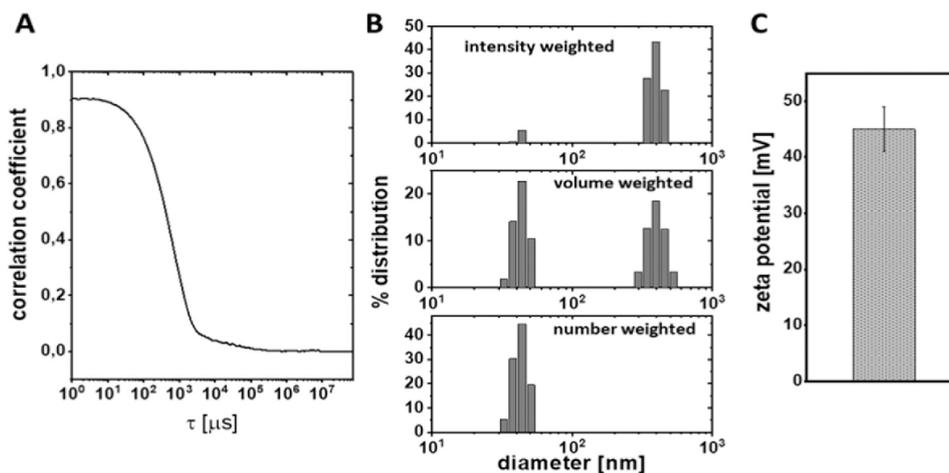


**Fig. 2.** Characterization of cationic liposomes loaded with Dex in acetate buffer pH 4 (10 mM, 0.15 M NaCl). (A) the correlation coefficient, (B) intensity, volume, and number weighted size distribution, (C) zeta potential (mean and standard deviation of three independent liposome preparations) measured by DLS and IdV.

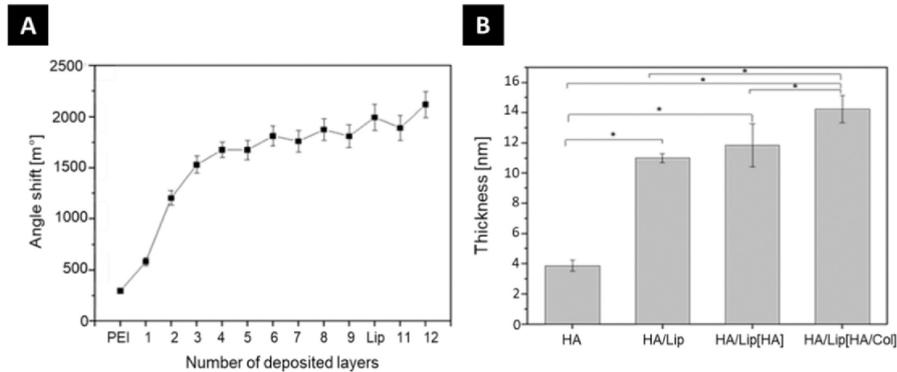


**Fig. 3.** (A) Layer growth of PEM systems of  $[HA/Col]_4$  HA/Lip  $[HA/Col]$  by SPR numbered as 1 to 12 (1st layer to 12th layer). Odd layer numbers correspond to HA coating and even layer numbers correspond to Col coating except the 10th layer, which corresponds to liposomes loaded with Dex (Lip);  $n = 20$ , mean  $\pm$  SD. (B) Progression of the layer thickness of PEM sequence  $[HA/Col]_4$  after adsorption of the additional layers of liposomes (Lip), hyaluronic acid (HA), and collagen I (Col) (see sequence details at the x-axis) determined by ellipsometry;  $n = 10$ , mean  $\pm$  SD, \* $p \leq 0.05$ .

15 min and washed three times with PBS. After permeabilization using 0.1% (v/v) Triton X-100 (Sigma-Aldrich) for 10 min, the non-specific binding sites were blocked with 1% bovine serum albumin solution (BSA, Carl Roth GmbH, Karlsruhe, Germany) in PBS at room temperature for 1 h. For visualization of chondrogenic markers, the cells were incubated with primary monoclonal antibodies raised against collagen type II (rabbit, Santa Cruz Biotechnology, Heidelberg, Germany) and a secondary antibody CY3 (anti-rabbit, Dianova, Hamburg, Germany) and ACAN (mouse, Santa Cruz Biotechnology, Heidelberg, Germany) and conjugated secondary CY2 (anti-mouse, Dianova, Hamburg, Germany). For detection of osteogenic markers, the cells were incubated with primary monoclonal antibodies raised against Col (mouse, Santa Cruz Biotechnology, Heidelberg, Germany) with secondary antibody anti-mouse (CY2) and (mouse, Santa Cruz Biotechnology, Heidelberg, Germany) with conjugated secondary anti-rabbit (CY3). The images were visualized using confocal laser scanning microscopy (CLSM 701, Carl Zeiss Micro-Imaging GmbH, Jena, Germany) using 20 $\times$  and 63 $\times$  oil immersion objectives. Images were processed with the ZEN 2008 software (Carl Zeiss).

### 2.12. Statistical analysis

All statistical analysis was performed with Origin 8G software. Mean, standard deviation, and analysis of significance were performed by one-way ANOVA (indicated as \*). A value of  $p < 0.05$  was considered as significantly different. Further, box-whisker diagrams are shown where appropriate. The box indicates the 25th and 75th percentiles, the median (dash), and the mean value (black square), respectively.

## 3. Results and discussion

### 3.1. Characterization of liposomes

The peptide-mimicking lipid OO4 bears ionizable amino functions and has an apparent pKa value of 6. The liposomes prepared solely from this lipid have a positive zeta potential over a wide pH range [51,52]. A positive charge of liposomes is needed for efficient embedding in LbL-based PEM formation. Here, the utilized liposomes are composed of a binary mixture of OO4/DOPE 1/3 (n/n). DLS and zeta potential measurements were performed to characterize the size and charge of the liposomes under conditions used for LbL. The results are presented in Fig. 2.

The autocorrelation function (Fig. 2A) demonstrates the high quality of DLS data with an intercept at 0.9, a sigmoidal decay of the signal, and

the absence of a noisy baseline which would indicate aggregation. The fitting of the autocorrelation function results in a bimodal size distribution curve (intensity weighted curve in Fig. 2B). The first size population is at diameter ( $d$ )  $\approx$  40–50 nm and a second one at  $d \approx$  300–500 nm. The size differences between both populations make it difficult to get quantitative information because the scattering intensity is approximately proportional to  $d^6$ . As such, the intensity distribution can be somewhat misleading, in that a small number of larger particles can dominate the distribution. Therefore, volume and number weighted size distribution curves were calculated, demonstrating that the 40–50 nm population is in a much higher quantity than expected from the intensity weighted curve [53]. In addition, zeta potential measurements show that the liposomes possess a positive surface charge required for immobilization on the PEM (Fig. 2C). DOPE is used as zwitterionic copolymer in the mixture to decrease the charge density of the liposomes. This becomes obvious comparing the high zeta potential of OO4 liposomes ( $\zeta > 40$  mV) with the liposomes OO4/DOPE ( $\zeta = 30$  mV) [24,51]. Furthermore, DOPE increases the fusogenic character of liposomes in acidic milieu and therewith triggers endosomal escape of payload after endocytosis, a phenomenon often discussed for lipid-mediated nucleic acid transfer [54].

### 3.2. Physical characterization of multilayers

SPR was used to investigate the layer deposition of PEM in situ. Fig. 3 (A) shows a linear growth behavior of PEM system until the third layer. During the further deposition steps, the layer growth was reduced pronouncedly. Every deposition step changes the angle shift, which corresponds to the absorbed mass of each layer [13,55]. However, after the 4th layer the mass adsorption reached an equilibrium which was well in line with previous studies [56]. Furthermore, the addition of liposomes as the 10th layer (PEM sequence  $[HA/Col]_4HA/Lip$ ) resulted in an additional mass deposition (angle shift increased from  $\sim$ 1700 to 2000 m<sup>2</sup>). The deposition of a further bilayer of HA/Col causes a further small increase of angle shift, which indicates the deposition of both polyelectrolytes.

To obtain more information about liposome deposition, the PEM layer thickness was measured by ellipsometry. This measurement was conducted with duplicates of dry films on a silicon substrate at 5 different spots per film ( $n = 10$ ). Fig. 3 shows an increasing thickness of PEM from  $4.1 \pm 0.2$  nm for the sequence  $[HA/Col]_4HA$  up to  $14.2 \pm 0.1$  nm for the sequence  $[HA/Col]_4HA/Lip[HA/Col]$  which is related to the increase of the number of layers of PEM. It is visible that the adsorption of liposomes makes the main contribution to the observed increase of

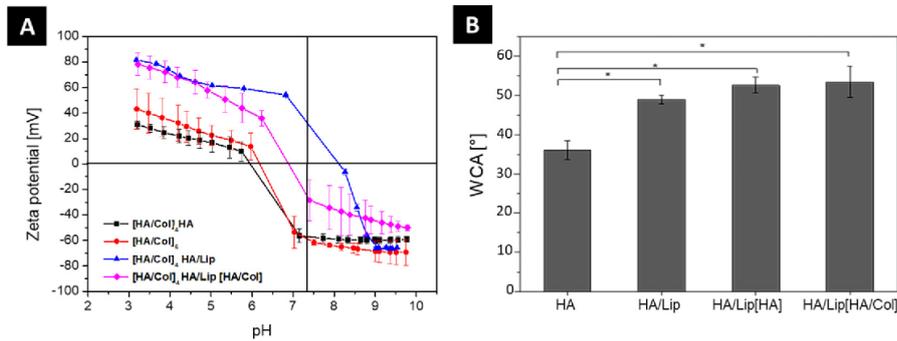


Fig. 4. A) Zeta potential measurements of the three different multilayers. Results represent means  $\pm$  SD of two independent experiments. B) Static water contact angle (WCA) measurement during multilayer formation. The x-axis demonstrates the film composition deposited on the basal part  $[\text{HA/Col}]_4$ . Results represent means  $\pm$  SD, \* $p \leq 0.05$  of three independent experiments.

PEM thickness. However, the relatively low thickness after adsorption of liposomes compared to their size obtained in DLS is a consequence of the drying procedure which results in the shrinking by the loss of the encapsulated aqueous core of liposomes [57]. Hence, it can be assumed that the thickness of hydrated multilayers is considerably larger compared to the thickness of dry layers because also HA tends to absorb water leading to swelling of PEM [58]. The ellipsometry results confirm the increase in mass deposition observed with SPR, particularly after liposomes were added.

Moreover, the surface topography was evaluated by atomic force microscopy (AFM). In previous studies, Zhao et al. showed the topography of HA/Col PEM which displayed a smooth surface with a small number of short collagen fibrils [13]. The AFM studies shown in Fig. S1 confirm the previous data showing a smooth surface with a roughness average (Ra) of  $1.731 \pm 0.721$  nm and root mean square roughness (Rq)  $2.914 \pm 1.698$  nm (see Table S1). After the deposition of the liposomes  $[\text{HA/Col}]_4\text{HA/Lip}$  an increment of the roughness to Ra  $17.96 \pm 6.219$  nm and Rq  $23.55 \pm 7.66$  nm can be seen in Table S1. Also, the images in Fig. S1 provide evidence that the liposomes are immobilized on the surface visible by the presence of round structures covering the whole surface area. The roughness value for the sequence  $[\text{HA/Col}]_4\text{HA/Lip}$   $[\text{HA/Col}]_4\text{HA/Lip}$  are Ra  $11.64 \pm 2.647$  nm and Rq  $15.23 \pm 3.389$  nm. The values indicate the presence of the liposomes after deposition of an additional bilayer where the liposomes changed their morphology and elongate diameter showing a rather flat structure on the surface due to the flexibility of liposomes and the strong Coulomb attractive force to

the deposited polyanion HA [46,57]. The structures are also maintained after deposition of an additional bilayer of HA/Col.

The knowledge of surface charge after each deposition step represents an important characterization of the buildup process of PEM [59]. Surface charge density, which corresponds to zeta potential, has also a pronounced effect on cell adhesion and fate [60]. Previous research has shown that PEM zeta potentials, particularly those made of hydrophilic biopolymers, reflect not only the charge distribution of the last polyelectrolyte layer but also of preceding ones due to the existence of swollen, conductive surface layers [61]. Fig. 4A shows the zeta potential of the final PEM and intermediate PEM assemblies as a function of pH value adjusted during the titration process. The pKa value of Col is around 5.5 [55]. Hence, it can be assumed that the Col will decrease continuously with increasing the pH value. In contrast, HA carries a negative net charge due to the presence of carboxylic groups with a pKa of 2.9 [62], which will further decrease the zeta potential when the pH value is increased during titration. The zeta potential of  $[\text{HA/Col}]_6$  multilayers (curve with red points) shifts from positive values in the acidic to negative potentials in the basic pH region. This indicates the contribution of both charged species, such as Col at low pH and HA at high pH to the zeta potential, related to the fact that not only the outermost layer but also inner layers of PEM contribute to the zeta potential as detected by Zimmermann & Werner [61,63]. The addition of a further layer of HA to  $[\text{HA/Col}]_4$  (curve with black squares) decreases the zeta potentials slightly and indicates the contribution of the

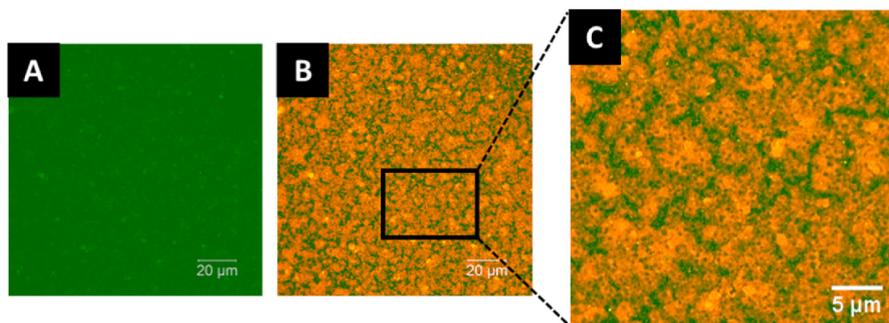
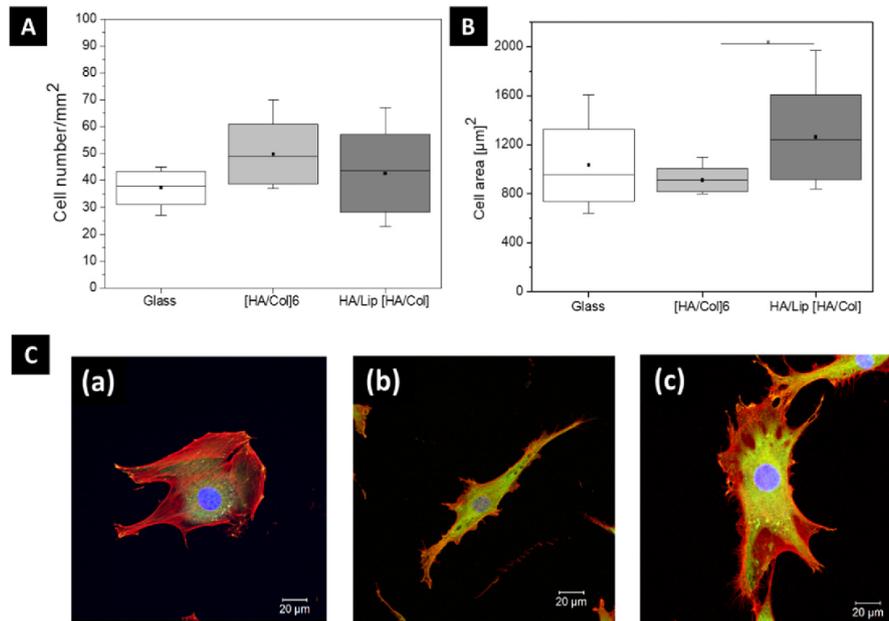


Fig. 5. CLSM images of PEM system after deposition of the liposomes:  $[\text{HA-FITC/Col}]_4\text{HA/Lip}[\text{HA-FITC/Col}]_4$  HA was labeled using FITC (green), liposomes with Rhodamine-DOPE conjugated (red) on PEM. A) FITC fluorescence distribution, B) merged image of FITC fluorescence and Rhodamine-DOPE fluorescence C) detail (black square in B) merged image of HA and liposomes distribution of the area in the black square [scale 20  $\mu\text{m}$  and 5  $\mu\text{m}$ ]. (For interpretation of the references to colour in this figure legend, the reader is referred to the web version of this article.)



**Fig. 6.** A) Quantification of cell count per square millimeter B) Cell spreading area ( $\mu\text{m}^2$ ) on each of the multilayers after 4 h; samples: Glass,  $[\text{HA}/\text{Col}]_6$ ,  $[\text{HA}/\text{Col}]_4^*$  HA/Lip  $[\text{HA}/\text{Col}]$  (Box plots with whiskers, representing first and third quartiles, medians and means). (\*) statistically significant with a  $p$ -value  $\leq 0.05$ . C) Merged CLSM image of adherent C3H10T1/2 cultured on the different PEM after 4 h of incubation in serum and serum-free medium. (a) Glass, (b)  $[\text{HA}/\text{Col}]_6$ , (c)  $[\text{HA}/\text{Col}]_4$  HA/Lip $[\text{HA}/\text{Col}]$ . The cells are stained for filamentous actin (red), vinculin-positive focal adhesions (green), and nucleus (blue). [Scale 20  $\mu\text{m}$ ]. (For interpretation of the references to colour in this figure legend, the reader is referred to the web version of this article.)

polyanion HA to the potential. The adsorption of liposomes  $[\text{HA}/\text{Col}]_4$ HA/Lip (blue triangles) leads to a dramatic increase of zeta potentials with a huge shift of point of zero charge (PZC) from pH 6 to pH 8.5 which represents the positive charge of the cationic liposomes. The coverage of the liposome layer with an additional bilayer of HA/Col decreases the zeta potential again, but it remains still higher than that of the  $[\text{HA}/\text{Col}]_4$  HA, which indicates that the liposomes underneath make still a contribution to the zeta potential of the system. The PZC of this system is 6.8, which means that both anionic and cationic species contribute to the potential. The zeta potential measurements show clearly that liposomes adsorb on the  $[\text{HA}/\text{Col}]_4$ HA multilayers and they remain also when an additional bilayer of HA/Col is immobilized on top of them.

On the other hand, surface wettability is another important factor that can affect the biological response to an implant because it affects protein adsorption and cell adhesion [64]. Fig. 4 (B) shows that  $[\text{HA}/\text{Col}]_4$ HA is hydrophilic with a WCA of  $\sim 35^\circ$ , which is related to the fact that HA is a hydrophilic polysaccharide [13]. After the adsorption of liposomes on PEM  $[\text{HA}/\text{Col}]_4$ HA/Lip, the WCA increased to a value of  $50^\circ$ , which corresponds to a moderately wettable surface due to the presence of amino groups, which make WCA in this range [65]. The subsequent  $[\text{HA}/\text{Col}]_4$ HA/Lip/HA displays an angle of  $\sim 53^\circ$ , and the final PEM  $[\text{HA}/\text{Col}]_4$ HA/Lip $[\text{HA}/\text{Col}]$  was characterized by a WCA of  $\sim 55^\circ$ , demonstrating that the wetting properties of liposomes are also dominant after deposition the final bilayer, which indicates an intermingled structure of liposomes and polyelectrolytes in the outermost layer of the system [66].

Further evidence for the entrapment of liposomes in the PEM system is shown in Fig. 5 presenting micrographs made by CLSM. Fig. 5 A shows a uniform distribution of HA labeled with FITC in the PEM  $[\text{HA}/\text{FITC}/\text{Col}]_4$ HA/Lip $[\text{HA}/\text{FITC}/\text{Col}]$  (green colour). Fig. 5B) displays the distribution of Rhodamine-DOPE fluorescence across the PEM (orange

colour), with higher magnification in Fig. 5 C demonstrating the presence of labeled liposomes. The image depicts the distribution of liposomes over the entire area; however, the image indicates the presence of some liposomes aggregates and a partially homogeneous distribution, which could be due to interactions between the positive surface charge of the liposomes and the layer arrangement with carboxylic groups of HA and Col fibrils.

### 3.3. Adhesion and growth of C3H10T1/2 cells

C3H10T1/2 cells are a well-characterized model for in vitro differentiation of multipotent cells into osteoblasts, chondrocytes, and adipocytes [39,40]. The cell adhesion studies were carried out by the quantification of cell number and cell area including visualization of actin filaments (red staining), vinculin-positive focal adhesions (green staining), and nuclei (blue staining). These studies are important to understand how the PEM system properties influence cell adhesion, which may have also an effect on subsequent cell differentiation [67]. Fig. 6 A shows a higher number of cells on the PEM surfaces compared to the cells on glass used as a control after 4 h, which is due presence of cell receptors for HA and Col. Further, the cells seeded on PEM  $[\text{HA}/\text{Col}]_6$  and  $[\text{HA}/\text{Col}]_4$ HA/Lip $[\text{HA}/\text{Col}]$  show no significant difference probably due to similar composition of terminal layer (HA and Col). The quantification of the cell area (Fig. 6 B) demonstrated a significant higher spreading of cells on  $[\text{HA}/\text{Col}]_4$ HA/Lip $[\text{HA}/\text{Col}]$  related to its higher WCA and zeta potential in contrast to the control and the basal PEM  $[\text{HA}/\text{Col}]_6$ . Fig. 6 C demonstrates the organization of the actin filaments on the different substrates. The cells on glass were characterized by a small aspect ratio of an irregular form and the actin filaments were organized mostly circumferentially. The cells cultured on the basal system  $[\text{HA}/\text{Col}]_6$  had a longitudinal distribution of the actin filaments. However, the cells on  $[\text{HA}/\text{Col}]_4$ HA/Lip $[\text{HA}/\text{Col}]$  displayed an

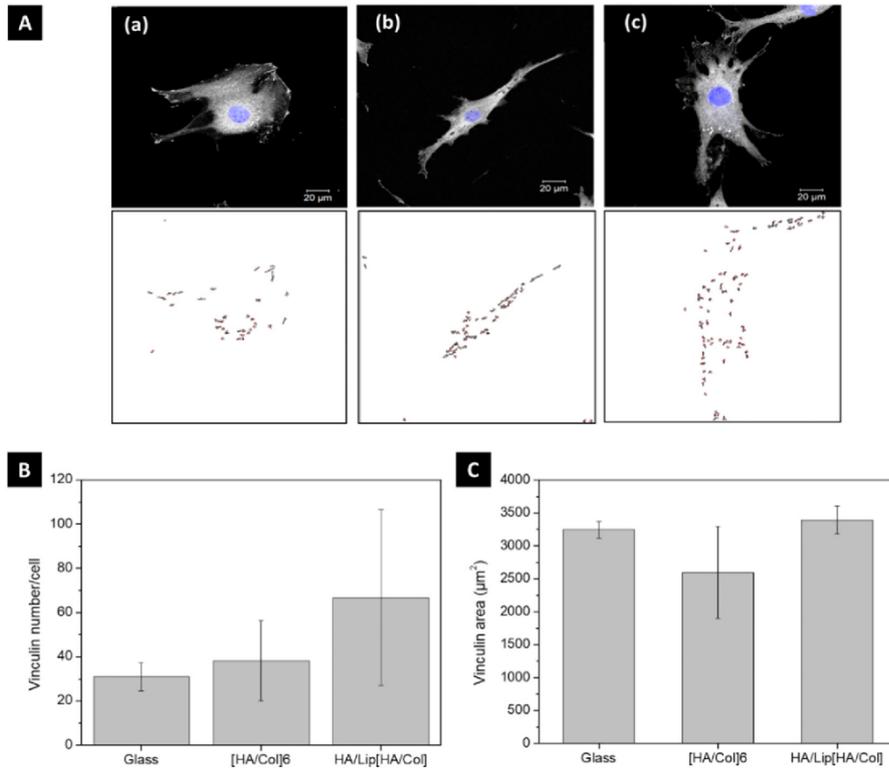


**Fig. 7.** A) Visualization of vinculin-positive focal adhesions in cells seeded on a) glass, b) [HA/Col]<sub>6</sub> and c) [HA/Col]<sub>4</sub>HA/Lip[HA/Col]. B, C) Quantification of vinculin-positive focal adhesions number per cell and vinculin per cell area  $\mu\text{m}^2$ . vinculin-positive focal adhesions was quantified by Image J. Results represent means  $\pm$  SD values,  $n = 5$ ,  $p \leq 0.05$ .

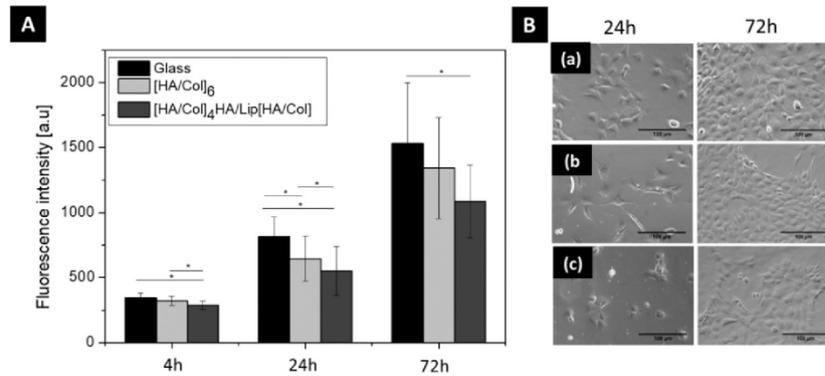


**Fig. 8.** A) Growth of C3H10T1/2 seed on glass and PEM system of [HA/Col]<sub>6</sub> and [HA/Col]<sub>4</sub>HA/Lip[HA/Col] measured by the QBlue assay after 4 h, 24 h, and 72 h. B) Phase-contrast images of cell seeding on glass and multilayers after 24 h and 72 h. (a) Glass, (b) [HA/Col]<sub>6</sub>, (c) [HA/Col]<sub>4</sub>HA/Lip[HA/Col]. Scale bar 100  $\mu\text{m}$ .

elongated and extended morphology which underlines that the embedded liposomes have a promoting effect on cell adhesion and spreading.

Fig. 7 displays the position of the vinculin-positive focal adhesions at the end of the actin filaments but also in central regions. Nevertheless, cell spreading was observed on both multilayers surfaces but the vinculin-positive focal adhesions amount was different. The PEM system

of [HA/Col]<sub>4</sub>HA/Lip [HA/Col] showed a higher number and larger length of vinculin positive staining compared to the basal PEM [HA/Col]<sub>6</sub>. Vinculin reinforces focal adhesion by crosslinking actin filaments to the structure molecules like talin [68]. This is an important step in cellular mechanics linking the cell to its substrate. Also, vinculin is recruited in integrin-mediated adhesions and the actin cytoskeletal network that is connected to the ECM. Therefore, the presence of

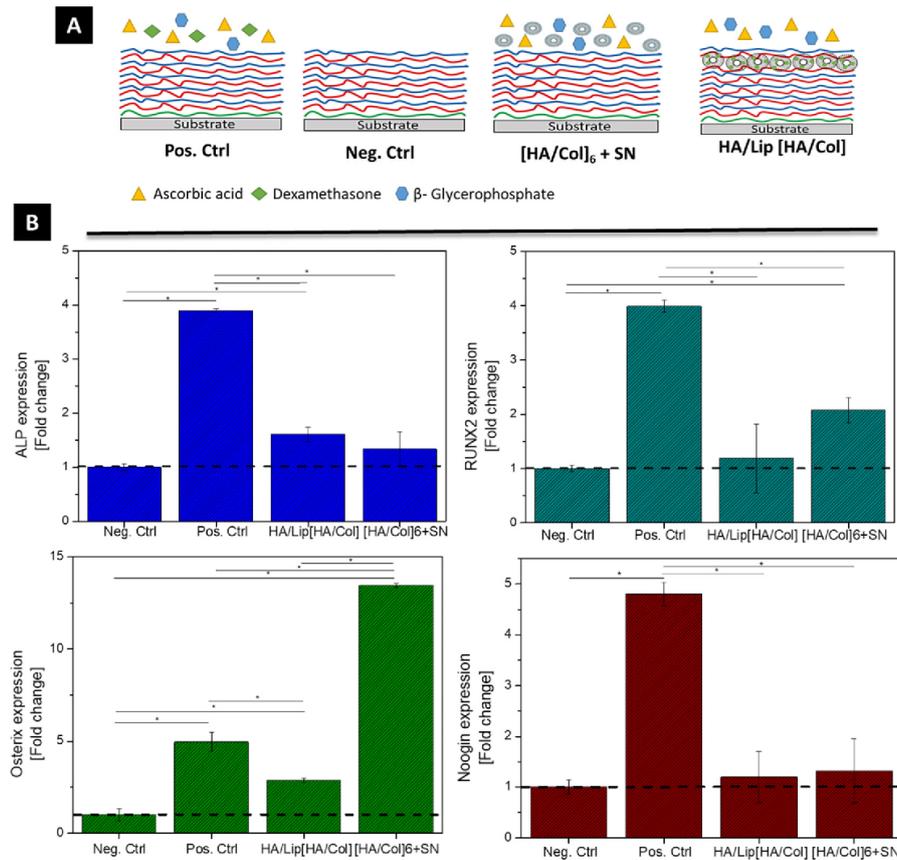


**Fig. 9.** A) Schematic illustration of the screened differentiation environments in the in vitro study. B) Relative expression of mRNA osteoblast markers (ALP, Runx2, Osterix, and Noggin) were determined after 14 days of incubation on PEM. qRT-PCR analyses were performed as described in the materials and methods. Data represent mean  $\pm$  SD values,  $n = 5$ ,  $p < 0.05$  and Scheffe-Post-Hoc test.

vinculin-positive focal adhesions in the samples gives an indication of integrin ligation and signal transduction processes [69].

Growth of C3H10T1/2 cells was studied by QBlue assay evaluating their metabolic activity to assure that cells can survive and multiply during longer culture for chondrogenic and osteogenic differentiation (Fig. 8). For this assay the samples were divided into three groups: the control group of C3H10T1/2 cells was seeded on glass slides and compared with cells growing on [HA/Col]<sub>6</sub> and on [HA/Col]<sub>4</sub>HA/Lip [HA/Col]. In Fig. 8A it is shown that cells seeded on glass and both PEM system with liposomes showed similar metabolic activity after 4 h of incubation, which corresponds roughly to the results of adhesion studies. A significant increase within each group was detected with increasing time of culture certifying that cell can also grow on PEM as prerequisite for the differentiation studies. The positive control after 48 h and 72 h showed a higher fluorescence intensity, compared to [HA/Col]<sub>6</sub> and [HA/Col]<sub>4</sub>HA/Lip [HA/Col]. As can be seen in the Fig. 8 B, cells were able to grow on all substrata over the time. However, the glass sample shows higher cell growth might due to the stronger substrate stiffness in comparison with the soft hydrated PEM systems where the HA has high water uptake capability and will decrease stiffness and roughness of the substratum [58,70]. It is well known that MSCs on soft substrates decrease the proliferative activity compared to cells grown on stiffer surfaces [71]. This consequence might not affect cell viability in vivo, but only their proliferative capacity [72].

Protein adsorption and cell adhesion are affected by the surface charge and wetting properties of the material [73,74]. For instance, negatively charged surfaces inhibit cell attachment, whereas positively charged surfaces stimulate [60]. The PEM system of [HA/Col]<sub>4</sub>HA/Lip [HA/Col] showed positive zeta potential after the adsorption of the liposomes, where it is possible to observe a high cell area and a larger number of vinculin-positive focal adhesions compared to the basal sample [HA/Col]<sub>6</sub>. In addition, the wettability of materials has been proven to have a considerable influence on cell growth and function [74]. The binding of liposomes and additional bilayer with Col a significantly increased WCA indicating a less hydrophilic surface. This reduction in the hydrophilicity decreases the hydration force of repulsion, promoting the cell adhesion process [50].

On the other hand, cell adhesion depends on the interactions of cells with their surrounding microenvironment, particularly ligands of different cell adhesion receptors [74]. HA and Col play important roles in the regulation of cell adhesion and spreading. For instance, HA can bind to a variety of cell surface receptors named hyaladherins, such as CD44 and RHAMM [75]. CD44 proteins are involved in a diversity of cellular functions, including growth and differentiation [75,76]. For Col, there are specific proteins that play a key role in this process, called integrins. The integrin family contains four collagen receptors such as  $\alpha 1\beta 1$ ,  $\alpha 2\beta 1$ ,  $\alpha 10\beta 1$   $\alpha 11\beta 1$ , whereas  $\alpha 2\beta 1$  integrin is the main receptor for Col [77]. Therefore, both samples of PEM systems present a higher

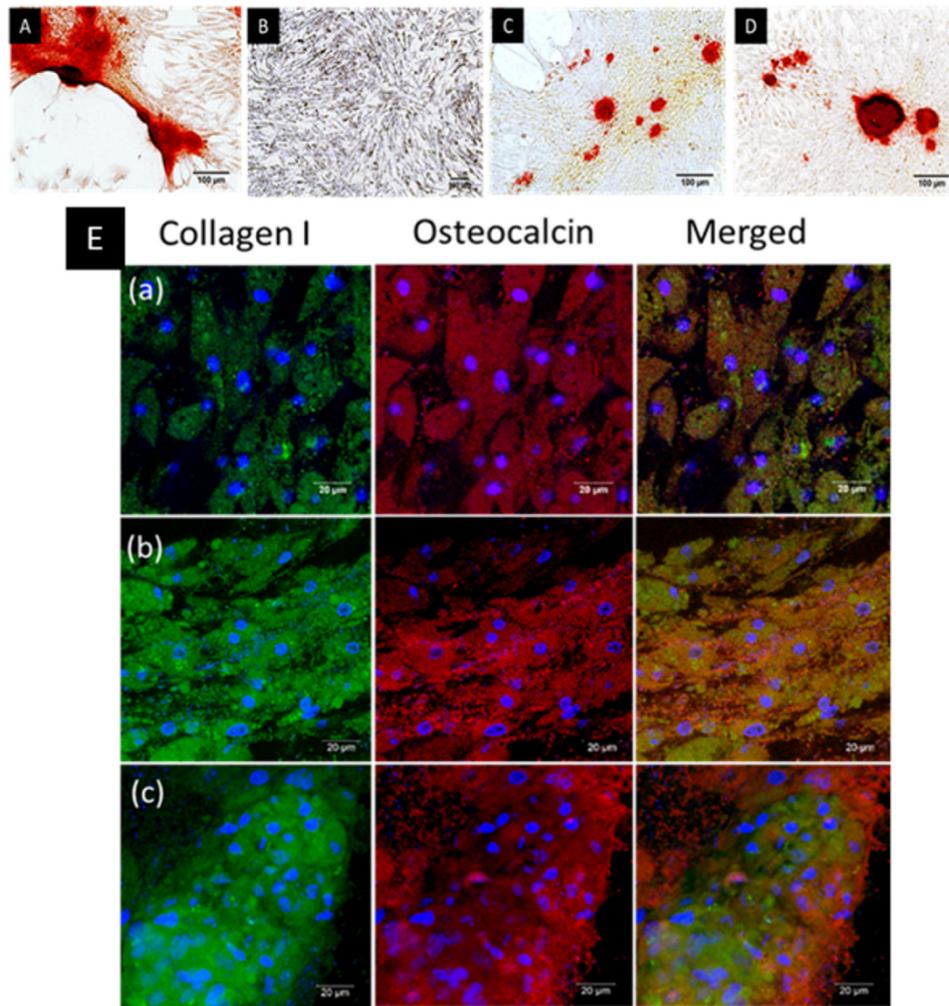


**Fig. 10.** Histochemical staining of C3H10T1/2 cells cultured on various test samples with basal medium and osteogenic medium. A) Positive control, [HA/Col]<sub>6</sub>, B) Negative control, [HA/Col]<sub>6</sub> basal medium, C) [HA/Col]<sub>6</sub> and liposomes in the supernatant, D) [HA/Col]<sub>6</sub>, HA/Lip[HA/Col]. Alizarin red staining was performed after 21 days. Calcium deposits were staining in red [scale 100 μm]. E) CLSM images of immunofluorescence staining of collagen I and osteocalcin of C3H10T1/2 cells cultured in osteogenic medium after 21 days. a) Positive control, [HA/Col]<sub>6</sub>, b) [HA/Col]<sub>6</sub> and liposomes in the supernatant, c) [HA/Col]<sub>6</sub>, HA/Lip [HA/Col]. Collagen I (green fluorescence), osteocalcin (red fluorescence), nuclei (blue fluorescence) Scale bar 20 μm. (For interpretation of the references to colour in this figure legend, the reader is referred to the web version of this article.)

number of vinculin-positive focal adhesions unlike the control (glass) due to the presence of fibrillary collagen as a terminal layer promoting the cell adhesion via integrin  $\alpha 2\beta 1$  receptor of Col [52]. The benefit of integrin-binding surfaces is an enhanced cell adhesion and expansion [78]. For instance, integrins are of focal adhesion complexes that contain linker proteins to the cytoskeleton like, talin, and  $\alpha$ -actinin and signaling transducers like vinculin and focal adhesion kinase [79]. These focal adhesions are involved in the adhesion process, function as the structural link between the cytoskeleton and ECM and activate signaling pathways to regulate transcription factors, involved in cell growth and cell differentiation [79,80].

### 3.4. Osteogenic differentiation of C3H10T1/2 cells

Previous studies confirmed that the cationic OO4/DOPE liposomes

embedded in a PEM system can be used for controlled release or transfer of compounds into cells [46]. To induce cell differentiation, Dex was incorporated in the lipid bilayer of the liposomes as described in the Materials and methods section. Dex activates the expression of Runx2 which acts as an expression factor for procollagen [38]. Further, Dex in combination with ascorbic acid (ASC) and  $\beta$ -glycerophosphate ( $\beta$ -Gly) has shown to regulate the osteogenesis of mouse MSCs with mineralization in vitro [44]. To determine if there were levels of osteogenic markers due to Dex effects on cells, the relative quantification of mRNA was performed by qRT-PCR after 14 days in a growth medium with ASC and  $\beta$ -Gly. The different conditions are represented in Fig. 9A. The qRT-PCR results (Fig. 9 B) demonstrated that Dex in the medium (positive control) or encapsulated in liposomes resulted in an upregulation of the gene expression of osteogenic markers (ALP, Runx2, osterix, and noggin) compared to the negative control, which was not treated with

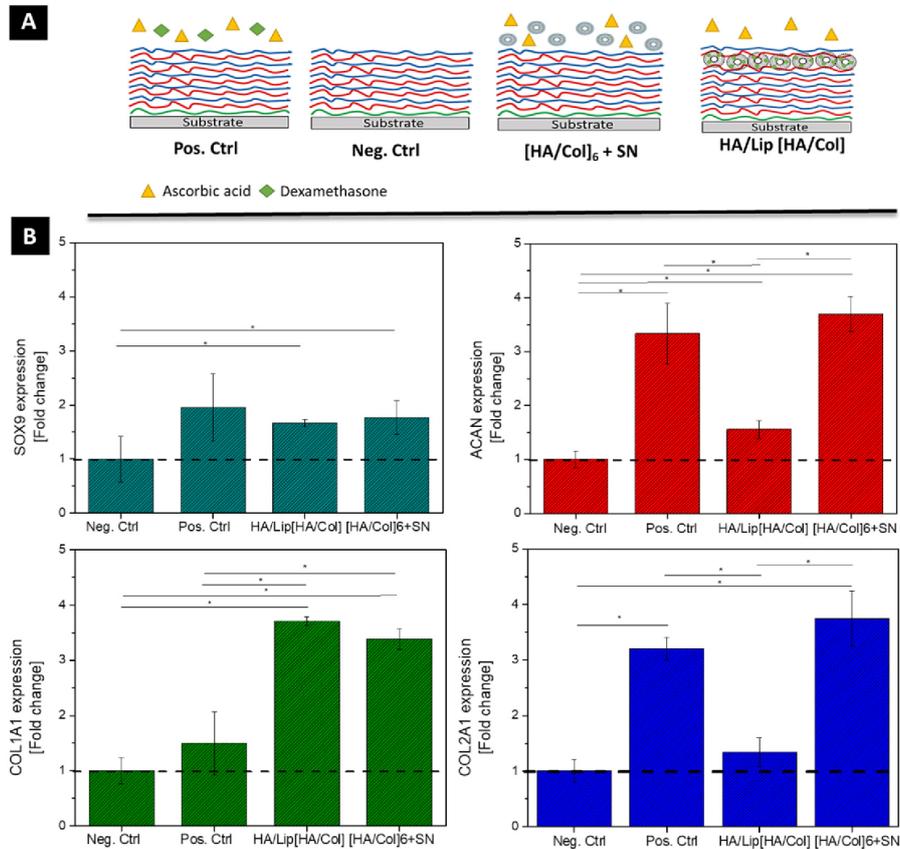


**Fig. 11.** A) Schematic illustration of the screened differentiation environments in the in vitro study. B) Relative expression of mRNA chondrogenic markers (Sox9, ACAN, Col1A1, and Col2A1) were determined after 14 days of incubation on PEM. qRT-PCR analyses were performed as described in the materials and methods. Data represent mean  $\pm$  SD values,  $n = 5$ ,  $p \leq 0.05$  and Scheffe-Post-Hoc test.

Dex. In addition, a higher level of ALP was found on the liposomes embedded into PEM. The high-level expression of ALP can be found because ALP is an early marker in osteogenesis and it promotes the formation of hydroxyapatite crystals in the bone matrix [81]. However, it is possible to observe an increase of other osteogenic markers like Runx2 and noggin (compared to negative control), but the expression of mRNA was lower compared to the positive control. Another important transcription factor is osterix. This transcription factor activates genes during the differentiation of pre-osteoblast to the final stage that is osteocytes [82]. In addition, Sox9, Runx2, and osterix play an important role in the decision by which the cells differentiate to osteoblast or chondrocytes [83]. The qRT-PCR shows increased expression levels in both systems with Dex-loaded liposomes. Further, the expression of the markers where the liposomes were added in the supernatant (SN) was high, which might be to the direct contact of the liposomes with the cell, compared to the liposomes embedded in the film. For that reason, to confirm the qRT-PCR results, the deposition of calcium phosphate at 21 days was studied by Alizarin red staining (Fig. 10 A).

This result is supported by the images obtained of C3H10T1/2 culture after histochemical staining by Alizarin Red S that interact with hydroxyapatite and results in red staining of mineralized nodules that corresponds to an ECM rich in calcium phosphates. These nodules were observed when cells were cultured in [HA/Col]<sub>4</sub>HA/Lip[HA/Col] and liposomes in the supernatant [HA/Col]<sub>6</sub> + SN in presence of the

osteogenic medium. These results confirm the previous data of qRT-PCR.

Another method to evaluate the osteogenic differentiation was through immunofluorescence staining of Col and OCN after 21 days of incubation (Fig. 10E). The positive staining confirmed the presence of Col and OCN, which are specific protein markers synthesized by osteoblast during maturation [84]. The presence of markers was found in both of PEM systems [HA/Col]<sub>4</sub>HA/Lip[HA/Col] and liposomes in the supernatant [HA/Col]<sub>6</sub> + SN. These results confirmed the protein production of osteogenic proteins at later stages but also supported that the liposomes with Dex can induce osteogenic differentiation.

On the other hand, connective tissues cells differ importantly in phenotype. The shape of MSC is involved in their specialized function, while at the same time drive to their multicellular organization [85]. For instance, cell spreading enables osteogenic matrix deposition during bone formation and these differences in cell morphology are due to the changes in the expression of the integrins, cadherins, and cytoskeletal proteins [67]. McBeath et al, demonstrated that cell spreading increased osteoblast differentiation in preosteoblastic progenitors [67]. Thus, previous results showed a high spreading presence in the PEM system [HA/Col]<sub>4</sub>HA/Lip[HA/Col] in which not only the Dex is involved in the differentiation, but also the spreading phenotypes of cells are related to osteogenic differentiation. In contrast, for chondrogenesis, the cells need to grow at high densities where the cell spreading on the surface decreases but cell-cell contact and paracrine signaling increase [67].

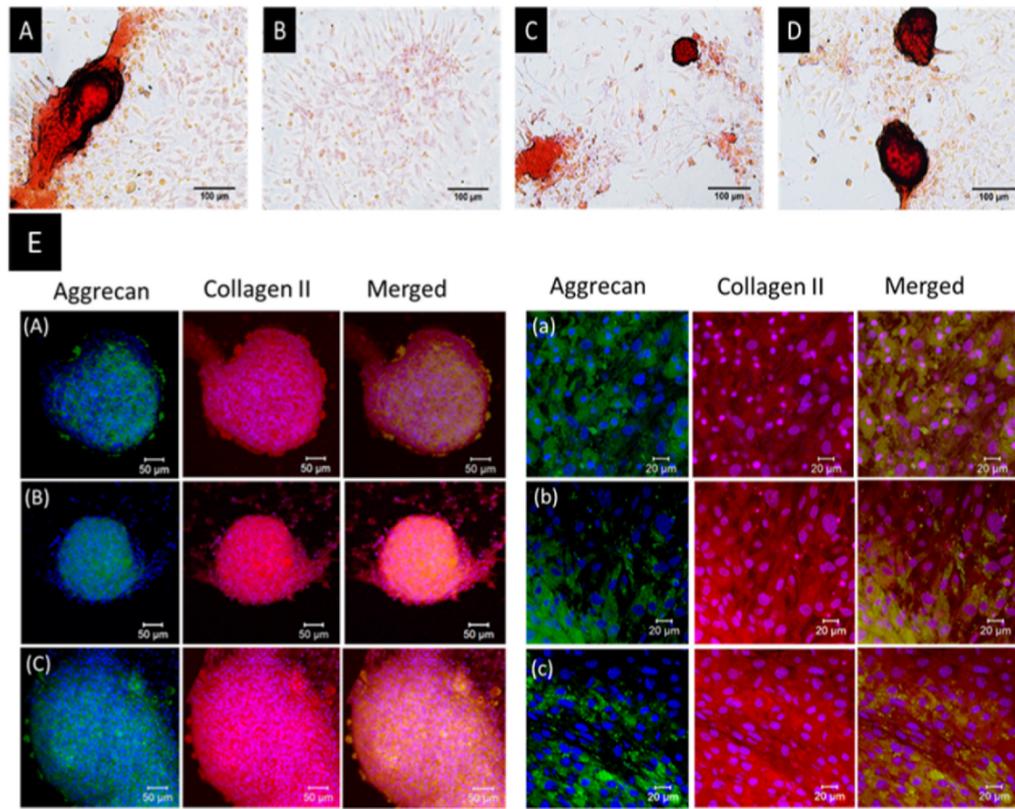


**Fig. 12.** Histochemical staining of C3H10T1/2 cells cultured on various test samples with basal medium and chondrogenic medium. A) Positive control, [HA/Col]<sub>6</sub>, B) Negative control, [HA/Col]<sub>6</sub> basal medium, C) [HA/Col]<sub>6</sub> and liposomes in the supernatant, D) [HA/Col]<sub>4</sub> HA/Lip [HA/Col]. Safranin O staining was performed after 21 days. Accumulation of glycosaminoglycans was staining in red [scale 100 µm]. E) CLSM images of immunofluorescence staining of aggrecan and collagen II of C3H10T1/2 cells cultured in the chondrogenic medium after 21 days. A, a) Positive control, [HA/Col I]<sub>6</sub>, B, b) [HA/Col]<sub>6</sub> and liposomes in the supernatant, C, c) [HA/Col]<sub>4</sub> HA/Lip [HA/Col]. Aggrecan (green fluorescence), collagen II (red fluorescence), nuclei (blue fluorescence). Left images: scale bar 50 µm. Right images: scale bar 20 µm. (For interpretation of the references to colour in this figure legend, the reader is referred to the web version of this article.)

### 3.5. Chondrogenic differentiation of C3H10T1/2 cells

Dex not only induces the Runx2 expression but can also be involved in the expression of Sox9 for chondrogenesis. The orientation of chondrogenic differentiation is connected to osteogenesis since both processes share the transcription factor of Sox9 [42]. Some authors refer that Dex increases Sox9 expression in primary chondrocyte cultures, in which Sox9 controls collagen II  $\alpha 1$  and ACAN gene expression [86]. However, the molecular mechanism by how Dex produces its effects is still unknown. The mesenchymal stem cells that go through chondrogenesis express proteins associated with hyaline cartilage such as ACAN and collagen type II [87,88]. For instance, hyaline cartilage is present on the articular surface of the bone with collagen type II as the main component of this cartilage, while fibro-cartilage is found on the meniscus containing fibers of Col [89]. The difference between these types of collagen is that Col forms heterotrimeric triple helices which are self-assembled and collagen type II forms homotrimeric molecules [90]. In addition, it is known that chondrogenic differentiation depends on cell density and the experimental system. Seeding the high density of cells can induce endochondral ossification due to the formation of dense cell-cell interaction regulated by N-cadherin's [49,91]. For that reason, chondrogenic markers such as Sox9, ACAN, Col, and collagen type II were measured by qRT-PCR after 14 days of incubation on the mRNA

level. Fig. 11 A shows the different conditions that were used to induce chondrogenic differentiation and the PEM systems. Fig. 11B shows the presence of these chondrogenesis markers Sox9, ACAN, Col, and collagen II in cells when they were exposed to Dex. Here, the Dex is immediately available for the positive control and the liposomes in the supernatant in comparison with the liposomes embedded into PEM. However, the PEM systems [HA/Col]<sub>4</sub>HA/Lip[HA/Col] shows similar Sox9 values as the positive control and the liposomes in the supernatant [HA/Col I]<sub>6</sub> + SN compared to the negative control. This result is an indicator that the cells were induced to undergo chondrogenesis. There were also increased mRNA values for ACAN and collagen type II for the PEM systems [HA/Col]<sub>4</sub>HA/Lip[HA/Col], but the values of the positive control and the PEM system [HA/Col]<sub>6</sub> + SN were not reached. Col shows a high expression in both PEM systems, with liposomes in the SN and embedded in the PEM.

It is known that chondrogenesis can be stimulated in the presence of Dex and increase GAGs expression [88]. Therefore, histochemical staining with safranin O that detects acidic GAGs (e.g. hyaluronan, chondroitin sulfate, etc.) was done after 21 days. Fig. 12A–D shows the staining of the accumulation of GAGs and clusters with condensation of cells, which was positive for the control (positive) and both PEM systems with liposomes embedded or in the SN.

The study of chondrogenic markers by immunostaining revealed that

ACAN was uniformly distributed through the cell cluster and at the periphery, and collagen type II was accumulated also within the cluster in all the samples (Fig. 12). Here, the detection of ACAN and collagen type II confirmed the chondrogenic differentiation. In addition, previous studies demonstrate that the presence of HA and Col induces chondrogenic differentiation because of the partially mimic of ECM of bone and cartilage [39]. The mesenchymal progenitor shares Sox9 and the addition of induction supplements such as Dex and induce the differentiation to chondrogenic or osteogenesis. Further, transcription factor Sox9 can control the chondrocyte proliferation and the progression to hypertrophic chondrocytes and go through osteogenic lineage [42,92].

In literature it was demonstrated that chondrogenesis is induced when cells are seeded in high density *in vitro* because this mimics the condensation during cartilage formation. Interestingly, the low cell density causes high cell spreading to induce osteogenic differentiation, however, for chondrogenic differentiation the high cell density decreases the cell spreading and increase the number of cadherins, and trigger chondrogenesis [93]. For that reason, the advantage of the [HA/Col]<sub>4</sub>/HA/Lip/[HA/Col] system is that the cells can differentiate into both osteogenic or chondrogenic pathways with minor changes in the conditions.

#### 4. Conclusion

The LbL technique can be used to create multifunctional surface coatings that can modify the composition and physicochemical properties of implants surfaces with liposomes adsorption to allow the delivery of compounds like Dex. This technique can develop ECM-inspired surface coatings for osteochondral implants to induce bone and cartilage differentiation. In previous studies [40], the PEM system and Dex-loaded liposomes demonstrated a uniform and stable adsorption with a successful transfer into cells to induce cell differentiation. The benefit of the immobilization of liposomes in PEM with a cover bilayer of HA/Col is to protect them from degradation and spontaneous release of Dex, reducing the systemic effects and having a local delivery. The PEM made of HA/Col with embedded liposomes provides also good cell adhesion which is an important for integration of implants related to cell growth and differentiation. An important point is probably the effect of combining adhesive cues by the ECM-like composition of PEM with chemical cues like Dex to activate pathways for cell differentiation. Hence, differentiation of C3H10T1/2 cells was more prominent on the PEM system with embedded Dex-loaded liposomes compared to the use of free liposomes in the SN. Overall, the combination of multilayers mimicking the matrix of bone and cartilage in combination with Dex might be interesting for future studies as coatings for osteochondral implants.

#### CRedit authorship contribution statement

**Brito-Barrera Y A:** Conceptualization, Methodology, Visualization Investigation, Writing - Original Draft. **Husteden C:** Investigation, Visualization, Writing - Review & Editing. **Alherz J:** Investigation, Visualization. **Fuhrmann B:** Visualization, Supervision **Wölk C:** Conceptualization, Supervision, Validation, Writing - Review & Editing. **Groth T:** Conceptualization, Supervision, Project administration, Writing- Reviewing and Editing.

#### Funding

Y.A.B.B supported by the CONACYT-México and German Academic Exchange Service (DAAD). The support by the Deutsche Forschungsgemeinschaft (DFG) project-ID [396823779] to C.W. is greatly acknowledged. TG acknowledges the kind support by the Ministry of Science and Higher Education of the Russian Federation within the framework of state support for the creation and development of World-Class Research Centers "Digital biodesign and personalized healthcare"

[075-15-2020-926].

#### Declaration of competing interest

The authors declare that they have no known competing financial interests or personal relationships that could have appeared to influence the work reported in this paper.

#### Acknowledgments

The authors thank the technical assistance of Mrs. Marlis Porobin for performing zeta potential measurements.

#### Appendix A. Supplementary data

Supplementary data to this article can be found online at <https://doi.org/10.1016/j.msec.2021.112516>.

#### References

- [1] Y. Lu, W. Zhang, J. Wang, G. Yang, S. Yin, T. Tang, X. Jiang, Recent advances in cell sheet technology for bone and cartilage regeneration: from preparation to application, *International J. Oral Sci.* (2019), <https://doi.org/10.1038/s41368-019-0050-5>.
- [2] A.M. Yousefi, M.E. Hoque, R.G. Prasad, N. Uth, Current strategies in multiphasic scaffold design for osteochondral tissue engineering: a review, 2015, <https://doi.org/10.1002/jbm.a.35356>. Wiley Online Library.
- [3] W. Swieszkowski, B.H.S. Tuan, K.J. Kurzydowski, D.W. Huttmacher, Repair and regeneration of osteochondral defects in the articular joints, *Biomol. Eng.* 24 (2007) 489–495, <https://doi.org/10.1016/j.bioeng.2007.07.014>.
- [4] M. Navarro, A. Michiardi, O. Castano, J.A. Planell, *Biomaterials in orthopaedics*, 2008, <https://doi.org/10.1098/tsif.2008.0151>.
- [5] J.M. Oliveira, S. Pina, R.L. Reis, J. San Roman (Eds.), *Osteochondral Tissue Engineering: Challenges, Current Strategies, and Technological Advances*, Springer International Publishing, Cham, 2018, <https://doi.org/10.1007/978-3-319-76735-2>.
- [6] J.F. Mano, R.L. Reis, Osteochondral defects: present situation and tissue engineering approaches, *J. Tissue Eng. Regen. Med.* 1 (2007) 261–273, <https://doi.org/10.1002/term.37>.
- [7] P. Gentile, I. Carmagnola, T. Nardo, V. Chiono, Layer-by-layer assembly for biomedical applications in the last decade, *Nanotechnology* 26 (2015), 422001, <https://doi.org/10.1088/0957-4484/26/42/422001>.
- [8] G. Decher, J.D. Hong, J. Schmitt, Buildup of ultrathin multilayer films by a self-assembly process. III. Consecutively alternating adsorption of anionic and cationic polyelectrolytes on charged surfaces, *Thin Solid Films* 210–211 (1992) 831–835, [https://doi.org/10.1016/0040-6090\(92\)90417-A](https://doi.org/10.1016/0040-6090(92)90417-A).
- [9] P. Gentile, I. Carmagnola, T. Nardo, V. Chiono, Layer-by-layer assembly for biomedical applications in the last decade, *IOPscience* (2015), <https://doi.org/10.1088/0957-4484/26/42/422001>.
- [10] P. Gentile, M.E. Frongia, M. Cardellach, C.A. Miller, G.P. Stafford, G.J. Leggett, P. V. Hatton, Functionalised nanoscale coatings using layer-by-layer assembly for imparting antibacterial properties to poly(lactide-co-glycolide) surfaces, *Acta Biomater.* 21 (2015) 35–43, <https://doi.org/10.1016/j.actbio.2015.04.009>.
- [11] W. Li, T. Guan, X. Zhang, Z. Wang, M. Wang, W. Zhong, J. Kong, The Effect of Layer-by-Layer Assembly Coating on the Proliferation and Differentiation of Neural Stem Cells, *ACS App. Mater. Interfaces* (2015), <https://doi.org/10.1021/am504456t>.
- [12] Y.T. Lai, E. Reading, G.L. Hura, K.L. Tsai, A. Laganowsky, F.J. Asturias, T.O. Yeates, Structure of a designed protein cage that self-assembles into a highly porous cube, *Nat. Chem.* (2014), <https://doi.org/10.1038/nchem.2107>.
- [13] M. Zhao, G. Altankov, U. Grabiec, M. Bennett, M. Salmeron-Sanchez, F. Dehghani, T. Groth, Molecular composition of GAG-collagen I multilayers affects remodeling of terminal layers and osteogenic differentiation of adipose-derived stem cells, *Acta Biomater.* 41 (2016) 86–99, <https://doi.org/10.1016/j.actbio.2016.05.023>.
- [14] H. Ai, S.A. Jones, Y.M. Lvov, Biomedical applications of electrostatic layer-by-layer nano-assembly of polymers 39 (2003) 23–44, <https://doi.org/10.1385/CBB:39:1:23>.
- [15] D.P. Pioletti, O. Gauthier, V.A. Stadelmann, B. Bujoli, J. Guicheux, P.-Y. Zambelli, J.-M. Boulter, Orthopedic implant used as drug delivery system: clinical situation and state of the research, *Curr. Drug Deliv.* 5 (2008) 59–63, <https://doi.org/10.2174/156720108783331041>.
- [16] B.S.G. Prasad, V.R.M. Gupta, N. Devanna, K. Jayasurya 5 (2014) 12.
- [17] G. Khang, J.M. Rhee, J.K. Jeong, J.S. Lee, M.S. Kim, S.H. Cho, H.B. Lee, Local drug delivery system using biodegradable polymers, *Macromol. Res.* 11 (2003) 207–223, <https://doi.org/10.1007/BF03218355>.
- [18] A. Aravamudan, M.D. Ramos, J. Nip, A. Subramanian, R. James, D.M. Harmon, G. S. Kurnbar, Osteoinductive small molecules: growth factor alternatives for bone tissue engineering, *Curr. Pharm. Des.* 19 (2013) 3420–3428, <https://doi.org/10.2174/1381612811319190008>.

- [19] M. Yuasa, T. Yamada, T. Taniyama, T. Masaoka, W. Xuetao, T. Yoshii, S. Sotome, Dexamethasone Enhances Osteogenic Differentiation of Bone Marrow- and Muscle-Derived Stromal Cells and Augments Ectopic Bone Formation Induced by Bone Morphogenetic Protein-2, 2015, <https://doi.org/10.1371/journal.pone.0116462>.
- [20] V. Llopis-Hernández, M. Cantini, C. González-García, Z.A. Cheng, J. Yang, P. M. Tsimboui, A.J. García, M.J. Dalby, M. Salmerón-Sánchez, Material-driven fibronectin assembly for high-efficiency presentation of growth factors, *Sci. Adv.* 2 (2016), e1600188, <https://doi.org/10.1126/sciadv.1600188>.
- [21] H. Monteiro, A. Martins, D. Ribeiro, S. Faria, N.A. Fonseca, J.N. Moreira, N. M. Neves, On the use of dexamethasone-loaded liposomes to induce the osteogenic differentiation of human mesenchymal stem cells, 2015, <https://doi.org/10.1002/term.1817>. Wiley Online Library.
- [22] C. Wölk, C. Janich, U. Bakowsky, A. Langner, G. Brezesinski, Malonic acid based cationic lipids – the way to highly efficient DNA-carriers, *Adv. Colloid Interf. Sci.* 248 (2017) 20–34, <https://doi.org/10.1016/j.cis.2017.08.003>.
- [23] S. Zhang, Y. Xu, B. Wang, W. Qiao, D. Liu, Z. Li, Cationic compounds used in lipoplexes and polyplexes for gene delivery, *J. Control. Release* 100 (2004) 165–180, <https://doi.org/10.1016/j.jconrel.2004.08.019>.
- [24] J. Gisselbrecht, C. Janich, S.R. Pinnapireddy, G. Hause, U. Bakowsky, C. Wölk, A. Langner, Overcoming the polyplex dilemma – explorative studies to characterise the efficiency and biocompatibility of newly designed lipofection reagents, *Int. J. Pharm.* 541 (2018) 81–92, <https://doi.org/10.1016/j.ijpharm.2018.02.029>.
- [25] X. Zhang, L. Dai, A. Wang, C. Wölk, B. Dobner, G. Brezesinski, J. Li, The directional observation of highly dynamic membrane tubule formation induced by engulfed liposomes, *Sci. Rep.* (2015), <https://doi.org/10.1038/srep16559>.
- [26] C.R. Dass, P.F. Choong, Targeting of small molecule anticancer drugs to the tumour and its vasculature using cationic liposomes: lessons from gene therapy, SpringerLink, 2006, <https://doi.org/10.1186/1475-2867-6-17>.
- [27] A. Kanazawa, T. Ikeda, T. Endo, Synthesis and antimicrobial activity of dimethyl- and trimethyl-substituted phosphonium salts with alkyl chains of various lengths, *Antimicrob. Agents Chemother.* (1994), <https://doi.org/10.1128/AAC.38.5.945>.
- [28] C. Barnier Quer, A. Elsharkawy, S. Romeijn, A. Kros, W. Jiskoot, Cationic liposomes as adjuvants for influenza hemagglutinin: more than charge alone, *Eur. J. Pharm. Biopharm.* 81 (2012) 294–302, <https://doi.org/10.1016/j.ejpb.2012.03.013>.
- [29] M.A. Mintzer, E. Simanek, Nonviral vectors for gene delivery, *Chem. Rev.* (2009), <https://doi.org/10.1021/cr800409e>.
- [30] V.E. Santo, M.E. Gomes, J.F. Mano, R.L. Reis, Controlled release strategies for bone, cartilage, and osteochondral engineering—part I: recapitulation of native tissue healing and variables for the design of delivery systems, 2013, <https://doi.org/10.1089/ten.teb.2012.0138>.
- [31] N. Patel 2 (2012) 7.
- [32] M. Michel, D. Vautier, J.-C. Voegel, P. Schaaf, V. Ball, Layer by layer self-assembled polyelectrolyte multilayers with embedded phospholipid vesicles, *Langmuir* 20 (2004) 4835–4839, <https://doi.org/10.1021/A049736q>.
- [33] D.V. Volodkin, P. Schaaf, H. Mohwald, J.-C. Voegel, V. Ball, Effective embedding of liposomes into polyelectrolyte multilayered films: the relative importance of lipid-polyelectrolyte and interpolyelectrolyte interactions, *Soft Matter* 5 (2009) 1394–1405, <https://doi.org/10.1039/B815048F>.
- [34] N. Graf, A. Tanno, A. Dochter, N. Rothfuchs, J. Vörös, T. Zambelli, Electrochemically driven delivery to cells from vesicles embedded in polyelectrolyte multilayers, *Soft Matter* 8 (2012) 3641–3648, <https://doi.org/10.1039/C2SM07272F>.
- [35] P.C. DeMuth, J.J. Moon, H. Suh, P.T. Hammond, D.J. Irvine, Releasable layer-by-layer assembly of stabilized lipid nanocapsules on microneedles for enhanced transcutaneous vaccine delivery, *ACS Nano* 6 (2012) 8041–8051, <https://doi.org/10.1021/nl302639r>.
- [36] R. Polak, R.M. Lim, M.M. Beppu, R.N. Pitombo, R.E. Cohen, M.F. Rubner 4 (18) (2015) 2832–2841, <https://doi.org/10.1002/adhm.201500604>.
- [37] V. Domínguez-Arca, R.R. Costa, A.M. Carvalho, P. Taboada, R.L. Reis, G. Prieto, I. Pashkuleva, Liposomes embedded in layer by layer constructs as simplistic extracellular vesicles transfer model, *Mater. Sci. Eng. C* 121 (2021), 111813, <https://doi.org/10.1016/j.msec.2020.111813>.
- [38] X. Ma, X. Zhang, Y. Jia, S. Zu, S. Han, D. Xiao, H. Sun, Y. Wang, Dexamethasone induces osteogenesis via regulation of hedgehog signalling molecules in rat mesenchymal stem cells, *Int. Orthop.* 37 (2013) 1399–1404, <https://doi.org/10.1007/s00264-013-1902-9>.
- [39] L. Zhao, G. Li, K.M. Chan, Y. Wang, P.-F. Tang, Comparison of multipotent differentiation potentials of murine primary bone marrow stromal cells and mesenchymal stem cell line C3H10T1/2, *Calcif. Tissue Int.* 84 (2009) 56–64, <https://doi.org/10.1007/s00223-008-9189-3>.
- [40] C.M. Shea, C.M. Edgar, T.A. Einhorn, L.C. Gerstenfeld, BMP treatment of C3H10T1/2 mesenchymal stem cells induces both chondrogenesis and osteogenesis, *J. Cell. Biochem.* 90 (2003) 1112–1127, <https://doi.org/10.1002/jcb.10734>.
- [41] L. Han, A.J. Grodzinsky, C. Ortiz, Nanomechanics of the cartilage extracellular matrix, *Annu. Rev. Mater. Res.* 41 (2011) 133–168, <https://doi.org/10.1146/annurev-matsci-062910-100431>.
- [42] F. Long, Building strong bones: molecular regulation of the osteoblast lineage, *Nat. Rev. Mol. Cell Biol.* (2012), <https://doi.org/10.1038/nrm3254>.
- [43] O. Ghali, O. Broux, G. Falgayrac, N. Haren, J.P. van Leeuwen, G. Penel, P. Hardouin, C. Chauveau, Dexamethasone in osteogenic medium strongly induces adipocyte differentiation of mouse bone marrow stromal cells and increases osteoblast differentiation, *BMC Cell Biol.* 16 (2015), <https://doi.org/10.1186/s12860-015-0056-6>.
- [44] F. Langenbach, J. Handschel, Effects of dexamethasone, ascorbic acid and  $\beta$ -glycerophosphate on the osteogenic differentiation of stem cells in vitro, *Stem Cell Res Ther* 4 (2013) 117, <https://doi.org/10.1186/scrt328>.
- [45] I. Sekiya, P. Koopman, K. Tsuji, S. Mertin, V. Hatley, Y. Yamada, K. Shinomiya, A. Nifuji, M. Noda, Dexamethasone enhances SOX9 expression in chondrocytes.
- [46] Y.A. Brito Barrera, G. Hause, M. Menzel, C.E.H. Schmelzer, E. Lehner, K. Mäder, C. Wölk, T. Groth, Engineering osteogenic microenvironments by combination of multilayers from collagen type I and chondroitin sulfate with novel cationic liposomes, *Mater. Today Bio.* 7 (2020), 100071, <https://doi.org/10.1016/j.mrbio.2020.100071>.
- [47] A. Köwitsch, M. Jurado Abreu, A. Chhalotra, M. Hiescher, S. Fischer, K. Mäder, T. Groth, Synthesis of thiolated glycosaminoglycans and grafting to solid surfaces, *Carbohydr. Polym.* 114 (2014) 344–351, <https://doi.org/10.1016/j.carbpol.2014.08.027>.
- [48] U. Hozzum, B. Ozdil, D. Pesen-Okvur, Step-by-step quantitative analysis of focal adhesions, *MethodsX* 1 (2014) 56–59, <https://doi.org/10.1016/j.mex.2014.06.004>.
- [49] M. Sarem, O. Otto, S. Tanaka, V.P. Shastri, Cell number in mesenchymal stem cell aggregates dictates cell stiffness and chondrogenesis, *Stem Cell Res. Ther.* 10 (2019) 10, <https://doi.org/10.1186/s13287-018-1103-y>.
- [50] K.J. Livak, T.D. Schmittgen, Analysis of relative gene expression data using real-time quantitative PCR and the  $2^{-\Delta\Delta CT}$  method, *Methods* 25 (2001) 402–408, <https://doi.org/10.1006/meth.2001.1262>.
- [51] S. Tassler, B. Dobner, L. Lampp, R. Ziolkowski, E. Malinowska, C. Wölk, G. Brezesinski, DNA delivery systems based on peptide-mimicking cationic lipids—the effect of the co-lipid on the structure and DNA binding capacity, *Langmuir* 35 (2019) 4613–4625, <https://doi.org/10.1021/acs.langmuir.8b04139>.
- [52] S. Tassler, C. Wölk, C. Janich, B. Dobner, G. Brezesinski, Lysine-based amino-functionalized lipids for gene transfection: the protonation state in monolayers at the air–liquid interface, *Phys. Chem. Chem. Phys.* 19 (2017) 20271–20280, <https://doi.org/10.1039/C7CP03107F>.
- [53] J. Stetefeld, S.A. McKenna, T.R. Patel, Dynamic light scattering: a practical guide and applications in biomedical sciences, *Biophys. Rev.* 8 (2016) 409–427, <https://doi.org/10.1007/s12551-016-0218-6>.
- [54] I.S. Zuhorn, U. Bakowsky, E. Polushkin, W.H. Visser, M.C.A. Stuart, J.B.F. N. Engberts, D. Hoekstra, Nonbilayer phase of lipoplex–membrane mixture determines endosomal escape of genetic cargo and transfection efficiency, *Mol. Ther.* 11 (2005) 801–810, <https://doi.org/10.1016/j.ymthe.2004.12.018>.
- [55] M. Zhao, L. Li, C. Zhou, F. Heyroth, B. Fuhrmann, K. Maeder, T. Groth, Improved stability and cell response by intrinsic cross-linking of multilayers from collagen I and oxidized glycosaminoglycans, *Biomacromolecules* (2014), <https://doi.org/10.1021/bm501286f>.
- [56] M. Zhao, R. Anouz, T. Groth, Effect of microenvironment on adhesion and differentiation of murine C3H10T1/2 cells cultured on multilayers containing collagen I and glycosaminoglycans, 2020, <https://doi.org/10.1177/2041731420940560>.
- [57] C. Husteden, F. Doberenz, N. Goergen, S.R. Pinnapireddy, C. Janich, A. Langner, F. Syrowatka, A. Repanas, F. Erdmann, J. Jedelská, U. Bakowsky, T. Groth, C. Wölk, Contact-triggered lipofection from multilayer films designed as surfaces for in situ transfection strategies in tissue engineering, *ACS Appl. Mater. Interfaces* 12 (2020) 8963–8977, <https://doi.org/10.1021/acsami.9b18968>.
- [58] P.D. Ward, S.L. Thiébaud, S.D. Gray, Hyaluronic acid: its role in voice, *J. Voice* 16 (2002) 303–309, [https://doi.org/10.1016/S0892-1997\(02\)00101-7](https://doi.org/10.1016/S0892-1997(02)00101-7).
- [59] M. Michel, V. Toniazza, D. Ruch, V. Ball, Deposition mechanisms in layer-by-layer or step-by-step deposition methods: from elastic and impermeable films to soft membranes with ion exchange properties, *ISRN Mater. Sci.* 2012 (2012), <https://doi.org/10.5402/2012/701695>.
- [60] G. Altankov, K. Riebau, T. Groth, The role of surface zeta potential and substratum chemistry for regulation of dermal fibroblasts interaction, in: *Mater. Sci. Eng. Technol.*, Wiley Online Library, 2003, <https://doi.org/10.1002/mawe.200300699>.
- [61] R. Zimmermann, O. Birkert, G. Gauglitz, C. Werner, Electrostatic Phenomena at Polymer Films for Biosensor Applications, 2003, <https://doi.org/10.1002/cpbe.200200475>. Wiley Online Library.
- [62] J. Almodóvar, L.W. Place, J. Gogolski, K. Erickson, M.J. Kipper, layer-by-layer assembly of polysaccharide-based polyelectrolyte multilayers: a spectroscopic study of hydrophilicity, composition, and ion pairing, *Biomacromolecules* 12 (2011) 2755–2765, <https://doi.org/10.1021/bm200519y>.
- [63] M.S. Niepel, K. Kirchhoff, M. Menzel, A. Heilmann, T. Groth, Controlling cell adhesion using ph-modified polyelectrolyte multilayer films, in: *Layer-by-layer Films for Biomedical Applications*, John Wiley & Sons, Ltd, 2015, pp. 1–30, <https://doi.org/10.1002/9783527675869.ch1>.
- [64] G. Altankov, F. Grinnel, T. Groth, Studies on the biocompatibility of materials: fibroblast reorganization of substratum-bound fibronectin on surfaces varying in wettability, 1996, [https://doi.org/10.1002/\(SICI\)1097-4636\(199603\)30:3<385::AID-JBM13>3.0.CO;2-J](https://doi.org/10.1002/(SICI)1097-4636(199603)30:3<385::AID-JBM13>3.0.CO;2-J). Wiley Online Library.
- [65] N. Fauchoux, R. Schweiss, K. Lützow, C. Werner, T. Groth, Self-assembled monolayers with different terminating groups as model substrates for cell adhesion studies, *Biomaterials* 25 (2004) 2721–2730, <https://doi.org/10.1016/j.biomaterials.2003.09.069>.
- [66] M. Schönhoff, Layered polyelectrolyte complexes: physics of formation and molecular properties, *J. Phys. Condens. Matter* 15 (2003) R1781–R1808, <https://doi.org/10.1088/0953-8984/15/49/R01>.
- [67] R. McBeath, D.M. Pirone, C.M. Nelson, K. Bhadriraju, C.S. Chen, Cell shape, cytoskeletal tension, and RhoA regulate stem cell lineage commitment, *Dev. Cell* 6 (2004) 483–495, [https://doi.org/10.1016/S1534-5807\(04\)00075-9](https://doi.org/10.1016/S1534-5807(04)00075-9).

- [68] W.H. Goldmann, Role of vinculin in cellular mechanotransduction, 2016, <https://doi.org/10.1002/cbin.10563>. Wiley Online Library.
- [69] M. Bennett, M. Cantini, J. Reboud, J.M. Cooper, P. Roca-Cusachs, M. Salmeron-Sanchez, Molecular clutch drives cell response to surface viscosity, *PNAS* 115 (2018) 1192–1197, <https://doi.org/10.1073/pnas.1710653115>.
- [70] D.E. Discher, P. Janmey, Y. Wang, Tissue cells feel and respond to the stiffness of their substrate, *Science* 310 (2005) 1139–1143, <https://doi.org/10.1126/science.1116995>.
- [71] A.S. Mao, J.-W. Shin, D.J. Mooney, Effects of substrate stiffness and cell-cell contact on mesenchymal stem cell differentiation, *Biomaterials* 98 (2016) 184–191, <https://doi.org/10.1016/j.biomaterials.2016.05.004>.
- [72] A. Nolte, S. Hossfeld, B. Schroepel, A. Mueller, D. Stoll, T. Walker, R. Krastev, Impact of polyelectrolytes and their corresponding multilayers to human primary endothelial cells, *J. Biomater. Appl.* (2013), <https://doi.org/10.1177/0885328212437610>.
- [73] V. Gribova, R. Anzely-Velty, C. Picart, Polyelectrolyte multilayer assemblies on materials surfaces: from cell adhesion to tissue engineering, *Chem. Mater.* (2013), <https://doi.org/10.1021/cm2032459>.
- [74] T. Groth, Z.M. Liu, M. Niepel, D. Peschel, K. Kirchhof, G. Altankov, N. Fauchoux, Chemical and Physical Modifications of Biomaterial Surfaces to Control Adhesion of Cells, SpringerLink, 2010, [https://doi.org/10.1007/978-90-481-8790-4\\_13](https://doi.org/10.1007/978-90-481-8790-4_13).
- [75] M. Kiesel, M.M. Martino, M. Ventura, J.A. Hubbell, J. Hilborn, D.A. Ossipov, Improving the osteogenic potential of BMP-2 with hyaluronic acid hydrogel modified with integrin-specific fibronectin fragment, *Biomaterials* 34 (2013) 704–712, <https://doi.org/10.1016/j.biomaterials.2012.10.015>.
- [76] H. Ponta, L. Sherman, P.A. Herdlich, CD44: from adhesion molecules to signalling regulators, *Nat. Rev. Mol. Cell. Biol.* 4 (2003) 33–45, <https://doi.org/10.1038/nrm1004>.
- [77] J. Jokinen, E. Dadu, P. Nykvist, J. Käpylä, D.J. White, J. Ivaska, P. Vehviläinen, H. Reunanen, H. Laajava, L. Häkkinen, J. Heino, Integrin-mediated cell adhesion to type I collagen fibrils, *J. Biol. Chem.* 279 (2004) 31956–31963, <https://doi.org/10.1074/jbc.M401409200>.
- [78] P.J. Wrighton, J.R. Klim, B.A. Hernandez, C.H. Koonce, T.J. Kamp, L.L. Kiessling, Signals from the surface modulate differentiation of human pluripotent stem cells through glycosaminoglycans and integrins, 2014, <https://doi.org/10.1073/pnas.1409525111>.
- [79] J.D. Humphrey, E.R. Dufresne, M.A. Schwartz, Mechanotransduction and extracellular matrix homeostasis, *Nat. Rev. Mol. Cell. Biol.* 15 (2014) 802–812, <https://doi.org/10.1038/nrm3896>.
- [80] A.J. Garcia, Get a grip: integrins in cell–biomaterial interactions, *ScienceDirect* (2005), <https://doi.org/10.1016/j.biomaterials.2005.05.029>.
- [81] X. Wu, S. Ding, Q. Ding, M.S. Gray, P.G. Schultz, A small molecule with osteogenesis-inducing activity in multipotent mesenchymal progenitor cells, *J. Am. Chem. Soc.* 124 (2002) 14520–14521, <https://doi.org/10.1021/ja0283908>.
- [82] K.M. Sinha, X. Zhou, Genetic and molecular control of osterix in skeletal formation, *J. Cell. Biochem.* 114 (2013) 975–984, <https://doi.org/10.1002/jcb.24439>.
- [83] A. Cheng, P.G. Genever, SOX9 determines RUNX2 transactivity by directing intracellular degradation 25 (2010) 2680–2689, <https://doi.org/10.1002/jbmr.174>.
- [84] F. Jafari, P. Hanaei, K. Gorjipour, Osteoblast differentiation on collagen scaffold with immobilized alkaline phosphatase, *Int. J. Organ Transplant Med.* 8 (2017) 195–202.
- [85] J. Settlemann, Tension precedes commitment—even for a stem cell, *Mol. Cell* 14 (2004) 148–150, [https://doi.org/10.1016/S1097-2765\(04\)00207-2](https://doi.org/10.1016/S1097-2765(04)00207-2).
- [86] I. Sekiya, P. Koopman, K. Tsuji, S. Mertin, V. Harley, Y. Yamada, K. Shinomiya, A. Niifuji, M. Noda, Dexamethasone enhances SOX9 expression in chondrocytes, *J. Endocrinol.* 169 (2001) 573–579, <https://doi.org/10.1677/joe.0.1690573>.
- [87] M.A. Pratta, W. Yao, C. Decicco, M.D. Tortorella, R.-Q. Liu, R.A. Copeland, R. Magolda, R.C. Newton, J.M. Tzaskos, E.C. Arner, Aggrecan protects cartilage collagen from proteolytic cleavage, *J. Biol. Chem.* 278 (2003) 45539–45545, <https://doi.org/10.1074/jbc.M303737200>.
- [88] H. Tanaka, C.L. Murphy, C. Murphy, M. Kimura, S. Kawai, J.M. Polak, Chondrogenic differentiation of murine embryonic stem cells: effects of culture conditions and dexamethasone, *J. Cell. Biochem.* 93 (2004) 454–462, <https://doi.org/10.1002/jcb.20171>.
- [89] A.C. Daly, S.E. Crichtley, E.M. Rencsok, D.J. Kelly, A comparison of different bioinks for 3D bioprinting of fibrocartilage and hyaline cartilage, *Biofabrication* 8 (2016), 045002, <https://doi.org/10.1088/1758-5090/8/4/045002>.
- [90] M.K. Gordon, R.A. Hahn, Collagens, *Cell Tissue Res.* 339 (1) (2010) 247–257, <https://doi.org/10.1007/s00441-009-0844-4>.
- [91] M.S. Niepel, B.K. Ekambaram, C.E.H. Schmedzler, T. Groth, Polyelectrolyte multilayers of poly (L-lysine) and hyaluronic acid on nanostructured surfaces affect stem cell response, *Nanoscale* 11 (2019) 2878–2891, <https://doi.org/10.1039/c8nr05529g>.
- [92] L. Yang, K.Y. Tsang, H.C. Tang, D. Chan, K.S.E. Cheah, Hypertrophic chondrocytes can become osteoblasts and osteocytes in endochondral bone formation, *PNAS* 111 (2014) 12097–12102, <https://doi.org/10.1073/pnas.1302703111>.
- [93] L. Gao, R. McBeath, C.S. Chen, Stem cell shape regulates a chondrogenic versus myogenic fate through Rac1 and N-cadherin, *Stem Cells* 28 (3) (2010) 564–572, <https://doi.org/10.1002/stream.308>.

## 2.6) Publikation IV

### **Lipoplex-functionalized thin-film surface coatings based on extracellular matrix components as local delivery system to control osteogenic stem cell differentiation**

C. Husteden, Y. A. Brito Barrera, S. Tegtmeier, J. Borges, J. Giselbrecht, M. Menzel, A. Langner, J. F. Mano, C.E.H. Schmelzer, C. Wölk, T. Groth

*\* C. Husteden und Y.A. Brito Barrera teilen sich die Erstautorenschaft für diese Publikation*

Advanced Healthcare Materials 2022

<https://doi.org/10.1002/adhm.202201978>

*Supporting Information* ist dem Anhang beigelegt.



## RESEARCH ARTICLE

ADVANCED  
HEALTHCARE  
MATERIALS

www.advhealthmat.de

# Lipoplex-Functionalized Thin-Film Surface Coating Based on Extracellular Matrix Components as Local Gene Delivery System to Control Osteogenic Stem Cell Differentiation

Catharina Husteden, Yazmin A. Brito Barrera, Sophia Tegtmeier, João Borges, Julia Giselbrecht, Matthias Menzel, Andreas Langner, João F. Mano, Christian E. H. Schmelzer, Christian Wölk,\* and Thomas Groth\*

A gene-activated surface coating is presented as a strategy to design smart biomaterials for bone tissue engineering. The thin-film coating is based on polyelectrolyte multilayers composed of collagen I and chondroitin sulfate, two main biopolymers of the bone extracellular matrix, which are fabricated by layer-by-layer assembly. For further functionalization, DNA/lipid-nanoparticles (lipoplexes) are incorporated into the multilayers. The polyelectrolyte multilayer fabrication and lipoplex deposition are analyzed by surface sensitive analytical methods that demonstrate successful thin-film formation, fibrillar structuring of collagen, and homogenous embedding of lipoplexes. Culture of mesenchymal stem cells on the lipoplex functionalized multilayer results in excellent attachment and growth of them, and also, their ability to take up cargo like fluorescence-labelled DNA from lipoplexes. The functionalization of the multilayer with lipoplexes encapsulating DNA encoding for transient expression of bone morphogenetic protein 2 induces osteogenic differentiation of mesenchymal stem cells, which is shown by mRNA quantification for osteogenic genes and histochemical staining. In summary, the novel gene-functionalized and extracellular matrix mimicking multilayer composed of collagen I, chondroitin sulfate, and lipoplexes, represents a smart surface functionalization that holds great promise for tissue engineering constructs and implant coatings to promote regeneration of bone and other tissues.

## 1. Introduction

Over the past few decades, the development of smart multifunctional biomaterials with the ability to control the behavior of stem cells on demand has become a powerful strategy in regenerative medicine and cell therapies.<sup>1,2]</sup> For instance, such stem cell-based therapies bear new chances to regenerate critical size bone defects from severe fractures or bone tissue loss after surgery. The osteogenic differentiation of mesenchymal stem cells is important for the healing of bone fractures and osteogenic diseases such as disorders of bone metabolism (osteoporosis).<sup>3–6]</sup> Various studies have determined characteristics and modifications of biomaterials that enable initiation of stem cell osteogenesis and represent promising approaches for clinical use. These approaches include materials that can mimic the bone microenvironment,<sup>7,8]</sup> materials with specific mechanical properties which stimulate bone tissue formation,<sup>9]</sup> and materials

C. Husteden, S. Tegtmeier, J. Giselbrecht, A. Langner  
Institute of Pharmacy  
Department of Medicinal Chemistry  
Martin Luther University Halle-Wittenberg  
Wolfgang-Langenbeck-Str. 4, 06120 Halle (Saale), Germany

Y. A. Brito Barrera, T. Groth  
Institute of Pharmacy  
Department of Biomedical Materials  
Martin Luther University Halle-Wittenberg  
Heinrich-Damerow-Str. 4, 06120 Halle (Saale), Germany  
E-mail: thomas.groth@pharmazie.uni-halle.de

The ORCID identification number(s) for the author(s) of this article can be found under <https://doi.org/10.1002/adhm.202201978>

© 2022 The Authors. Advanced Healthcare Materials published by Wiley-VCH GmbH. This is an open access article under the terms of the Creative Commons Attribution License, which permits use, distribution and reproduction in any medium, provided the original work is properly cited.

DOI: 10.1002/adhm.202201978

J. Borges, J. F. Mano  
Department of Chemistry  
CICECO – Aveiro Institute of Materials  
University of Aveiro  
Campus Universitário de Santiago, Aveiro 3810-193, Portugal  
M. Menzel, C. E. H. Schmelzer  
Department of Biological and Macromolecular Materials  
Fraunhofer Institute for Microstructure of Materials and Systems (IMWS)  
Walter-Hülse-Str. 1, 06120 Halle (Saale), Germany

C. Wölk  
Institute of Pharmacy  
Pharmaceutical Technology  
Faculty of Medicine  
Leipzig University  
04317 Leipzig, Germany  
E-mail: christian.woelk@medizin.uni-leipzig.de

T. Groth  
Interdisciplinary Center of Materials Science  
Martin-Luther-University Halle-Wittenberg  
Heinrich-Damerow-Str. 4, 06120 Halle (Saale), Germany

which can release or control the activity of osteoinductive growth factors.<sup>[10–12]</sup>

A straightforward strategy for the functionalization of biomaterials involves emulating the properties of the extracellular matrix (ECM) for the formation of an artificial microenvironment that enables a precise control of cell behavior and function.<sup>[13]</sup> Due to interaction of ECM components with cell surface receptors such as integrins, ECM regulates cell proliferation, migration, and differentiation.<sup>[14,15]</sup> Indeed, the ECM is a highly versatile and dynamic compartment that can support development, function, and regeneration of tissues and organs by modulating the production, degradation, and remodeling of its components.<sup>[16]</sup> Therefore, the development of surface coatings mimicking the native ECM structure and function is of considerable interest to functionalize implant materials. In this context, a simple and versatile method that can effectively immobilize bio-functional molecules onto various materials and surfaces, with dynamic control of the surface topological and mechanical properties, is of utmost interest. The layer-by-layer (LbL) technology, well-known from the pioneering work by Decher et al. on the development of polyelectrolyte multilayers (PEMs) on solid surfaces by alternating deposition of oppositely charged polyelectrolytes, has evolved into a very simple and cost effective yet highly versatile and efficient surface modification and functionalization technology. LbL technique allows the production of multifunctional thin film coatings with precise control of the film composition, structure, properties, and functions at the nanoscale.<sup>[17,18]</sup> A further advantage of LbL is that it can be performed by different methods such as dip-coating, spray coating, and spin-coating protocols allowing the coating of different materials and designs also in a time-saving manner.<sup>[18]</sup> Indeed, PEMs have been broadly used as reservoir for either the surface immobilization or encapsulation of bioactive molecules, more precisely drugs and proteins, to engineer bio-functional materials by choice of polyelectrolytes and complexation conditions for regenerative medicine strategies.<sup>[19–23]</sup> Type I collagen (Col) and chondroitin sulfate (Cs) are components of the ECM of bone. Col is the main organic component of the bone ECM and a perfect material in tissue engineering because of its excellent biodegradability, biocompatibility, and cell-attracting properties. In fact, Col has drawn much attention for biomaterial development due to the existence of binding sites for cell receptors, cytokines, and other ECM components.<sup>[19,24–26]</sup> Cs is involved in cell recognition, intracellular signaling, and on the interaction between ECM components and cell-surface glycoproteins.<sup>[27]</sup> As such, Cs can enhance bone regeneration; thus, being used for the functionalization of PEMs for improved mineral deposition and osteogenesis.<sup>[28]</sup>

The functionalization of biomaterials with tissue relevant growth factors is also a promising strategy in tissue engineering. In the field of bone tissue engineering, the bone morphogenetic protein-2 (BMP-2) is a promising cytokine. Several studies have demonstrated that the growth factor BMP-2 can be applied to stimulate bone healing and improve osteogenesis/osteointegration.<sup>[29–33]</sup> For example, recombinant BMP-2 is applied in the clinic for treatment of non-union bone injuries, open tibia fractures, and spinal fusion in FDA-approved systems for bone regeneration.<sup>[8,34]</sup> However, due to some persistent issues, including the need of loading large amounts of the recombinant BMP-2 into the biomaterial, a burst release of supra-

physiological concentrations of BMP-2 as well as the risk of unregulated and ectopic bone formation *in vivo*, the current clinical utilization of BMP-2 has limitations,<sup>[35]</sup> which forces the development of micro- or nanostructured delivery systems for BMP-2<sup>[36]</sup> or novel gene-activated matrices.<sup>[37]</sup>

To overcome the existing drawbacks of BMP-2 functionalized biomaterials, spatially limited acting *in situ* transfection systems gained attention to ensure a local cytokine production mediated by transfected cells. Surface-mediated transfection strategies are based on a concept in which viral or non-viral vectors embedded in matrix materials can promote a local, physiological, and/or sustained expression of a gene encoding for a therapeutic protein.<sup>[38]</sup> By immobilizing plasmid DNA (pDNA) on surfaces, such as implants, surface-mediated gene delivery achieved remarkable transient cell transfection and therapeutic effects, both *in vivo* and *in vitro*.<sup>[39,40]</sup> Despite their potential for tissue engineering, the use of viral vectors for gene delivery is limited by a high risk of immunogenicity and a certain risk for carcinogenicity. Therefore, current research is increasingly focusing on non-viral vectors.<sup>[41]</sup> Promising new methods are studied to find non-viral vectors to achieve comparable gene transfer efficiency to viral vector equivalents. New transfection systems such as polymers, lipids, nanoparticles, and physical methods are studied to reduce cost, and increase safety and transfection efficiency.<sup>[42,43]</sup> For example, Olden et al. used cationic polyplexes for gene delivery into primary human T cells.<sup>[44]</sup> Non-viral gene delivery approaches have been specifically explored in cell-based therapies because of their desirable safety profiles and simplicity of the preparation process when compared to viral vectors.<sup>[45]</sup> However, non-viral vectors are not suitable for systemic application in bone regeneration because DNA complexes carry the risk of transfection of undesired cell types and systemic side effects *in vivo*.

Previous studies have consistently demonstrated that electrostatic-driven LbL assembly is a powerful and simple technique to functionalize biomaterials with nucleic acids aiming for non-viral gene delivery.<sup>[46–49]</sup> Thus, non-viral, surface-mediated gene delivery may represent an ideal strategy to control cell response in the close vicinity of an implant material avoiding any systemic complications in patients. Lipoplexes (LPX), a subtype of nucleic acid lipid nanoparticles, belong to the non-viral gene delivery systems. For example, in a proof-of-concept study by Holmes, Lipofectamine 2000-based LPX has been immobilized in PEMs and successfully transferred a model gene to typical screening cell lines (NIH3T3 fibroblasts and HEK293 kidney cells), but not to stem cells.<sup>[50]</sup> However, we recently developed a LPX formulation composed of dioleoylphosphatidylethanolamine (DOPE) and the ionizable lipid *N*-{6-amino-1-[*N*-(9Z)-octadec-9-enylamino]-1-oxohexan-(2S)-2-yl]-*N'*-[2-[*N,N*-bis(2-aminoethyl)amino]ethyl]-2[(9Z)-octadec-9-enyl]propan diamide (OO4), a lipid composite which demonstrated superiority in terms of efficient cellular uptake and DNA delivery in cell culture experiments, compared to Lipofectamine 2000.<sup>[51,52]</sup> Moreover, we could show recently that surface coatings composed of either Col/Cs or Col/hyaluronic acid PEMs with dexamethasone (Dex) loaded OO4/DOPE liposomes could induce either osteogenic or chondrogenic differentiation of multipotent stem cells. This was related to the type of multilayer mimicking the composition of target ECM, such as bone or cartilage.<sup>[53,54]</sup> Furthermore, we developed in a

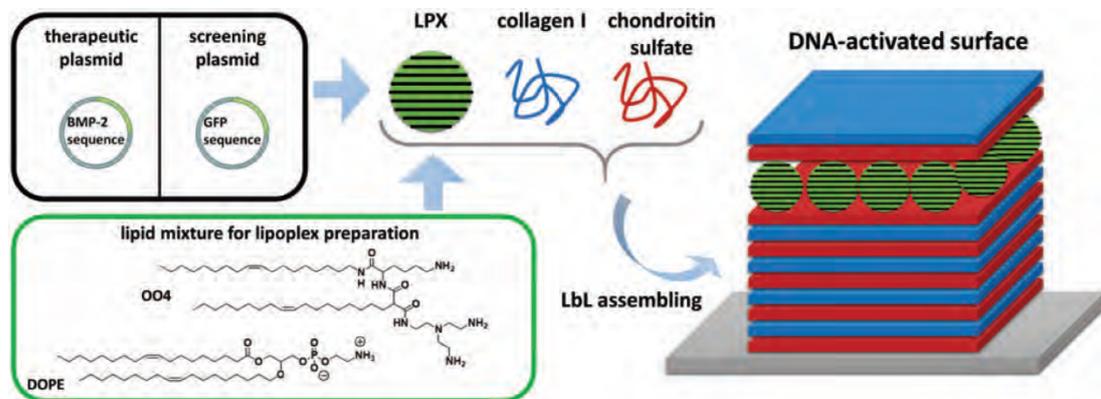


**Figure 1.** Schematic illustration of the DNA-activated bone-ECM-mimicking surface coating. The lipid components OO4/DOPE were formulated to cationic liposomes. The cationic liposomes were assembled with DNA encoding either of the reporter gene green fluorescent protein (GFP) or the therapeutic gene BMP-2, to LPX. LPX were assembled into DNA-activated surface coatings as tool for in situ transfection using the LBL technique.

proof-of-concept study, a strategy to incorporate LPX into PEMs composed of hyaluronic acid and chitosan and demonstrated the successful transfection of murine myoblasts and the epithelium of the chorion allantois membrane of the chicken embryo.<sup>[48]</sup>

In the present study, we combined both approaches, such as the ECM-mimicking character of PEM and their ability to be used as carrier for in situ transfection, to develop a gene-activated ECM-mimicking surface coating to direct stem cells' fate. We focused on a bone ECM-mimicking PEMs consisting of Col and Cs loaded with LPX composed of OO4/DOPE lipid composite (see **Figure 1**). The DNA as biological active compound encoded a BMP-2 sequence to stimulate surface-mediated, transient expression of BMP-2 in human adipose-derived mesenchymal stem cells (hADSCs) to induce osteogenesis due to autocrine and paracrine effects of the cytokine. The work focused on three main objectives: 1) a material science part, in which we characterized the multilayer formation processes, especially the embedding of OO4/DOPE LPX and the surface properties of LPX-loaded PEMs. 2) In addition, general studies on cell proliferation, hADSCs attachment, and transfection were performed. 3) We studied the ability of the system to induce osteogenic stem cell differentiation by gene expression analysis and mineralization assays. Summarizing, we present a new approach to engineer a bone-ECM inspired gene-activated surface coating which allows controlling stem cells function, and consequently, represents a promising tool to develop multifunctional surface coatings for regenerative medicine strategies.

## 2. Experimental Section

### 2.1. Materials

If not stated otherwise, all chemicals were purchased from Sigma–Aldrich/Merck (Taufkirchen, Germany). Col was provided from Sichuan Mingrang Bio-Tech (Sichuan, China). The pDNA pCMV-GFP (3.5 kbp, 260 kDa) was acquired from Plasmid Factory (Bielefeld, Germany). The synthesis and characterization of the used cationic lipid OO4 was described in the authors' pre-

vious work.<sup>[55]</sup> The phospholipids DOPE, 1,2-dioleoyl-*sn*-glycero-3-phosphoethanolamine-*N*-(7-nitro-2-1,3-benzoxadiazol-4-yl) (ammonium salt) (NBD-DOPE) ( $\lambda_{\text{max}}^{\text{ex}} = 460 \text{ nm}$  and  $\lambda_{\text{max}}^{\text{em}} = 535 \text{ nm}$ ), and 1,2-dioleoyl-*sn*-glycero-3-phosphoethanolamine-*N*-(lissamine rhodamine B sulfonyl) (ammonium salt) (Rho-DOPE) ( $\lambda_{\text{max}}^{\text{ex}} = 560 \text{ nm}$  and  $\lambda_{\text{max}}^{\text{em}} = 583 \text{ nm}$ ) were acquired from Avanti Polar Lipid, Inc. (Alabaster, AL, USA).

### 2.2. Methods

#### 2.2.1. Preparation of Cationic Liposomes

For liposome preparation, lipids were separately dissolved in chloroform/methanol (8:2, v/v) as lipid stock. The stocks were combined in the desired molar ratio (OO4/DOPE 1/3 *n/n*, OO4/DOPE/Rho-DOPE 1/3/0.04 *n/n/n*, OO4/DOPE/NBD-DOPE 1/3/0.04 *n/n/n*) and the organic solvent was evaporated for 1 h at 200 mbar at a rotary evaporator. After formation of dry lipid film, a solution of 150 mM NaCl 10 mM acetic acid adjusted to pH4 was added to a final total lipid concentration of 1 mg mL<sup>-1</sup>. Afterward, the lipid dispersion was incubated at 50 °C while shaking gently for 30 min at 1400 rpm (Eppendorf Thermomixer 5436) followed by sonication at 37 kHz and 50 °C for 5 min.

#### 2.2.2. Plasmid DNA Isolation

pDNA with the human BMP-2 gene controlled by a human cytomegalovirus promoter controlled and containing a neomycin resistance gene (pCMV-BMP-2) was purchased from OriGene Technologies GmbH (Herford, Germany). It was cloned and amplified using *Escherichia coli* DH5 $\alpha$  safety strain (Invitrogen, Carlsbad, CA, USA). Plasmid purification was performed using a Plasmid Maxi Prep Kit (Qiagen, Venlo, Netherlands) according to manufacturer instructions, and the resulting pDNA (pDNA) was resuspended in MilliQ water. The pDNA concentration and

purity were measured using a UV spectrophotometer at 260 and 280 nm and gel electrophoretic analysis.

### 2.2.3. Lipoplex Formation

LPX were prepared by combining pDNA with OO4/DOPE 1/3 (*n/n*) liposomes to a N/P ratio (N = primary amines of the cationic lipids; P = phosphate groups of the nucleic acid) of 4 in sterile-filtered solution of 150 mM NaCl with 10 mM sodium acetate buffer solution (pH 4). pDNA was pipetted to the liposomes and gently mixed, followed by an incubation period of 15 min at room temperature.

### 2.2.4. Characterization of Lipoplexes and Liposomes

The size was determined by dynamic light scattering (DLS) and zeta potential by laser Doppler velocimetry (LDV) using a Zetasizer Nano ZS ZEN3600 (Malvern Panalytical, Malvern, UK) as described previously.<sup>[53]</sup> Briefly, DLS measurements at a scattering angle of 173° consist of 15 runs with a duration time of 20 s for each. For size calculations, a viscosity  $\eta = 0.8872$  mPa s and a refractive index of 1.33 were assumed. LDV was performed in a clear disposable folded capillary cell (DTS1060, Malvern Panalytical) with 30 runs at a voltage of 60 V. For data evaluation, the viscosity ( $\eta = 0.8872$  mPa s), dielectric constant ( $\epsilon = 78.5$  F m<sup>-1</sup>), and refractive index ( $n = 1.33$ ) of water were applied. Particle size distribution curves and zeta potential were calculated using Zetasizer Software 7.13 (Malvern Panalytical). All measurements were performed three times at 25 °C.

### 2.2.5. Preparation of Polyelectrolyte Multilayers

The polyelectrolyte solutions were prepared as follows: Polyethylenimine (PEI,  $M_w \approx 750$  kDa) was dissolved in 0.15 M NaCl solution to a concentration of 5 mg mL<sup>-1</sup> at pH 7.4. Cs ( $M_w \approx 25$  kDa) was dissolved in 0.15 M NaCl solution to a concentration of 0.5 mg mL<sup>-1</sup> at pH 4. Col ( $M_w \approx 100$  kDa) was dissolved in 0.2 M acetic acid to a concentration of 2 mg mL<sup>-1</sup> (stirring overnight). The final solution of Col was obtained by diluting the stock solution in 0.2 M acetic acid supplied with 0.15 M NaCl at pH 4.

PEMs were assembled on surfaces (mainly glass coverslips, but also silicon wafers) cleaned using the RCA protocol.<sup>[56]</sup> PEI was used as the first layer to obtain a positive charge on the substrate followed by adsorption of Cs as an anionic layer and afterward, Col as the cationic layer. PEMs were fabricated by immersing the glass coverslips or silicon wafers in the polyelectrolyte solution for 15 min (PEI, Cs) and 20 min (Col) and one layer of LPX for 2 h 30 min. Due to the different  $M_w$  of the polyelectrolytes, the larger Col molecules require more time for diffusion. For that reason, the adsorption time of Col was prolonged to 20 min following existing LbL protocols.<sup>[57]</sup> By alternating adsorption of Cs and Col, a basal PEM consisting of four polyelectrolyte bilayers and a final Cs layer was fabricated [Cs/Col]<sub>4</sub>Cs, followed by LPX adsorption [Cs/Col]<sub>4</sub>Cs/LPX. Last, a Cs/Col cover layer was deposited to prepare the gene-activated PEM [Cs/Col]<sub>4</sub>Cs/LPX/Cs/Col. Each adsorption step was followed by rinsing with 0.15 M NaCl solution at pH 4 (3 × 5 min).

### 2.2.6. Confocal Laser Scanning Microscopy to Study Lipid and DNA Deposition on PEM

A rhodamine-labeled lipid formulation of OO4/DOPE/Rho-DOPE 1/3/0.04 (*n/n/n*) ( $\lambda_{\text{max}}^{\text{ex}} = 560$  nm;  $\lambda_{\text{max}}^{\text{em}} = 583$  nm) and Cy5 labeled pDNA ( $\lambda_{\text{max}}^{\text{ex}} = 649$  nm;  $\lambda_{\text{max}}^{\text{em}} = 670$  nm) was used to screen for LPX deposition on the PEMs.<sup>[53]</sup> DNA was covalently tagged with Cy5 using the Label IT Nucleic Acid Labeling Kit from Mirus (Madison, WI, USA), according to the manufacturer's instructions. After production of [Cs/Col]<sub>4</sub>Cs/LPX using the fluorescence-tagged LPX, the PEM was washed three times, and the Cs/Col cover layer was deposited to obtain the final construct [Cs/Col]<sub>4</sub>Cs/LPX/Cs/Col for microscopical analysis. The films were fixed with Aquatex mounting medium (Merck, Darmstadt, Germany) and stored overnight at 7 °C to cure the mounting medium before examining the distribution of the fluorophores by confocal laser scanning microscopy (CLSM) (LSM 710, Carl Zeiss, Oberkochen, Germany).

For time dependent evaluation of DNA embedding in the PEMs, the LPX were prepared with Cy5 labeled pDNA and embedded in the PEMs. The PEMs were stored in phosphate-buffered saline (PBS) and Cy5 fluorescence was screened by CLSM at different time points using identical parameter settings for taking the micrographs. The fluorescence intensity was determined with 12 images per sample in triplicates using ImageJ.

### 2.2.7. pDNA Loading Efficiency on the PEM Studied With Gel Electrophoresis

DNA loading of PEMs was quantified by agarose gel electrophoresis using an established protocol for indirect quantification (see for visualization of method also Figure S1, Supporting Information).<sup>[48]</sup> After basal PEM [Cs/Col]<sub>4</sub>Cs preparation on coverslips in 24-well plates, the coverslips were rinsed with 0.15 M NaCl (pH 4) and then transferred into a new 24-well plate for the incubation with LPX. Various OO4/DOPE 1/3 (*n/n*) N/P 4 LPX concentrations (0.26 to 3.15  $\mu\text{g pDNA cm}^{-2}$ ) were used for incubation under gentle shaking for 2 h 30 min. Subsequently, the supernatant of each well was transferred into tubes for quantification of DNA in LPX, and PEMs were afterward washed twice with 0.15 M NaCl solution (pH 4). The washing solutions were also transferred into separate tubes for quantification of DNA in detached LPX. DNA quantification was performed by gel electrophoresis after releasing the DNA from LPX. Briefly, 50  $\mu\text{L}$  supernatant/washing solution was mixed with 10  $\mu\text{L}$  of blue/orange 6x loading dye (G190A) and 4  $\mu\text{L}$  1% heparin v/w. Heparin was used to release complexed DNA from LPX. Electrophoresis was performed on 1% agarose gel containing 0.308  $\mu\text{g mL}^{-1}$  Ethidium bromide in 1% Tris-acetate-EDTA buffer (pH 8) for 1 h at 90 V, while a 1 kb DNA ladder (G571A) (Promega, Madison, WI, USA) was used for size determination. Quantification was possible using a pDNA standard dilution series (0.01, 0.1, 0.2, 0.3, 0.5, and 0.8  $\mu\text{g pDNA}$ ) to obtain a calibration curve. The fluorescent DNA bands were quantified with a UVP UVsolo touch (Analytik Jena AG, Jena, Germany) for imaging and the software Vision-Works LS Analysis Software from Analytik Jena AG for fluorescence signal quantification. All samples were tested in triplicates. The sensitivity of the used method was <0.015 mg cm<sup>-2</sup>.

### 2.2.8. Quartz Crystal Microbalance With Dissipation Monitoring

A Q-Sense Pro quartz-crystal microbalance with dissipation monitoring (QCM-D, Biolin Scientific, Gothenburg, Sweden) was used to monitor LPX deposition on PEMs in detail. Freshly cleaned gold-coated 5 MHz AT-cut quartz crystal sensors (QSX301 Gold, Q-Sense) were used as substrate for the build-up of the PEM thin films. The solutions were injected into a flow chamber with a mounted quartz crystal at a constant flow rate of 50 mL min<sup>-1</sup>. The quartz crystal was excited at multiple overtones (1st, 3rd, 5th, 7th, 9th, 11th, and 13th, corresponding to 5, 15, 25, 35, 45, 55, and 65 MHz, respectively) and shifts in frequency ( $\Delta f_n$ ) and energy dissipation ( $\Delta D$ ) were monitored in real-time. The frequency of each overtone was normalized to the fundamental resonant frequency of the quartz crystal substrate ( $\Delta f_n/n$ , in which  $n$  denotes the overtone number). An adsorption time of 6 min for each polyelectrolyte layer and an intermediate rinsing step of 4 min with acetate buffer 0.1 M pH 5.5 were established. LPX solution was injected and measured for 2 h in steady state without a constant flow to mimic deposition conditions of the film preparation mentioned above. The hydrodynamic thickness of the PEMs at each deposition cycle as well as at the end of the deposition cycles was estimated using the Voigt-based viscoelastic model implemented in the Q-Sense Dfnd software (Broadfit function), assuming a fluid density of 1000 kg m<sup>-3</sup>, a layer density of 1000 kg m<sup>-3</sup>, and a fluid viscosity of 1 mPa s.

### 2.2.9. Water Contact Angle Measurements

Static water contact angle (WCA) measurements were analyzed at room temperature using an OCA15+ device from Dataphysics (Filderstadt, Germany). The sessile drop method was applied using 1  $\mu$ L of water with the Ellipse-fitting method. Reported contact angles represent mean values and standard deviation of five measurements per sample of duplicates.

### 2.2.10. Atomic Force Microscopy

Atomic force microscopy (AFM, Nanowizard IV, JPK-Instruments, Berlin, Germany) in combination with an inverted fluorescence microscope (Olympus IX71, Olympus, Olympus Europa, Hamburg, Germany) was performed in quantitative imaging mode (QI) to investigate the surface roughness and topography as well as record corresponding fluorescence images. Topographical images were recorded using a silicon cantilever (qp-BioT, Nanosensors, Neuchatel, Switzerland) in a standard liquid cell (JPK-Instruments) containing 0.15 M NaCl solution. A force map area of 5  $\times$  5  $\mu$ m<sup>2</sup> was recorded with a resolution of 512  $\times$  512 pixel<sup>2</sup>. Post-processing and roughness analysis were performed using the software JPK Data Processing V5.0.85 and Gwyddion (Gwyddion V2.58, 64-bit).

### 2.2.11. Fluorescence Recovery After Photobleaching

FRAP (fluorescence recovery after photobleaching) experiments using CLSM were performed to evaluate the LPX mobility in the PEM. This technique was developed by Axelrod et al. (1976) as a

method to study mobility of substances for example proteins.<sup>[58]</sup> In FRAP, a specific area is photobleached by intense laser light, removing fluorescence from this area, and screening afterward, the degree of fluorescence reappearance in this region. The used fluorophore for this study was NBD-DOPE. The fluorophore was used to prepare fluorescence tagged liposomes (OO4/DOPE/NBD-DOPE 1/3/0.04 n/n/n) which were applied for LPX formation with pCMV-GFP. The fluorescence tagged LPX were adsorbed to [Cs/Col]<sub>4</sub>Cs basal PEMs for 2 h 30 min. The LPX-loaded PEM was finalized with an additional cover layer of Cs/Col to [Cs/Col]<sub>4</sub>Cs/LPX/Cs/Col. FRAP studies of NBD-LPX loaded PEMs were performed using an LSM 710 confocal microscope. A magnification of 40x with an oil objective was used for that experiment. A defined area in the PEM was photobleached (laser 488 nm, 20 cycles with a laser line attenuator transmission 100%). After defined periods of time, the area was examined for NBD-fluorescence using the same setup parameters. Images were processed with the ZEN2012 software (Carl Zeiss). The analysis of images to quantify RFU was performed with Image J.

### 2.2.12. Cell Culture

Cryopreserved hADSCs (StemPro) were obtained from Thermo Fisher Scientific (Waltham, MA, USA) and thawed and grown in Dulbecco's modified Eafless medium (DMEM) supplemented with 10% fetal bovine serum (FBS) and 1% antibiotic and antifungal solution at 37 °C (basal culture medium, BM) in a humidified 5% CO<sub>2</sub>/95% air atmosphere. Cells of almost confluent cultures were washed once with sterile PBS followed by treatment with 0.25% trypsin/0.02% EDTA at 37 °C for 3 min. Trypsin was neutralized with DMEM with 10% FBS, and the cells were resuspended in DMEM after centrifugation at 250  $\times$  g for 5 min. Last, the cells were seeded on PEMs-coated glass coverslips with a cell density of 1  $\times$  10<sup>5</sup> cells per mL. Cells used in this study were from passage P1-P6, and 50% of the culture media was changed three times a week.

For the purpose of osteogenic differentiation experiments, the pDNA pCMV-BMP2, which encodes for BMP-2, was used for LPX preparation. After the cells had reached 90% confluence, the medium was changed to induce the osteogenic differentiation. The cells were cultured in the osteogenic induction medium (OM) containing 0.1  $\mu$ M Dex, 10 mM sodium  $\beta$ -glycerophosphate ( $\beta$ -Gly), and 0.05 mM ascorbic acid-2-phosphate (ASC), in addition to BM as described above. For the positive control, the StemPro Osteogenic-Differentiation Kit from Thermo Fisher Scientific (Waltham, MA, USA) was used according to the manufacturer's protocol. This medium contains components and cytokines for an optimized osteogenic differentiation of hADSCs and other stem cells provided by the supplier. As negative control group, the cells received BM. In addition, hADSCs cultured on [Cs/Col]<sub>6</sub> in OM were used as LPX-free positive control. The cells were incubated for 24 or 28 days and medium was changed once a week. All samples were tested for mineralization and gene expression of osteogenic markers (see below).

### 2.2.13. Cell Adhesion Studies

Glass coverslips were coated with different PEMs composites: [Cs/Col]<sub>6</sub> (LPX free system), [Cs/Col]<sub>4</sub>Cs/LPX (system with LPX

on surface), and [Cs/Col]<sub>4</sub>Cs/LPX/Cs/Col/ (final LPX loaded PEM); placed in 24 well plates, hADSCs were seeded on the samples in DMEM at 37 °C for 4 h. Then, cells attached to PEMs were fixed with 4% paraformaldehyde solution for 10 min and rinsed twice with PBS for further studies. Cells were permeabilized with 0.1% Triton X-100 in PBS v/v (Sigma) for 10 min, rinsed with PBS, and nonspecific binding sites were blocked by incubation with 1% w/v bovine serum albumin (BSA, Merck, Darmstadt, Germany) in PBS at room temperature for 1 h. Vinculin was stained using monoclonal anti-vinculin clone hVIN-1 mouse ascites fluid antibody (1:200, Sigma–Aldrich, Germany); and a secondary goat anti-mouse IgG, Alexa Fluor 647 (1:1000,  $\lambda^{\text{ex}}_{\text{max}} = 650$  nm and  $\lambda^{\text{em}}_{\text{max}} = 583$  nm, Thermo Fisher Scientific, Waltham, MA, USA). The actin cytoskeleton was stained with phalloidin-Atto 488 (1:50,  $\lambda^{\text{ex}}_{\text{max}} = 500$  nm and  $\lambda^{\text{em}}_{\text{max}} = 520$  nm, Sigma–Aldrich, Germany) at room temperature for 30 min. Cell nuclei were stained by BOBO-1 Iodide (1:200,  $\lambda^{\text{ex}}_{\text{max}} = 462$  nm and  $\lambda^{\text{em}}_{\text{max}} = 481$  nm, Invitrogen, Darmstadt, Germany), incubating the samples for 30 min. Before microscopic evaluation, samples were washed with PBS and mounted with Roti-Mount FluorCare (Carl Roth GmbH, Karlsruhe, Germany). Fluorescence micrographs were taken with a LSM 710 confocal microscope using 10 $\times$ , 20 $\times$  objectives for cell adhesion and spreading analysis. A 63 $\times$  oil immersion objective was used to visualize nuclei, actin cytoskeleton, and focal adhesions. Images were processed with the ZEN2012 software (Carl Zeiss). The analysis of images to quantify cell count and cell area was performed with Image J.

#### 2.2.14. Cell Proliferation Studies With QBlue Cell Viability Assay

hADSC cells were seeded on LPX-loaded PEMs with and without cover layer: [Cs/Col]<sub>4</sub>Cs/LPX; [Cs/Col]<sub>4</sub>Cs/LPX/Cs/Col. Cells seeded on clean glass coverslip and the LPX-free PEMs [Cs/Col]<sub>6</sub> were used as controls. Cultures were incubated at 37 °C for 24 h, 2 and 4 days, respectively. After the incubation time, the cell viability was determined by QBlue cell viability assay kit (Biochain, Hayward, NJ, USA). The cells were washed once with PBS to remove the medium. Then, 500  $\mu$ L of Qblue solution with colorless medium (10:1) was added to each well and incubated at 37 °C for 3 h. Finally, 100  $\mu$ L of supernatant from each sample was added to a black 96 well plate and the fluorescence intensity was measured at 544 nm excitation and 590 nm emission with plate reader (FLUOstar Omega, BMG Labtech, Ortenberg, Germany). All samples were tested in triplicates.

#### 2.2.15. DNA Uptake Into Stem Cells

To visualize the DNA uptake from LPX-loaded PEMs, we prepared fluorescence-tagged LPX using Cy-5 ( $\lambda^{\text{ex}}_{\text{max}} = 649$  nm and  $\lambda^{\text{em}}_{\text{max}} = 666$  nm) labeled pDNA-GFP (Label IT Nucleic Acid Labeling Reagents, pDNA-GFP labeled according to manufacturer's instructions) for the LPX preparation. After hADSCs were cultured for 48 h on the [Cs/Col]<sub>4</sub>Cs/LPX/Cs/Col coating, cells were screened for Cy-5 positive structures while additional staining of nuclei and actin was performed for visualization of intracellular distribution of pDNA-GFP. For this purpose, the cells were fixed, permeabilized, and blocked as described above. The

order of cell staining was designed as follows: a) Phalloidin-Atto 488 (1:50) for staining filamentous actin and b) BOBO-1 (1:200) for staining the nucleus. All dyes were incubated for 30 min at room temperature and protected from light. PBS washing (three times, each 5 min) was performed after incubation with fluorescent dyes. Afterward, all samples were briefly washed with ultrapure water and mounted with Mowiol 4–88 containing 25 mg mL<sup>-1</sup> 1,4-diazabicyclo [2.2.2]-octane (Carl Roth GmbH, Karlsruhe, Germany), a mounting medium providing high fluorescence stability for storage at 4 °C in the dark. Samples were analyzed with a LSM 710 confocal microscope.

#### 2.2.16. Flow Cytometry Measurements to Determine the Reporter Gene Expression

Cells with a cell density of  $1 \times 10^5$  cells per mL were seeded on PEMs containing pDNA-GFP encapsulating LPX. After an incubation period of 24 h at 37 °C and 5% CO<sub>2</sub>, the expression of the reporter gene encoding for green fluorescent protein (GFP) was measured by flow cytometry. Briefly, cells were detached with 0.05% trypsin/0.02% EDTA solution from the PEMs and centrifuged at 220  $\times g$  for 5 min, rinsed, and re-suspended in 500  $\mu$ L of PBS containing 1% BSA. A BD Accuri C6 Plus flow cytometer (BD Bioscience, Franklin Lakes, NJ, USA) was used to analyze 10 000 cells per sample for GFP expression quantifying the relative fluorescence (GFP:  $\lambda^{\text{ex}}_{\text{max}} = 488$  nm and  $\lambda^{\text{em}}_{\text{max}} = 510$  nm). Single cells were gated by size (FSC-H) and granularity (SSC). The calculated single cell population was gated to detect GFP-expressing by calculating the relative number of transfected cells and dead cells. The BD Accuri C6 Software was used for all data evaluation. All samples were tested in duplicate.

#### 2.2.17. Mineralization Experiments

**Alizarin-Red-Assay:** After 24 days of the osteogenic differentiation experiments, calcium phosphate deposition was investigated by Alizarin Red S staining. Briefly, the samples were washed once with PBS and fixed with 4% paraformaldehyde for 10 min. After washing twice with distilled water, Alizarin Red S (2%, pH 4.2, Roth) solution was added into each well and incubated for 45 min under light exclusion at room temperature. Last, the excess dye was removed by washing with distilled water. Images were taken in transmission mode with a Nikon ECLIPSE Ti2, Tokyo, Japan equipped with a CCD camera (DCIN, Tokyo, Japan).

**OsteoImage Kit:** The commercial mineralization kit (OsteoImage, Lonza) was used to visualize the hydroxyapatite portion of bone-like nodules deposited by cells by measuring fluorescence measurement ( $\lambda^{\text{ex}}_{\text{max}} = 495$  nm and  $\lambda^{\text{em}}_{\text{max}} = 519$  nm). This assay, as described by the manufacturer, uses a fluorescent staining reagent that binds specifically to the hydroxyapatite portion of the biomaterialized structures. The intensity of the green fluorescence is proportional to the amount of hydroxyapatite in the sample. After 24 days of the osteogenic differentiation, samples were incubated with OsteoImage according to the manufacturer's instructions and examined with a LSM 710 confocal microscope.

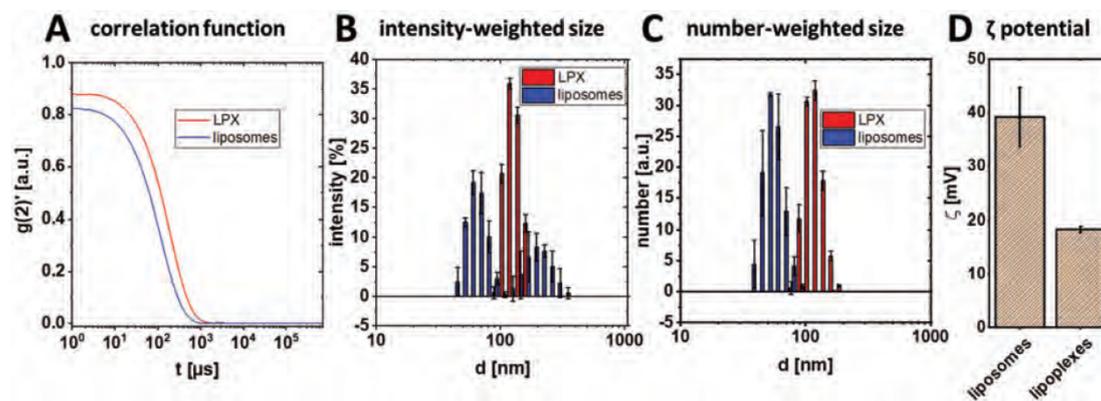


**Figure 2.** Correlation functions (representative of three measurements) A) of DLS measurements and the resulting B) intensity-weighted and C) number-weighted size distribution curves of OO4/DOPE liposomes (blue line) and LPX (0.1  $\mu\text{g}$  pDNA, N/P 4) (red line) in 0.15 M NaCl containing 10 mM sodium acetate buffer at pH 4. D) Zeta potential results of OO4/DOPE liposomes and LPX. Results are means and standard deviations of three measurements (B–D).

### 2.2.18. Gene Expression Analysis

After 28 days of differentiation, the mRNA was extracted from samples using Aurum Total RNA Mini Kit spin columns from BioRad (Hercules, CA, USA) according to the manufacturer's recommended procedure. First, strand cDNA was synthesized using an iScript Advanced cDNA Synthesis Kit for RT-qPCR (real-time quantitative polymerase chain reaction, Biorad) in 20  $\mu\text{L}$  reactions, according to the manufacturer's instructions. A CFX Connect RT-qPCR Detection System (Biorad) and pre validated primer sets PrimePCR Probe Assays from Biorad were used for gene expression analysis of the transcription factor Noggin (assay ID: qHsaCEP0054879), Collagen type 1 alpha 1 (Col1A1; assay ID: qHsaCEP0050510), Run-related transcription factor 2 (RunX2; assay ID: qHsaCEP0051329), Alkaline Phosphatase (ALP; assay ID: qHsaCEP0024224), and BMP-2 (assay ID: qHsaCEP0029912). RPLP0 (assay ID: qHsaCEP0041375) was used as housekeeping gene. Data analysis was performed using the BioRad CFX Manager Software 3.0. The following scheme was used for the RT-qPCR: 95  $^{\circ}\text{C}$  for 30 s followed by 39 cycles at 95  $^{\circ}\text{C}$  for 15 s and 60  $^{\circ}\text{C}$  for 30 s. The relative expression levels of each gene were calculated and normalized to the housekeeping gene RPLP0 using the DDGt method ( $2^{-\Delta\Delta\text{Ct}}$ ).<sup>[59]</sup>

### 2.2.19. Statistical Analysis

All statistical analyses were performed with Origin 8G software. If not stated otherwise, experiments were performed in triplicates ( $n = 3$ ) and the results presented as means  $\pm$  standard deviation (SD). If the number of experiments  $n$  was different from 3, the value of  $n$  was given in the caption. Analysis of significance was performed by one-way ANOVA followed by Scheffé post hoc test with  $\alpha = 0.05$ . A value of  $p < 0.05$  was considered as a significant difference and was indicated by an asterisk. Further, box plots are shown where appropriate. The box indicates the 25th and 75th

percentiles, the median (dash), and mean value (black square), respectively.

## 3. Results and Discussion

### 3.1. Characterization of Lipoplexes

The lipid formulation OO4/DOPE 1/3 ( $n/n$ ) (hereinafter referred to as OO4/DOPE) was used to prepare LPX as transfection active component for the gene-activated surface coating. OO4 is a cationic peptide-mimicking amphiphile designed in our group<sup>[43,55]</sup> and provided the positive charge for DNA complexation as well as PEMs assembly. DOPE is a commonly used co-lipid for lipid-based transfection agents. For efficient immobilization of LPX into PEMs via electrostatic interaction, a positive net charge was essential. DLS and zeta potential measurements were carried out to obtain information on particle size and charge of OO4/DOPE liposomes and, more substantially, of LPX under IBL preparation conditions. The data are presented in Figure 2. The autocorrelation function (Figure 2A) was characterized by intercepts at 0.9 for LPX (red) and 0.8 for liposomes (blue), a sigmoidal decay of the signal and the absence of a noisy baseline, indicating a good quality of DLS data for reasonable fitting. For the liposomes, the intensity-weighted size distribution showed a bimodal function, with a particle size population at diameter ( $d$ )  $\approx$  50–100 nm and  $d \approx$  200–400 nm (Figure 2B). For multimodal size distributions, the intensity-weighted curve can be misleading because the scattering intensity is proportional to  $d^6$ . Hence, small numbers of larger particles can dominate the distribution function. Therefore, the number-weighted size distribution curves were calculated (Figure 2C), showing that the 50–100 nm population was in a much higher quantity than expected from the intensity-weighted curve (compare blue size distribution curves). In contrast, LPX showed an unimodal size distribution with  $d \approx$  100–200 nm, in both intensity- and number-weighted curves (Figure 2B,C). The observed changes in particle size of LPX, compared to the liposomes, are probably due to the lipid

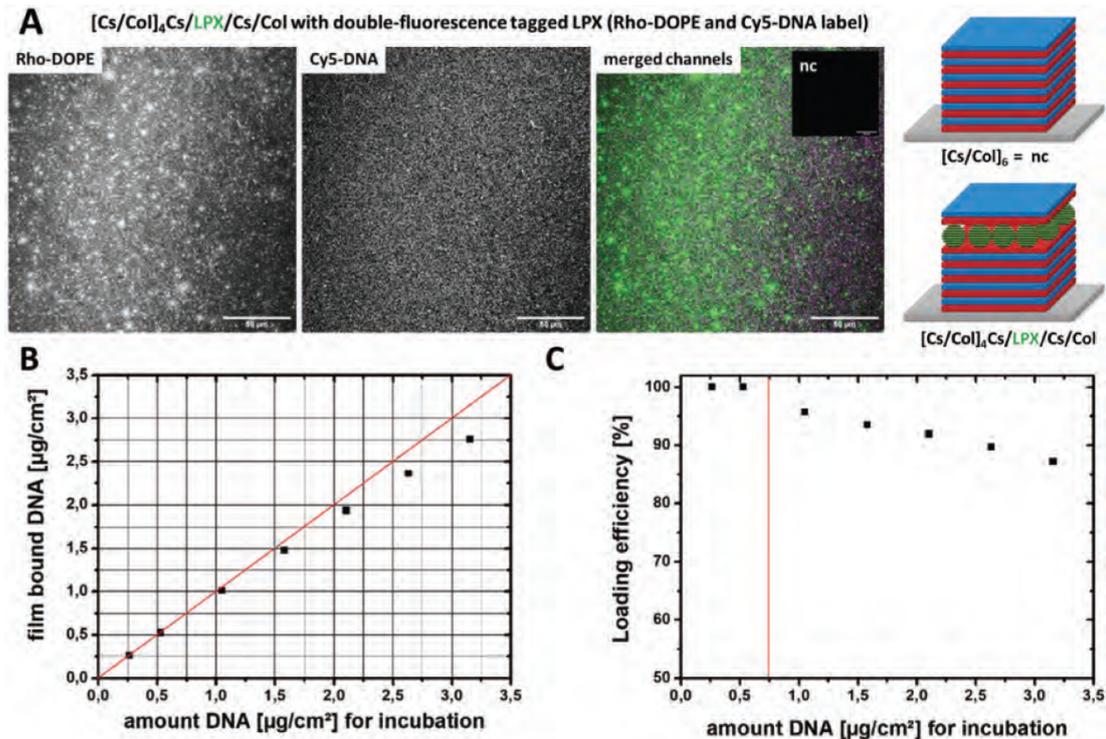


**Figure 3.** A) CLSM micrograph (40 $\times$  magnification) of [Cs/Col]<sub>4</sub>Cs/LPX/Cs/Col PEMs with fluorescently tagged LPX. The following fluorescence labels were used: Rho-DOPE as lipid label (left image in grey scale, green in the merged right image) and Cy5-labeled pDNA (middle image grey scale, magenta in the merged image right), which were used to visualize LPX attached to the PEMs. The inset on the merged image (right), labeled with nc = negative control, was the LPX-free negative control [Cs/Col]<sub>6</sub>, which was examined under the same conditions as proof for the absence of auto-fluorescence effects of the polyelectrolytes. The scale bars indicate 50  $\mu\text{m}$ . Images were analyzed using ImageJ. B) Schematic illustration of the PEM sequence codes [Cs/Col]<sub>4</sub>Cs/LPX/Cs/Col (sample) and [Cs/Col]<sub>6</sub> (negative control). C) Film-bound amount of DNA in  $\mu\text{g}/\text{cm}^2$  in [Cs/Col]<sub>4</sub>Cs/LPX/Cs/Col films as a function of the total DNA concentrations in the incubation medium (0.26–3.15  $\mu\text{g}/\text{cm}^2$  LbL substrate). The calculation of the film-bound DNA was based on the indirect quantification of the non-bound DNA using agarose gel experiments presented in Figure S2, Supporting Information (n = 3). The red line shows the theoretical values of 100% binding efficiency. D) The calculated DNA loading efficiency from (C). Above is an LPX incubation with total DNA amount of  $0.75 \mu\text{g}/\text{cm}^2$  PEM substrate (indicated by the red line); the loading efficiency decreases below 100%. (B,D) show the means  $\pm$  SD of triplicates. The bars indicate that the SD are below  $0.04 \mu\text{g}/\text{cm}^2$ ; and therefore, are not seen due to resolution of the graphs.

membrane reorganization process during the complex formation between DNA and the cationic liposomes, based on the templating effect of DNA.<sup>[60,61]</sup> Comparing zeta potential measurements of liposomes and LPX, a decrease in the zeta potential from  $\zeta \approx 38 \text{ mV}$  to  $\zeta \approx 18 \text{ mV}$  was observed (Figure 2D) due to complex formation between the positively charged liposomes and the negatively charged DNA. Nevertheless, the positive net charge of the LPX for embedding into PEMs was proven.

### 3.2. Structural Characterization of PEMs with Focus on LPX Embedding

The embedding of LPX into PEMs composed of Cs and Col was demonstrated by CLSM using dual fluorescence-tagged LPX: The pDNA was covalently labeled with Cy5 and the lipid composite was modified with 1.25-mol% Rho-DOPE as fluorescence

label (Figure 3A). The images indicate a homogeneous distribution of the labeled DNA as well as the lipid in the PEM [Cs/Col]<sub>4</sub>Cs/LPX/Cs/Col, considering the film curvature which leads to out-of-focus effects in the edge regions. Nevertheless, both channels do not fit in all details (merged images Figure 3A), an observation which can be explained by the fact that at a lipid-DNA loading ratio of N/P 4, some DNA-free cationic liposomes exist besides LPX.<sup>[62]</sup> The LPX-free control [Cs/Col]<sub>6</sub> (Figure 3A, insert labeled with nc = negative control) shows no autofluorescence of the polyelectrolytes using the same experimental setup.

The DNA loading efficiency of [Cs/Col]<sub>4</sub>Cs/LPX/Cs/Col films was determined in more detail. It was not possible to quantify DNA embedded in PEMs directly by gel electrophoresis or fluorescence passed assays in a reproducible manner. The appearance of colloids after disintegration of LPX-loaded PEMs, resulting in quenching and light-scattering effects,<sup>[63]</sup> may explain this problem. Recently, we described a method for an indirect

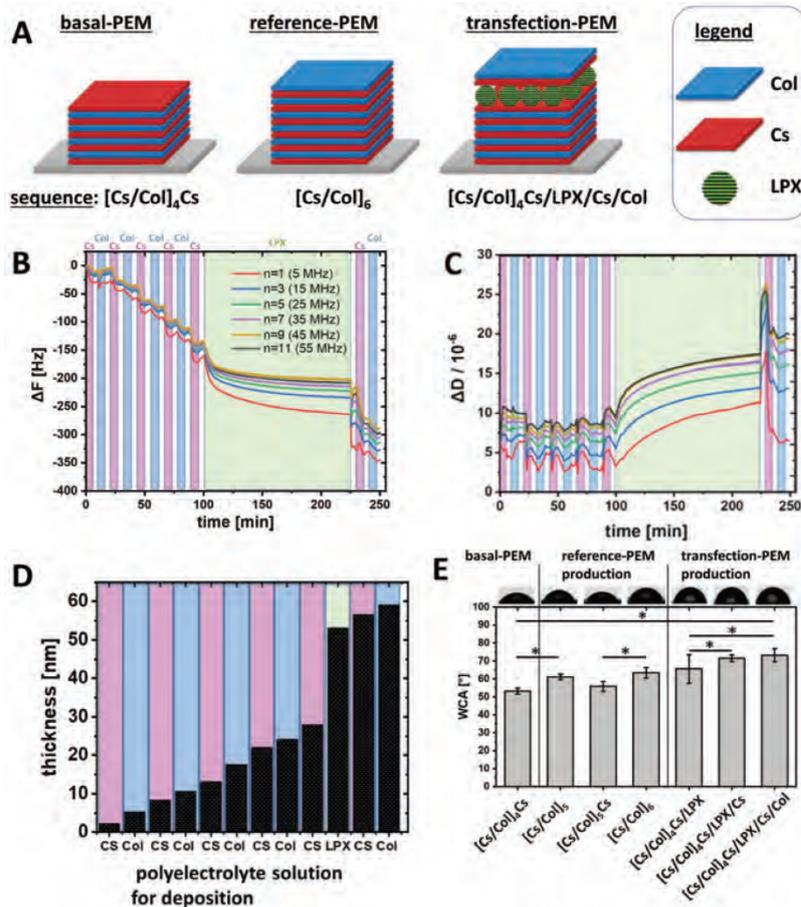


**Figure 4.** A) Schematic illustration of the LBL sequence codes of investigated PEMs. B–D) Build-up of  $[\text{Cs}/\text{Col}]_4\text{Cs}/\text{LPX}/\text{Cs}/\text{Col}$  multilayered thin films onto Au-plated quartz crystal sensors via incubation with polyelectrolyte solutions to achieve LBL deposition. QCM-D monitoring of the normalized frequency ( $\Delta F$ , panel B) and dissipation ( $\Delta D$ , panel C) shifts. The frequency shifts of different overtones are presented. The dissipation shift is shown for the 7th overtone (35 MHz). The background color indicates the incubation/washing medium: magenta = Cs; blue = Col; green = LPX; white = washing buffer (B, C). Cumulative hydrodynamic thickness evolution for the  $[\text{Cs}/\text{Col}]_4\text{Cs}/\text{LPX}/\text{Cs}/\text{Col}$  PEM production, obtained using the Voigt-based viscoelastic model (D). E) Static WCA measurement of intermediate and final PEM structures. The x-axis demonstrates the film composition deposited as sequence code. Results represent means  $\pm$  SD with  $n = 10$ ; significance was tested using one-way ANOVA followed by Scheffé post hoc test,  $\alpha = 0.05$ ,  $*p \leq 0.05$ .

quantification of DNA-LPX loading into PEMs by quantifying the fraction of DNA which was not incorporated in PEMs.<sup>148</sup> For this purpose, the DNA of the supernatant and washing solutions, which was most likely complexed in LPX, was quantified via gel electrophoresis, a method which needed a pre-incubation with heparin to release all DNA from LPX (for details, see Figures S1 and S2, Supporting Information). The results are presented in Figure 3B,C. The incorporation of different amounts of DNA, from 0.26 to 3.15  $\mu\text{g cm}^{-2}$ , was evaluated. Up to a loading amount of  $\approx 0.75 \mu\text{g cm}^{-2}$ , the LPX can be efficiently incorporated into the LBL system (loading efficiency of 100%, Figure 3C). PEMs with concentrations above 0.75  $\mu\text{g cm}^{-2}$  resulted in loading efficien-

cies below 100% (Figure 3C). In other studies on polyplex-loaded PEMs, a much lower DNA content of 25–30  $\text{ng cm}^{-2}$  was described, showing that PEMs consisting of Cs and Col and loaded with LPX represent an excellent system for gene-activated PEMs.<sup>64</sup> To evaluate whether LPX are desorbed from the PEM during subsequent rinsing steps, the washing solutions were also examined for DNA content, showing no burst release of adsorbed LPX or released DNA from the PEMs (for details, see Figure S2, Supporting Information).

QCM-D measurements were performed to monitor the material deposition during the LBL assembly process in situ. In Figure 4B, the frequency shift of different overtones is plotted.

The stepwise decrease of  $\Delta F$  indicates the successful deposition of material, Cs, Col, or LPX, respectively, after each incubation step. Multilayer growth was thus proven for each deposition step. The interaction of the charged biopolymer or LPX with the oppositely charged surface was effective under the chosen assembly conditions with a pH value of 4 and 150 mM NaCl as electrolyte solution. The time to reach the adsorption equilibrium was much longer for LPX when compared to Cs and Col. Nevertheless, the time periods needed for deposition provide evidence that we reached the adsorption equilibrium with the PEM preparation protocol used in this study (Section 2.2.5). The following rinsing step did not result in an increase of  $\Delta F$ ; thus, excluding the eventual desorption of adsorbed LPX. The evaluation of the dissipation changes demonstrated a pronounced increase in  $\Delta D$  during LPX adsorption (Figure 4C, green area). Obviously, the plastic proportion in the viscoelastic behavior increased, concluding that the PEM gets softer and more hydrated due to the adsorption of LPX. The high  $\Delta D$  value remained also after the deposition of the Cs and Col cover layers on the PEM film (final sequence [Cs/Col]<sub>4</sub>Cs/LPX/Cs/Col). Obviously, the LPX dominated the film mechanics even with the outermost Cs/Col layers. Previous structural investigation has demonstrated that the LPX composed of OO4/DOPE are soft matter nanoparticles with a liquid crystalline substructure;<sup>651</sup> consequently, a viscoelastic behaviour was expected. Furthermore, the cumulative hydrodynamic thickness evolution during the construction of the multilayer film was calculated from QCM-D data (Figure 4D). A linear increase of thickness was observed for the deposition of either Cs or Col. The thickness increase of  $\approx 30$  nm after LPX deposition was much higher compared to the biopolymers. Nevertheless, the DLS size distribution curves (Figure 2B,C) resulted in a main LPX diameter of 100–150 nm, a much higher value. Two facts may explain the discrepancy: 1) The LPX do not cover the whole area (we have evidence for that conclusion from CLSM micrographs; see also Figure 3A) combined with the fact that the QCM-D determined thickness is a mean thickness. 2) As mentioned above, LPX are soft matter nanoparticles, and a deformation and flattening of the LPX nanoparticles after adsorption on the surface can be expected.

The wetting behaviour of surfaces is an important parameter because moderate wettable surfaces with WCA  $\approx 60^\circ$  promote protein adsorption and cell adhesion.<sup>661</sup> Figure 4E shows the WCA of selected intermediates and the final construct of the DNA-activated PEM and the LPX-free reference PEM of comparable layer number. Starting from the basal-PEM [Cs/Col]<sub>4</sub>Cs, which was the substrate for the LPX adsorption, a WCA of  $\approx 53^\circ$  was measured, indicating a moderate wettability related to the presence of Cs as more hydrophilic molecule with carboxylic and sulfate groups.<sup>671</sup> When LbL was continued with Col adsorption (sequences [Cs/Col]<sub>5</sub>), a WCA of  $\approx 61^\circ$  was detected, which is related to additional presence of amino groups in the protein which are less wettable than anionic groups. The alternating WCA lower for anionic Cs and higher for Col terminal layers indicates the dominance of these molecules in the outermost layer of PEMs.

The adsorption of LPX (PEMs sequence [Cs/Col]<sub>4</sub>Cs/LPX) resulted in an increase of WCA to  $\approx 66^\circ$  compared to the previous WCA of  $\approx 53^\circ$  terminal Cs layer which is related to the cationic nature of the LPX. A further coating with Cs (PEM se-

quence [Cs/Col]<sub>4</sub>Cs/LPX/Cs) caused an increase of WCA to  $72^\circ$  which may be related to some structural rearrangements of LPX upon contact with Cs which may be related to the presence of hydrophobic parts of lipid species, observed also in a previous study with liposomes.<sup>1531</sup> The terminal Col coating [Cs/Col]<sub>4</sub>Cs/LPX/Cs/Col resulted in no significant change in WCA ( $\approx 73^\circ$ ) which indicates some intermingling of LPX layer with Cs and Col in the terminal layer related also to the much larger size of LPX compared to both polyelectrolytes.<sup>1541</sup>

AFM was performed to study the surface topography and mechanical properties of the different PEMs (Figure 5). To investigate the elasticity and the force curve, the samples were compressed by the AFM tip and the force mapping mode was applied while the tip scanned a specific area of the sample.<sup>681</sup> The force mapping mode measured the interaction forces such as adhesion or electrostatics and gives an idea regarding the stiffness and topography. The interest in testing mechanical properties and topography of surface coatings is related to their effect on cell behavior, such as spreading, proliferation, and differentiation.<sup>69,701</sup> In addition, intermediate LbL process steps were investigated to learn more about the LPX deposition and the embedding process. The basal-PEM [Cs/Col]<sub>4</sub>Cs, which was the substrate for LPX adsorption, showed a homogeneous nanofibrous network that can be assigned to Col deposition and fibrillation with a roughness of  $\approx 12$  nm (Figure 5A, Table 1). Previous studies demonstrated that Col/Cs PEMs are characterized by a fibrillary structure of Col.<sup>157,67,711</sup> Due to its high charge density, Cs is known to promote the Col self-assembly to fibrils.<sup>1721</sup> After the adsorption of LPX, the surface topography changed showing a less organized fibrillary substructure (Figure 5B) but an increase of the roughness  $\approx 23$  nm (Table 1). Diffuse structures of different sizes were observed for the [Cs/Col]<sub>4</sub>Cs/LPX film. In addition, the remaining fibrous structures appeared with a larger thickness of higher variability and more extended smeared structures (Figure 5B, arrowhead). The addition of a covering Cs layer induced the reappearance of the fibrillary topography with a roughness of  $\approx 15$  nm (Figure 5C, Table 1). The final DNA activated PEMs [Cs/Col]<sub>4</sub>Cs/LPX/Cs/Col was characterized by an extended fibrillar structure, comparable to the basal-PEM (compare Figure 5A with Figure 5D; Figure S3, Supporting Information). The addition of the soft matter nanoparticles such as LPX might modify the arrangement of the Col fibers and it can influence the roughness. The behavior is also expressed by the roughness parameters shown in Table 1.  $R_a$  and  $R_q$  increased after LPX adsorption ([Cs/Col]<sub>4</sub>Cs  $\rightarrow$  [Cs/Col]<sub>4</sub>Cs/LPX) but decreased again to the initial values for the full PEMs. The same tendency can be seen in the waviness parameters  $R3z$  ISO,  $W_a$ , and  $W_q$  (Table S1, Supporting Information).

Figure 5E presents the  $E_0$  modulus distribution curves of the highest and lower points in the measured area. The sequence [Cs/Col]<sub>4</sub>Cs was characterized by a broad distribution with a maximum value at  $E_0 = 199$  kPa while a minimum value was seen above 50 kPa. The mechanical properties of the basal layer show the Col fibers with higher stiffness (maximum) than the surrounding area (minimum). It is known that highly negatively charged polysaccharides such as Cs have interfusing characteristics in PEMs and can act as a cross-linker for Col, supporting also the organization of fibrils and making these areas of PEMs stiffer.<sup>1531</sup> The adsorption of LPX reduced the stiffness of

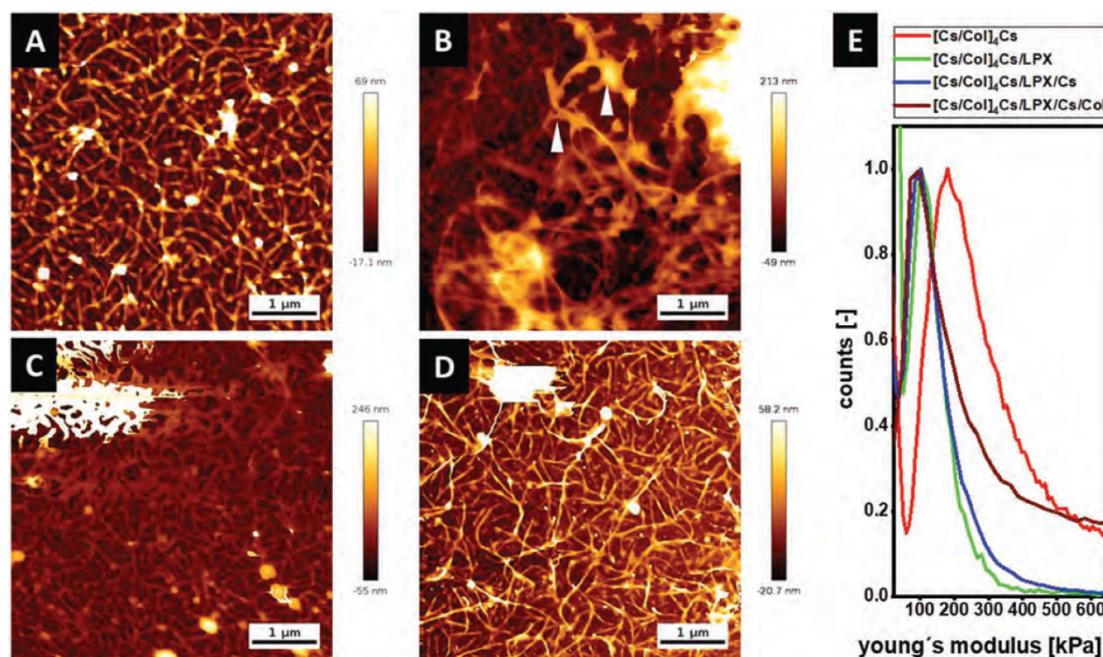


**Figure 5.** A–D) Topography images  $[\text{Cs/Col}]_4\text{Cs}$  (A),  $[\text{Cs/Col}]_4\text{Cs/LPX}$  (B),  $[\text{Cs/Col}]_4\text{Cs/LPX/Cs}$  (C), and  $[\text{Cs/Col}]_4\text{Cs/LPX/Cs/Col}$  determined by AFM [Scale bar  $1\ \mu\text{m}$ ] (D). E) Distribution curves of Young's modulus ( $E_0$ ) with a force map of a defined area (see also Figure S4, Supporting Information).

**Table 1.** Roughness parameters of area mean roughness ( $R_a$ ), area root mean squared roughness ( $R_q$ ) of PEMs sequences before and after LPX deposition. 1D roughness analysis, according to DIN EN ISO 4287, 4288, 3274, mean values  $\pm$  SD calculated from ten separate lines,  $l_n = 5\ \mu\text{m}$ ,  $D_c = 1\ \mu\text{m}$ , cutoff filter: 0.02 measured by AFM.

	$R_a$ [nm]	$R_q$ [nm]	$E$ modulus [kPa]
$[\text{Cs/Col}]_4\text{Cs}$	$9.6 \pm 0.9$	$12.2 \pm 1.3$	$199.5 \pm 6.3$
$[\text{Cs/Col}]_4\text{Cs/LPX}$	$18.6 \pm 2.7$	$23.5 \pm 3.3$	$111 \pm 3.1$
$[\text{Cs/Col}]_4\text{Cs/LPX/Cs}$	$12.0 \pm 1.8$	$15.5 \pm 2.4$	$103 \pm 3.5$
$[\text{Cs/Col}]_4\text{Cs/LPX/Cs/Col}$	$9.4 \pm 1$	$12.8 \pm 1.8$	$98 \pm 4.5$

the PEMs showing a shift of  $E_0$  distribution curve to a maximum value of 111 kPa for  $[\text{Cs/Col}]_4\text{Cs/LPX}$ . An explanation is that LPX represent liquid crystalline soft matter particles, which can reduce the stiffness.<sup>[65]</sup> It is interesting to note that further adsorption of Cs, and then, Col caused a further decrease of  $E_0$  to 103 and 98 kPa, respectively.<sup>[73]</sup> Furthermore, this observation is also in line with the effect of the LPX observed for the  $\Delta D$  values discussed in the QCM-D section above.

In summary of WCA and AFM studies, the complete PEMs  $[\text{Cs/Col}]_4\text{Cs/LPX/Cs/Col}$  is characterized by moderate wettability

and a higher roughness promoting cell adhesion.<sup>[74]</sup> What's more, a decrease in the stiffness of PEM was observed when LPX and the additional Cs/Col bilayer were added; the observed  $E$  modulus in the range of 100 kPa was still supporting cell attachment and spreading as found in other studies.<sup>[69]</sup>

### 3.3. Mobility of LPX Incorporated in PEMs

Potential time dependent changes of the LPX layer in the PEMs  $[\text{Cs/Col}]_4\text{Cs/LPX/Cs/Col}$  stored in PBS were studied using CLSM. Although because of their relatively large size and the electrostatic interaction with the polyanion Cs, a fast diffusion of LPX in the multilayer system was not expected. Nevertheless, two different experiments were performed to investigate if LPX have a certain mobility in PEMs. In the first experimental setup, Cy5 labelled DNA was used for the preparation of LPX which were afterward embedded in the PEMs. These samples were examined regarding the Cy5 fluorescence intensity at different time points of incubation in PBS by CLSM: directly after PEMs construction, as well as 24 h, 4 days, and 35 days after fabrication of PEMs. The results are shown in Figure 6A. A weak trend of a decrease in Cy5 fluorescence was observed, but all detected differences were not statistically significant. Therefore, it can be assumed that the DNA of the LPX remained entrapped in the PEMs within the time interval of 35 days. The large size of DNA (3.5 kbp, 260 kDa) in LPX and the complexation with the cationic lipids are certainly the reasons for the stability of the system.

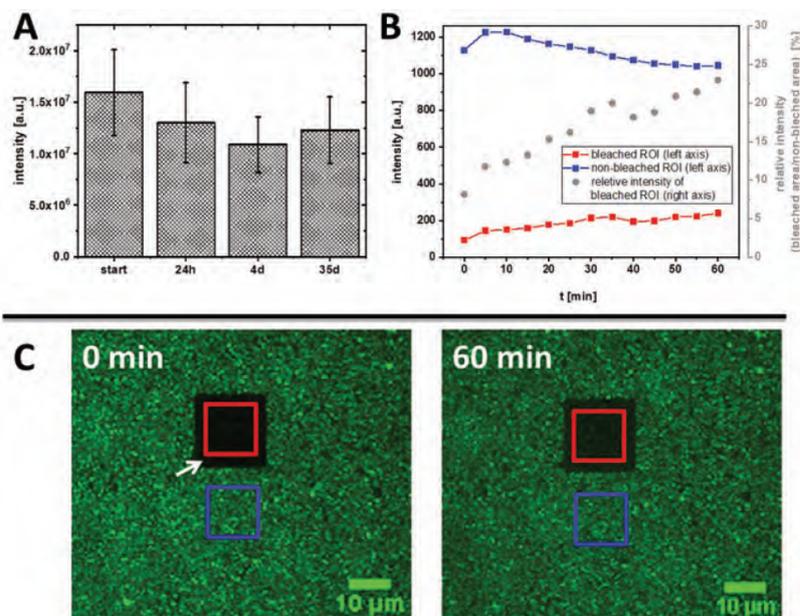


**Figure 6.** A) Fluorescence intensity of covalently labeled Cy5 DNA in LPX immobilized in PEM [Cs/Col]<sub>4</sub>Cs/LPX/Cs/Col. CLSM-based intensity determination was done directly after the film construction (start) and after 1, 4, and 35 days. The results are given as means  $\pm$  SD ( $n = 36$ ). Significance was tested using one-way ANOVA followed by Scheffé post hoc test,  $\alpha = 0.05$ ,  $*p \leq 0.05$ , no significant difference was found. B,C) Results of FRAP studies. Fluorescence intensity of NBD-DOPE was used as fluorescence probe in LPX (1 mol-% of the lipid composite). A defined area was bleached with high laser intensity and micrographs for intensity determination were taken in a period of 60 min after bleaching. Images were analyzed using ImageJ (B). CLSM images of [Cs/Col]<sub>4</sub>Cs/LPX/Cs/Col loaded with NBD-labeled LPX directly (0 min) and 60 min after bleaching. The white arrow indicates the bleached region which appeared black due to successful fluorophore inactivation. The red square indicates the area applied to the fluorescence intensity determination of the bleached region in diagram (B); the blue square indicates the reference area of a non-bleached region (C).

In the second experimental setup, FRAP experiments were performed (Figure 6B,C). Here, the lipid components of LPX were fluorescence tagged. NBD-DOPE as efficiently bleachable fluorophore was used for the LPX preparation. Then, the PEM with embedded LPX was bleached at an area by applying high laser intensity (red box, Figure 6C). This photobleached area was examined for recovery of NBD fluorescence for 60 min. Indeed, a weak but steady increase in NBD fluorescence was detected in the bleached area. However, only  $\approx 10\%$  of the intensity of the non-bleached reference area reappeared after 60 min (Figure 6B, red symbols). Note that the fluorescence in the control region was slightly decreasing (Figure 6B, blue symbols), an effect most-likely assigned to photo bleaching. This would imply that the calculated relative intensity change (Figure 6B, blue symbols) is biased, and the real reappearance is lower. Hence, only a small fraction of non-bleached fluorophores diffused into the bleached region, indicating that lipid components of LPX have certain mobility. Smaller molecules can diffuse in PEMs, as for example demonstrated for small model peptides.<sup>[75]</sup>

Summarizing, it can be concluded that the DNA is stably entrapped in LPX which will also be evident by the subsequent transfection studies.

### 3.4. Cell Studies

#### 3.4.1. Cell Adhesion and Proliferation of Mesenchymal Stem Cells on LPX-Loaded PEMs

Interaction of hADSCs with PEMs substrates was studied by staining nuclei used for cell counting, actin cytoskeleton used for cell spreading analysis, and the evaluation of focal adhesion (FA) as marker of cell-ECM contact points. Cells cultured on glass as positive control showed an extended phenotype with longitudinal organization of actin filaments and well-developed vinculin-positive FA in the cell periphery, indicating a normal behavior of these cells (Figure 7A, actin fibers shown in green). Cells cultured on LPX-free PEMs [Cs/Col]<sub>6</sub> were characterized by a longitudinal distribution of the actin filaments as well (Figure 7B, actin fibers shown in green). Many vinculin-positive FA were detected (Figure 7B, red signal in the merged image and signal in the lower single channel image). Cells on the intermediate PEM construct [Cs/Col]<sub>4</sub>Cs/LPX were less extended, but also, a longitudinal organization of actin filaments was observed (Figure 7C, actin fibers shown in green). Slightly fewer and larger vinculin-positive FA were predominantly observed at the cell periphery (Figure 7C, red signal in the merged image and signal

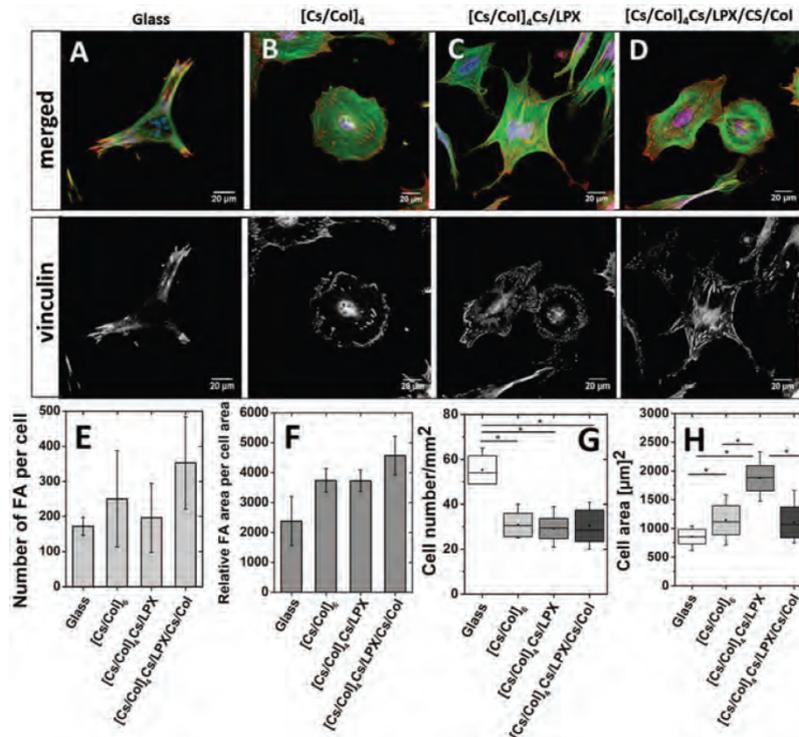


**Figure 7.** A–D) Merged CLSM image of adherent hADSCs cultured on the different PEMs after 4 h of incubation in serum. Glass slide (A), [Cs/Col]<sub>6</sub> (B), [Cs/Col]<sub>4</sub>Cs/LPX (C), and [Cs/Col]<sub>4</sub>Cs/LPX/Cs/Col (D). The cells were stained for filamentous actin (green), vinculin-positive FA (red), and nuclei (blue) in the merged images. The vinculin channel is shown separately in gray scale below the merged image. The scale bar represents 20 µm. E) Gives the quantification of vinculin-positive FA number per cell and F) relative vinculin-positive FA area per cell determined by Image J for representative six cells ( $n = 6$ ; significance was tested using one-way ANOVA followed by Scheffé post hoc test,  $\alpha = 0.05$ ,  $*p \leq 0.05$ , no significant difference was found). G) Quantification of cell count per square millimeter and H) cell spreading area ( $\mu\text{m}^2$ ) on each of the PEMs after 4 h ( $n = \text{ten images per condition}$ ). (Box plots with whiskers, representing first and third quartiles, medians and means. The star (\*) indicates statistically significant differences using one-way ANOVA followed by Scheffé post hoc test,  $\alpha = 0.05$ , with a  $p$ -value  $\leq 0.05$  (F,G).

in the lower single channel image). Cells cultured on PEMs [Cs/Col]<sub>4</sub>Cs/LPX/Cs/Col showed spread hADSCs with parallel arrangement of actin filaments (Figure 7D, green staining) and extended cell protrusions. Distinct vinculin-positive FA were observed at the cell protrusions and cell periphery (Figure 7D, red staining merged image and signal in the lower single channel image). The quantitative evaluation of FA showed no statistically significant differences between the positive control and PEMs; for both, the number of FA per cell and the relative area of vinculin positive FA. In addition, no statistical difference was found between the different PEMs. However, a trend to higher values was observed for PEMs [Cs/Col]<sub>4</sub>Cs/LPX/Cs/Col (Figure 7E,F). The higher number of cells on the positive control in comparison to all PEMs shown in Figure 7G is probably related to the stiffness of glass that promotes cell attachment.<sup>176)</sup> On the other hand, the quantification of the cell area (Figure 7H) demonstrated that hADSCs on glass had a smaller cell area in contrast to [Cs/Col]<sub>4</sub>Cs/LPX PEM that showed higher cell spreading (Figure 7H). The determined cell areas for the reference PEMs

[Cs/Col]<sub>6</sub> and [Cs/Col]<sub>4</sub>Cs/LPX/Cs/Col were comparable and in between the values of glass and [Cs/Col]<sub>4</sub>Cs/LPX PEM. As is known, cell spreading is a promoter of osteogenic differentiation so the PEMs made of Cs/Col may support osteogenesis of hADSCs.<sup>177)</sup> Moreover, the presence of Col as component of all PEMs can be considered as a promoter of mitogenic signal transduction through integrin receptors such as  $\alpha 2\beta 1$  integrin, the main receptor for Col.<sup>159)</sup>

The proliferation of hADSCs was studied by QBlue assay evaluating metabolic activity of cells seeded on glass slides (positive control), PEMs [Cs/Col]<sub>6</sub>, [Cs/Col]<sub>4</sub>Cs/LPX, and [Cs/Col]<sub>4</sub>Cs/LPX/Cs/Col. In Figure 8, it is shown that cells seeded on glass showed higher metabolic activity in contrast to PEMs, which relates to the results of adhesion studies. For all three surface coatings, a significant increase of the metabolic cell activity from day 1 to day 4 was observed (Figure 8) indicating cell growth with no differences among them on day 1. Comparing the cell growth on subsequent days, it was seen that [Cs/Col]<sub>6</sub> provided superior conditions while the presence of LPX in the

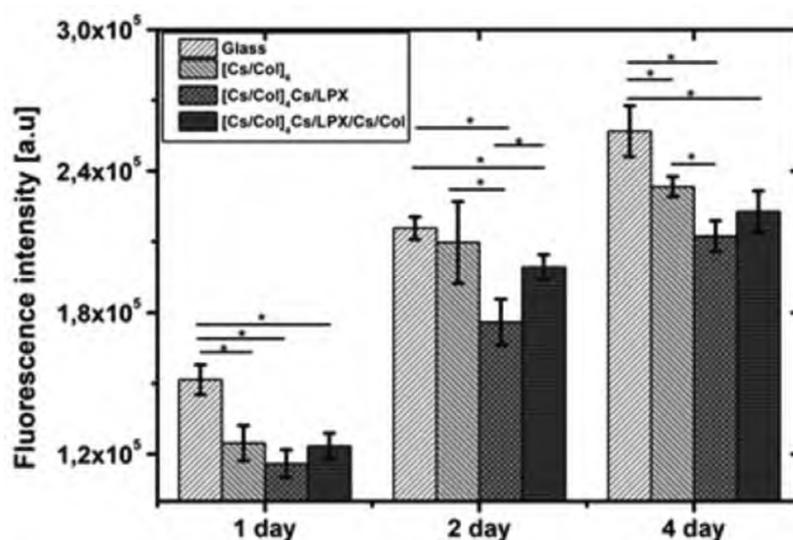


**Figure 8.** Growth of hADSCs seeded on PEMs sequence of glass slide (control), [Cs/Col]<sub>6</sub>, [Cs/Col]<sub>4</sub>Cs/LPX, and [Cs/Col]<sub>4</sub>Cs/LPX/Cs/Col measured by the QBlue assay after 24, 48, and 96 h. The values represent means  $\pm$  SD with  $n = 3$ . The star (\*) indicates statistically significant differences using one-way ANOVA followed by Scheffé post hoc test,  $\alpha = 0.05$ , with a  $p$ -value  $\leq 0.05$ .

two other systems had a slightly inhibiting effect on cell growth with significantly lower values comparing [Cs/Col]<sub>4</sub>Cs/LPX with [Cs/Col]<sub>6</sub>. This may be related to the cationic nature of LPX that may exert certain toxicity though adhesion studies did not provide any hints for that.<sup>[51]</sup> Overall, all PEMs enabled attachment, spreading and growth of cells, as a prerequisite for subsequent cell differentiation studies.

### 3.4.2. Transfection Studies

Successful transfer of DNA from [Cs/Col]<sub>4</sub>Cs/LPX/Cs/Col into hADSCs is essential for a clinical in situ transfection strategy. To study the cellular uptake, LPX were loaded with Cy5 labeled DNA. The fluorescent tagged LPX were embedded in the [Cs/Col]<sub>4</sub>Cs/LPX/Cs/Col multilayer. Afterward, hADSCs were seeded onto the fluorescent tagged in situ transfection system and cells were evaluated after 2 days by CLSM (Figure 9). Cellular uptake of the Cy5 labeled DNA was demonstrated, showing a Cy5 fluorescence signal accumulated in the perinuclear region (Figure 9, yellow arrows). However, it is described in the literature that the Cy5 label preferentially tends to accumulate in mitochondria because of their higher mitochondrial membrane potential compared to normal cells, which is why DNA is hardly recognizable in the cell nucleus.<sup>[78,79]</sup> The mechanism of LPX-uptake by cells from the PEMs [Cs/Col]<sub>4</sub>Cs/LPX/Cs/Col is not understood in detail. However, a cell-mediated endocytosis can be assumed despite the presence of a cover layer because it was demonstrated previously that mesenchymal stem cells can actively remodel Col of Cs/Col-based PEMs.<sup>[57]</sup> Moreover, we recently described successful endocytosis of liposomes from CS/Col-based PEMs into

C2C12 myoblasts adhering to the coating.<sup>[54]</sup> It is further known that endocytotic uptake is the main route for LPX into cells.<sup>[62,80]</sup> To proof efficient DNA transfer to the nucleus, reporter gene transfection experiments were also performed.

The DNA transfer activity of the gene-activated PEM was evaluated using a pDNA encoding for GFP as reporter gene (Figure 10). Besides the DNA-activated PEM [Cs/Col]<sub>4</sub>Cs/LPX/Cs/Col, the intermediate PEM [Cs/Col]<sub>4</sub>Cs/LPX (surface adsorbed LPX which were not protected by a cover layer) and the LPX-free reference PEM [Cs/Col]<sub>6</sub> with LPX in the supernatant, were used for comparison. These controls enable an assessment of the influence of the cover layer on the transfection on the one hand and whether embedding LPX in PEMs has an impact on the transfection efficiency on the other. After 24 h, the highest efficiency was detected for the system [Cs/Col]<sub>4</sub>Cs/LPX ( $\approx 16\%$  GFP positive cells), while the final PEM [Cs/Col]<sub>4</sub>Cs/LPX/Cs/Col showed a slightly reduced efficiency ( $\approx 12\%$  GFP positive cells). The control with LPX in the supernatant showed the lowest intensity. At 48 h after incubation, no significant differences were observed among the three groups and efficiency values of  $\approx 17$ – $20\%$  GFP positive hADSCs were detected. The immobilization of LPX seems to trigger a fast contact between LPX and cells, leading to higher efficiency of the systems with PEM bound LPX after 24 h. This kinetic effect levels off after 48 h. The results demonstrated that LPX immobilization had no diminishing effect on the efficacy of the LPX formulation in the time frame studied. In addition, the transfection efficacy of  $20\%$  was promising to proceed experiments with BMP-2 encoding DNA as autocrine and paracrine effects could be expected when  $20\%$  of the hADSCs growing on the PEMs express the gene of interest.<sup>[81]</sup>

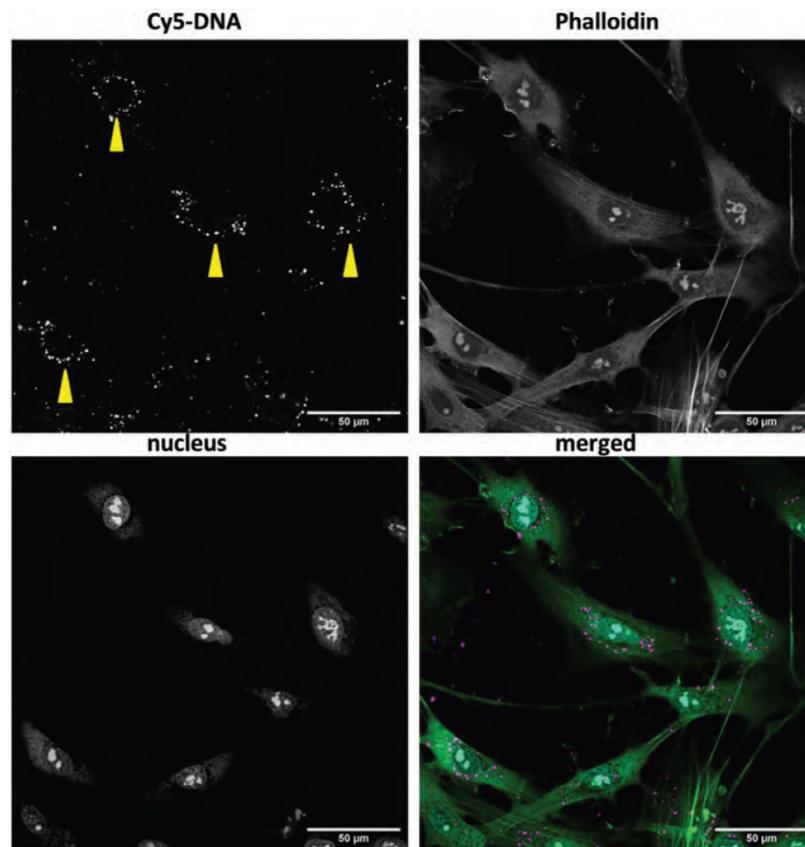


**Figure 9.** CLSM micrograph of transfected hADSCs after 48 h grown on [Cs/Col]<sub>4</sub>Cs/LPX/Cs/Col with Cy-5 labeled DNA (merged image magenta). The cells are stained for filamentous actin with Phalloidin-Atto 488 (merged image green) and nucleus with BOBO-1 (merged image cyan). Images were taken at 40× magnification and evaluated with ImageJ. The bar represents 50 µm. Images are given as single channels and merged. The provided image is an optical cross section taken by CLSM analysis. An additional optical cross section at lower z-value near the PEMs surface is given in Figure S5, Supporting Information.

#### 3.4.3. Osteogenic Differentiation of Mesenchymal Stem Cells on BMP-2-Gene Activated LPX-Loaded PEMs

In this section, the transfection-active surface coating [Cs/Col]<sub>4</sub>Cs/LPX/Cs/Col was loaded with LPX with complex BMP-2-encoding DNA. Potentially, successful BMP-2 expression can lead to autocrine or paracrine BMP-2 effects by transfected cells. Gene expression analysis of specific osteoblast markers was performed by mRNA quantification. The expression of five osteogenesis-related genes (RunX-2, BMP-2, ALP, Col1A1 and Noggin) was quantified by RT-qPCR 28 days after hADSCs were seeded on [Cs/Col]<sub>4</sub>Cs/LPX/Cs/Col (Figure 11). As medium for the experiments, we have chosen OM, which contained essential components for osteogenic differentiation:  $\beta$ -Gly serves as a source of phosphate in hydroxyapatite structures, Dex has an enhancing stimulus on BMP-2 effect, and ASC is an enhancer of collagen type 1 secretion.<sup>[82,83]</sup> The following controls were chosen: cells cultured in BM on surfaces without PEM coating

were used as negative control due to the absence of inductors for osteogenic differentiation (Figure 11, non-coated; BM). As positive control, hADSCs were cultured on surfaces without PEM coating using the StemPro Osteogenic-Differentiation Kit provided by the supplier of the stem cells (Figure 11, non-coated; StemPro). StemPro has an optimized mix of supplements and cytokines to reliably induce differentiation to osteocytes. As further necessary control, hADSCs in OM growing on [Cs/Col]<sub>6</sub> in the absence of LPX were examined because of two reasons: 1) we know from our previous work that PEMs composed of ECM components can also trigger differentiation and want to estimate that effect<sup>[53,54,57]</sup> and 2) due to the possibility to trigger osteogenic differentiation by Dex of the OM.<sup>[84]</sup> Nevertheless, as biogenic glucocorticoids exert profound effects on bone and are essential for human osteoblast differentiation, we decided to keep Dex in the OM. The presence of BMP-2 in Dex containing OM has enhancing effects on the osteogenic differentiation of stem cells.<sup>[85]</sup>

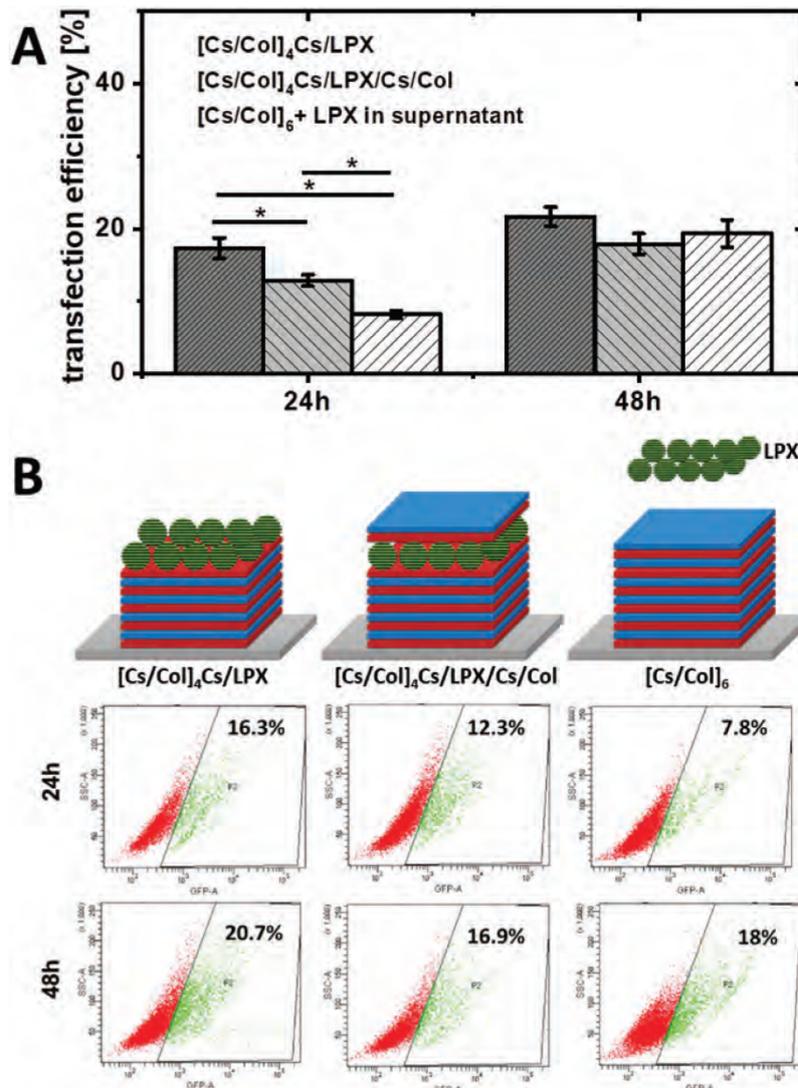


**Figure 10.** Transfection efficiency of the three examined PEMs sequences: [Cs/Col]<sub>4</sub>Cs/LPX, [Cs/Col]<sub>4</sub>Cs/LPX/Cs/Col, and [Cs/Col]<sub>6</sub> (LPX in supernatant). A) Transfection efficiency as fraction of GFP positive cells at 24 and 48 h after beginning of cell incubation. Error bars represent means  $\pm$  SD ( $n = 3$ ), statistically significant differences using one-way ANOVA followed by Scheffé post hoc test,  $\alpha = 0.05$ , with a  $p$ -value  $\leq 0.05$ . B) Representative flow cytometry dot plots representing light scatter of cell light scattering (SSC) and the fluorescence intensity in the GFP-sensitive channel (GFP-A) of hADSCs seeded on [Cs/Col]<sub>6</sub> (LPX in supernatant), [Cs/Col]<sub>4</sub>Cs/LPX, and [Cs/Col]<sub>4</sub>Cs/LPX/Cs/Col. Green color corresponds to GFP positive cells with a higher fluorescence signal compared to the auto fluorescence of cells, and red color to the GFP-negative cells. The negative control of cells growing on [Cs/Col]<sub>6</sub> in the absence of LPX is presented in Figure S6, Supporting Information.

Analysis of the expression level of the mentioned osteogenic markers demonstrated that cells grown on BMP-2 gene-activated [Cs/Col]<sub>4</sub>Cs/LPX/Cs/Col exhibited enhanced expression of all osteo-specific genes compared to the negative control (Figure 11). For BMP-2, [Cs/Col]<sub>4</sub>Cs/LPX/Cs/Col showed a clearly increased expression by 15-fold. This observation demonstrated the suc-

cessful transfection and expression of the encoded gene in the DNA-activated PEMs. The positive control (non-coated; Stem-Pro) also showed a 5-fold increased BMP-2 expression but significantly lower compared to the [Cs/Col]<sub>4</sub>Cs/LPX/Cs/Col multilayer. Osteogenic differentiation can also be associated with increased BMP-2 expression, which accelerates the differentiation

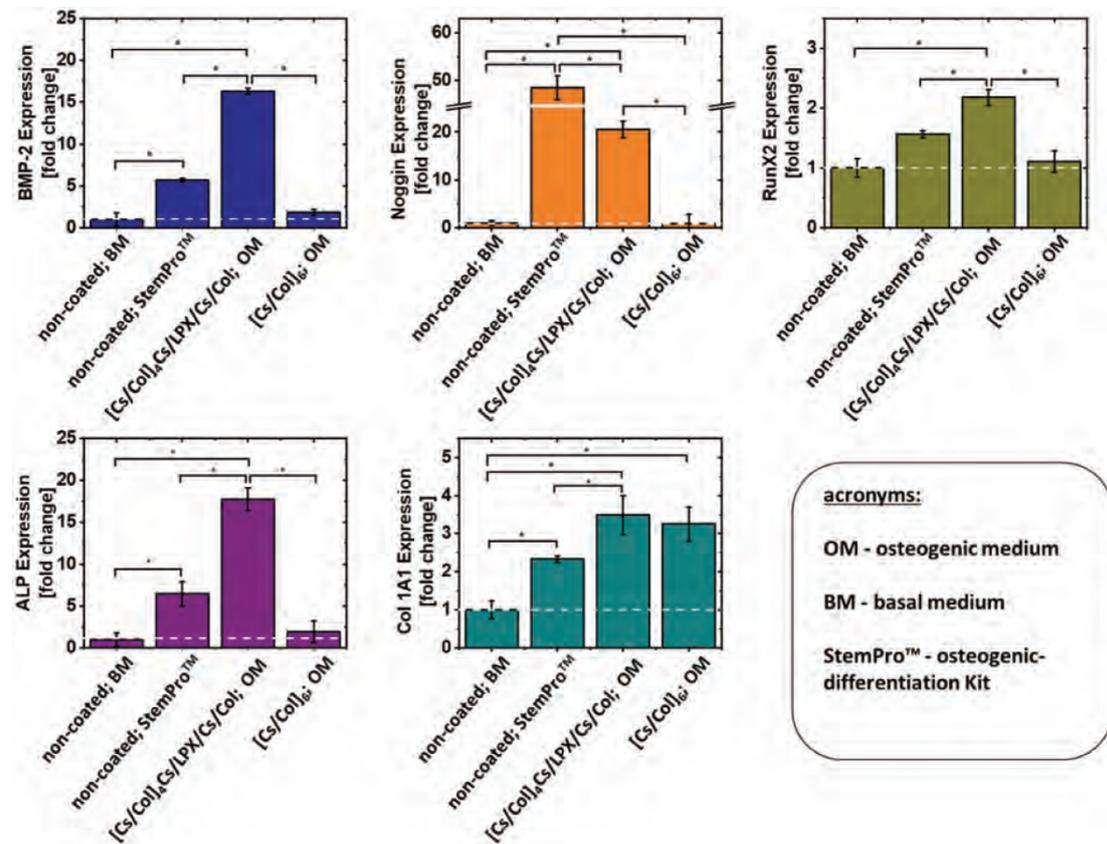


**Figure 11.** RT-qPCR analysis of representative osteogenic markers: BMP-2, ALP, Col 1A1, Noggin, and RunX2. The results represent the gene expression at day 28 of the osteogenic differentiation experiments. For the BMP-2 gene activated PEMs [Cs/Col]<sub>4</sub>Cs/LPX/Cs/Col hADSCs were seeded on the multilayer in OM, containing  $\beta$ -Gly, Dex, and ASC but no BMP-2 or other cytokines). Multilayer film control without LPX hADSCs was grown on [Cs/Col]<sub>6</sub> in OM as medium to check for differentiation triggered by the two ECM components. For positive control, cells grew on non-coated wells and were treated with StemPro osteogenic-differentiation Kit from Thermo Fisher Scientific, containing supplements and cytokines for efficient osteogenic differentiation of hADSCs (non-coated; StemPro). For negative control, hADSCs grew on non-coated wells and were treated with BM (non-coated; BM). Results represent means  $\pm$  SD, with  $n = 3$ ; statistically significant differences using one-way ANOVA followed by Scheffé post hoc test,  $\alpha = 0.05$ , with a  $p$ -value  $\leq 0.05$ .

process.<sup>[86]</sup> The LPX-free PEM control film ([Cs/Col]<sub>6</sub>; OM) showed no significant difference to the negative control (non-coated; BM) for the BMP-2 expression. As an antagonist of BMP-2, we investigated the expression of the osteogenic marker Noggin.<sup>[87]</sup> Noggin was significantly upregulated for the positive control (non-coated; StemPro), and the transfection system [Cs/Col]<sub>4</sub>Cs/LPX/Cs/Col also showed an increased expression of this marker (Figure 11). This was significantly higher for the positive control; although, the BMP-2 expression was significantly lower compared to the BMP-2 gene-activated PEM. It is known from literature that Noggin has a biphasic dose-dependent expression, and it has been reported that at lower BMP-2 concentrations (0.01 to 1  $\mu\text{g mL}^{-1}$ ), Noggin induction is enhanced. By contrast, induction of Noggin is diminished when BMP-2 concentrations are shifted from 1 to 50  $\mu\text{g mL}^{-1}$ .<sup>[88]</sup> This behavior could explain why the positive control has a lower BMP-2 ex-

pression but more than twice as much Noggin expression as cells growing on the [Cs/Col]<sub>4</sub>Cs/LPX/Cs/Col multilayer. Nevertheless, this explanation remains speculative because the BMP-2 amount in our experiments was not quantified, a focus of ongoing research. The third marker, RunX2, is one of the most important transcription factors, which is especially important in the early phase of osteogenic differentiation as it is upregulated in pre-osteoblasts and downregulated in mature osteoblasts.<sup>[89]</sup> For the sample [Cs/Col]<sub>4</sub>Cs/LPX/Cs/Col and the positive control, RunX2 is upregulated. The BMP-2 gene-activated PEM has significantly higher RunX2 values compared to all controls (Figure 11). The same expression pattern is found for ALP (Figure 11), which is needed to generate phosphate ions from natural sources for the hydroxyapatite matrix of bone tissues. The significantly highest ALP expression is found in cells growing on the [Cs/Col]<sub>4</sub>Cs/LPX/Cs/Col. The last screened marker was

Col1A1 because expression of the Col1A1 gene occurs mainly during the shift from early to mature stages of osteoblast maturation, when the osteoblasts start building the ECM.<sup>[90]</sup> The [Cs/Col]<sub>4</sub>Cs/LPX/Cs/Col, the positive control (non-coated; StemPro), and the LPX-free PEMs reference ([Cs/Col]<sub>6</sub>; OM) show a significantly increased Col1A1 expression compared to the negative control (non-coated; BM) (Figure 11). That result can be expected for the [Cs/Col]<sub>4</sub>Cs/LPX/Cs/Col and the positive control because the other osteogenic markers are also increased in the expression analysis. For the LPX-free [Cs/Col]<sub>6</sub> reference, Col1A1 is the only marker screened in this study which has statistically significant increase compared to the negative control (non-coated; BM). A closer look to the results for BMP-2, RunX2, and ALP expression of cells on LPX-free PEMs ([Cs/Col]<sub>6</sub>; OM) shows a slight but non-significant increase of gene expression compared to the negative control (non-coated; BM). It is known from previous research that Col/Cs PEMs can promote osteogenic differentiation,<sup>[57]</sup> which was why we have chosen these composites as main component for the DNA-activated PEM. Nevertheless, these studies demonstrated the additive effect of the ECM mimicking PEMs in combination with the in situ BMP-2 transfection.

To further evaluate osteogenic differentiation, all samples were tested for mineralization (Figure 12). At the final stage of osteoblast differentiation, the formation of mineralized nodules was a crucial phenomenon that indicates the maturation of osteoblasts. To evaluate this, Alizarin red staining was used to screen the degree of mineralization by visualizing calcium nodules after 24 days (stained red spots). Cells cultured on BMP-2 gene activated [Cs/Col]<sub>4</sub>Cs/LPX/Cs/Col and positive control (non-coated, StemPro) developed large Alizarin positive nodules, a strong indication of hADSC undergoing osteogenesis. The poor performance of mineral nodules for hADSCs growing on [Cs/Col]<sub>6</sub> in OM may result from the lack of BMP-2, again demonstrating the enhancing effect of in situ BMP-2 transfection. As the bone ECM contains hydroxyapatite, a phosphate mineral with the composition Ca<sub>10</sub>(PO<sub>4</sub>)<sub>6</sub>(OH)<sub>2</sub>, a method for a mineral-specific staining provides more information than non-specific Alizarin staining. OsteoImage™, a commercially available hydroxyapatite specific fluorescence dye, was used to screen for these osteo-specific mineral deposition. The images from this staining confirm the results from alizarin red staining (Figure 12). Both the positive control (non-coated, StemPro) and the BMP-2 gene activated [Cs/Col]<sub>4</sub>Cs/LPX/Cs/Col show pronounced hydroxyapatite structures after 24 days, which are absent in the negative control (non-coated, BM) and for hADSCs on [Cs/Col]<sub>6</sub> in OM. Concluding, the data from RT-qPCR are supported by these staining for the inorganic ECM components of bone tissue. The BMP-2 gene-activated PEM can induce osteogenic differentiation of hADSCs comparable to the positive control.

#### 4. Conclusion

The main goal of this work was to develop a novel gene-functionalized ECM-mimicking multilayered thin film for implants coating. We demonstrated that it is possible to entrap LPX into PEMs composed of the bone ECM components Cs and Col

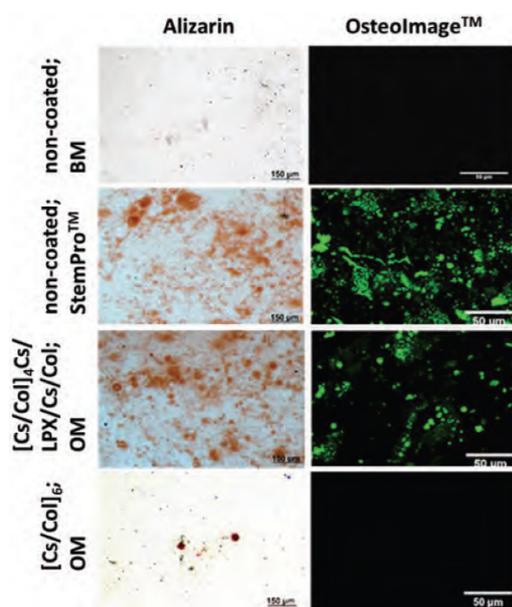


**Figure 12.** Histochemical (Alizarin) and fluorescence (OsteoImage™) staining for inorganic bone matrix at day 24 of the differentiation experiment. The alizarin staining appears for calcium structures red, while OsteoImage™ fluorescently stains hydroxyapatite with high specificity for CLSM investigation (here shown in green). To prove osteogenic differentiation with the developed PEMs, hADSCs were seeded on BMP-2 gene-activated [Cs/Col]<sub>4</sub>Cs/LPX/Cs/Col in OM. PEMs without LPX was investigated with cells growing on [Cs/Col]<sub>6</sub> in OM. For positive control, cells grew on non-coated wells using the StemPro osteogenic-differentiation Kit to induce osteogenic differentiation. For negative control, hADSCs grew on non-coated wells using BM. Micrographs were taken for Alizarin staining at 10× magnification (bar represents 150 μm) and for OsteoImage™ staining at 40× magnification (bar represents 50 μm).

to engineer a nanoparticle functionalized thin film surface coating. The affinity of stem cells to the surface coating was proven as well as its ability of contact triggered transfection of cells growing on the gene-activated PEMs, triggering their differentiation into the osteogenic lineage. The transfection activity allows an in situ cytokine production which is spatially and temporally restricted due to the contact triggered transfection of cells with a non-viral gene delivery system, which only allows episomal gene uptake in cells resulting in a transient genetic modification. Hence, this PEM system is promising for clinical application as implant coating for bone tissue regeneration due to its camouflaging effect by mimicking bone ECM, providing an effective biological niche for osteogenic cell differentiation. The presented PEM-LPX system can also be used as an mRNA delivery system because mRNA also allows transient protein expression with promising opportunities for regenerative medicine.<sup>[91]</sup> Therefore, this system is of high interest to develop novel alternatives for implant coating for future in vivo use in bone tissue regeneration and in other tissue engineering applications.

## Supporting Information

Supporting Information is available from the Wiley Online Library or from the author.

## Acknowledgements

C.H. and Y.A.B.B. contributed equally to this work. The authors are thankful for the help and support of Dr. Navarrete Santos during flow cytometry measurements and data analysis. Y.A.B.B. was supported by the Consejo Nacional de Ciencia y Tecnología (CONACYT-México) and Deutscher Akademischer Austauschdienst (DAAD) for funding. Furthermore, she received a grant from the International Graduate School AGRIPOLY supported by the European Regional Development Fund (ERDF) and Ministerium für Wissenschaft und Wirtschaft, Land Sachsen-Anhalt. C.H. was supported by DAAD which funded the exchange to University Aveiro. This work was funded by the Fraunhofer Internal Programs under Grant No. Attract 069-608203 (C.E.H.S.) and by the Programa Operacional Regional do Centro – Centro 2020, in the component FEDER, and by national funds (OE) through Fundação para a Ciência e a Tecnologia/Ministério da Ciência, Tecnologia e Ensino Superior (FCT/MCTES), in the scope of the project “SUPRASORT” (PTDC/QUI-OUT/30658/2017, CENTRO-01-0145-FEDER-030658). This work was developed within the scope of the project CICECO – Aveiro Institute of Materials, UIDB/50011/2020, UIDP/50011/2020 & LA/P/0006/2020, financed by national funds through the FCT/MEC (PIDDAC). The support by the Deutsche Forschungsgemeinschaft (DFG) project-ID 396823779 (C.W.) is acknowledged. J.B. gratefully acknowledges FCT for the individual Assistant Researcher contract (2020.00758.CEECIND).

Open Access funding enabled and organized by Projekt DEAL.

## Conflict of Interest

The authors declare no conflict of interest.

## Data Availability Statement

Research data are not shared.

## Keywords

bone morphogenic protein 2, chondroitin sulfate, collagen I, human adipose-derived mesenchymal stem cells, lipoplexes, osteogenic differentiation, polyelectrolyte multilayers

Received: August 5, 2022

Revised: October 25, 2022

Published online:

- [1] R. A. Marklein, J. A. Burdick, *Adv. Mater.* **2010**, *22*, 175.  
 [2] E. Piva, A. F. Silva, J. E. Nör, *J. Endod.* **2014**, *40*, S33.  
 [3] P. Rosset, F. Deschaseaux, P. Layrolle, *Orthop. Traumatol.: Surg. Res.* **2014**, *100*, S107.  
 [4] A. H. Undale, J. J. Westendorf, M. J. Yaszemski, S. Khosla, *Mayo Clin. Proc.* **2009**, *84*, 893.  
 [5] V. Paspaliaris, G. Kolios, *Stem Cells Int.* **2019**, *2019*, 1730978.  
 [6] X. Lin, S. Patil, Y.-G. Gao, A. Qian, *Front. Pharmacol.* **2020**, *11*, 757.  
 [7] D. S. W. Benoit, M. P. Schwartz, A. R. Durney, K. S. Anseth, *Nat. Mater.* **2008**, *7*, 816.  
 [8] J.-H. Hwang, U. Han, M. Yang, Y. Choi, J. Choi, J.-M. Lee, H.-S. Jung, J. Hong, J.-H. Hong, *Acta Biomater.* **2019**, *86*, 247.  
 [9] M. B. Keogh, F. J. O'Brien, J. S. Daly, *Acta Biomater.* **2010**, *6*, 4305.  
 [10] M. L. Macdonald, R. E. Samuel, N. J. Shah, R. F. Padera, Y. M. Beben, P. T. Hammond, *Biomaterials* **2011**, *32*, 1446.  
 [11] C. Salvi, X. Lyu, A. M. Peterson, *Biomacromolecules* **2016**, *17*, 1949.  
 [12] Y.-I. Chung, K.-M. Ahn, S.-H. Jeon, S.-Y. Lee, J.-H. Lee, G. Tae, *J. Controlled Release* **2007**, *121*, 91.  
 [13] M. B. Rahmany, M. Van Dyke, *Acta Biomater.* **2013**, *9*, 5431.  
 [14] B.-H. Luo, C. V. Carman, T. A. Springer, *Annu. Rev. Immunol.* **2007**, *25*, 619.  
 [15] F. Gattazzo, A. Urciuolo, P. Bonaldo, *Bioch. Biophys. Acta* **2014**, *1840*, 2506.  
 [16] R. O. Hynes, *Science* **2009**, *326*, 1216.  
 [17] G. Decher, J.-D. Hong, *Macromol. Symp.* **1991**, *46*, 321.  
 [18] J. Borges, J. F. Mano, *Chem. Rev.* **2014**, *114*, 8883.  
 [19] A. M. Ferreira, P. Gentile, V. Chiono, G. Ciardelli, *Acta Biomater.* **2012**, *8*, 3191.  
 [20] X. He, Y. Wang, G. Wu, *Appl. Surf. Sci.* **2012**, *258*, 9918.  
 [21] S. Shu, C. Sun, X. Zhang, Z. Wu, Z. Wang, C. Li, *Acta Biomater.* **2010**, *6*, 210.  
 [22] P. Gentile, I. Carnagnola, T. Nardo, V. Chiono, *Nanotechnology* **2015**, *26*, 422001.  
 [23] V. Z. Prokopovic, A. S. Vikulina, D. Sustr, E. M. Shchukina, D. G. Shchukin, D. V. Volodkin, *ACS Appl. Mater. Interfaces* **2017**, *9*, 38908.  
 [24] K. Gelse, *Adv. Drug Delivery Rev.* **2003**, *55*, 1531.  
 [25] C. Dong, Y. Lv, *Polymers* **2016**, *8*, 42.  
 [26] M. Büttner, S. Möller, M. Keller, D. Huster, J. Schiller, M. Schnabelrauch, P. Dieter, U. Hempel, *J. Cell. Physiol.* **2013**, *228*, 330.  
 [27] N. S. Hwang, S. Varghese, H. J. Lee, P. Theprungsirikul, A. Canver, B. Sharma, J. Elisseeff, *FEBS Lett.* **2007**, *581*, 4172.  
 [28] H. D. Kim, E. A. Lee, Y.-H. An, S. L. Kim, S. S. Lee, S. J. Yu, H. L. Jang, K. T. Nam, S. G. Im, N. S. Hwang, *ACS Appl. Mater. Interfaces* **2017**, *9*, 21639.  
 [29] P. Cai, Z. Xue, W. Qi, H. Wang, *Colloids Surf. A* **2013**, *434*, 110.  
 [30] T.-M. De Witte, L. E. Fratila-Apachitei, A. A. Zadpoor, N. A. Peppas, *Regener. Biomater.* **2018**, *5*, 197.  
 [31] D. B. Asserson, H. Orbay, D. E. Sahar, *J. Craniofacial Surg.* **2019**, *30*, 703.  
 [32] P. C. Bessa, M. Casal, R. L. Reis, *J. Tissue Eng. Regener. Med.* **2008**, *2*, 1.  
 [33] P. C. Bessa, M. Casal, R. L. Reis, *J. Tissue Eng. Regener. Med.* **2008**, *2*, 81.  
 [34] A. W. James, G. Lachaud, J. Shen, G. Asatrian, V. Nguyen, X. Zhang, K. Ting, C. Soo, *Tissue Eng., Part B* **2016**, *22*, 284.  
 [35] A. Ramasubramanian, S. Shiigi, G. K. Lee, F. Yang, *Pharm. Res.* **2011**, *28*, 1328.  
 [36] I. El Bialy, W. Jiskoot, M. Reza Nejadnik, *Pharm. Res.* **2017**, *34*, 1152.  
 [37] R. E. De La Vega, A. Atasoy-Zeybek, J. A. Panos, M. Van Griensven, C. H. Evans, E. R. Balmayor, *Transl. Res.* **2021**, *236*, 1.  
 [38] C. Jewell, D. Lynn, *Adv. Drug Delivery Rev.* **2008**, *60*, 979.  
 [39] E. M. Saurer, C. M. Jewell, D. A. Roenneburg, S. L. Bechler, J. R. Torrealba, T. A. Hacker, D. M. Lynn, *Biomacromolecules* **2013**, *14*, 1696.  
 [40] He Zhang, J.-J. Huang, J. Wang, Mi Hu, X.-C. Chen, W. Sun, Ke-F Ren, J. Ji, *ACS Biomater. Sci. Eng.* **2019**, *5*, 6610.  
 [41] C. E. Thomas, A. Ehrhardt, M. A. Kay, *Nat. Rev. Genet.* **2003**, *4*, 346.  
 [42] M. Rezaee, R. K. Oskuee, H. Nassiri, B. Malaekhe-Nikouei, *J. Controlled Release* **2016**, *236*, 1.  
 [43] C. Wölk, C. Janich, U. Bakowsky, A. Langner, G. Brezesinski, *Adv. Colloid Interface Sci.* **2017**, *248*, 20.  
 [44] B. R. Olden, Y. Cheng, J. L. Yu, S. H. Pun, *J. Controlled Release* **2018**, *282*, 140.  
 [45] H. Kavanagh, S. Dunne, D. S. Martin, E. Mcfadden, L. Gallagher, J. Schwaber, S. Leonard, S. O'dea, *Cytotherapy* **2021**, *23*, 852.

- [46] V. Graceffa, *J. Genet. Eng. Biotechnol.* **2021**, *19*, 90.
- [47] H. Zhang, K.-F. Ren, H. Chang, J.-L. Wang, J. Ji, *Biomaterials* **2017**, *116*, 95.
- [48] C. Husteden, F. Doberenz, N. Goergen, S. R. Pinnapireddy, C. Janich, A. Langner, F. Syrowatka, A. Repanas, F. Erdmann, J. Jedelskaj, U. Bakowsky, T. Groth, C. Wolk, *ACS Appl. Mater. Interfaces* **2020**, *12*, 8963.
- [49] S. D. Hujaya, G. Marchioli, K. Roelofs, A. A. Van Apeldoorn, L. Moroni, M. Karperien, J. M. J. Paulusse, J. F. J. Engbersen, *J. Controlled Release* **2015**, *205*, 181.
- [50] C. A. Holmes, M. Tabrizian, *ACS Appl. Mater. Interfaces* **2013**, *5*, 524.
- [51] J. Giselbrecht, C. Janich, S. R. Pinnapireddy, G. Hause, U. Bakowsky, C. Wölk, A. Langner, *Int. J. Pharm.* **2018**, *541*, 81.
- [52] X. Zhang, L. Dai, A. Wang, C. Wölk, B. Dobner, G. Brezesinski, Y. Tang, X. Wang, J. Li, *Sci. Rep.* **2015**, *5*, 16559.
- [53] Y. A. Brito Barrera, C. Husteden, J. Alherz, B. Fuhrmann, C. Wölk, T. Groth, *Mater. Sci. Eng., C* **2021**, *131*, 112516.
- [54] Y. A. Brito Barrera, G. Hause, M. Menzel, C. E. H. Schmelzer, E. Lehner, K. Mäder, C. Wölk, T. Groth, *Mater. Today Bio* **2020**, *7*, 100071.
- [55] C. Wölk, S. Drescher, A. Meister, A. Blume, A. Langner, B. Dobner, *Chemistry* **2013**, *19*, 12824.
- [56] G. W. Gale, R. J. Small, K. A. Reinhardt, in *Handbook of Silicon Wafer Cleaning Technology*, 2nd ed. (Eds: K. A. Reinhardt, W. Kern), William Andrew Publishing, Norwich, NY **2008**, pp. 201–265.
- [57] M. Zhao, G. Altankov, U. Grabiec, M. Bennett, M. Salmeron-Sanchez, F. Dehghani, T. Groth, *Acta Biomater.* **2016**, *41*, 86.
- [58] D. Axelrod, D. E. Koppel, J. Schlessinger, E. Elson, W. W. Webb, *Biophys. J.* **1976**, *16*, 1055.
- [59] K. J. Livak, T. D. Schmittgen, *Methods* **2001**, *25*, 402.
- [60] B. A. Lobo, A. Davis, G. Koe, J. G. Smith, C. R. Middaugh, *Arch. Biochem. Biophys.* **2001**, *386*, 95.
- [61] E. Pozharski, R. C. Macdonald, *Biophys. J.* **2002**, *83*, 556.
- [62] N. Erdmann, C. Wölk, I. Schulze, C. Janich, M. Folz, S. Drescher, M. Dittrich, A. Meister, J. Vogel, T. Groth, B. Dobner, A. Langner, *Eur. J. Pharm. Biopharm.* **2015**, *96*, 349.
- [63] F. Caruso, H. Lichtenfeld, E. Donath, H. Möhwald, *Macromolecules* **1999**, *32*, 2317.
- [64] F. Meyer, V. Ball, P. Schaaf, J. C. Voegel, J. Ogier, *Biochim. Biophys. Acta, Biomembr.* **2006**, *1758*, 419.
- [65] S. Tassler, B. Dobner, L. Lampp, R. Ziolkowski, E. Malinowska, C. Wölk, G. Brezesinski, *Langmuir* **2019**, *35*, 4613.
- [66] N. Fauchoux, R. Schweiss, K. Lützw, C. Werner, T. Groth, *Biomaterials* **2004**, *25*, 2721.
- [67] M. Zhao, L. Li, C. Zhou, F. Heyroth, B. Fuhrmann, K. Maeder, T. Groth, *Biomacromolecules* **2014**, *15*, 4272.
- [68] N. Chen, B. Bhushan, *J. Microsc.* **2006**, *221*, 203.
- [69] A. J. Engler, L. Richert, J. Y. Wong, C. Picart, D. E. Discher, *Surf. Sci.* **2004**, *570*, 142.
- [70] B. K. Ekambaram, M. S. Niepel, B. Fuhrmann, G. Schmidt, T. Groth, *ACS Biomater. Sci. Eng.* **2018**, *4*, 1820.
- [71] R. Anouz, A. Repanas, E. Schwarz, T. Groth, *Macromol. Biosci.* **2018**, *18*, 1800283.
- [72] M. Sharabi, *Front. Mater.* **2022**, *8*, 793647.
- [73] J. Campbell, A. S. Vikulina, *Polymers* **2020**, *12*, 1949.
- [74] S. Cai, C. Wu, W. Yang, W. Liang, H. Yu, L. Liu, *Nanotechnol. Rev.* **2020**, *9*, 971.
- [75] D. Sustr, C. Duschl, D. Volodkin, *Eur. Polym. J.* **2015**, *68*, 665.
- [76] D. E. Discher, P. Janmey, Y.-L. Wang, *Science* **2005**, *310*, 1139.
- [77] R. Mcbeath, D. M. Pirone, C. M. Nelson, K. Bhadriraju, C. S. Chen, *Dev. Cell* **2004**, *6*, 483.
- [78] S. Lorenz, S. Tomcin, V. Mailänder, *Microsc. Microanal.* **2011**, *17*, 440.
- [79] A. R. Nödling, E. M. Mills, X. Li, D. Cardella, E. J. Sayers, S.-H. Wu, A. T. Jones, L. Y. P. Luk, Y.-H. Tsai, *Chem. Commun.* **2020**, *56*, 4672.
- [80] C. Janich, C. Wölk, F. Erdmann, T. Groth, G. Brezesinski, B. Dobner, A. Langner, *J. Controlled Release* **2015**, *220*, 295.
- [81] K. Yang, H.-J. Park, S. Han, J. Lee, E. Ko, J. Kim, J. S. Lee, J. H. Yu, K. Y. Song, E. Cheong, S.-R. Cho, S. Chung, S.-W. Cho, *Biomaterials* **2015**, *63*, 177.
- [82] F. Langenbach, J. Handschel, *Stem Cell Res. Ther.* **2013**, *4*, 117.
- [83] M. Yuasa, T. Yamada, T. Taniyama, T. Masaoka, W. Xuetao, T. Yoshii, M. Horie, H. Yasuda, T. Uemura, A. Okawa, S. Sotome, *PLoS One* **2015**, *10*, e0116462.
- [84] O. Ghali, O. Broux, G. Falgayrac, N. Haren, J. P. Van Leeuwen, G. Penel, P. Hardouin, C. Chauveau, *BMC Cell Biol.* **2015**, *16*, 9.
- [85] M. Jäger, J. Fischer, W. Dohrn, X. Li, D. C. Ayers, A. Czibere, W. C. Prall, S. Lensing-Höhn, R. Krauspe, *J. Orthop. Res.* **2008**, *26*, 1440.
- [86] G. Zheng, Z. Xie, P. Wang, J. Li, M. Li, S. Cen, S. A Tang, W. Liu, G. Ye, Y. Li, S. Wang, X. Wu, H. Su, Y. Wu, H. Shen, *Cell Death Dis.* **2019**, *10*, 350.
- [87] L. J. Brunet, J. A. McMahon, A. P. McMahon, R. M. Harland, *Science* **1998**, *280*, 1455.
- [88] C. Chen, H. Uludağ, Z. Wang, H. Jiang, *J. Cell. Biochem.* **2012**, *113*, 3672.
- [89] T. Komori, *Adv. Exp. Med. Biol.* **2010**, *658*, 43.
- [90] N. A. Twine, L. Chen, C. N. Pang, M. R. Wilkins, M. Kassem, *Bone* **2014**, *67*, 23.
- [91] E. R. Balmayor, *Curr. Opin. Biotechnol.* **2022**, *74*, 8.

## 2.7) Manuskript I

### **Osteogenic Stem Cell Differentiation Induced by Contact Triggered In Situ BMP-2 Transfection from DNA lipid Nanoparticle Loaded Multilayer Films**

C. Husteden, S. Tegtmeyer, J. Weber, R. Eckenstaler, F. Erdmann, F. Seifert, R. A. Benndorf, A. Langner, T. Groth, C. Wölk

*Supporting Information* ist dem Anhang beigelegt.

# Osteogenic Stem Cell Differentiation Induced by Contact Triggered In Situ BMP-2 Transfection from DNA-lipid Nanoparticle Loaded Multilayer Films

Catharina Husteden<sup>a</sup>, Sophia Tegtmeyer<sup>a</sup>, Juliane Weber<sup>a</sup>, Robert Eckenstaler<sup>b</sup>, Frank Erdmann<sup>c</sup>, Franziska Seifert<sup>d</sup>, Ralf A. Benndorf<sup>b</sup>, Andreas Langner<sup>a</sup>, Thomas Groth<sup>e</sup>, Christian Wölk<sup>f\*</sup>

a Martin Luther University Halle-Wittenberg, Institute of Pharmacy, Department of Medicinal Chemistry, Wolfgang-Langenbeck-Str. 4, 06120 Halle (Saale), Germany

b Martin Luther University Halle-Wittenberg, Institute of Pharmacy, Department of Clinical Pharmacy and Pharmacotherapy, Kurt-Mothes-Str. 3, 06120 Halle (Saale), Germany

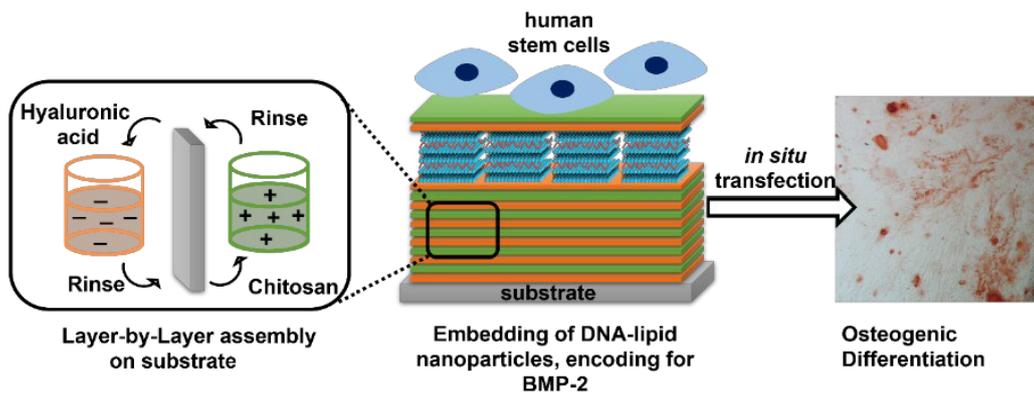
c Martin Luther University Halle-Wittenberg, Institute of Pharmacy, Department of Pharmacology, Kurt-Mothes-Str. 3, 06120 Halle (Saale), Germany

d Martin Luther University Halle-Wittenberg, Institute of Pharmacy, Chair of Downstream Processing, Weinbergweg 22, 06120 Halle (Saale), Germany

e Martin-Luther-University Halle-Wittenberg, Interdisciplinary Center of Materials Science, Department of Biomedical Materials, Heinrich-Damerow-Str. 4, 06120 Halle (Saale), Germany

f Institute of Pharmacy, Pharmaceutical Technology, Faculty of Medicine, Leipzig University, 04317 Leipzig, Germany

\*Corresponding author: Christian Wölk ([christian.woelk@medizin.uni-leipzig.de](mailto:christian.woelk@medizin.uni-leipzig.de))

**TABLE OF CONTENT****KEYWORDS**

biomaterials, bone morphogenetic proteins, DNA-loaded lipid nanoparticles, human stem cells, Layer-by-Layer, non-viral gene delivery, osteogenic differentiation

## ABSTRACT

Critical-size bone defects are associated with incomplete or lack of regeneration. The current clinical application of growth factors (GF) by conventional delivery systems is hampered by high dosages with undesired side effects on patients and their rapid degradation. Hence, novel therapeutic strategies are required. The presented research applies a recently developed transfection-active ultrathin film as a potential surface coating for implants to promote osteogenic differentiation of stem cells through functionalization with nucleic acids. The surface coatings are composed of the polyelectrolytes hyaluronic acid and chitosan and assembled by the Layer-by-Layer (LbL) method. DNA lipid nanoparticles (DNA-LNP) are embedded in the film, which encapsulate the DNA encoding for bone morphogenetic protein 2 (BMP-2). The optimization of the film surface by adhesive protein modification promotes mesenchymal stem cells attachment as a prerequisite for DNA-LNP endocytosis. The efficient uptake of the DNA-loaded lipid nanoparticles from the polyelectrolyte multilayer (PEM) into stem cells is demonstrated by fluorescence-labelled DNA-LNPs and transfection studies. Gene expression analysis of osteogenic markers and histological staining methods show that the combination of PEM with DNA-LNPs permits an efficient *in situ* transfection of stem cells, leading to osteogenic differentiation of human mesenchymal stem cells (hMSC). In summary, we can demonstrate that the *in-situ* transfection system can control the fate of hMSC through transient expression of cytokines like BMP-2. This innovative gene-activated surface coating is a promising tool that potentially enables the production of cytokines under spatial control through *in situ* transfection at the bone defect and opens new avenues for replacement of GF application.

## 1. INTRODUCTION

Bone fractures, bone loss, bone defects and non-healing bone unions as a result of trauma or disease constitute major clinical problems [1]. From a health economic point of view, severe bone injuries cause immense costs: direct costs of medical treatment, indirect costs due to absence from work and intangible costs due to a reduced quality of life for patients [2]. Therefore, there is an urgent need for new therapeutic strategies. Bone tissue engineering aims to design materials or strategies that effectively promote bone tissue regeneration. Currently, an encouraging approach for the treatment of bone disorders is the use of protein/drug therapy, with local application of osteo-inductive growth factors such as bone morphogenetic proteins (BMPs) [3]. In particular, BMP-2 has been demonstrated to be the most notable cytokine and plays a key role in stimulating bone regeneration by binding to the specific BMP-2 membrane receptor on osteogenic precursor cells resulting in an activation of cellular signal transduction pathway for osteo-differentiation [3-5]. In fact, BMP-2 has been used clinically to heal non-union bone injuries, open tibia fractures and used for spinal fusion in FDA-approved systems for bone regeneration [6, 7]. The use of growth factors is therefore a promising strategy to establish new bone tissue engineering approaches.

However, the administration of recombinant BMP-2 remains problematic due to its short biological half-life, high cost, and frequent side effects such as oedema and ectopic bone formation when administered in supra-physiological amounts [8-10]. Indeed, gene therapy has proven advantageous compared to strategies using recombinant proteins, since transfection/transduction-mediated cellular production of cytokines or growth factors allows their release at physiological levels. Moreover, the local nucleic acid release systems (termed gene-activated matrices) allow a spatial control of protein production at the site of injury [11-15]. Furthermore, DNA is usually less expensive and more stable than most proteins used for therapeutic applications [14, 16]. In this context, studies have been carried out using non-protected plasmid DNA, encoding the protein of interest, which has been chemically or physically immobilized on substrates [17-19]. However, non-complexed DNA is exposed to the extracellular environment when released from the delivery system which results in rapid enzymatic degradation *in vivo*. Hence, any systems in which the DNA is protected are beneficial for therapeutic applications [20]. Therefore, for controlled local delivery of cytokine-encoding nucleic acids, appropriate delivery systems are required.

Transfection-active surface coatings can be prepared using the Layer-by-Layer (LbL) assembly, which is a widely used technique based on the alternating deposition of positively and negatively charged polyelectrolytes [25, 26]. Biogenic polyelectrolytes hyaluronan (HA) and chitosan (CHI) can be used for this purpose, since they represent polyanions and polycations, respectively. In addition, they have suitable properties for medical applications such as biocompatibility, biodegradability, and no immunogenicity and permit to mimic the composition of extracellular matrix to some extent [27, 28]. In addition, CHI possesses antibacterial properties, while the polyanion hyaluronan possesses anti-inflammatory properties that might be beneficial for the fabrication of functional coatings of bone implants [29-31]. Our previous studies revealed that positively charged DNA-LNPs embedded in multilayers (PEMs) fabricated with HA and CHI represent a promising transfection system, which provides a contact-triggered nucleic acid transfer without burst release tendencies [21]. In this proof-of-concept study we focused on the engineering aspect of DNA-LNP-functionalized PEMs. The DNA-activated PEM was successfully used to transfect the model cell line C2C12, a myoblast cell line from mice, and cells of the chorioallantoic membrane of the chicken embryo with the reporter gene encoding for green fluorescent protein (GFP). The transfection active component of LNPs was an equimolar mixture of the cationic lipid OH4 ((*N*-{6-amino-1-[*N*-(9*Z*)-octadec-9-enylamino]-1-oxohexan-(2*S*)-2-yl}-*N'*-{2-[*N,N*-bis(2-aminoethyl)amino]ethyl}-2-hexadecylpropandiamide)) and the zwitterionic co-lipid DOPE, a lipid-based non-viral nucleic acid delivery system providing efficient DNA transfer in different cell lines [22-24].

The present article aims to transfer the DNA-activated PEM concept to the clinically relevant topic bone regeneration by adapting it to the transfection of adipose-derived human mesenchymal stem cells (hMSC). The directed control of hMSC differentiation has enormous therapeutic potential. Hence, we focus here on the functionalization of the HA and CHI-based *in situ* transfection system [HA,CHI]<sub>5</sub>HA-(DNA-LNP)-[HA,CHI]<sub>1</sub>, developed in the above mentioned proof-of-concept study [21], with BMP-2 encoding DNA-LNPs, to use these DNA-activated LbL system to induce the osteogenic differentiation of hMSCs. Since attachment of cells is required for *in situ* transfection, hMSC growth and differentiation an optimization of the DNA-loaded PEM-with adhesive glycoproteins was studied to improve the attachment of hMSCs. We further screened for transfection efficacy in hMSCs using GFP-encoding DNA as reporter gene and for the potential to induce osteogenic differentiation of hMSCs using a BMP-2 sequence. In summary,

the designed gene-activated PEM loaded with BMP-2-encoding DNA-LNPs (Figure 1) triggered osteogenic differentiation of hMSCs, as demonstrated by gene expression analysis and immunofluorescence staining of extracellular matrix components which reveals that LbL based PEM have a high potential as DNA-activated surface coating suitable for bone regeneration.

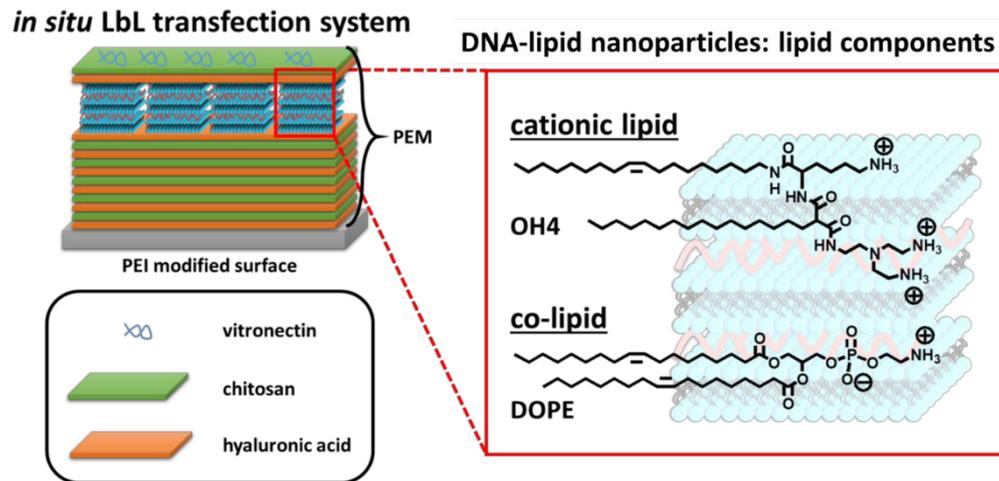


**Figure 1.** Schematic illustration of the concept of the gene-activated LbL system for the contact-triggered *in situ* transfection system. The polyelectrolyte multilayer system is composed of chitosan and hyaluronic acid. To achieve functionalization with nucleic acids, lipid nanoparticles loaded with nucleic acids, consisting of the lipids OH4 and DOPE, were embedded. The final coating of vitronectin improves interaction with stem cells.

## 2. MATERIALS AND METHODS

### 2.1 Materials

Native low-molecular weight chitosan (CHI,  $M_W \approx 62$  kDa, 85% degree of deacetylation) from Heppe Medical Chitosan GmbH (Halle, Germany) and hyaluronic acid sodium salt (HA) with an average molecular weight of 1.3 MDa from Kraeber & Co GmbH (Ellerbek, Germany) were used as polyelectrolytes for multilayer formation. Polyethylenimine (PEI, branched,  $M_W \approx 750$  kDa, Sigma Aldrich, Taufkirchen, Germany) was deposited as a priming layer in multilayer build-up. The plasmid DNA pCMV-GFP (pDNA-GFP) was acquired from Plasmid Factory (Bielefeld, Germany). The phospholipids 1,2-dioleoyl-*sn*-glycero-3-phosphoethanolamine (DOPE) and 1,2-dioleoyl-*sn*-glycero-3-phosphoethanolamine-*N*-(lissamine rhodamine B sulfonyl) (ammonium salt) (Rho-DOPE) were acquired from Avanti Polar Lipid, Inc. (Birmingham, AL, USA). The synthesis and characterization of OH4 (*N*-{6-amino-1-[*N*-(9Z)-octadec-9-enylamino]-1-

oxohexan-(2*S*)-2-yl}-*N'*-{2-[*N,N*-bis(2-aminoethyl)amino]ethyl}-2-hexadecylpropan diamide) was described in our previous work [32]. All chemicals and solutions, unless otherwise stated, were purchased from Sigma Aldrich (Taufkirchen, Germany).

## 2.2 Preparation of cationic liposomes

Cationic vesicles were prepared using the film hydration procedure [33]. OH4 and DOPE were separately dissolved in chloroform:methanol (8:2 v:v) and combined to an equimolar ratio. The organic solvent was removed by vacuum evaporation at 50°C for 30 min at 500 mbar and for further 1 h at <15 mbar. After the formation of solvent free lipid films, sterile filtered 10 mM MES buffer (pH 6.5, Carl Roth GmbH & Co. Kg, Karlsruhe, Germany) was added to give a final concentration of 1 mg/mL. Afterwards, the lipid dispersion was incubated at 50°C for 30 min while shaking (1400 rpm, Eppendorf Thermomixer 5436, Hamburg, Germany) followed by sonication at 37 kHz for 10 min at 30°C.

## 2.3 Plasmid DNA isolation (pDNA-BMP2)

Plasmid DNA encoding for human bone morphogenetic protein 2 (BMP-2) controlled by a human cytomegalovirus promoter (CMV) and containing a neomycin resistance gene was purchased from OriGene Technologies GmbH (Herford, Germany). These plasmids were cloned and amplified using *Escherichia Coli* DH5 $\alpha$  safety strain (Invitrogen™, Carlsbad, CA, USA). Plasmid purification was performed using a Plasmid Maxi Prep Kit (Qiagen, Hilden, Germany) according to manufacturer instructions, and the resulting plasmid DNA (pDNA) was resuspended in MilliQ water (Milli Q-plus system, Merck Millipore, Burlington, MA, USA). The plasmid DNA concentration and purity was measured using a UV spectrophotometer (Analytik Jena GmbH, Jena, Germany) at 260 and 280 nm and gel electrophoretic analysis.

## 2.4 DNA-LNP formation

DNA-LNP were prepared by combining plasmid DNA (pDNA) with the OH4:DOPE 1:1 (n:n) liposomes to an N/P ratio of 4 (ratio of primary amines of the cationic lipids – N to phosphate groups of the nucleic acid – P) resulting in DNA loaded compact nanoparticles [34]. As solvent sterile-filtered 10 mM MES buffer (pH 6.5) was used. The pDNA solution was added to the lipid dispersion in one step followed by gentle mixing with the pipet and an incubation period of 15 min at room temperature.

## **2.5 Basal polyelectrolyte multilayer (PEM) assembly using the Layer-by-Layer (LbL) method**

PEM assembly was prepared directly on the bottom of the used well plate (96-well plate, 24-well plate, or CELLview™ microscopy wells; well size comparable to 96-well; all Greiner Bio-One GmbH, Frickenhausen, Germany). The size of the well plate depended on the type of experiment: all experiments, which were evaluated at the CLSM or plate reader, were carried out in a CELLview™ microscopy well plate or 96-well plates. FACS and differentiation studies of stem cells (qPCR and alizarin assays) were performed in 24-well plates. All solutions were prepared using ultrapure water (Milli Q-plus system, Merck Millipore) and filtered through a 0.22 µm membrane filter (VWR, Darmstadt, Germany). Multilayer coating was performed at room temperature under gently shaking. CHI, HA, and PEI solutions were prepared at a concentration of 2 mg/mL in 0.15 M NaCl buffer, adjusted to pH 4.0. The washing steps were always carried out with 0.15 M NaCl, adjusted to pH 4.0. LbL build up was achieved using the pipet approach, wherein each polyelectrolyte solution was applied directly into well of a well plate. PEI was deposited as a priming layer to introduce a positive charge to the surface, providing support for the multilayer assembly. After adsorption of PEI for 15 min at room temperature with simultaneous shaking, the samples were rinsed twice with washing solution. The substrates were then incubated alternately with HA solution for 15 min, washed twice with 0.15 NaCl solution for 5 min each, followed by incubation with CHI solution for 15 min. Basal layers were generated by repeating the HA/CHI deposition for five cycles with an additional negatively charged layer of HA, named [HA/CHI]<sub>5</sub>HA. Subsequently, the basal PEM was used for loading with positively charged DNA-LNPs.

## **2.6 Loading of PEMs with DNA-LNPs**

Preformed DNA-LNPs, characterized by efficient DNA encapsulation and positive zeta potential [22, 32], were directly loaded on the basal PEM according to the LbL pipet approach, a loading protocol developed in previous research [21]. The preformed DNA-LNP solution was made up to 100 µL (for 96-well plates) or 300 µL (for 24-well plates) with 10 mM MES buffer pH 6.5 and transferred to the basal-PEM-film for adsorption as terminal layer, shaken gently for 2 h, and then rinsed three times with 0.15 M NaCl (adjusted to pH 4.0). After LNP embedding, the LbL method was used to deposit an additional layer of HA and a terminal CHI layer using the procedures

described above. This step was performed to protect the DNA-LNP layer and reduce desorption effects. The final PEM sequence was [HA,CHI]<sub>5</sub>HA-(DNA-LNP)-[HA,CHI]<sub>1</sub>.

### **2.7 Film modification with adhesive glycoproteins (protein immobilization)**

To improve the attachment of hMSCs on the multilayer system, two different adhesive glycoproteins were tested as a terminal coating of DNA-LNP-loaded PEMs. Human plasma fibronectin (FN) or human vitronectin (VTN; Stemcell Technologies, Cologne, Germany) were adsorbed on [HA,CHI]<sub>5</sub>HA-(DNA-LNP)-[HA,CHI]<sub>1</sub> PEMs. Different protein solutions (2.5, 5, 10, and 20 µg/100 µL in Hanks Balanced Salt Solution (HBSS buffer, Gibco, Thermo Fisher Scientific, Braunschweig, Germany)) were prepared from FN and VTN and incubated for 12 h at 8°C. After incubation, the PEMs were extensively washed with PBS (Gibco, Thermo Fisher Scientific) to remove unbound glycoprotein.

### **2.8 Quantification of adsorbed glycoproteins via immune fluorescence staining**

The [HA,CHI]<sub>5</sub>HA-(DNA-LNP)-[HA,CHI]<sub>1</sub> multilayers were produced in CELLview™ well plates. Multilayer films were incubated with VTN or FN as described above. The non-specific binding sites were further blocked using 1% (w/v) bovine serum albumin solution (BSA) in PBS at room temperature for 1 h. The order of staining for vitronectin-coated multilayers was designed as followed: (a) monoclonal anti-vitronectin antibody for 1 h; (b) anti-IgG secondary antibody for detection of the target primary antibody for 30 min. For FN staining (a) monoclonal anti-fibronectin antibody for 1 h and (b) anti-IgG secondary antibody for 30 min were used. For further information on antibodies and dyes, see Table 1 and Table 2. PBS washing (3 times, each 5 min) was performed after each staining step. Afterwards, all samples were briefly dipped in ultrapure water and mounted to object holders employing Mowiol 4-88 containing 25 mg/mL 1,4-diazabicyclo[2.2.2]-octane (Carl Roth GmbH & Co. Kg). Micrographs of the samples were carried out with a CLSM (LSM 710, Carl Zeiss, Oberkochen, Germany) at constant gain and laser intensity, as well as the same spectral range for fluorescence emission detection.

### **2.9 Cell Culture**

Commercially available adipose derived hMSCs (StemPro™) were obtained from Thermo Fisher Scientific. The hMSCs were stored and cultured according to the manufacture's recommendations. MesenPRO RS™ medium (BM) from Thermo Fisher Scientific was used for cultivation of hMSCs and was applied to the cells according to the manufacturer's instructions.

Cultured cells were grown at 37°C in a humidified 5% CO<sub>2</sub>/95% air atmosphere. The medium was replaced at a rate of 50% every 3 days until the cells reached 90% confluence, after which they were passaged and replaced into a new culture flask (Greiner Bio-One GmbH). Before the transfection system was applied in cell culture, they were washed twice with PBS for 5 min each and subsequently immersed in MesenPRO RS™ media for 15 min. Unless otherwise stated, a cell density of 1×10<sup>5</sup> cells/mL was utilized.

### 2.10 Cell Viability Studies

[HA,CHI]<sub>5</sub>HA-(DNA-LNP)-[HA,CHI]<sub>1</sub>-VTN coatings were seeded with hMSCs in CELLview™ slides for 24 h. Subsequently, cells were stained with LIVE/DEAD™ cell imaging kit (Thermo Fisher Scientific; living cells stained with calcein,  $\lambda_{\text{ex}}^{\text{max}} = 494 \text{ nm}$ ,  $\lambda_{\text{em}}^{\text{max}} = 517 \text{ nm}$ ; ethidium homodimer 1, if bound to DNA  $\lambda_{\text{ex}}^{\text{max}} = 528 \text{ nm}$ ,  $\lambda_{\text{em}}^{\text{max}} = 617 \text{ nm}$ ) according to the manufacturer's instructions. The control for living cells used in the experimental setup was the CELLview™ slide surface treated with 20 µg/mL fibronectin to have a surface with high biocompatibility. As control for dead cells, cells were treated at 60°C for 30 min to have a sample with non-viable cells [35, 36]. All samples were examined with CLSM (LSM 710) at constant gain and laser intensity, as well as the same spectral range for fluorescence emission detection.

### 2.11 Transfection efficiency studies (FACS analysis)

Cells were incubated for two different incubation periods (24 h and 48 h) at 37°C in a humidified incubator and 5% CO<sub>2</sub>. The PEM system [HA,CHI]<sub>5</sub>HA-(DNA-LNP)-[HA,CHI]<sub>1</sub>-VTN was loaded with pDNA-GFP. GFP expressing cells were quantified by flow cytometry. Briefly, after each incubation period cells were detached with 0.05% trypsin/0.02% EDTA solution from the PEM-film and centrifuged at 220 x g and 4°C for 5 min. After washing with PBS, the cells were resuspended in 500 µL of PBS containing 1% BSA. The relative fluorescence units were determined with a BD Accuri™ C6 Plus flow cytometer (BD Bioscience, Franklin Lakes, NJ, USA). Single cells were gated by size (FSC-H) and granularity (SSC) with the associated device software. Per measurement 10,000 cells were analysed (GFP:  $\lambda_{\text{ex}}^{\text{max}}$ : 488 nm,  $\lambda_{\text{em}}^{\text{max}}$ : 510 nm). The gated single cell population was used to detect GFP expressing cells by calculating the relative amount of transfected cells. All samples were tested in triplicates.

### 2.12 Immune fluorescence staining of cells

In all immunofluorescence staining experiments with hMSCs, the cells were washed with PBS after the respective incubation time and then fixed with 4% para formaldehyde in PBS for 15 min

at room temperature. After washing with PBS for three times (each 5 min), 0.5% (v/v) Triton-X-100 was added for permeabilization (10 min), followed by PBS rinsing (3 times, each 5 min). The non-specific binding sites were further blocked using 1% (w/v) bovine serum albumin solution (BSA) in PBS at room temperature for 1 h. The antibodies and fluorescent dyes used for the respective experiments are mentioned in the respective section. All dyes and antibodies were diluted in 1% (w/v) BSA in PBS, and cells were incubated in each solution at room temperature. PBS washing (3 times, each 5 min) was performed after incubation with fluorescent dyes. Each antibody incubation step was followed by washing with PBS for 30 min under gentle shaking, twice. Afterwards, all samples were briefly washed with ultrapure water and mounted with Mowiol 4-88 containing 25 mg/mL 1,4-diazabicyclo[2.2.2]-octane. Samples were analysed with CLSM (LSM 710). The Zeiss efficient navigation (ZEN 2011) software and Fiji [37] were used for qualitative image analysis and quantitative cell count, respectively, where results represent three replicates per sample. If fluorescence intensities were quantified and compared, constant gain and laser intensity, as well as the same spectral range for fluorescence emission detection were applied.

### 2.13 Cell adhesion studies

After 24 h of incubation of hMSCs seeded on [HA,CHI]<sub>5</sub>HA-(DNA-LNP)-[HA,CHI]<sub>1</sub>-VTN, the cells were treated as described in section 2.12. For immunofluorescence staining, the following antibodies were used: monoclonal anti-vinculin clone hVIN-1 mouse ascites fluid antibody, goat anti-mouse IgG secondary antibody Alexa Fluor 647 and Phalloidin-Atto 488 incubated for 1 h each. BOBO-1 was incubated for 30 min. The antibodies were diluted as shown in the table 1 below. Cell images were analysed using CellProfiler<sup>TM</sup> cell image analysis software (see Supporting Information Figure S1) [38].

**Table 1:** Primary antibodies

Primary Antibodies	Dilution in 1% BSA	Biological source	Manufacturer
Vinculin	1:200	mouse	Sigma Aldrich, Taufkirchen, Germany
Collagen I	1:100	mouse	Santa Cruz, TX, USA

Osteocalcin	1:100	mouse	Santa Cruz, TX, USA
Vitronectin	1:40	mouse	Sigma Aldrich, Taufkirchen, Germany
Fibronectin	1:400	rabbit	Sigma Aldrich, Taufkirchen, Germany

**Table 2:** Secondary-Antibodies and dyes

<b>Secondary Antibodies and dyes</b>	<b>Conjugate</b>	<b>Dilution in 1% BSA</b>	<b>Excitation maxima</b>	<b>Emission maxima</b>	<b>Manufacturer</b>
Goat anti-Mouse IgG (H+L)	AlexaFluor™ 647	1:1000	650 nm	665 nm	Thermo Fisher Scientific, Braunschweig, Germany
Goat anti-Rabbit IgG (H+L)	AlexaFluor™ 647	1:1000	650 nm	665 nm	Thermo Fisher Scientific, Braunschweig, Germany
Goat anti-Mouse IgG (H+L)	Cy-2	1:200	490 nm	510 nm	Dianova, Hamburg, Germany
Rabbit anti-Mouse IgG (H+L)	Cy-3	1:200	550 nm	570 nm	Dianova, Hamburg, Germany

Phalloidin Atto 488	Atto 488	1:50	501 nm	523 nm	Sigma Aldrich, Taufkirchen, Germany
BOBO-1 <sup>TM</sup> Iodide		1:200	462 nm	481 nm	Invitrogen <sup>TM</sup> , Carlsbad, CA, USA
TO-PRO <sup>TM</sup> -3 Iodide		1:400	642 nm	661 nm	Invitrogen <sup>TM</sup> , Carlsbad, CA, USA

#### 2.14 Localization of labelled DNA after transfection

To visualize the DNA after a transfection period of 72 h, pDNA-GFP was labelled with a Cy-5-Conjugate (LabelIT<sup>®</sup> Nucleic Acid Labeling Reagents, Mirus Bio LLC, Madison, WI, USA) according to manufacturer's instructions. After incubation, the cells were fixed, permeabilized and blocked as described above. The order of staining was designed as follows: (a) Phalloidin-Atto 488 for staining filamentous actin for 1 h and (b) BOBO-1 for staining the nucleus with an incubation period of 30 min (Table 2). All dyes were incubated at room temperature and protected from light.

#### 2.15 Detection of fibronectin matrix

To study the development of a FN matrix secreted and organized by hMSCs the cells were cultured for 72 h on [HA,CHI]<sub>5</sub>HA-(DNA-LNP)-[HA,CHI]<sub>1</sub>-VTN. After incubation, the cells were fixed, permeabilized, and blocked as described above. Actin filaments were stained using Phalloidin-Atto 488, while secreted FN was visualized by a polyclonal anti-FN antibody followed by AlexaFluor 647-labelled anti-rabbit antibody (Table 1 and 2). All antibodies and dyes were incubated for 1 h.

#### 2.16 Osteogenic differentiation

Trypsinized hMSCs were seeded in MesenPRO RS<sup>TM</sup> media directly onto pDNA-BMP2-functionalized [HA,CHI]<sub>5</sub>HA-(DNA-LNP)-[HA,CHI]<sub>1</sub>-VTN and were incubated at 37 °C for 24 h to allow the cells to adhere to the surface. Cells used in this study were from passage 1 to 6 and

50% of the culture media was changed three times a week. After the cells had reached 90% confluence, the medium was changed to induce osteogenic differentiation. The cells were cultured in osteogenic induction medium (OM) containing 0.1  $\mu\text{M}$  dexamethasone, 10 mM sodium  $\beta$ -glycerophosphate, and 0.05 mM ascorbic acid-2-phosphate, in addition to the basal cell culture medium (BM) as described above. For the positive control, StemPro™ Osteogenic-Differentiation Kit from Thermo Fisher Scientific was applied according to the manufacturer's protocol. As negative control group, the cells grew on [HA,CHI]<sub>6</sub>-VTN and received BM (MesenPRO RS™ medium). The cells were incubated for four different time points: 7, 14, 21, and 28 days, medium was changed once a week. All samples were tested for ALP activity and mineralization (see below).

### 2.17 Alkaline phosphatase activity

Alkaline phosphatase (ALP) activity was quantified by the specific conversion of p-nitrophenyl phosphate (pNPP) into p-nitrophenol (pNP). After 7, 14, 21, and 28 days, the culture media was removed, and the cells washed with PBS buffer. 1% Triton-X was added to the cells and incubated for 20 min at 4°C. The resulting supernatant was collected and centrifuged at 13,000 rpm at 4°C for 5 min. Afterwards, 60  $\mu\text{L}$  of buffer solution containing 2 mg/mL pNPP was added to 20  $\mu\text{L}$  of the supernatant in a 96-well plate. The enzyme reaction was carried out at 37 °C for 1 h protected from light. The reaction was stopped by addition of 80  $\mu\text{L}$  2 M NaOH. The absorbance of formed pNP was determined at  $\lambda = 405$  nm in a microplate reader (FLUOstar Omega, BMG Labtech, Ortenberg, Germany). A standard curve was extrapolated by using pNP values ranging from 0 to 20 nmol/well. The total protein content was quantified to normalize the ALP activity. For this purpose, 200  $\mu\text{L}$  Bicinchoninic acid (BCA) working solution was added to 20  $\mu\text{L}$  cell lysate per well in a 96-well plate and was incubated at 37 °C for 30 min. Afterwards, the absorption was measured at 550 nm with the microplate reader.

### 2.18 Mineralization assays

After each incubation period, calcium phosphate deposition was investigated by Alizarin Red S staining. Briefly, the samples were washed once with PBS and fixed with 4% paraformaldehyde for 10 min. After twice washing with distilled water, Alizarin Red S (2%, pH 4.2, Carl Roth GmbH & Co. Kg) solution was added into each well, incubated for 45 min under light exclusion at room temperature. Finally, the excess dye was removed by washing with distilled water. Images were

taken in transmission mode with a Nikon ECLIPSE Ti2, Tokyo, Japan) equipped with a CCD camera (DCIN, Tokyo, Japan).

The commercial mineralization kit (OsteoImage™ Mineralization Assay, Lonza, Basel, Switzerland) was used to visualize specifically hydroxyapatite portion of bone-like nodules deposited by cells by measuring the fluorescence at  $\lambda_{\text{ex}}^{\text{max}} = 495 \text{ nm}$  /  $\lambda_{\text{em}}^{\text{max}} = 519 \text{ nm}$ . This assay, as described by the manufacturer, uses a fluorescent staining reagent that binds specifically to the hydroxyapatite portion of the biomineralized structures. The intensity of the green fluorescence is proportional to the amount of hydroxyapatite in the sample. All samples were examined with CLSM (LSM 710). To ensure comparability, constant gain and laser intensity as well as the same spectral range were used for fluorescence emission detection.

### **2.19 Osteocalcin and collagen I staining**

After 14 days of incubation with osteogenic medium (OM) cells were fixed, permeabilized and blocked as described above. For immune fluorescence staining, the following antibodies were used: Collagen I, CY-2, Osteocalcin, CY-3, and ToPro 3. The antibodies were diluted as summarized in Table 1 and Table 2. Each antibody solution was incubated for 30 min. All samples were examined with CLSM (LSM 710)

### **2.20 RNA Extraction and quantitative PCR**

After 28 days of incubation with osteogenic medium (OM) the RNA was extracted from samples using Aurum Total RNA Mini Kit spin columns from BioRad (Hercules, CA, USA) according to the manufacturer's recommended procedure. First strand cDNA was synthesized using an iScript Advanced cDNA Synthesis Kit for RT-qPCR (Biorad) in 20  $\mu\text{L}$  reactions, according to the manufacturer's instructions. RT-qPCR was performed under standard enzyme and cycling conditions on a CFX Connect Real-Time PCR Detection System (Biorad). Primer sets were pre-validated by PrimePCR Probe Assays from Biorad (for transcription factor Noggin (Nog; assay ID: qHsaCEP0054879), Collagen type 1 alpha 1 (Col1a1; assay ID: qHsaCEP0050510), Run-related transcription factor 2 (RunX2; assay ID: qHsaCEP0051329), Alkaline Phosphatase (Alpl; assay ID: qHsaCEP0024224) and BMP-2 (Alpl; assay ID: qHsaCIP0029912). The reference gene RPLP0 (assay ID: qHsaCEP0041375) was also used in this study. Data analysis was performed using the BioRad CFX Manager Software 3.0. The conditions of RT-qPCR were as follows: 95°C for 30 s followed by 39 cycles at 95°C for 15 s and 60°C for 30 s. The relative expression levels

for each gene were calculated and normalized to the reference gene RPLP0 by the delta-delta- $C_t$  method ( $2^{-\Delta\Delta C_t}$ )[39].

### 2.21 Statistical Analysis

All statistical analyses were performed with Origin 8G software. Means, standard deviations were calculated. Analysis of significance was performed by one-way ANOVA followed by Scheffé post hoc test. A value of  $p < 0.05$  was considered significantly different indicated by an asterisk. The level of significance  $\alpha$  was set to 5%. Further, box plots are shown where appropriate. The box indicates the 25th and 75th percentiles, and the dash indicates the median, respectively.

## 3. RESULTS AND DISCUSSION

In the published proof-of-concept study, the LbL system [HA,CHI]<sub>5</sub>HA-(DNA-LNP)-[HA,CHI]<sub>1</sub> was finally coated with fibronectin to improve the attachment of C2C12 cells [21]. In the present study, this *in situ* transfection system was planned to be used to transfect hMSCs to initiate the osteogenic differentiation [40]. First cell seeding tests indicated an inadequate cell interaction. Therefore, the optimal conditions for efficient cell adhesion had to be screened for hMSCs, since cell adhesion and spreading is related to differentiation [41]. Hence, an optimization of the glycoprotein modification of the [HA,CHI]<sub>5</sub>HA-(DNA-LNP)-[HA,CHI]<sub>1</sub> had to be done. The adsorption of fibronectin (FN) or vitronectin (VTN) on the film surface was studied by immune fluorescence staining and confocal microscopy. Both glycoproteins have binding motives for integrin receptors of the cell surface [42, 43]. Five different concentrations of adhesive proteins (0, 2.5, 5, 10, and 20  $\mu\text{g}$  per 100  $\mu\text{L}$ ) were screened and the fluorescence intensity was determined (Figure 2). With increasing amount of both glycoproteins in the incubation medium, the amount of adsorbed proteins increased. In the case of VTN, significantly increased relative fluorescence units (RFU) were found for each increase in protein amount, with a tendency to reach a plateau at 20  $\mu\text{g}$ . For FN the plateau effect of adsorption was more obvious due to an absence of a significant difference between 10  $\mu\text{g}$  and 20  $\mu\text{g}$  of incubated glycoprotein. According to this data we applied the concentration of 20  $\mu\text{g}/100\mu\text{L}$  (0.2  $\mu\text{g}/\mu\text{L}$ ) for the modification of [HA,CHI]<sub>5</sub>HA-(DNA-LNP)-[HA,CHI]<sub>1</sub> with FN or VTN for the cell adhesion and cell viability studies (Figure 3).

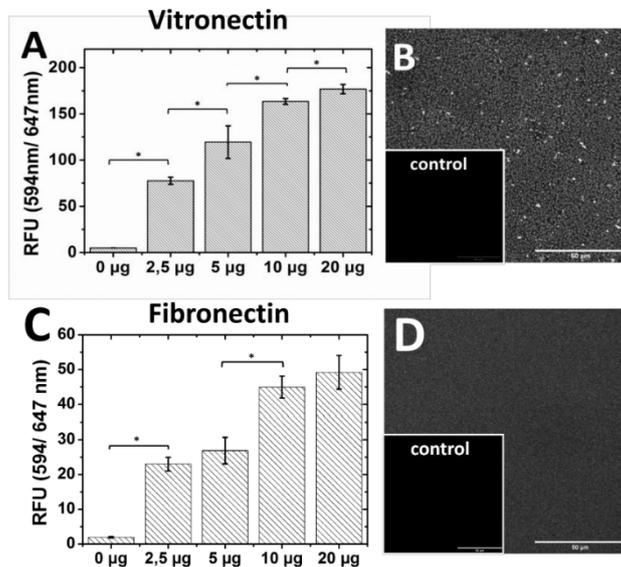


**Figure 2.** A/C) Fluorescence intensity of  $[\text{HA,CHI}]_5\text{HA}-(\text{DNA-LNP})-[\text{HA,CHI}]_1$  with a final coating of (A) vitronectin (VTN) or (B) fibronectin (FN) of different concentrations (0 µg to 20 µg in 100 µL incubating a film area of 0.34 cm<sup>2</sup>). The fluorescence was determined using confocal microscopy after immune fluorescence staining of films. The staining was performed after carefully washing of the surface with the aim to quantify only the glycoprotein fraction bound to the PEM system. CLSM pictures were analysed for RFU determination using Fiji software evaluating 10 images per condition. Bars represent the means ± SD of n = 10. The stars indicate significant differences determined by a one-way-ANOVA test ( $\alpha = 0.05$ ,  $p < 0.05$ ), followed by a Scheffé-Post-Hoc Test. B/D) Representative CLSM image of  $[\text{HA,CHI}]_5\text{HA}-(\text{DNA-LNP})-[\text{HA,CHI}]_1$  with (B) VTN coating or (D) FN coating resulting from an incubation with a solution of 20 µg glycoprotein per 100 µL. The control image shows  $[\text{HA,CHI}]_5\text{HA}-(\text{DNA-LNP})-[\text{HA,CHI}]_1$  in absence of VTN or FN using the same antibody staining and imaging conditions. The bars in (B) and (D) represent 50 µm.

After 24 h of incubation, hMSCs applied to the glycoprotein modified surfaces showed increased cell viability compared to the untreated  $[\text{HA,CHI}]_5\text{HA}-(\text{DNA-LNP})-[\text{HA,CHI}]_1$  surface (Figure 3A). Viability was determined using fluorescence-based live-dead staining (living cells → green, dead cells → red). Differences were observed in the cell attachment studies. FN and VTN coatings resulted in a significant higher number of cells attached to the PEM compared to the untreated  $[\text{HA,CHI}]_5\text{HA}-(\text{DNA-LNP})-[\text{HA,CHI}]_1$  system (Figure 3B, upper diagram). The cell count on VTN-coated PEMs was comparable to the positive control, which was an empty well. The cell number determined for FN-coated  $[\text{HA,CHI}]_5\text{HA}-(\text{DNA-LNP})-[\text{HA,CHI}]_1$  was significant lower. The cell area also provides information about the quality of cell attachment. A larger area indicates a better affinity and may also promote osteogenesis of hMSC [44]. For both glycoprotein coatings,

significantly increased cell areas were observed compared to the untreated PEM (Figure 3B, lower diagram). The cell area determined for both glycoprotein modifications was not significantly different to the positive control, though for FN a tendency to smaller cell areas was observed. In conclusion, VTN modification of  $[\text{HA,CHI}]_5\text{HA}-(\text{DNA-LNP})-[\text{HA,CHI}]_1$  was associated with a better cell adhesion profile for hMSCs compared to FN. These observations led us to use VTN as the glycoprotein of choice for the terminal PEM modification.

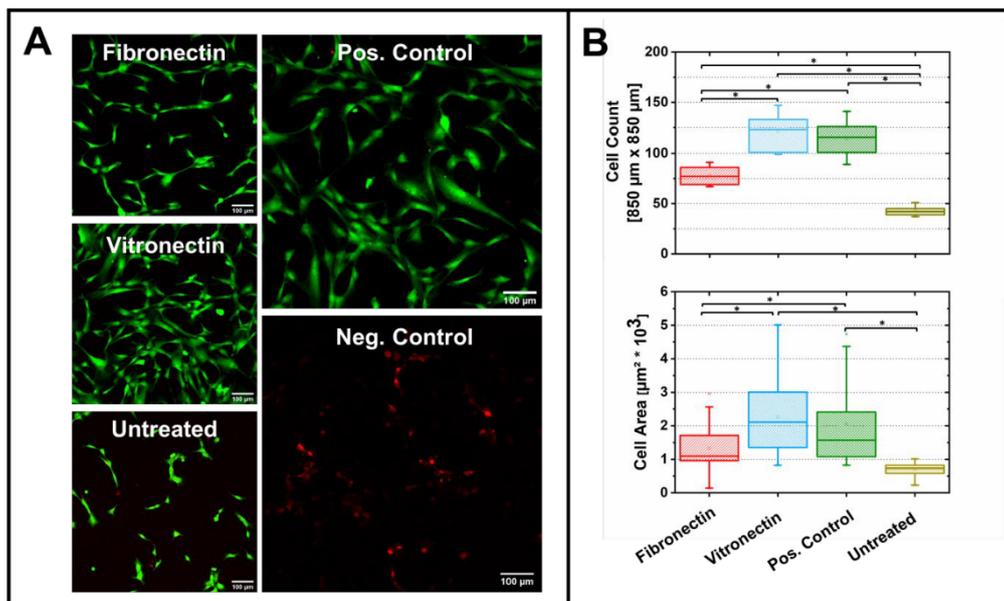


**Figure 3.** (A) hMSCs stained after 24 h of incubation using LIVE/DEAD™ cell imaging. Living cells are shown in green and dead cells in red. The cells grew on  $[\text{HA,CHI}]_5\text{HA}-(\text{DNA-LNP})-[\text{HA,CHI}]_1$  PEMs with a final coating of two different adhesive glycoproteins: FN and VTN. The  $[\text{HA,CHI}]_5\text{HA}-(\text{DNA-LNP})-[\text{HA,CHI}]_1$  without final peptide modification is labelled as untreated. The positive control used in this experiment was a PEM-free surface treated with 20 µg/100µL FN. As negative control, hMSCs were treated at 60°C for 30 min to induce cell death. (B) Quantification of cell area and cell number of hMSCs growing under the same conditions as in (A). Image analysis was performed using Fiji software with investigation of at least 10 images per condition. The stars indicate significant differences determined by a one-way-ANOVA test ( $\alpha = 0.05$ ), followed by a Scheffé-Post-Hoc Test.

To obtain more insight into the quality of cell adhesion on  $[\text{HA,CHI}]_5\text{HA}-(\text{DNA-LNP})-[\text{HA,CHI}]_1$ -VTN films, the presence of focal adhesions was determined using immune fluorescence staining of vinculin (Figure 4). In the absence of vinculin-positive focal adhesions, cell–matrix and cell–cell adhesion as well as migration rates are dramatically impaired, indicating that vinculin plays a crucial role in focal adhesion initiation [45, 46]. Figure 4 demonstrates that hMSCs on  $[\text{HA,CHI}]_5\text{HA}-(\text{DNA-LNP})-[\text{HA,CHI}]_1$ -VTN were characterized by a strong

organization of actin filaments distributed longitudinally (green) and vinculin-positive focal adhesions were detected at the end of actin filaments (magenta). (DNA-LNP)-loaded multilayers had a comparable number of vinculin-positive focal adhesions per  $\mu\text{m}^2$  to the positive control (Figure 4E). The positive control was a FN-modified glass surface (20  $\mu\text{g}$  FN/ 100  $\mu\text{L}$ ) seeded with hMSCs, as also used for the adhesion studies presented in Figure 3.

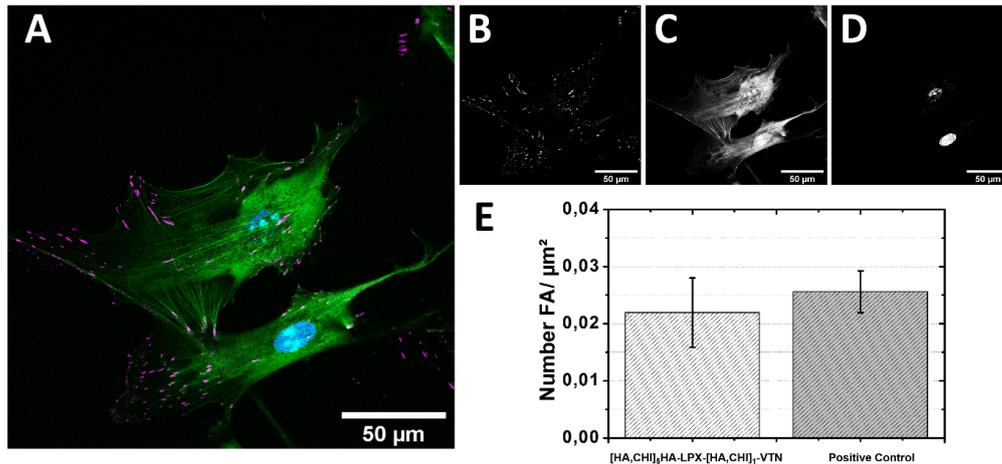


**Figure 4.** (A) CLSM micrographs of hMSCs after 24 h stained by immune fluorescence for vinculin. The cells were seeded on [HA,CHI]<sub>5</sub>HA-(DNA-LNP)-[HA,CHI]<sub>1</sub>-VTN. Vinculin is shown in magenta, actin in green and nuclei in blue. (B) Alexa Fluor 647 signal ascribed to vinculin. (C) Phalloidin -Atto 488 signal ascribed to filamentous actin. (D) BOBO-1 signal for nuclei staining. (E) Analysis of number of focal adhesions per  $\mu\text{m}^2$  compared to a positive control (hMSCs on FN coated glass surface). The analysis was carried out by evaluating 20 confocal images per condition with the software CellProfiler™. Mean and standard deviation are given. The difference between sample and positive control was not significant using t-test with a significance level of 0.05. The procedure of focal adhesion counting is shown in the SI Figure S1.

Extracellular matrix (ECM) remodelling is involved in the regulation of cell proliferation and differentiation processes of hMSCs. A prominent component of the ECM is fibronectin, a highly functional component due to binding sites for extracellular matrix components collagen-I, proteoglycans with heparan sulfate side chains and integrins [47]. Immune fluorescence staining of hMSC on [HA,CHI]<sub>5</sub>HA-(DNA-LNP)-[HA,CHI]<sub>1</sub>-VTN indicated cell-associated fibronectin (magenta) after 72 h of incubation (Figure 5). The cells produced and deposited fibronectin at their surface and organized it into fibrillary structures as also shown in previous studies [48-50]. This observation confirmed an increased activity of hMSCs on the DNA-LNP-loaded PEMs by means of *de novo* synthesis of FN.

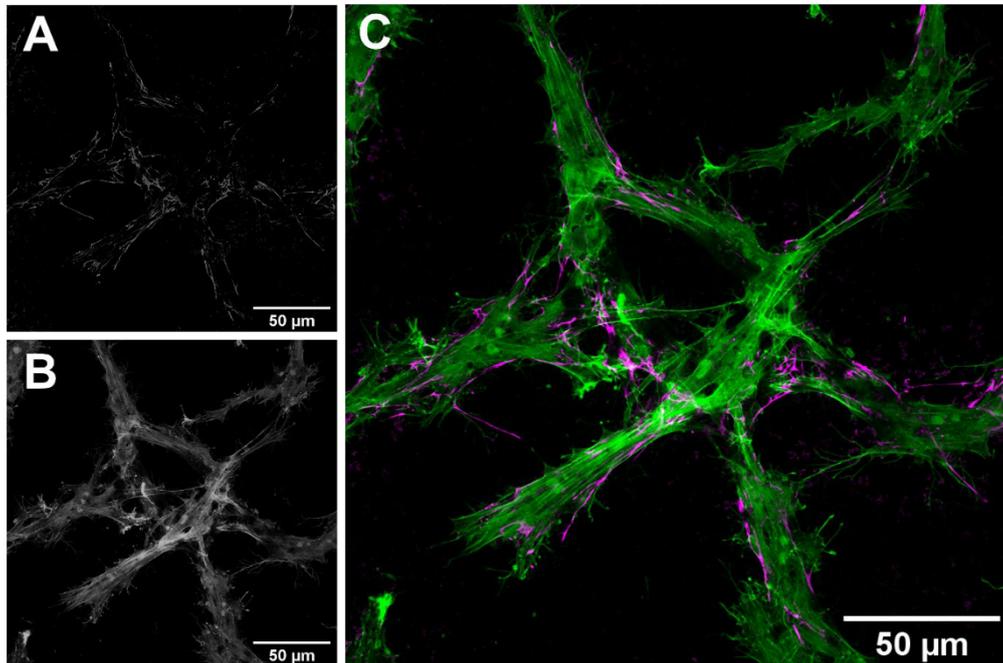


**Figure 5.** Fibronectin matrix secreted and organized by hMSCs after 72 h of incubation on [HA,CHI]<sub>5</sub>HA-(DNA-LNP)-[HA,CHI]<sub>1</sub>-VTN. (A) Fibronectin (magenta in merged image C) was stained with a polyclonal anti-FN antibody followed by AlexaFluor 647-labeled anti-rabbit antibody. (B) Actin filaments were visualized using Phalloidin Atto 488 staining (green magenta in merged image C). (C) Merged fluorescence channels of (A) and (B).

For successful *in situ* transfection, the cellular uptake of the DNA-LNPs is necessary. To study the cellular uptake Cy-5 labelled pDNA was loaded in the DNA-LNPs. The fluorescently tagged DNA-LNPs were embedded in the [HA,CHI]<sub>5</sub>HA-(DNA-LNP)-[HA,CHI]<sub>1</sub>-VTN system. Afterwards, hMSCs were seeded onto the fluorescently tagged *in situ* transfection system and after 3 days the cells were evaluated by CLSM for DNA-LNPs uptake (Figure 6). Cellular uptake of Cy-5-labeled DNA was evidenced by a fluorescence signal that accumulated in the perinuclear region (arrow Figure 6D). Additional representative images can be found in the supplementary information Figure S2.

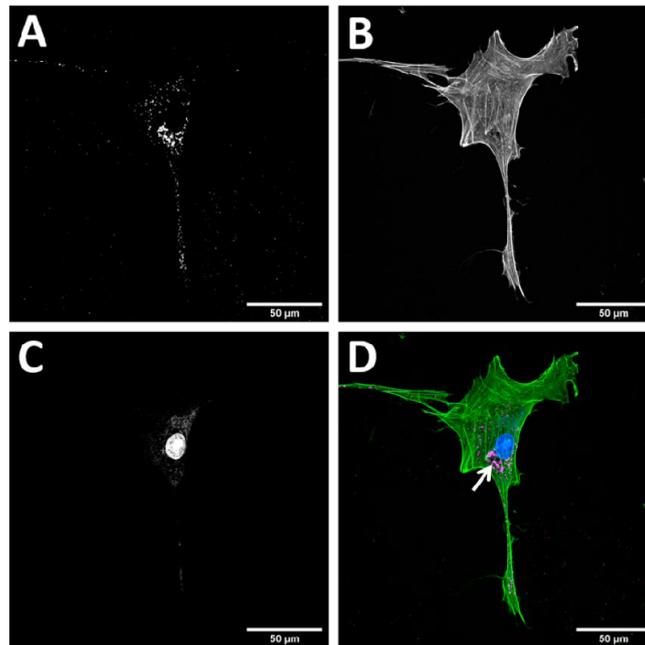


**Figure 6.** CLSM micrograph of transfected hMSCs after 72 h seeded on [HA,CHI]<sub>5</sub>HA-(DNA-LNP)-[HA,CHI]<sub>1</sub>-VTN with Cy-5-labeled DNA. **(A)** Cy-5 LabelIT®-labeled DNA **(B)** Phalloidin-Atto 488 for staining filamentous actin and **(C)** BOBO-1 for staining the nucleus. **(D)** merged image showing Cy-5 LabelIT®-labeled DNA of LNPs (magenta), Phalloidin-Atto 488 labelled actin (green) and BOBO-1 labeled nucleus (blue). The scale bar represents 50 µm.

The transfection efficacy was evaluated using plasmid DNA encoding for GFP. Figure 7A shows representative flow cytometry results of hMSCs which grew on the [HA,CHI]<sub>5</sub>HA-(DNA-LNP)-[HA,CHI]<sub>1</sub>-VTN system. The number of GFP-positive cells varies in a time-dependent manner. After 24h, 5.5% of the cells were GFP-positive, while 48h post-seeding on the film, 15.7% of the cells were transfected. These results suggest that the top layer consisting of hyaluronic acid and chitosan above the DNA-LNP-layer has a transfection-delaying effect. In order to investigate this effect in more detail, live cell imaging CLSM studies were performed (Figure 7B, C). For this purpose, we used increasing thicknesses of the cover layers ([HA,CHI]<sub>1</sub>, [HA,CHI]<sub>3</sub>, [HA,CHI]<sub>5</sub>) to separate the cells from the DNA-LNP-layer with the aim of getting more information of the transfection kinetics as a function of the cover layer thickness. The results are plotted as fluorescence intensity per well versus time (Figure 7B). Representative fluorescence micrographs are shown in Figure 7C. After a lag time of approximately 5h, cells grown on the standard system

[HA,CHI]<sub>5</sub>HA-(DNA-LNP)-[HA,CHI]<sub>1</sub>-VTN show an increasing fluorescence intensity due to GFP expression of transfected hMSCs. After that, the intensity increased steadily during the evaluated period of 20h. If the embedded DNA-LNPs were covered by an increasing number of cover layers, the transfection efficiency decreased within the screened time frame. We can expect that the access of the hMSCs to the DNA-LNP-layer is hindered by the presence of cover layers. As the thickness of the top layer increases, a longer time is required to reach the DNA-LNP layer for efficient DNA uptake. The system [HA,CHI]<sub>5</sub>HA-(DNA-LNP)-[HA,CHI]<sub>3</sub>-VTN is characterized by an prolonged lag time and a slower increase of the fluorescence intensity caused by transfected cells compared to the standard system [HA,CHI]<sub>5</sub>HA-(DNA-LNP)-[HA,CHI]<sub>1</sub>-VTN. The system [HA,CHI]<sub>5</sub>HA-(DNA-LNP)-[HA,CHI]<sub>5</sub>-VTN was on the control level of the DNA-LNP-free LbL film within the investigated time frame. In conclusion, the transfection system has the potential for a prolonged release of nucleic acids and might also represent a protective barrier against premature degradation in a physiological environment. Nevertheless, this has not been investigated in detail in this work.

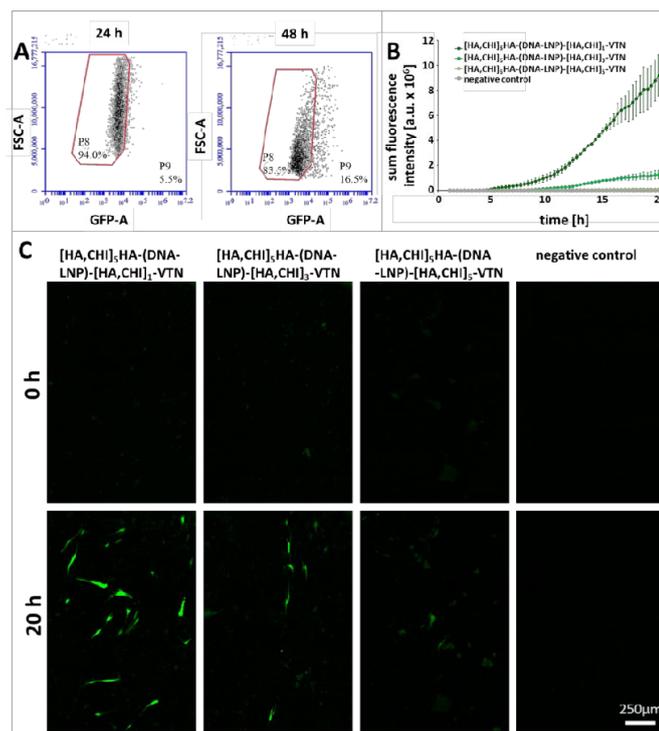


**Figure 7.** Transfection efficiency of PEM *in situ* transfection systems loaded with DNA-LNP bearing pDNA which encodes for GFP. A) Representative transfection efficiency of hMSCs cells growing on [HA,CHI]<sub>5</sub>HA-(DNA-LNP)-[HA,CHI]<sub>1</sub>-VTN for two different time points: 24 h and 48 h and determined by FACS as % GFP-positive cells. B) Evaluation of the transfection efficiency by live cell imaging of the green fluorescence of cells in a well plate as a function of the thickness of the cover layer (layer covering the (DNA-LNP) layer; following cover layers were investigated: [HA,CHI]<sub>1</sub>, [HA,CHI]<sub>3</sub>, [HA,CHI]<sub>5</sub>). The results are from two independent measurements, with each measurement performed in triplicate. C) Representative fluorescence micrographs on the time points 0h and 20h of the transfection experiment shown in (B). GFP fluorescence is shown in green.

After proven DNA transfer processes of the system [HA,CHI]<sub>5</sub>HA-(DNA-LNP)-[HA,CHI]<sub>1</sub>-VTN into hMSCs, the system was tested with a plasmid DNA encoding for BMP-2. The strategy aimed to induce differentiation of stem cells by *in situ* transfection with a relevant cytokine for osteogenic differentiation [51]. Two commonly used standard assays were utilized to screen for osteogenic differentiation: the activity of ALP, an enzyme which is needed to generate phosphate ions from phosphate esters for hydroxyapatite production [52, 53], and a staining of calcium phosphate deposition as direct indicator of hydroxyapatite (alizarin red staining) [54]. As negative control, hMSCs were seeded on a DNA-free LbL film [HA,CHI]<sub>6</sub>-VTN to exclude the effect of differentiation due to cell spreading-related integrin signalling during cell-surface contact [44]. As positive control, the hMSCs were treated with StemPro™ Osteogenic-Differentiation Medium containing BMP-2, which is known to induce osteogenic differentiation. Compared to the negative control, a significantly increased ALP activity for the [HA,CHI]<sub>5</sub>HA-(DNA-LNP)-[HA,CHI]<sub>1</sub>-VTN system on day 14, 21, and 28 after start of the differentiation experiment was observed, while on day 7 the ALP level was comparable (Figure 8A). Comparing the *in situ* transfection system with the positive control, a kinetic difference in ALP activity was observed (Figure 8A). The positive control showed a significantly higher ALP level on day 7, whereas on day 28 only the [HA,CHI]<sub>5</sub>HA-(DNA-LNP)-[HA,CHI]<sub>1</sub>-VTN showed a significant increase in ALP activity. In contrast, on day 28 the positive control had an ALP level comparable to the negative control. Such peak effects of ALP activity, as observed in the positive control, are known from literature [55, 56]. For the (DNA-LNP)-loaded transfection system [HA,CHI]<sub>5</sub>HA-(DNA-LNP)-[HA,CHI]<sub>1</sub>-VTN, a delay in BMP-2 formation and the associated initiation of osteogenic differentiation can be assumed due to the aforementioned time delay in transfection, while BMP-2 was present in the positive control from the beginning of the experiment. The alizarin red staining proved efficient calcium deposition for the [HA,CHI]<sub>5</sub>HA-(DNA-LNP)-[HA,CHI]<sub>1</sub>-VTN sample and the positive control after 21 and 28 days, while the negative control showed no red staining indicating the absence of mineralized nodules (Figure 8B).

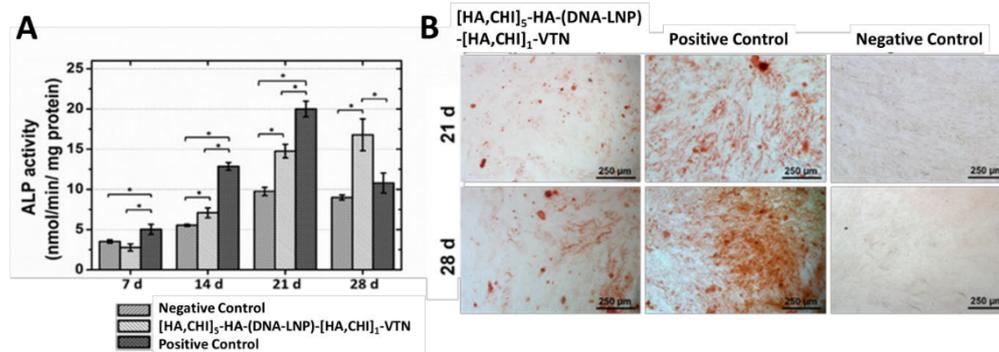


**Figure 8.** A) Quantification of ALP activity of hMSCs seeded on [HA,CHI]<sub>5</sub>HA-(DNA-LNP)-[HA,CHI]<sub>1</sub>-VTN for different culture periods. The negative control was grown on [HA,CHI]<sub>6</sub>-VTN and treated with basal medium without BMP-2 supplements, while the positive control was cultured in absence of PEM and received StemPro™ Osteogenic-Differentiation Medium. Results are expressed as mean ± SD n=3 for each bar. The stars indicate significant differences determined by a one-way-ANOVA test ( $\alpha = 0.05$ ), followed by a Scheffé-Post-Hoc test. B) *In vitro* osteoblast differentiation of hMSCs grown on DNA-LNP-loaded PEMs. hMSCs were induced to differentiate into osteoblasts for 21 and 28 days. Cells were stained with alizarin red S (red stain) for matrix mineralization (magnification,  $\times 10$ ). The controls were treated comparably as mentioned in (A). Images were taken in transmission mode with a Nikon ECLIPSE Ti2, Tokyo, Japan) equipped with a CCD camera (DCIN, 12 V, EXT1/0, Tokyo, Japan).

Since the extracellular bone matrix contains hydroxyapatite, a phosphate mineral with the composition  $\text{Ca}_{10}(\text{PO}_4)_6(\text{OH})_2$ , a method for a mineral-specific staining provides more information than non-specific alizarin calcium staining. According to the manufacturer, OsteoImage™ is a fluorescent dye for specific hydroxyapatite staining. It can be used qualitatively and quantitatively. Figure 9 shows a positive hydroxyapatite staining for the [HA,CHI]<sub>5</sub>HA-(DNA-LNP)-[HA,CHI]<sub>1</sub>-VTN and the BMP-2-containing positive control after 21 and 28 days. The quantitative evaluation of the OsteoImage™ signal showed a significant increase in hydroxyapatite levels from day 14 to day 28. A significant higher fluorescence for the positive control at day 28 was observed. This effect may also be due to the delayed BMP-2 expression of the DNA-LNP-loaded transfection system. Nevertheless, the *in situ* transfection system [HA,CHI]<sub>5</sub>HA-(DNA-LNP)-[HA,CHI]<sub>1</sub>-VTN is able to induce the production of hydroxyapatite matrix.

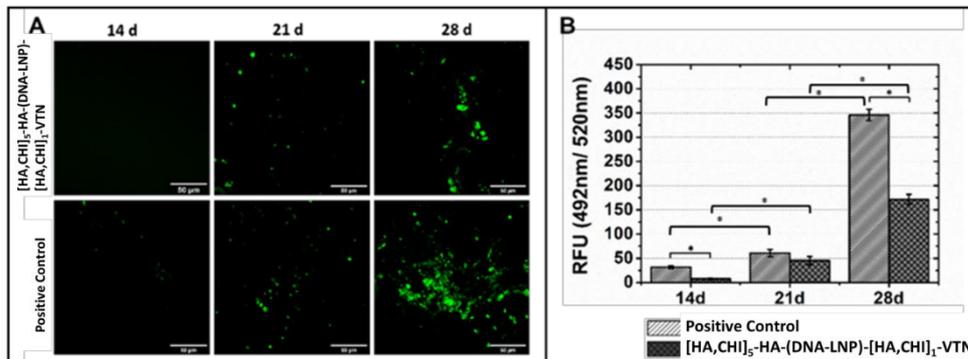


**Figure 9.** Hydroxyapatite content of the differentiation experiment with hMSCs growing on [HA,CHI]<sub>5</sub>HA-(DNA-LNP)-[HA,CHI]<sub>1</sub>-VTN loaded with pDNA-BMP-2 (Sample) compared with the positive control (BMP-2-treated hMSCs) after different incubation times. (A) The amount of hydroxyapatite was determined using an OsteoImage™ assay. The fluorescent staining reagent (green) binds to the hydroxyapatite portion of the mineralized matrix. For CLSM pictures of the negative control, see SI Figure S3. (B) An increase in the deposition of hydroxyapatite occurred in the sample and the positive control over time. Fluorescence intensity of CLSM pictures was calculated using ImageJ. Bars represent the means  $\pm$  SD of  $n = 3$ . Statistical analysis was done with one-way-ANOVA test ( $\alpha = 0.05$ ), followed by a Scheffé-Post-Hoc Test

However, the extracellular matrix of bone tissues also consists of organic components. Collagenous peptides are a main component with approximately 90% collagen I as the dominant species [57]. Among the other extracellular matrix components of bone proteoglycans, glycoproteins, SIBLINGs (Small Integrin-Binding Ligand N-Linked Glycoproteins), and  $\gamma$ -carboxyglutamic acid-containing proteins play an important role. The last group has osteocalcin as the main representative, which has a high affinity to hydroxyapatite and is a commonly used specific marker for extracellular bone matrix [57]. Figure 10 shows the immunostaining for collagen I and osteocalcin. For this study, an early time point was chosen, day 14, at which first evidence for hydroxyapatite deposition was apparent (Figure 9B). Both, the positive control and the [HA,CHI]<sub>5</sub>HA-(DNA-LNP)-[HA,CHI]<sub>1</sub>-VTN system, showed a positive staining for both marker proteins of the extracellular matrix on day 14 of the differentiation process (Figure 10).

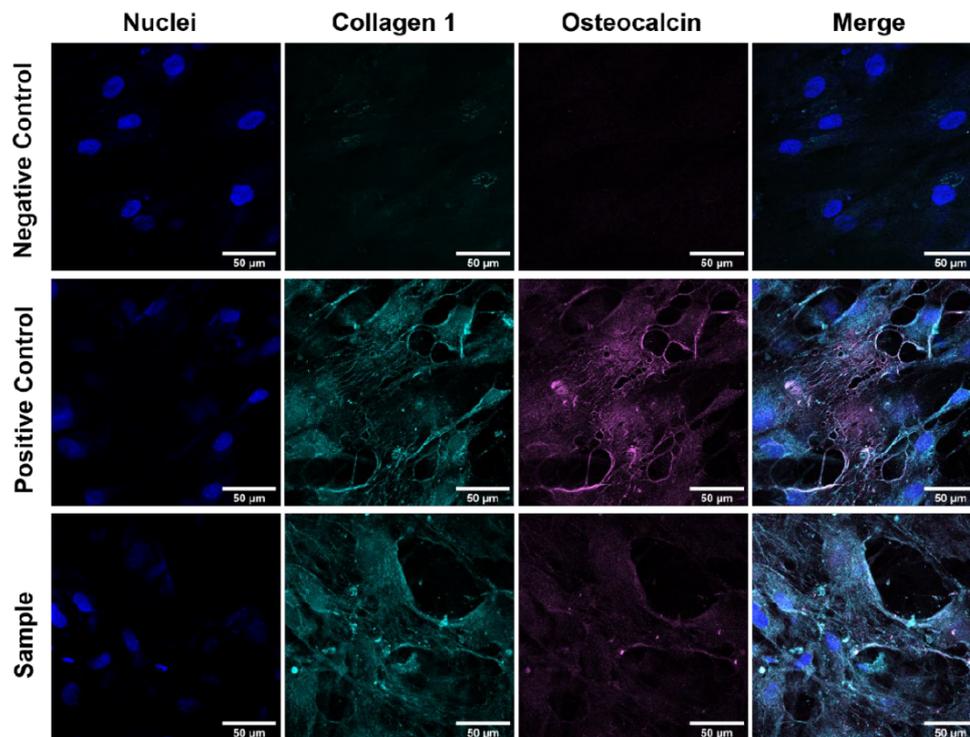


**Figure 10.** Immunofluorescence micrographs for extracellular matrix proteins which are typical markers for osteogenic differentiation, namely collagen 1 and osteocalcin. The collagen 1 antibody was visualized with a CY-2 secondary antibody (cyan blue) and the osteocalcin antibody with a CY-3 secondary antibody (magenta). Nuclei were stained by TO-PRO 3 (dark blue). Cells on DNA-LNP-loaded PEMs (Sample) were treated with osteogenic medium without BMP-2. Cells for positive control were treated with StemPro™ Osteogenic-Differentiation Kit. For the negative control group, the cells grown on a DNA-LNP free PEM received basal medium (BM). Images were taken with the CLSM. The scale bar represents 50 µm.

We also checked the osteogenic differentiation at the gene expression level by quantifying the mRNA using qPCR on day 28 of the differentiation experiments, the latest time point evaluated in our studies. The overview of the results is given in Figure 11. Expression of BMP-2 was of particular interest to prove success of *in-situ* transfection. BMP-2 expression was significantly increased in hMSCs that grew on pDNA-BMP2-loaded [HA,CHI]<sub>5</sub>HA-(DNA-LNP)-[HA,CHI]<sub>1</sub>-VTN PEMs compared to the negative control and the DNA-LNP-free PEM. The increased expression of BMP-2 can be explained by the successful transfection of hMSCs due to contact with the [HA,CHI]<sub>5</sub>HA-(DNA-LNP)-[HA,CHI]<sub>1</sub>-VTN film. The positive control also shows an upregulation of the BMP-2 expression, but the amount was significantly lower than determined

for our *in situ* transfection system. Hence, BMP-2 expression occurs during osteogenic differentiation of mesenchymal stem cells [57]. BMP-2 induces the upregulation of BMP-2 antagonists like noggin to keep spatial and temporal control of the process of osteogenesis [58, 59]. The qPCR results demonstrate a significant increase of noggin mRNA for the positive control and the [HA,CHI]<sub>5</sub>HA-(DNA-LNP)-[HA,CHI]<sub>1</sub>-VTN system. This can be explained by the production of BMP-2 of transfected cells or cells during osteogenic differentiation or the presence of exogenous BMP-2 in the positive control. The noggin mRNA level was significantly higher in our *in situ* transfection system. Nevertheless, this should not be interpreted as a disadvantage; rather, a natural mechanism works to keep cytokine activity in balance and to avoid ectopic ossification.

A comparable expression pattern was found for ALP and RunX2. The latter is a transcription factor that plays an important role in osteogenic and chondrogenic differentiation of stem cells [60]. Gene expression was upregulated in the positive control and the [HA,CHI]<sub>5</sub>HA-(DNA-LNP)-[HA,CHI]<sub>1</sub>-VTN system, compared to the negative control and cells on the DNA-LNP-free PEMs. Between [HA,CHI]<sub>5</sub>HA-(DNA-LNP)-[HA,CHI]<sub>1</sub>-VTN and positive control no significant difference was detected. At this point, a discrepancy is noticed between ALP expression level and enzyme activity observed for the positive control (compare Figure 8A with Figure 11). Maybe at this time point cells react with an increase of ALP biosynthesis due to the low ALP activity in the system. COL 1A1 is significantly increased in the LbL system and the positive control, while the positive control also shows a significantly higher mRNA level compared to the *in situ* transfection system. In summary, typical osteogenic markers are increasingly expressed in cells grown on the pDNA-BMP2-loaded PEM system [HA,CHI]<sub>5</sub>HA-(DNA-LNP)-[HA,CHI]<sub>1</sub>-VTN.

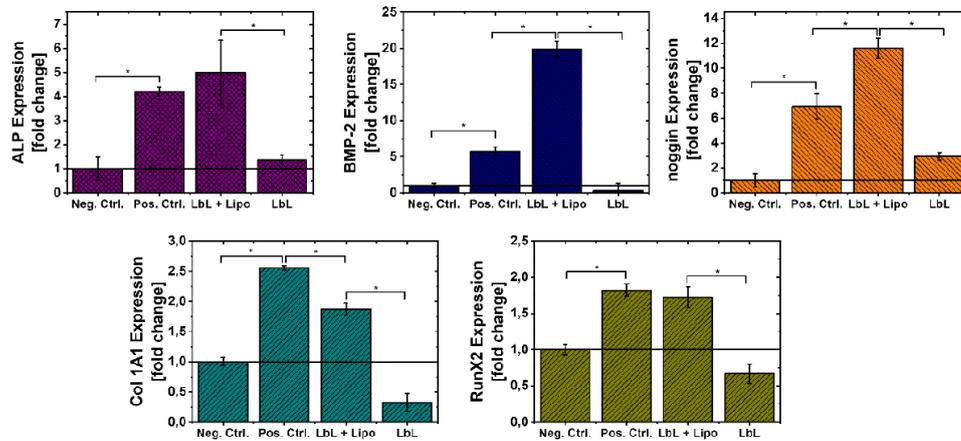


**Figure 11.** Relative mRNA expression of osteoblast markers (ALP, RunX2, noggin, BMP-2, Col 1A1) was determined at day 28 of the osteogenic differentiation process. Two negative controls were used: the DNA-free PEM [HA,CHI]<sub>6</sub>-VTN (termed as LbL) and cells grown on the uncoated cell culture dish (termed as Neg. Ctrl.). The sample indicated as LbL+Lipo is the *in situ* transfection system [HA,CHI]<sub>5</sub>HA-(DNA-LNP)-[HA,CHI]<sub>1</sub>-VTN. The positive control represents hMSCs treated with BMP2. Real-time qPCR analyses were performed as described in the materials and methods. The values are presented as mean ± S.D. (n=3).

#### 4. CONCLUSIONS

The presented study demonstrates the power of gene-activated polyelectrolyte multilayers in controlling fate of stem cells. We were able to transfer our proof-of-concept *in situ* transfection system, for delivery of nucleic acid into cells grown on functionalized surfaces, to the induction of osteogenic differentiation of human stem cells. The presented system based on sequential layers of hyaluronic acid and chitosan with embedded DNA-LNPs and a surface modification with vitronectin (engineered sequence: [HA,CHI]<sub>5</sub>HA-(DNA-LNP)-[HA,CHI]<sub>1</sub>-VTN), which allows an efficient interaction and transfection of mesenchymal stem cells. Osteogenic differentiation experiments were performed with BMP-2-encoding DNA embedded in the transfection system [HA,CHI]<sub>5</sub>HA-(DNA-LNP)-[HA,CHI]<sub>1</sub>-VTN. Different osteogenic markers have proven the differentiation of mesenchymal stem cells into the osteogenic lineage. The therapeutic potential of the system stems from its applicability to various surfaces to functionalize them for enhanced osteogenic activity. This offers various possibilities for translating the results into clinical applications, for example by coating of implants of various geometries or by functionalization of

microparticles. This therapeutic potential also arises from its fabrication by the flexible LbL deposition method using the biogenic polymers chitosan and hyaluronic acid. Beyond the osteogenic activity of the surface coating resulting from the *in situ* transfection of cells with the BMP-2 gene, the system may also benefit from the anti-inflammatory activity of hyaluronic acid and the antibacterial activity of chitosan [30]. However, preclinical *in vivo* experiments on bone fractures, for example, now need to be performed to further validate the potential clinical value of the system.

## 5. ASSOCIATED CONTENT

**Supporting Information:** Focal adhesion quantification using CellProfiler™, additional CLSM micrograph of transfected cells, OsteoImage™ images of negative control

## 6. AUTHOR INFORMATION

### Declaration of competing interest

The authors declare that they have no known competing financial interests or personal relationships that could have appeared to influence the work reported in this paper.

### Corresponding Author

Christian Wölk – Institute of Pharmacy, Pharmaceutical Technology, Faculty of Medicine, Leipzig University, 04317 Leipzig; Email: christian.woelk@medizin.uni-leipzig.de; orcid.org/0000-0002-8067-7307

### Author Contributions

The manuscript was written through contributions of all authors. All authors have given approval to the final version of the manuscript.

## 7. ACKNOWLEDGMENTS

This work was supported by Deutsche Forschungsgemeinschaft (DFG, German Research Foundation) project-ID 396823779 (C.W.) and by grants from Vereinigung der Freunde und Förderer des Instituts für Pharmazie MLU Halle-Wittenberg (to C.H.).

## 8. REFERENCES

1. Arvidson, K., et al., *Bone regeneration and stem cells*. Journal of Cellular and Molecular Medicine, 2011. 15(4): p. 718-746.
2. Bonafede, M., D. Espindle, and A.G. Bower, *The direct and indirect costs of long bone fractures in a working age US population*. J Med Econ, 2013. 16(1): p. 169-78.
3. Bessa, P.C., M. Casal, and R.L. Reis, *Bone morphogenetic proteins in tissue engineering: the road from laboratory to clinic, part II (BMP delivery)*. Journal of Tissue Engineering and Regenerative Medicine, 2008. 2(2-3): p. 81-96.
4. Beederman, M., et al., *BMP signaling in mesenchymal stem cell differentiation and bone formation*. Journal of biomedical science and engineering, 2013. 6(8A): p. 32-52.
5. Yang, J., et al., *Bone morphogenetic proteins: Relationship between molecular structure and their osteogenic activity*. Food Science and Human Wellness, 2014. 3(3): p. 127-135.
6. James, A.W., et al., *A Review of the Clinical Side Effects of Bone Morphogenetic Protein-2*. Tissue engineering. Part B, Reviews, 2016. 22(4): p. 284-297.
7. Hwang, J.-H., et al., *Artificial cellular nano-environment composed of collagen-based nanofilm promotes osteogenic differentiation of mesenchymal stem cells*. Acta Biomaterialia, 2019. 86: p. 247-256.
8. Poynton, A.R. and J.M. Lane, *Safety Profile for the Clinical Use of Bone Morphogenetic Proteins in the Spine*. Spine, 2002. 27(16S): p. S40-S48.
9. Carragee, E.J., E.L. Hurwitz, and B.K. Weiner, *A critical review of recombinant human bone morphogenetic protein-2 trials in spinal surgery: emerging safety concerns and lessons learned*. The Spine Journal, 2011. 11(6): p. 471-491.
10. Shimer, A.L., F.C. Öner, and A.R. Vaccaro, *Spinal reconstruction and bone morphogenetic proteins: Open questions*. Injury, 2009. 40: p. S32-S38.
11. Lieberman, J.R., et al., *The effect of regional gene therapy with bone morphogenetic protein-2-producing bone-marrow cells on the repair of segmental femoral defects in rats*. J Bone Joint Surg Am, 1999. 81(7): p. 905-17.
12. Fang, J., et al., *Stimulation of new bone formation by direct transfer of osteogenic plasmid genes*. Proceedings of the National Academy of Sciences, 1996. 93(12): p. 5753-5758.
13. Bonadio, J., *Tissue engineering via local gene delivery: Update and future prospects for enhancing the technology*. Advanced Drug Delivery Reviews, 2000. 44(2): p. 185-194.
14. Heyde, M., et al., *Gene therapy used for tissue engineering applications†*. Journal of Pharmacy and Pharmacology, 2010. 59(3): p. 329-350.
15. De la Vega, R.E., et al., *Gene therapy for bone healing: lessons learned and new approaches*. Translational Research, 2021. 236: p. 1-16.
16. Jose, L.S., et al., *Non-Viral Gene Delivery to Mesenchymal Stem Cells: Methods, Strategies and Application in Bone Tissue Engineering and Regeneration*. Current Gene Therapy, 2011. 11(1): p. 46-57.
17. O'Rourke, S., M. Keeney, and A. Pandit, *Non-viral polyplexes: Scaffold mediated delivery for gene therapy*. Progress in Polymer Science, 2010. 35(4): p. 441-458.
18. Ramalingam, K., et al., *Gene delivery using dendrimer/pDNA complexes immobilized in electrospun fibers using the Layer-by-Layer technique*. RSC Advances, 2016. 6(99): p. 97116-97128.
19. Ji, W., et al., *Bioactive Electrospun Scaffolds Delivering Growth Factors and Genes for Tissue Engineering Applications*. Pharmaceutical Research, 2011. 28(6): p. 1259-1272.
20. Grigsby, C.L. and K.W. Leong, *Balancing protection and release of DNA: tools to address a bottleneck of non-viral gene delivery*. Journal of the Royal Society, Interface, 2010. 7 Suppl 1(Suppl 1): p. S67-S82.

21. Husteden, C., et al., *Contact-Triggered Lipofection from Multilayer Films Designed as Surfaces for in Situ Transfection Strategies in Tissue Engineering*. ACS Applied Materials & Interfaces, 2020. 12(8): p. 8963-8977.
22. Janich, C., et al., *Composites of malonic acid diamides and phospholipids — Impact of lipoplex stability on transfection efficiency*. Journal of Controlled Release, 2015. 220: p. 295-307.
23. Janich, C., et al., *Efficient Transfection of Large Plasmids Encoding HIV-1 into Human Cells—A High Potential Transfection System Based on a Peptide Mimicking Cationic Lipid*. Pharmaceutics, 2020. 12(9): p. 805.
24. Janich, C., et al., *Fast therapeutic DNA internalization – A high potential transfection system based on a peptide mimicking cationic lipid*. European Journal of Pharmaceutics and Biopharmaceutics, 2017. 118: p. 38-47.
25. Decher, G. and J.-D. Hong, *Buildup of ultrathin multilayer films by a self-assembly process, 1 consecutive adsorption of anionic and cationic bipolar amphiphiles on charged surfaces*. Makromolekulare Chemie. Macromolecular Symposia, 1991. 46(1): p. 321-327.
26. Borges, J. and J.F. Mano, *Molecular Interactions Driving the Layer-by-Layer Assembly of Multilayers*. Chemical Reviews, 2014. 114(18): p. 8883-8942.
27. Knopf-Marques, H., et al., *Hyaluronic Acid and Its Derivatives in Coating and Delivery Systems: Applications in Tissue Engineering, Regenerative Medicine and Immunomodulation*. Advanced Healthcare Materials, 2016. 5(22): p. 2841-2855.
28. Rabea, E.I., et al., *Chitosan as Antimicrobial Agent: Applications and Mode of Action*. Biomacromolecules, 2003. 4(6): p. 1457-1465.
29. Anouz, R. and T. Groth, *Chapter 13 Biomimetic Surface Modifications of Biomaterials Using a Layer-by-layer Technique*, in *Soft Matter for Biomedical Applications*. 2021, The Royal Society of Chemistry. p. 326-362.
30. Zhou, G., et al., *Reducing the inflammatory responses of biomaterials by surface modification with glycosaminoglycan multilayers*. J Biomed Mater Res A, 2016. 104(2): p. 493-502.
31. Alkhoury, H., et al., *Studies on the Mechanisms of Anti-Inflammatory Activity of Heparin- and Hyaluronan-Containing Multilayer Coatings-Targeting NF- $\kappa$ B Signalling Pathway*. Int J Mol Sci, 2020. 21(10).
32. Janich, C., et al., *Composites of malonic acid diamides and phospholipids – Structural parameters for optimal transfection efficiency in A549 cells*. European Journal of Lipid Science and Technology, 2014. 116(9): p. 1184-1194.
33. Szoka, F., Jr. and D. Papahadjopoulos, *Comparative properties and methods of preparation of lipid vesicles (liposomes)*. Annu Rev Biophys Bioeng, 1980. 9: p. 467-508.
34. Stefaniu, C., et al., *Relationship between structure and molecular interactions in monolayers of specially designed aminolipids*. Nanoscale Advances, 2019. 1(9): p. 3529-3536.
35. Klein, S., et al., *Differential Effects of Coating Materials on Viability and Migration of Schwann Cells*. Materials, 2016. 9(3): p. 150.
36. Altankov, G., F. Grinnell, and T. Groth, *Studies on the biocompatibility of materials: fibroblast reorganization of substratum-bound fibronectin on surfaces varying in wettability*. Journal of biomedical materials research, 1996. 30 3: p. 385-91.
37. Schindelin, J., et al., *Fiji: an open-source platform for biological-image analysis*. Nature Methods, 2012. 9(7): p. 676-682.
38. Carpenter, A.E., et al., *CellProfiler: image analysis software for identifying and quantifying cell phenotypes*. Genome Biol, 2006. 7(10): p. R100.
39. Livak, K.J. and T.D. Schmittgen, *Analysis of relative gene expression data using real-time quantitative PCR and the 2(-Delta Delta C(T)) Method*. Methods, 2001. 25(4): p. 402-8.
40. Shafaei, H. and H. Kalarestaghi, *Adipose-derived stem cells: An appropriate selection for osteogenic differentiation*. Journal of Cellular Physiology, 2020. 235(11): p. 8371-8386.
41. Wang, Y.-K. and C.S. Chen, *Cell adhesion and mechanical stimulation in the regulation of mesenchymal stem cell differentiation*. Journal of cellular and molecular medicine, 2013. 17(7): p. 823-832.

42. Karamanos, N.K., et al., *A guide to the composition and functions of the extracellular matrix*. The FEBS Journal. n/a(n/a).
43. Shekaran, A. and A.J. García, *Extracellular matrix-mimetic adhesive biomaterials for bone repair*. J Biomed Mater Res A, 2011. 96(1): p. 261-72.
44. McBeath, R., et al., *Cell Shape, Cytoskeletal Tension, and RhoA Regulate Stem Cell Lineage Commitment*. Developmental Cell, 2004. 6(4): p. 483-495.
45. Goldmann, W.H., *Role of vinculin in cellular mechanotransduction*. Cell Biology International, 2016. 40(3): p. 241-256.
46. Bays, J.L. and K.A. DeMali, *Vinculin in cell-cell and cell-matrix adhesions*. Cellular and molecular life sciences : CMLS, 2017. 74(16): p. 2999-3009.
47. Parisi, L., et al., *A glance on the role of fibronectin in controlling cell response at biomaterial interface*. Japanese Dental Science Review, 2020. 56(1): p. 50-55.
48. Dalton, C.J. and C.A. Lemmon, *Fibronectin: Molecular Structure, Fibrillar Structure and Mechanochemical Signaling*. Cells, 2021. 10(9): p. 2443.
49. Zhao, M., et al., *Molecular composition of GAG-collagen I multilayers affects remodeling of terminal layers and osteogenic differentiation of adipose-derived stem cells*. Acta Biomaterialia, 2016. 41: p. 86-99.
50. Altankov, G. and T. Groth, *Fibronectin matrix formation by human fibroblasts on surfaces varying in wettability*. Journal of Biomaterials Science, Polymer Edition, 1997. 8(4): p. 299-310.
51. Ryoo, H.-M., M.-H. Lee, and Y.-J. Kim, *Critical molecular switches involved in BMP-2-induced osteogenic differentiation of mesenchymal cells*. Gene, 2006. 366(1): p. 51-57.
52. Orimo, H., *The Mechanism of Mineralization and the Role of Alkaline Phosphatase in Health and Disease*. Journal of Nippon Medical School, 2010. 77(1): p. 4-12.
53. Wu, X., et al., *A Small Molecule with Osteogenesis-Inducing Activity in Multipotent Mesenchymal Progenitor Cells*. Journal of the American Chemical Society, 2002. 124(49): p. 14520-14521.
54. Qureshi, A.T., et al., *Chapter Five - Human Adipose-Derived Stromal/Stem Cell Isolation, Culture, and Osteogenic Differentiation*, in *Methods in Enzymology*, O.A. MacDougald, Editor. 2014, Academic Press. p. 67-88.
55. Pablo Rodriguez, J., et al., *Cytoskeletal organization of human mesenchymal stem cells (MSC) changes during their osteogenic differentiation*. Journal of Cellular Biochemistry, 2004. 93(4): p. 721-731.
56. Chen, M., et al., *Improvement of Distribution and Osteogenic Differentiation of Human Mesenchymal Stem Cells by Hyaluronic Acid and  $\beta$ -Tricalcium Phosphate-Coated Polymeric Scaffold In Vitro*. Biores Open Access, 2015. 4(1): p. 363-73.
57. Lin, X., et al., *The Bone Extracellular Matrix in Bone Formation and Regeneration*. Frontiers in Pharmacology, 2020. 11(757).
58. Winkler, D.G., et al., *Noggin and sclerostin bone morphogenetic protein antagonists form a mutually inhibitory complex*. J Biol Chem, 2004. 279(35): p. 36293-8.
59. Abe, E., et al., *Essential requirement of BMPs-2/4 for both osteoblast and osteoclast formation in murine bone marrow cultures from adult mice: antagonism by noggin*. J Bone Miner Res, 2000. 15(4): p. 663-73.
60. Long, F., *Building strong bones: molecular regulation of the osteoblast lineage*. Nature Reviews Molecular Cell Biology, 2012. 13(1): p. 27-38.

### 3) Generelle Diskussion

Die Ergebnisse der kumulativ zusammengestellten Publikationen und Manuskripte verdeutlichen, dass durch eine gezielte Funktionalisierung von PEM nach dem Konzept des *In-situ*-TE aktiv Mechanismen der Knochenregeneration stimuliert werden können. Im Folgenden wird das Potenzial der jeweiligen Funktionalisierungsstrategie im TE dargestellt sowie generelle Hürden und Herausforderungen bei der klinischen Translation erörtert.

#### 3.1) Potenzial der Funktionalisierungsstrategien

Neue Strategien für die Therapie von Knochendefekten bietet das Konzept des TE. Es zielt darauf ab, defektes Knochengewebe zu ersetzen, um die Funktionalität wiederherzustellen und die Heilung zu fördern. Obwohl seit Jahrzehnten an neuen Strategien geforscht wurde, konnte bis heute kein TE-Produkt für die *In-vivo*-Anwendung als Knochenersatzmaterial den bisherigen Goldstandard – das Autotransplantat – ablösen. Das Ziel dieser Arbeit war es, unter Verwendung der LbL-Technik neue Funktionalisierungsstrategien für nanoskalige Beschichtungen zu entwickeln, welche die Leistung von Knochenimplantaten verbessern können, indem sie *in situ* zelluläre Reaktionen auslösen.

Der Einsatz von Liposomen als *Drug-Delivery*-Systeme für DEX und für die Funktionalisierung von PEMs bietet verschiedene Vorteile: (1) DEX ist vor Abbau und spontaner Freisetzung geschützt; (2) DEX kann lokal an Target-Zellen abgegeben werden; (3) die Bioverfügbarkeit des Arzneimittels kann verbessert und systemische Nebenwirkungen können reduziert werden. Diese Verwendung von Liposomen erlaubt die Verkapselung diverser bioaktiver Substanzen, die je nach Art entweder im inneren Liposomen-Kompartiment (hydrophile Moleküle) oder innerhalb der Lipiddoppelschicht (lipophile Moleküle) oder in beiden (amphiphile Moleküle) sequestriert werden können. Die Kombination dieser Nanopartikel mit einer Matrix aus ECM-Komponenten wie COL und HA stellt dabei eine Mikroumgebung bereit, die der eines nativen Gewebes ähnelt und nützlich sein kann, um das Verhalten von Zellen zu kontrollieren. Diese Strategie hat sich in Publikation III an einer Modellzelllinie bewährt. Neben osteogenen Markern konnten darüber hinaus chondrogene Genmarker hochreguliert werden, die eine zukünftige Anwendung für osteochondrale Defekte denkbar machen. Obwohl demonstriert werden konnte, dass ein Prozess der Differenzierung in die osteochondrale Linie erfolgte, ist nicht geklärt, in welchem Ausmaß dieser stattfand. Diese Information ist jedoch wichtig, um abschätzen zu können, für welche Defektgrößen und -arten das Liposomen-beladene PEM-

System einsatzfähig sein könnte und damit auch die Wahl des entsprechenden *In-vivo*-Tiermodells. In Antikörper-basierten Assays wie ELISA kann zukünftig eine Quantifizierung von osteo- und chondrogenen Proteinen durchgeführt werden, die weitere Beurteilungen und Interpretationen erlaubt.

Die komplexere *In-situ*-TE-Strategie der Funktionalisierung mittels nicht-viraler Vektoren verspricht großes Potenzial, die Osteogenese aktiv zu fördern, und bietet damit eine attraktive Alternative zur klinischen Anwendung des Wachstumsfaktors rhBMP-2. Durch die Verwendung der Gentherapie kann das Regenerationspotenzial *in situ* von MSCs unterstützt werden. Nach erfolgter Transfektion der Zielzellen mit geeigneten therapeutischen Gensequenzen werden lokal osteogene Mediatoren produziert, die wesentlich zur Optimierung der Geweberegeneration und der Implantatintegration beitragen können. Durch Konjugation der Genvektoren mit Biomaterialien entstehen genaktivierte Materialien, die neben ihrer Aufgabe als osteokonduktive Matrix zusätzlich die Funktion haben, das Konstrukt mit einem intrinsischen Regenerationsmechanismus auszustatten. Durch die Verwendung eines nicht viralen Vektors lassen sich die Zytokine transient exprimieren, sodass eine Überproduktion des Signalmoleküls und damit einhergehende mögliche Nebenwirkungen verhindert werden. Beide untersuchten Systeme aus CS/COL mit OO4:DOPE (1:3, N/P:4) und HA/CHI mit OH4:DOPE (1:1, N/P:4) demonstrierten die erfolgreiche Beladung mit Nanopartikeln und die Adhäsion sowie die Proliferation von kultivierten MSCs auf ihrer Oberfläche. Die Ergebnisse dieser Arbeit zeigen, dass die erfolgreiche Aufnahme von LPX mit BMP-2-kodierender Plasmid-DNA durch MSCs zu deren Differenzierung in die osteogene Linie führt. Während für HA/CHI eine finale Modifizierung für eine erfolgreiche Besiedelung mit MSCs mit adhäsiven Glykoproteinen wie Fibronectin oder Vitronectin notwendig war, konnte bei dem CS/COL darauf verzichtet werden, ohne fokale Adhäsion und Viabilität einzubüßen. Die Ergebnisse gelten streng genommen nur für die verwendeten *In-vitro*-Zelllinien. Ihr *In-vivo*-Transfektionspotenzial ließ sich jedoch für HA/CHI mit OH4:DOPE (1:1, N/P:4) in ersten durchgeführten Experimenten am Hühnerei-Test an der Chorion-Allantois-Membran (HET-CAM) demonstrieren, die vom Kooperationspartner (AG Bakowsky, Philipps-Universität Marburg) durchgeführt wurden. Dass die Entwicklungsmöglichkeiten der LPX-beladenen PEMs noch nicht ausgeschöpft sind, belegen erste durchgeführte Experimente im Manuskript I, in denen die Anzahl der terminalen Bilayer aus HA/CHI auf der LPX-Schicht variiert wurde. Dabei liefern CLSM-Aufnahmen erste Hinweise auf eine zeitlich

kontrollierbare Transfektion in Abhängigkeit der gewählten Deckschicht-Dicke. Je dicker diese Deckschicht aus HA/CHI auf den LPX war, desto später setzte eine Transfektion ein. Obwohl dahingehend noch weitere Studien notwendig sind, deutet dieses Experiment darauf hin, dass durch die gewählte Lage der LPX im PEM-System Einfluss auf die Transfektionskinetik genommen werden kann. Das macht sie zu vielversprechenden Kandidaten für eine zeitlich kontrollierbare kontaktvermittelte Lipofektion. Weiterhin besteht die Möglichkeit, mehrere LPX in das PEM-System einzubetten, um synergistische Effekte bei der Knochenregeneration zu erzielen. Dahingehend gibt es bereits erste durchgeführte Experimente, die eine praktische Umsetzbarkeit dieses Vorhabens veranschaulichen. Hierbei wurden zwei unterschiedliche Reportergene verwendet, jeweils mit OH4:DOPE (1:1, N/P:4) komplexiert und an unterschiedlichen Positionen im PEM-Konstrukt eingebettet.

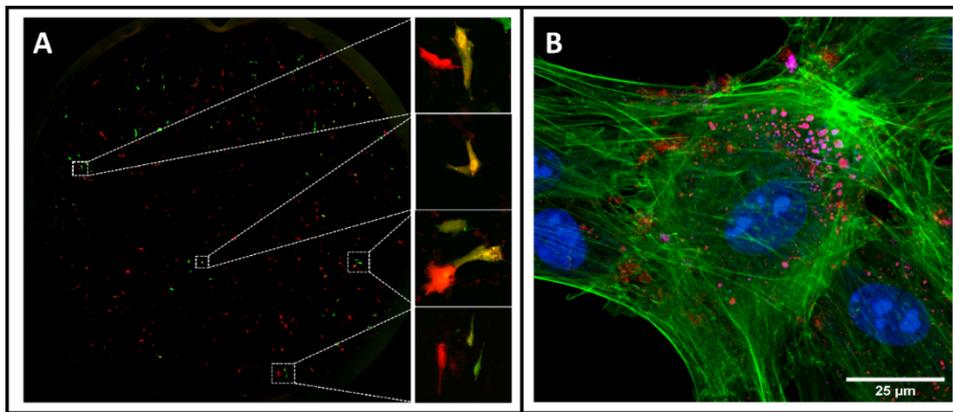


**Abbildung 16:** CLSM-Aufnahmen von co-transfizierten MSCs. (A) CLSM-Bilder von co-transfizierten MSCs nach 48 h. MSCs wuchsen auf PEMs mit zwei Lipoplex-Schichten, getrennt durch eine Doppelschicht [HA,CHI]1 und bedeckt mit einer Doppelschicht [HA,CHI]1. Die untere DNA-Schicht enthält Turbo-GFP ( $c = 0,5 \mu\text{g/well}$ ), das für das grün fluoreszierende Protein kodiert, und die obere DNA-Schicht enthält pLego-mcherry ( $c = 0,5 \mu\text{g/well}$ ), das für ein rot fluoreszierendes Protein kodiert. Co-transfizierte Zellen sind in der Vergrößerung (gelb) zu sehen. (B) CLSM-Bilder von transfizierten MSCs nach 72 h Aussaat auf Lipoplex-beladenen PEMs mit Cy-5-markierter DNA (rot) und Rhodamin-TM-markierter DNA (pink). Phalloidin-Atto 488 wurde zum Färben von filamentösem Aktin verwendet und BOBO-1 zum Färben des Kerns.

In Fluoreszenz-basierten Assays konnte anschließend gezeigt werden, dass Zellen von beiden Transgenen erfolgreich transfiziert wurden und die entsprechenden Proteine exprimiert haben (siehe Abbildung 16). Dieser Ansatz kann weiterverfolgt und durch therapeutische Transgene ersetzt werden, z. B. durch BMP-2 in Kombination mit VEGFA, dessen Bedeutung im nächsten Abschnitt näher erläutert wird. Diese Weiterentwicklung des LPX-beladenen Systems ist bereits im Rahmen eines DFG-Projektes – aufbauend auf den bisherigen Ergebnissen – geplant.

### 3.2) Generelle Hürden im Tissue Engineering

In fortgeschrittenen Studien im Knochen-TE wurde in der jüngeren Vergangenheit sowohl *in vitro* als auch *in vivo* das Potenzial zur Differenzierung einer Vielzahl von Zellen in Osteoblasten verdeutlicht und die unterstützende Rolle von Signalmolekülen und/oder Biomaterialien erklärt. Ein vollständiger Ersatz des defekten Knochens durch Biomaterialien ist jedoch bis heute noch nicht erreicht. Die Schaffung von funktionellem Knochen unter Laborbedingungen mittels TE ist immer noch eine Herausforderung, obwohl verschiedene Arten von Stammzellen eine osteogene Abstammungsdifferenzierung gezeigt haben. Für das TE-Konzept ergeben sich diverse Hürden, bedingt durch die Vielschichtigkeit im Verbund aus Biomaterial, Funktionalisierung mit bioaktiven Faktoren sowie *In-vitro*-Kultivierung von Zielzellen. In Tabelle 7 sind bedeutsame Einschränkungen und Herausforderungen zusammengefasst. Wesentliche Problemstellungen sind nach wie vor die Kultivierung verlässlicher Spenderzellen sowie die Wahl geeigneter Tiermodelle zur Testung. Weitere Herausforderungen sind die Hürden der klinischen Zulassung und der Wirtschaftlichkeit sowie die Untersuchung möglicher Nebenwirkungen und die langfristige Evaluation des Erfolges der TE-Behandlung. Weiterhin liegt die Schwierigkeit darin, eine optimale Vaskularisierung des Knochengewebes sicherzustellen.<sup>168</sup> In zahlreichen Studien wurde der Einfluss der Vaskularisierung im Knochen-TE untersucht und die Korrelation zwischen Osteogenese und dem Vaskularisierungsgrad demonstriert. Neben dem notwendigen Gasaustausch bedingt eine angemessene Vaskularisierung auch die Nährstoffversorgung und den Abtransport metabolischer Nebenprodukte wie Milchsäure oder Kohlendioxid.<sup>168,169</sup> Eine unzureichende Vaskularisierung würde folglich die langfristige Lebensfähigkeit des *in vivo* gebildeten Knochengewebes einschränken. In Anbetracht der vielen Schwierigkeiten, welche die klinische Translation von TE-Konzepten mit sich bringt, ist es daher wahrscheinlich, dass zukünftig der Fokus insbesondere auf kostengünstigeren TE-Strategien liegen wird, die ein synergistisches Konstrukt aus osteogenen und angiogenen Faktoren vorweisen können.

Während sich das Anwendungsgebiet von LPX-beladenen PEMs in den hier vorgestellten Studien bisher auf den Einsatz von osteogenen Defekten beschränkt, könnten fehlende angiogene Zytokine in *In-vivo*-Experimenten eine beeinträchtigte Integration des TE-Konstruktes hervorrufen. Daher stellt die Modifizierung zu Doppeltransfektionssystemen, wie im vorherigen Kapitel angedeutet, eine vielversprechende Weiterentwicklung der LPX-beladenen PEMs dar. Da eine Vaskularisierung bei chondrogenen Gewebe eher von

geringfügiger Bedeutung ist, könnten Liposomen-beladene Oberflächenbeschichtungen mit ihrem möglichen Einsatzgebiet für osteochondrale Defekte eher auf die Nutzung von angiogenen Zytokinen verzichten.<sup>170</sup> Diese Hypothese muss jedoch zwingend in weiterführenden Studien untersucht werden.

<b>Grundlegende Herausforderungen</b>	<ul style="list-style-type: none"> <li>➤ Zellen (Auswahl, Zelltyp, Isolation, Vermehrung)</li> <li>➤ Gerüste (mechanisch kompatibel, Porosität)</li> <li>➤ Auswahl der Biomoleküle</li> <li>➤ Vaskularisierung</li> <li>➤ Integration in das Zielgewebe</li> </ul>
<b>Limitiertes Fachwissen</b>	<ul style="list-style-type: none"> <li>➤ Beitrag von Spender- und Wirtszelle</li> <li>➤ geeignete immunmodulatorische Biomaterialien/Wirkstoffe</li> <li>➤ mögliche Nebenwirkungen/Komplikationen</li> <li>➤ Wahl des passenden Tiermodells</li> </ul>
<b>Herausforderungen bei der Evaluierung</b>	<ul style="list-style-type: none"> <li>➤ Bewertung der Qualität/Funktionalität des neugebildeten Knochens</li> <li>➤ Langzeitkontrolle des regenerierten Knochens</li> </ul>
<b>Klinische Herausforderungen</b>	<ul style="list-style-type: none"> <li>➤ behördliche Zulassung</li> <li>➤ GMP-gerechte Herstellung</li> <li>➤ kostenintensiv</li> <li>➤ patientenspezifisch</li> </ul>

**Tabelle 7:** Herausforderungen und Einschränkungen im Knochen-TE. Geändert nach AMINI et al.<sup>168</sup>

### 3.3) Regulatorische Herausforderungen für die klinische Translation

Seit Dezember 2008 ist europaweit die Anwendung von biotechnologisch bearbeiteten Gewebeprodukten, also von TE-Produkten, durch die zentrale Verordnung (EC) Nr. 1394/2007, auch Verordnung über ‚Arzneimittel für neuartige Therapien‘ (*Advanced Therapy Medicinal Product*, ATMP) genannt, strikt reguliert.<sup>171</sup> Bei ATMPs handelt es sich um Arzneimittel zur Anwendung bei Menschen, die auf Genen, Gewebe oder Zellen basieren.<sup>172</sup> Damit sind die regulatorischen und bürokratischen Hürden der Zulassung deutlich höher als bei klassischen Arzneimitteln, die durch das Bundesinstitut für Arzneimittel und Medizinprodukte (BfArM) reguliert sind. Die Zuständigkeiten der deutschen Bundesbehörden überschneiden sich bei Kombinationsprodukten aus Zellmaterial und Medizinprodukten, da Letztere in den Verantwortungsbereich des BfArM fallen, zelluläre Bestandteile aber vom Paul-Ehrlich-Institut beurteilt werden. Neben den zu überwindenden bürokratischen Hürden müssen bei der Produktion von TE-Produkten zusätzlich hohe GMP-Standards (engl. *Good Manufacturing Practice*, EU-Richtlinie 2003/94/EC) erfüllt werden.<sup>171</sup> Bisher fanden daher nur wenige Substitute als sogenanntes

*Tissue Engineered Product* eine Zulassung zur therapeutischen Anwendung. Sie sind in Tabelle 8 (Stand November 2022) aufgelistet. Insbesondere Ersatzmaterialien für Knorpelgewebe gelang bisher der klinische Zugang, da bei dieser Applikation auf eine entsprechende Vaskularisierung verzichtet werden kann.<sup>170</sup>

Name	Hersteller	Lizenzdatum
BioSeed-C Autologes 3D-Chondrozytentransplantat,	BioTissue Technologies GmbH	04.06.2014
co.don chondrosphere, 10-70 Sphäroide/cm <sup>2</sup> , matrixassoziierte Zellen zur Implantation	co.don AG, Teltow	12.12.2013
Holoclar	Holostem Therapie Avanzate (HTA) Srl, Italien	17.02.2015
MACI (Zulassung ruht seit 11/2014)	Genzyme Europe B.V., NL	27.06.2013
Muko-Zelle	MukoCell GmbH	23.12.2013
NOVOCART 3D	TETECAG	29.08.2014
Obnitix	medac Gesellschaft für klinische Spezialpräparate mbH	24.08.2016
Spherox	co.don AG, Teltow	10.07.2017
t2c001, autologe, aus dem Knochenmark stammende Vorläuferzellen	t2cure GmbH, Frankfurt	31.03.2014

**Tabelle 8:** Aktuell zugelassene Produkte aus Gewebezüchtung.<sup>173</sup>

Beide untersuchten Funktionalisierungsstrategien zielen zunächst auf eine *In-vitro*-Kultivierung von MSCs ab. Die regulatorischen und bürokratischen Hürden der Zulassung sind damit deutlich höher, da sie als ATMPs eingestuft werden. Liposomen-beladene PEMs würden als klassische zellbasierte TE-Konstrukte bewertet werden, während eine Einordnung von LPX-beladenen PEMs als Gentherapeutikum, durch die Verwendung von genetischem Material, unumgänglich ist. Durch den Verzicht einer extrakorporalen *In-vitro*-MSC-Kultivierung könnte die Mehrheit der Sicherheitsrisiken und der damit einhergehenden behördlichen Vorschriften wegfallen. Grundsätzlich besteht für beide Konzepte das Potenzial, als zellfreie *In-vivo*-Knochenersatzmaterialien preiswert und mit einer standardisierten Qualität produziert zu werden. Eine geringere regulatorische Komplexität ist durch das Fehlen von genetischem Material aber nur für Liposomen-beladene Oberflächenbeschichtungen umsetzbar. Eine *In-vivo*-Rekrutierung von MSCs mittels Liposomen-funktionalisierter Oberflächenbeschichtungen wäre durch die biomimetrische ECM-imitierende Oberfläche theoretisch möglich, müsste jedoch in entsprechenden *In-vivo*-Experimenten nachgewiesen werden.

#### 4) Zusammenfassung und Ausblick

Im Rahmen dieser Dissertationsschrift wurden neue Strategien für die Behandlung von Knochendefekten untersucht, um effektive und biokompatible Knochenersatzmaterialien zielgerichtet weiterzuentwickeln. Die Einfachheit und Wirksamkeit der LbL-Technik ermöglicht verschiedene Modifikationen an der Implantatoberfläche, um die Zelladhäsion zu regulieren und die morphologische Differenzierung zu steuern. Die Grenzfläche zwischen Implantat und Knochenstruktur wurde dabei für eine Konditionierung von osteogenen Prozessen ausgenutzt. Zwei Konzepte zur Funktionalisierung von Multischichtsystemen wurden in dieser Arbeit untersucht. Zum einen fand eine Funktionalisierung mittels LPX statt, zum anderen eine mittels Wirkstoff-beladener Liposome. Mit diesen Strategien werden im Wesentlichen zwei Ziele verfolgt: (1) Durch die Verwendung von ECM-Komponenten oder biokompatiblen Biomaterialien ist die Herstellung eines osteokonduktiven Gerüsts möglich, das die Interaktion mit MSCs optimieren kann; (2) durch Funktionalisierung mit Nukleinsäuren, die für BMP-2 kodieren, oder verkapseltem DEX kann dem System ein intrinsisches osteoinduktives Potenzial verliehen werden.

Anhand physikochemischer und biologischer Methoden wurden beide Strategien intensiv auf ihre Realisierbarkeit untersucht und charakterisiert. Im Folgenden werden die wichtigsten Ergebnisse der für die Dissertation relevanten Publikationen und Manuskripte zusammengefasst:

1. In Publikation I wurde die Funktionalisierungsstrategie mittels nicht-viraler Genvektoren untersucht. Ein Schwerpunkt war die Testung verschiedener Techniken zur Immobilisierung von DNA in ein Polyelektrolyt-Multischichtsystem aus CHI und HA. Für die Einbettung der DNA wurde zum einen das Reportergen (pCMV-GMP) verwendet und zum anderen die Lipidformulierung OH4:DOPE (1:1; N/P:4). Die Einarbeitungsmethode mittels vorgeformter LPX hat sich dabei als effektivste Beladungsstrategie herauskristallisiert, neben der Langmuir-Blodgett-Methode und der separierten Adsorption von Liposomen und DNA. In Studien wird belegt, dass die LPX-beladenen PEMs als nanostrukturiertes System vorliegen, indem die LPX nach Adsorption ihre Struktur durch Deformations- und Neuordnungsprozesse verändern. Weiterhin deuten Zeta-Potenzial-Messungen darauf hin, dass die einzelnen PEM- und LPX-Schichten teilweise ineinander eindringen und es zu

Durchmischungsprozessen während der Filmbildung kommt. Die LPX-beladenen PEMs demonstrieren eine hohe Beladungsfähigkeit mit DNA, die auch nach einer Woche noch stabil in den PEMs eingebaut ist. Weiterhin zeigt eine terminale Modifizierung der Filme mit Fibronectin eine ausgeprägte Zell-Adhäsion und -Viabilität an einer Modellzelllinie. Als *Proof-of-Concept*-Artikel verdeutlicht der LPX-beladene PEM-Film in *In-vitro*- und ersten *In-vivo*-Experimenten sein Potenzial zur Transfektion von Zellen.

2. Im Fokus des Manuskripts I stand die Übertragung der *Proof-of-Concept*-Studie (Publikation I) zur Abgabe von DNA in Zellen, die auf funktionalisierten Oberflächen gewachsen sind, auf die Induktion der osteogenen Differenzierung menschlicher Stammzellen. Aufbauend auf Publikation I wurden im Manuskript I sowohl das Reportergen pCMV-GFP durch eine therapeutisch aktive Gensequenz für BMP-2 ausgetauscht als auch die Modellzelllinie (C2C12-Zellen) durch Studien an humanen mesenchymalen Stammzellen ersetzt. Eine terminale Modifizierung mit Vitronectin anstelle von Fibronectin zeigte neben einer verbesserten Zellviabilität auch eine ausgeprägte fokale Adhäsion, die vergleichbar ist mit der einer Positivkontrolle (Fibronectin-modifiziertes Glas). Bildgebende Methoden belegen darüber hinaus die erfolgreiche Aufnahme von DNA in die Zelle innerhalb von 72 h. Weiterhin zeigte eine Modifizierung der Dicke der Deckschicht ein verändertes zeitabhängiges Transfektionsverhalten. Osteogene Differenzierungs-experimente wurden mit BMP-2-kodierender DNA durchgeführt, die in das Transfektionssystem eingebettet wurde. Verschiedene osteogene Marker sowie das Vorhandensein von Calcium- und HAP-Strukturen haben die Differenzierung von mesenchymalen Stammzellen in die osteogene Linie nachgewiesen.
3. In Publikation III wurden DEX-beladene Liposomen als Funktionalisierungsstrategie untersucht, um eine lokale Abgabe und einen Schutz dieses Medikamentes zur Stimulierung der osteo- und chondrogenen Differenzierung multipotenter Stammzellen zu erreichen. Für die Herstellung der Liposomen wurde die Formulierung OO4:DOPE (1:3, N/P:4) verwendet. Um ein lokales biomimetrisches Abgabesystem zu erzeugen, wurden die ECM-Komponenten HA und COL zur PEM-Bildung genutzt. Die Experimente belegen einen erfolgreichen Einschluss der Liposomen in das PEM-System. Weiterhin demonstrieren die DEX-beladenen PEMs eine gute Zelladhäsion an einer Modellzelllinie für die *In-vitro*-Differenzierung (C3H10T1/2-Zellen). Die Kombination aus den adhäsiven

Eigenschaften durch die ECM-nachahmende Zusammensetzung der PEMs und den chemischen Impulsen durch DEX liefert eine osteo- und chondrogene Differenzierung von C3H10T1/2-Zellen. Dies macht sie als Beschichtungsoption für osteochondrale Implantate interessant.

4. Mit der Publikation IV wurde das Ziel verfolgt, eine genaktivierte Oberflächenbeschichtung basierend auf COL und CS, zwei Biopolymeren der ECM des Knochengewebes, herzustellen. Diese wurden mit LPX funktionalisiert, die aus der Lipidformulierung OO4:DOPE (1:3, N/P:4) und einem Reportergen (pCMV-GFP) oder einer Gensequenz bestehen, die für das Osteogenese-indizierende BMP-2 kodiert. Der erste Teil dieser Studie konzentrierte sich auf die oberflächensensitive Charakterisierung, die eine fibrilläre Strukturierung von COL und eine homogene Einbettung der LPX veranschaulicht. Der zweite Teil fokussierte sich auf biologische Untersuchungen an MSCs. Auf der genaktivierten Oberfläche wurden MSCs kultiviert, um die osteogene Differenzierung *in vitro* zu untersuchen. Diese zeigten sowohl Zellproliferation als auch eine effiziente Transfektion, die eine Zelldifferenzierung in Richtung der osteogenen Linie induzierte. Das genfunktionalisierte und ECM-nachahmende PEM-System stellt eine intelligente Oberflächenfunktionalisierung dar, um das Schicksal von Stammzellen aufgrund räumlich induzierter Expression von Wachstumsfaktor-kodierender Nukleinsäure zu kontrollieren.

Abschließend kann festgehalten werden, dass durch die vorgestellten Studien zwei auf LbL basierende Funktionalisierungsstrategien von Oberflächenbeschichtungen charakterisiert werden konnten. Darüber hinaus konnte ihre intrinsische Fähigkeit, das Differenzierungsverhalten von MSCs zu kontrollieren, in ersten *In-vitro*-Experimenten gezeigt werden. Diese Studien bilden die Grundlage für künftige *In-vivo*-Experimente.

Aufbauend auf dieser Dissertation sind weitere Forschungsarbeiten nötig, um bisher ungeklärte Aspekte zu untersuchen und/oder die Systeme zu verbessern. Aus der Literatur wird deutlich, dass ein *Crosslinking* der PEMs die mechanischen Eigenschaften dieser verbessern kann, was sich positiv auf Zelladhäsion und Stoffwechselaktivität auswirken kann.<sup>174-176</sup> So könnten z. B. Thiol-modifizierte Polyelektrolyte eingesetzt werden, die reversibel kovalente Disulfid-Bindungen durch Oxidation zweiter Thiolgruppen ausbilden.

Wie zuvor angedeutet sollten auf die wirksame *In-vitro*-Stimulierung der Osteogenese umfangreiche *In-vivo*-Experimente folgen. Denkbar wäre eine Implantation des mit MSC besiedelten funktionalisierten PEM-Systems in einen künstlich erzeugten Knochendefekt von Mäusen. Dadurch ließe sich eine *In-vivo*-Anwendung der funktionalisierten PEMs abschätzen, die mithilfe von histologischen Analysen und/oder  $\mu$ CT-Schnittbildverfahren beurteilt werden könnte.

Neben der Osteogenese ist, wie zuvor beschrieben, die Angiogenese eine bedeutsame Komponente für eine erfolgreiche Knochenregeneration. Daher wäre neben der Verwendung von osteoinduktivem Material wie BMP-2-kodierender DNA oder DEX auch die Anwendung von VEGF zur Stimulierung der Angiogenese sinnvoll. Ein möglicher Ansatzpunkt wäre z. B. die Einbettung einer weiteren LPX-Schicht, um ein Doppeltransfektionssystem herzustellen.

Abschließend kann festgehalten werden: Die hohen medizinischen und behördlichen Anforderungen und das Zusammenspiel einzelner TE-Komponenten machen funktionalisierte Biomaterialien zu komplexen Applikationsmöglichkeiten in der regenerativen Medizin. Kleine Abwandlungen in dem komplexen Zusammenspiel aus Biomaterialien, (Gen-)Vektoren und Zielzellen können empfindliche Auswirkungen im Gesamtsystem provozieren. In Abhängigkeit von der medizinischen Indikation und den Materialeigenschaften müssen die Konzipierungen individuell adaptiert und verbessert werden. Wird dieser Aufwand jedoch investiert, bietet die Anwendung funktionalisierter Biomaterialien gegenüber herkömmlichen Behandlungsmöglichkeiten vielversprechendes therapeutisches Potenzial.

## 5) Literaturverzeichnis

1. Rodan, G.A. Introduction to bone biology. *Bone* **13**, S3-S6 (1992).
2. Sommerfeldt, D. & Rubin, C. Biology of bone and how it orchestrates the form and function of the skeleton. *European Spine Journal* **10**, S86-S95 (2001).
3. Chun, D.S., Baker, K.C. & Hsu, W.K. Lumbar pseudarthrosis: a review of current diagnosis and treatment. *Neurosurgical Focus FOC* **39**, E10 (2015).
4. Crawford, C.H.I., Carreon, L.Y., Mummaneni, P., Dryer, R.F. & Glassman, S.D. Asymptomatic ACDF Nonunions Underestimate the True Prevalence of Radiographic Pseudarthrosis. *Spine* **45**, E776-E780 (2020).
5. Dietz, N. et al. Recombinant Human Bone Morphogenetic Protein–2 Use in Adult Spinal Deformity Surgery: Comparative Analysis and Healthcare Utilization at 24 Months' Follow-up. *Global Spine Journal* **12**, 92-101 (2022).
6. Zura, R. et al. Epidemiology of Fracture Nonunion in 18 Human Bones. *JAMA Surgery* **151**, e162775-e162775 (2016).
7. Rupp, M. et al. Diaphyseal long bone nonunions — types, aetiology, economics, and treatment recommendations. *International Orthopaedics* **42**, 247-258 (2018).
8. Wang, Y., Newman, M.R. & Benoit, D.S.W. Development of controlled drug delivery systems for bone fracture-targeted therapeutic delivery: A review. *European Journal of Pharmaceutics and Biopharmaceutics* **127**, 223-236 (2018).
9. Stewart, S.K. Fracture Non-Union: A Review of Clinical Challenges and Future Research Needs. *Malays Orthop J* **13**, 1-10 (2019).
10. Brydone, A.S., Meek, D. & Maclaine, S. Bone grafting, orthopaedic biomaterials, and the clinical need for bone engineering. *Proceedings of the Institution of Mechanical Engineers, Part H: Journal of Engineering in Medicine* **224**, 1329-1343 (2010).
11. Perez, J.R. et al. Tissue Engineering and Cell-Based Therapies for Fractures and Bone Defects. *Frontiers in Bioengineering and Biotechnology* **6** (2018).
12. Buckwalter, J.A., Einhorn, T.A., Simon, S.R. & Surgeons, Orthopaedic Basic Science: Biology and Biomechanics of the Musculoskeletal System. *American Academy of Orthopaedic Surgeons*, (2000).
13. Boskey, A.L. Mineralization of Bones and Teeth. *Elements* **3**, 385-391 (2007).
14. Florencio-Silva, R., Sasso, G.R.d.S., Sasso-Cerri, E., Simões, M.J. & Cerri, P.S. Biology of Bone Tissue: Structure, Function, and Factors That Influence Bone Cells. *BioMed Research International* **2015**, 421746 (2015).
15. Lopes, D., Martins-Cruz, C., Oliveira, M.B. & Mano, J.F. Bone physiology as inspiration for tissue regenerative therapies. *Biomaterials* **185**, 240-275 (2018).
16. Wei, S., Ma, J.-X., Xu, L., Gu, X.-S. & Ma, X.-L. Biodegradable materials for bone defect repair. *Military Medical Research* **7**, 54 (2020).
17. Yin, T. & Li, L. The stem cell niches in bone. *The Journal of Clinical Investigation* **116**, 1195-1201 (2006).
18. Jiang, W. & Liu, H. in *Nanocomposites for Musculoskeletal Tissue Regeneration*. 241-257 *Woodhead Publishing*, Oxford; (2016).
19. Gori, J.L. et al. Vascular niche promotes hematopoietic multipotent progenitor formation from pluripotent stem cells. *The Journal of Clinical Investigation* **125**, 1243-1254 (2015).
20. Zhu, G. et al. Bone physiological microenvironment and healing mechanism: Basis for future bone-tissue engineering scaffolds. *Bioactive Materials* **6**, 4110-4140 (2021).
21. Zhang, W. et al. Cell-Derived Extracellular Matrix: Basic Characteristics and Current Applications in Orthopedic Tissue Engineering. *Tissue Engineering Part B: Reviews* **22**, 193-207 (2015).
22. Blair, H.C., Sun, L.I. & Kohanski, R.A. Balanced Regulation of Proliferation, Growth, Differentiation, and Degradation in Skeletal Cells. *Annals of the New York Academy of Sciences* **1116**, 165-173 (2007).

23. Sroga, G.E., Karim, L., Colón, W. & Vashishth, D. Biochemical characterization of major bone-matrix proteins using nanoscale-size bone samples and proteomics methodology. *Molecular & cellular proteomics : MCP* **10**, M110.006718 (2011).
24. Anselme, K. Osteoblast adhesion on biomaterials. *Biomaterials* **21**, 667-681 (2000).
25. Gentili, C. & Cancedda, R. Cartilage and bone extracellular matrix. *Current pharmaceutical design* **15**, 1334-1348 (2009).
26. Kattimani, V.S., Kondaka, S. & Lingamaneni, K.P. Hydroxyapatite—Past, Present, and Future in Bone Regeneration. *Bone and Tissue Regeneration Insights* **7**, BTRI.S36138 (2016).
27. Lin, X., Patil, S., Gao, Y.G. & Qian, A. The Bone Extracellular Matrix in Bone Formation and Regeneration. *Frontiers in pharmacology* **11**, 757 (2020).
28. Han, Y., You, X., Xing, W., Zhang, Z. & Zou, W. Paracrine and endocrine actions of bone—the functions of secretory proteins from osteoblasts, osteocytes, and osteoclasts. *Bone research* **6**, 16 (2018).
29. Steeve, K.T., Marc, P., Sandrine, T., Dominique, H. & Yannick, F. IL-6, RANKL, TNF- $\alpha$ /IL-1: interrelations in bone resorption pathophysiology. *Cytokine & Growth Factor Reviews* **15**, 49-60 (2004).
30. Chen, H. et al. Prostaglandin E2 mediates sensory nerve regulation of bone homeostasis. *Nature Communications* **10**, 181 (2019).
31. Hu, K. & Olsen, B.R. The roles of vascular endothelial growth factor in bone repair and regeneration. *Bone* **91**, 30-38 (2016).
32. Manolagas, S.C. & Jilka, R.L. Bone marrow, cytokines, and bone remodeling. Emerging insights into the pathophysiology of osteoporosis. *The New England journal of medicine* **332**, 305-311 (1995).
33. Thomas, S. & Jaganathan, B.G. Signaling network regulating osteogenesis in mesenchymal stem cells. *Journal of cell communication and signaling* **16**, 47-61 (2022).
34. Bellido, T. Osteocyte-driven bone remodeling. *Calcified tissue international* **94**, 25-34 (2014).
35. Boyce, B.F. & Xing, L. Functions of RANKL/RANK/OPG in bone modeling and remodeling. *Archives of biochemistry and biophysics* **473**, 139-146 (2008).
36. Novais, A., Chatzopoulou, E., Chaussain, C. & Gorin, C. The Potential of FGF-2 in Craniofacial Bone Tissue Engineering: A Review. *Cells* **10**, 932 (2021).
37. Itzstein, C., Coxon, F.P. & Rogers, M.J. The regulation of osteoclast function and bone resorption by small GTPases. *Small GTPases* **2**, 117-130 (2011).
38. Zhao, H. Membrane trafficking in osteoblasts and osteoclasts: new avenues for understanding and treating skeletal diseases. *Traffic (Copenhagen, Denmark)* **13**, 1307-1314 (2012).
39. Bhattarai, H.K., Shrestha, S., Rokka, K. & Shakya, R. Vitamin D, Calcium, Parathyroid Hormone, and Sex Steroids in Bone Health and Effects of Aging. *Journal of osteoporosis* **2020**, 9324505 (2020).
40. Rucci, N. Molecular biology of bone remodelling. *Clinical cases in mineral and bone metabolism : the official journal of the Italian Society of Osteoporosis, Mineral Metabolism, and Skeletal Diseases* **5**, 49-56 (2008).
41. Baldwin, P. et al. Autograft, Allograft, and Bone Graft Substitutes: Clinical Evidence and Indications for Use in the Setting of Orthopaedic Trauma Surgery. *Journal of Orthopaedic Trauma* **33**, 203-213 (2019).
42. Greenwald, A.S. et al. Bone-Graft Substitutes: Facts, Fictions, and Applications. *JBJS* **83**, S98-103 (2001).
43. Hierholzer, C., Sama, D., Toro, J.B., Peterson, M. & Helfet, D.L. Plate Fixation of Ununited Humeral Shaft Fractures: Effect of Type of Bone Graft on Healing. *JBJS* **88**, 1442-1447 (2006).
44. Brigman, B.E., Hornicek, F.J., Gebhardt, M.C. & Mankin, H.J. Allografts about the Knee in Young Patients with High-Grade Sarcoma. *Clinical Orthopaedics and Related Research*® **421**, 232-239 (2004).

45. Bus, M.P.A. et al. Intercalary Allograft Reconstructions Following Resection of Primary Bone Tumors: A Nationwide Multicenter Study. *JBJS* **96**, e26 (2014).
46. Van Heest, A. & Swiontkowski, M. Bone-graft substitutes. *The Lancet* **353**, S28-S29 (1999).
47. Gamradt, S.C. & Lieberman, J.R. Bone Graft For Revision Hip Arthroplasty: Biology and Future Applications. *Clinical Orthopaedics and Related Research*® **417** (2003).
48. Drosos, G.I., Touzopoulos, P., Ververidis, A., Tilkeridis, K. & Kazakos, K. Use of demineralized bone matrix in the extremities. *World journal of orthopedics* **6**, 269-277 (2015).
49. Gruskin, E., Doll, B.A., Futrell, F.W., Schmitz, J.P. & Hollinger, J.O. Demineralized bone matrix in bone repair: History and use. *Advanced Drug Delivery Reviews* **64**, 1063-1077 (2012).
50. Yin, P. et al. A Systematic Review and Meta-Analysis of Ilizarov Methods in the Treatment of Infected Nonunion of Tibia and Femur. *PLOS ONE* **10**, e0141973 (2015).
51. Alford, A.I., Nicolaou, D., Hake, M. & McBride-Gagyi, S. Masquelet's induced membrane technique: Review of current concepts and future directions. *Journal of Orthopaedic Research* **39**, 707-718 (2021).
52. Le Baron, M., Vivona, J.-P., Maman, P., Volpi, R. & Flecher, X. Can the Reamer/Irrigator/Aspirator System replace anterior iliac crest grafting when treating long bone nonunion? *Orthopaedics & Traumatology: Surgery & Research* **105**, 529-533 (2019).
53. Raven, T.F. et al. Use of Masquelet technique in treatment of septic and atrophic fracture nonunion. *Injury* **50**, 40-54 (2019).
54. Taylor, B.C., Hancock, J., Zitzke, R. & Castaneda, J. Treatment of Bone Loss With the Induced Membrane Technique: Techniques and Outcomes. *Journal of Orthopaedic Trauma* **29**, 554-557 (2015).
55. Paley, D. Problems, obstacles, and complications of limb lengthening by the Ilizarov technique. *Clinical orthopaedics and related research*, 81-104 (1990).
56. Guerado, E., Cano, J.R. & Fernandez-Sanchez, F. Pin tract infection prophylaxis and treatment. *Injury* **50**, S45-S49 (2019).
57. Dimitriou, R., Mataliotakis, G.I., Angoules, A.G., Kanakaris, N.K. & Giannoudis, P.V. Complications following autologous bone graft harvesting from the iliac crest and using the RIA: A systematic review. *Injury* **42**, S3-S15 (2011).
58. Giannoudis, P.V., Einhorn, T.A. & Marsh, D. Fracture healing: the diamond concept. *Injury* **38 Suppl 4**, S3-6 (2007).
59. Henkel, J. et al. Bone Regeneration Based on Tissue Engineering Conceptions — A 21st Century Perspective. *Bone research* **1**, 216-248 (2013).
60. Ramalingam, M. & Velayudhan, S.R. Advances in Induced Pluripotent Stem Cells: Nanomaterial Perspectives. *Journal of Bionanoscience* **10**, 163-170 (2016).
61. Stevens, M.M. Biomaterials for bone tissue engineering. *Materials Today* **11**, 18-25 (2008).
62. Chen, F.-M., Zhao, Y.-M., Jin, Y. & Shi, S. Prospects for translational regenerative medicine. *Biotechnology Advances* **30**, 658-672 (2012).
63. Schlickewei, W. & Schlickewei, C. The Use of Bone Substitutes in the Treatment of Bone Defects – the Clinical View and History. *Macromolecular Symposia* **253**, 10-23 (2007).
64. Hudecki, A., Kiryczyński, G. & Łos, M.J. in *Stem Cells and Biomaterials for Regenerative Medicine*. (eds. M.J. Łos, A. Hudecki & E. Wiecheć) 85-98 (Academic Press, 2019).
65. Faour, O., Dimitriou, R., Cousins, C.A. & Giannoudis, P.V. The use of bone graft substitutes in large cancellous voids: Any specific needs? *Injury* **42**, S87-S90 (2011).
66. García-Gareta, E., Coathup, M.J. & Blunn, G.W. Osteoinduction of bone grafting materials for bone repair and regeneration. *Bone* **81**, 112-121 (2015).
67. Devi, G.V.Y., Anil, S. & Venkatesan, J. in *Engineering Materials for Stem Cell Regeneration*. (ed. F.A. Sheikh) 691-706 (2021).
68. Kazimierzczak, P. & Przekora, A. Osteoconductive and Osteoinductive Surface Modifications of Biomaterials for Bone Regeneration: A Concise Review. *Coatings* **10**, 971 (2020).
69. Zhang, Y. et al. Effect of microtopography on osseointegration of implantable biomaterials and its modification strategies. *Front Bioeng Biotechnol* **10**, 981062 (2022).

70. Albertini, M. et al. Advances in surfaces and osseointegration in implantology. Biomimetic surfaces. *Med Oral Patol Oral Cir Bucal* **20**, e316-325 (2015).
71. Ghanem, A. et al. Role of Osteogenic Coatings on Implant Surfaces in Promoting Bone-To-Implant Contact in Experimental Osteoporosis: A Systematic Review and Meta-Analysis. *Implant Dentistry* **26** (2017).
72. Bose, S., Robertson, S.F. & Bandyopadhyay, A. Surface modification of biomaterials and biomedical devices using additive manufacturing. *Acta Biomaterialia* **66**, 6-22 (2018).
73. Fousova, M., Vojtech, D., Jablonska, E., Fojt, J. & Lipov, J. Novel Approach in the Use of Plasma Spray: Preparation of Bulk Titanium for Bone Augmentations. *Materials (Basel)* **10** (2017).
74. Bosco, R., Van Den Beucken, J., Leeuwenburgh, S. & Jansen, J. Surface Engineering for Bone Implants: A Trend from Passive to Active Surfaces. *Coatings* **2**, 95-119 (2012).
75. Devlin-Mullin, A. et al. Atomic Layer Deposition of a Silver Nanolayer on Advanced Titanium Orthopedic Implants Inhibits Bacterial Colonization and Supports Vascularized de Novo Bone Ingrowth. *Adv Healthc Mater* **6** (2017).
76. Alkekhia, D., Hammond, P.T. & Shukla, A. Layer-by-Layer Biomaterials for Drug Delivery. *Annual review of biomedical engineering* **22**, 1-24 (2020).
77. Cao, S., Zhao, Y., Hu, Y., Zou, L. & Chen, J. New perspectives: In-situ tissue engineering for bone repair scaffold. *Composites Part B: Engineering* **202**, 108445 (2020).
78. Anouz, R. & Groth, T. in *Soft Matter for Biomedical Applications* 326-362 *The Royal Society of Chemistry* (2021).
79. Zhang, X. et al. Progress on the layer-by-layer assembly of multilayered polymer composites: Strategy, structural control and applications. *Progress in Polymer Science* **89**, 76-107 (2019).
80. Sahebalzamani, M. et al. Advancing bone tissue engineering one layer at a time: a layer-by-layer assembly approach to 3D bone scaffold materials. *Biomaterials Science* **10**, 2734-2758 (2022).
81. El Haitami, A.E. et al. Covalent layer-by-layer assemblies of polyelectrolytes and homobifunctional spacers. *Langmuir : the ACS journal of surfaces and colloids* **26**, 12351-12357 (2010).
82. Schlenoff, J.B., Dubas, S.T. & Farhat, T. Sprayed Polyelectrolyte Multilayers. *Langmuir : the ACS journal of surfaces and colloids* **16**, 9968-9969 (2000).
83. Ferreira, A.M., Tonda-Turo, C., Mancuso, E. & Gentile, P. Multilayer nanoscale functionalization to treat disorders and enhance regeneration of bone tissue. *Nanomedicine: Nanotechnology, Biology and Medicine* **19**, 22-38 (2019).
84. Cho, J., Char, K., Hong, J.-D. & Lee, K.-B. Fabrication of Highly Ordered Multilayer Films Using a Spin Self-Assembly Method. *Advanced Materials* **13**, 1076-1078 (2001).
85. Feng, Z. & Yan, F. Preparation and tribological studies of nanocomposite films fabricated using spin-assisted layer-by-layer assembly. *Surface and Coatings Technology* **202**, 3290-3297 (2008).
86. Boudou, T., Crouzier, T., Ren, K., Blin, G. & Picart, C. Multiple Functionalities of Polyelectrolyte Multilayer Films: New Biomedical Applications. *Advanced Materials* **22**, 441-467 (2010).
87. Ai, H., Jones, S.A. & Lvov, Y.M. Biomedical applications of electrostatic layer-by-layer nano-assembly of polymers, enzymes, and nanoparticles. *Cell biochemistry and biophysics* **39**, 23-43 (2003).
88. Gentile, P., Carmagnola, I., Nardo, T. & Chiono, V. Layer-by-layer assembly for biomedical applications in the last decade. *Nanotechnology* **26**, 422001 (2015).
89. Kirchof, K., Hristova, K., Krasteva, N., Altankov, G. & Groth, T. Multilayer coatings on biomaterials for control of MG-63 osteoblast adhesion and growth. *Journal of materials science. Materials in medicine* **20**, 897-907 (2009).
90. Ma, L., Zhou, J., Gao, C. & Shen, J. Incorporation of basic fibroblast growth factor by a layer-by-layer assembly technique to produce bioactive substrates. *Journal of biomedical materials research. Part B, Applied biomaterials* **83**, 285-292 (2007).
91. Petrilă, L.-M., Bucatariu, F., Mihai, M. & Teodosiu, C. in *Materials*, Vol. 14 (2021).

92. Tavakoli-darestani, R., Manafi-rasi, A. & Kamrani-rad, A. Dexamethasone-loaded hydroxyapatite enhances bone regeneration in rat calvarial defects. *Molecular Biology Reports* **41**, 423-428 (2014).
93. Pullisaar, H., Reseland, J.E., Haugen, H.J., Brinchmann, J.E. & Østrup, E. Simvastatin coating of TiO<sub>2</sub> scaffold induces osteogenic differentiation of human adipose tissue-derived mesenchymal stem cells. *Biochemical and Biophysical Research Communications* **447**, 139-144 (2014).
94. Langenbach, F. & Handschel, J. Effects of dexamethasone, ascorbic acid and  $\beta$ -glycerophosphate on the osteogenic differentiation of stem cells in vitro. *Stem Cell Research & Therapy* **4**, 117 (2013).
95. Weinstein, R.S. Glucocorticoid-Induced Osteoporosis and Osteonecrosis. *Endocrinology and Metabolism Clinics of North America* **41**, 595-611 (2012).
96. Sun, Z. et al. A Dexamethasone-Eluting Porous Scaffold for Bone Regeneration Fabricated by Selective Laser Sintering. *ACS Applied Bio Materials* **3**, 8739-8747 (2020).
97. Tseng, W.-C. & Huang, L. Liposome-based gene therapy. *Pharmaceutical Science & Technology Today* **1**, 206-213 (1998).
98. Monteiro, N. et al. On the use of dexamethasone-loaded liposomes to induce the osteogenic differentiation of human mesenchymal stem cells. *Journal of Tissue Engineering and Regenerative Medicine* **9**, 1056-1066 (2015).
99. Israelachvili, J.N., Mitchell, D.J. & Ninham, B.W. Theory of self-assembly of lipid bilayers and vesicles. *Biochimica et Biophysica Acta (BBA) - Biomembranes* **470**, 185-201 (1977).
100. Felgner, P.L. et al. Lipofection: a highly efficient, lipid-mediated DNA-transfection procedure. *Proceedings of the National Academy of Sciences of the United States of America* **84**, 7413-7417 (1987).
101. Zidovska, A., Evans, H.M., Ahmad, A., Ewert, K.K. & Safinya, C.R. The role of cholesterol and structurally related molecules in enhancing transfection of cationic liposome-DNA complexes. *The journal of physical chemistry. B* **113**, 5208-5216 (2009).
102. Hirsch-Lerner, D. et al. Effect of "helper lipid" on lipoplex electrostatics. *Biochimica et Biophysica Acta (BBA) - Biomembranes* **1714**, 71-84 (2005).
103. Ponti, F., Campolungo, M., Melchiori, C., Bono, N. & Candiani, G. Cationic lipids for gene delivery: many players, one goal. *Chemistry and Physics of Lipids* **235**, 105032 (2021).
104. Lienemann, P.S., Lutolf, M.P. & Ehrbar, M. Biomimetic hydrogels for controlled biomolecule delivery to augment bone regeneration. *Advanced Drug Delivery Reviews* **64**, 1078-1089 (2012).
105. Azevedo, H.S. & Pashkuleva, I. Biomimetic supramolecular designs for the controlled release of growth factors in bone regeneration. *Advanced Drug Delivery Reviews* **94**, 63-76 (2015).
106. Kirker-Head, C.A. Potential applications and delivery strategies for bone morphogenetic proteins. *Advanced Drug Delivery Reviews* **43**, 65-92 (2000).
107. James, A.W. Review of Signaling Pathways Governing MSC Osteogenic and Adipogenic Differentiation. *Scientifica* **2013**, 684736 (2013).
108. Chen, G., Deng, C. & Li, Y.P. TGF- $\beta$  and BMP signaling in osteoblast differentiation and bone formation. *International journal of biological sciences* **8**, 272-288 (2012).
109. Al-Sammarraie, N. & Ray, S.K. Bone morphogenetic protein signaling in spinal cord injury. *Neuroimmunology and Neuroinflammation* **8**, 53-63 (2021).
110. BMP-2 Evaluation in Surgery for Tibial Trauma Study Group et al. Recombinant Human Bone Morphogenetic Protein-2 for Treatment of Open Tibial Fractures: A Prospective, Controlled, Randomized Study of Four Hundred and Fifty Patients. *JBJS* **84**, 2123-2134 (2002).
111. Friedlaender, G.E. et al. Osteogenic protein-1 (bone morphogenetic protein-7) in the treatment of tibial nonunions. *J Bone Joint Surg Am* **83-A Suppl 1**, S151-S158 (2001).
112. Carragee, E.J., Hurwitz, E.L. & Weiner, B.K. A critical review of recombinant human bone morphogenetic protein-2 trials in spinal surgery: emerging safety concerns and lessons learned. *The Spine Journal* **11**, 471-491 (2011).

113. Liang, Z., Luo, Y. & Lv, Y. Mesenchymal stem cell-derived microvesicles mediate BMP2 gene delivery and enhance bone regeneration. *Journal of Materials Chemistry B* **8**, 6378-6389 (2020).
114. Chan, D.S., Garland, J., Infante, A., Sanders, R.W. & Sagi, H.C. Wound complications associated with bone morphogenetic protein-2 in orthopaedic trauma surgery. *J Orthop Trauma* **28**, 599-604 (2014).
115. Mizrahi, O. et al. BMP-6 is more efficient in bone formation than BMP-2 when overexpressed in mesenchymal stem cells. *Gene Therapy* **20**, 370-377 (2013).
116. Bez, M. et al. In situ bone tissue engineering via ultrasound-mediated gene delivery to endogenous progenitor cells in mini-pigs. *Science Translational Medicine* **9**, eaal3128 (2017).
117. Noël, D. et al. Short-Term BMP-2 Expression Is Sufficient for In Vivo Osteochondral Differentiation of Mesenchymal Stem Cells. *Stem Cells* **22**, 74-85 (2004).
118. Lei, P., Padmashali, R.M. & Andreadis, S.T. Cell-controlled and spatially arrayed gene delivery from fibrin hydrogels. *Biomaterials* **30**, 3790-3799 (2009).
119. Klugherz, B.D. et al. Gene delivery from a DNA controlled-release stent in porcine coronary arteries. *Nature Biotechnology* **18**, 1181-1184 (2000).
120. Nam, H.Y., Park, J.H., Kim, K., Kwon, I.C. & Jeong, S.Y. Lipid-based emulsion system as non-viral gene carriers. *Archives of pharmacol research* **32**, 639-646 (2009).
121. Collon, K., Gallo, M.C. & Lieberman, J.R. Musculoskeletal tissue engineering: Regional gene therapy for bone repair. *Biomaterials* **275**, 120901 (2021).
122. Tenchov, R., Bird, R., Curtze, A.E. & Zhou, Q. Lipid Nanoparticles-From Liposomes to mRNA Vaccine Delivery, a Landscape of Research Diversity and Advancement. *ACS nano* (2021).
123. Nayerossadat, N., Maedeh, T. & Ali, P.A. Viral and nonviral delivery systems for gene delivery. *Adv Biomed Res* **1**, 27 (2012).
124. Pardi, N., Hogan, M.J., Porter, F.W. & Weissman, D. mRNA vaccines — a new era in vaccinology. *Nature Reviews Drug Discovery* **17**, 261-279 (2018).
125. Matulis, D., Rouzina, I. & Bloomfield, V.A. Thermodynamics of Cationic Lipid Binding to DNA and DNA Condensation: Roles of Electrostatics and Hydrophobicity. *Journal of the American Chemical Society* **124**, 7331-7342 (2002).
126. Bloomfield, V.A. DNA condensation by multivalent cations. *Biopolymers* **44**, 269-282 (1997).
127. Zuhorn, I.S. et al. Phase Behavior of Cationic Amphiphiles and Their Mixtures with Helper Lipid Influences Lipoplex Shape, DNA Translocation, and Transfection Efficiency. *Biophysical Journal* **83**, 2096-2108 (2002).
128. Koynova, R. & Tenchov, B. Cationic lipids: molecular structure/ transfection activity relationships and interactions with biomembranes. *Topics in current chemistry* **296**, 51-93 (2010).
129. Balbino, T.A. et al. Microfluidic Assembly of pDNA/Cationic Liposome Lipoplexes with High pDNA Loading for Gene Delivery. *Langmuir : the ACS journal of surfaces and colloids* **32**, 1799-1807 (2016).
130. Ewert, K.K. et al. Cationic liposome-nucleic acid complexes for gene delivery and silencing: pathways and mechanisms for plasmid DNA and siRNA. *Topics in current chemistry* **296**, 191-226 (2010).
131. Elouahabi, A. & Ruyschaert, J.-M. Formation and Intracellular Trafficking of Lipoplexes and Polyplexes. *Molecular Therapy* **11**, 336-347 (2005).
132. Parker, A.L., Newman, C., Briggs, S., Seymour, L. & Sheridan, P.J. Nonviral gene delivery: techniques and implications for molecular medicine. *Expert Reviews in Molecular Medicine* **5**, 1-15 (2003).
133. Rosenbaum, A.J., Grande, D.A. & Dines, J.S. The use of mesenchymal stem cells in tissue engineering: A global assessment. *Organogenesis* **4**, 23-27 (2008).
134. Marion, N.W. & Mao, J.J. in *Methods in Enzymology*, Vol. 420 339-361 (Academic Press, 2006).

135. Carlesso, N. & Cardoso, A.A. Stem cell regulatory niches and their role in normal and malignant hematopoiesis. *Curr Opin Hematol* **17**, 281-286 (2010).
136. Higuchi, A., Ling, Q.-D., Chang, Y., Hsu, S.-T. & Umezawa, A. Physical Cues of Biomaterials Guide Stem Cell Differentiation Fate. *Chemical Reviews* **113**, 3297-3328 (2013).
137. Stevens, M.M. & George, J.H. Exploring and Engineering the Cell Surface Interface. *Science* **310**, 1135-1138 (2005).
138. Place, E.S., Evans, N.D. & Stevens, M.M. Complexity in biomaterials for tissue engineering. *Nature Materials* **8**, 457-470 (2009).
139. Li, J. et al. Biophysical and Biochemical Cues of Biomaterials Guide Mesenchymal Stem Cell Behaviors. *Frontiers in Cell and Developmental Biology* **9** (2021).
140. Sun, Y., Chen, C.S. & Fu, J. Forcing stem cells to behave: a biophysical perspective of the cellular microenvironment. *Annu Rev Biophys* **41**, 519-542 (2012).
141. Aiyelabegan, H.T. & Sadroddiny, E. Fundamentals of protein and cell interactions in biomaterials. *Biomedicine & Pharmacotherapy* **88**, 956-970 (2017).
142. McMurray, R.J., Dalby, M.J. & Tsimbouri, P.M. Using biomaterials to study stem cell mechanotransduction, growth and differentiation. *J Tissue Eng Regen Med* **9**, 528-539 (2015).
143. Chiu, L.H. et al. The effect of type II collagen on MSC osteogenic differentiation and bone defect repair. *Biomaterials* **35**, 2680-2691 (2014).
144. Gao, C., Peng, S., Feng, P. & Shuai, C. Bone biomaterials and interactions with stem cells. *Bone research* **5**, 17059 (2017).
145. Janich, C. et al. Composites of malonic acid diamides and phospholipids – Structural parameters for optimal transfection efficiency in A549 cells. *European Journal of Lipid Science and Technology* **116**, 1184-1194 (2014).
146. Janich, C. et al. Composites of malonic acid diamides and phospholipids — Impact of lipoplex stability on transfection efficiency. *Journal of Controlled Release* **220**, 295-307 (2015).
147. Janich, C. et al. Fast therapeutic DNA internalization – A high potential transfection system based on a peptide mimicking cationic lipid. *European Journal of Pharmaceutics and Biopharmaceutics* **118**, 38-47 (2017).
148. Janich, C. et al. Structures of malonic acid diamide/phospholipid composites and their lipoplexes. *Soft Matter* **12**, 5854-5866 (2016).
149. Wölk, C., Janich, C., Bakowsky, U., Langner, A. & Brezesinski, G. Malonic acid based cationic lipids – The way to highly efficient DNA-carriers. *Advances in Colloid and Interface Science* **248**, 20-34 (2017).
150. Giselsbrecht, J. et al. Overcoming the polycation dilemma – Explorative studies to characterise the efficiency and biocompatibility of newly designed lipofection reagents. *International Journal of Pharmaceutics* **541**, 81-92 (2018).
151. Zhang, X. et al. The Directional Observation of Highly Dynamic Membrane Tubule Formation Induced by Engulfed Liposomes. *Scientific Reports* **5**, 16559 (2015).
152. Ferreira, A.M., Gentile, P., Chiono, V. & Ciardelli, G. Collagen for bone tissue regeneration. *Acta Biomaterialia* **8**, 3191-3200 (2012).
153. Kim, H.D. et al. Chondroitin Sulfate-Based Biomaterializing Surface Hydrogels for Bone Tissue Engineering. *ACS Applied Materials & Interfaces* **9**, 21639-21650 (2017).
154. Knopf-Marques, H. et al. Hyaluronic Acid and Its Derivatives in Coating and Delivery Systems: Applications in Tissue Engineering, Regenerative Medicine and Immunomodulation. *Advanced Healthcare Materials* **5**, 2841-2855 (2016).
155. Rabea, E.I., Badawy, M.E.T., Stevens, C.V., Smagghe, G. & Steurbaut, W. Chitosan as Antimicrobial Agent: Applications and Mode of Action. *Biomacromolecules* **4**, 1457-1465 (2003).
156. Zhai, P. et al. The application of hyaluronic acid in bone regeneration. *International Journal of Biological Macromolecules* **151**, 1224-1239 (2020).
157. Jansen, K. et al. A hyaluronan-based nerve guide: in vitro cytotoxicity, subcutaneous tissue reactions, and degradation in the rat. *Biomaterials* **25**, 483-489 (2004).

158. Hasnain, M.S., Ahmad, S.A., Chaudhary, N., Hoda, M.N. & Nayak, A.K. in Applications of Nanocomposite Materials in Orthopedics. (eds. Inamuddin, A.M. Asiri & A. Mohammad) 1-37 (Woodhead Publishing, 2019).
159. Yi, H. et al. Biofabrication with Chitosan. *Biomacromolecules* **6**, 2881-2894 (2005).
160. Saravanan, S., Leena, R.S. & Selvamurugan, N. Chitosan based biocomposite scaffolds for bone tissue engineering. *International Journal of Biological Macromolecules* **93**, 1354-1365 (2016).
161. Raafat, D. & Sahl, H.-G. Chitosan and its antimicrobial potential – a critical literature survey. *Microbial Biotechnology* **2**, 186-201 (2009).
162. Alkhoury, H. et al. Studies on the Mechanisms of Anti-Inflammatory Activity of Heparin- and Hyaluronan-Containing Multilayer Coatings—Targeting NF- $\kappa$ B Signalling Pathway. *International Journal of Molecular Sciences* **21**, 3724 (2020).
163. Aranaz, I. et al. Functional Characterization of Chitin and Chitosan. *Current Chemical Biology* **3**, 203-230 (2009).
164. Salbach-Hirsch, J. et al. Sulfated Glycosaminoglycans Support Osteoblast Functions and Concurrently Suppress Osteoclasts. *Journal of Cellular Biochemistry* **115**, 1101-1111 (2014).
165. Büttner, M. et al. Over-sulfated chondroitin sulfate Derivatives induce osteogenic differentiation of hMSC independent of BMP-2 and TGF- $\beta$ 1 signalling. *Journal of Cellular Physiology* **228**, 330-340 (2013).
166. Bosman, F.T. & Stamenkovic, I. Functional structure and composition of the extracellular matrix. *The Journal of Pathology* **200**, 423-428 (2003).
167. Zhao, M. et al. Improved Stability and Cell Response by Intrinsic Cross-Linking of Multilayers from Collagen I and Oxidized Glycosaminoglycans. *Biomacromolecules* **15**, 4272-4280 (2014).
168. Amini, A.R., Laurencin, C.T. & Nukavarapu, S.P. Bone tissue engineering: recent advances and challenges. *Crit Rev Biomed Eng* **40**, 363-408 (2012).
169. Das, A. & Botchwey, E. Evaluation of angiogenesis and osteogenesis. *Tissue Eng Part B Rev* **17**, 403-414 (2011).
170. Vinatier, C. & Guicheux, J. Cartilage tissue engineering: From biomaterials and stem cells to osteoarthritis treatments. *Annals of Physical and Rehabilitation Medicine* **59**, 139-144 (2016).
171. Janicki, P. & Richter, W. Neue Ansätze für die in situ Regeneration und das Tissue Engineering von Knochen. *Deutsche Zeitschrift für Sportmedizin*, 30-35 (2012).
172. Paul-Ehrlich-Institut <https://www.pei.de/EN/medicinal-products/atmp> (21.10.2022).
173. Paul-Ehrlich-Institut <https://www.pei.de/EN/medicinal-products/atmp/tissue-engineered-products/tissue-engineered-products-node.html>. (18.10.2022).
174. Wang, L.-m. et al. Dynamic stiffness of polyelectrolyte multilayer films based on disulfide bonds for in situ control of cell adhesion. *Journal of Materials Chemistry B* **3**, 7546-7553 (2015).
175. Ren, K., Crouzier, T., Roy, C. & Picart, C. Polyelectrolyte Multilayer Films of Controlled Stiffness Modulate Myoblast Cell Differentiation. *Advanced Functional Materials* **18**, 1378-1389 (2008).
176. Schneider, A. et al. Polyelectrolyte Multilayers with a Tunable Young's Modulus: Influence of Film Stiffness on Cell Adhesion. *Langmuir : the ACS journal of surfaces and colloids* **22**, 1193-1200 (2006).

## 6) Anhang

### Supporting Information Publikation I

#### **Contact-Triggered Lipofection from Multilayer Films Designed as Surfaces for in Situ Transfection Strategies in Tissue Engineering**

C. Husteden, F. Doberenz, N. Goergen, S. R. Pinnapireddy, C. Janich, A. Langner, F. Syrowatka, A. Repanas, F. Erdmann, J. Jedelská, U. Bakowsky, T. Groth, C. Wölk.

ACS Applied Materials & Interfaces 2020

*<https://doi.org/10.1021/acsami.9b18968>*

## Supporting Information

### Contact-Triggered Lipofection from Multilayer Films Designed as Surfaces for In Situ Transfection Strategies in Tissue Engineering

Catharina Husteden,<sup>a</sup> Falko Doberenz,<sup>b</sup> Nathalie Goergen,<sup>c</sup> Shashank Reddy Pinnapireddy,<sup>c</sup> Christopher Janich,<sup>a</sup> Andreas Langner,<sup>a</sup> Frank Syrowatka,<sup>d</sup> Alexandros Repanas,<sup>b</sup> Frank Erdmann,<sup>e</sup> Jarmila Jedelská,<sup>c</sup> Udo Bakowsky,<sup>c</sup> Thomas Groth,<sup>b, d, f</sup> Christian Wölk<sup>a, g\*</sup>

**a** Martin Luther University Halle-Wittenberg, Institute of Pharmacy, Department of Medicinal Chemistry, Wolfgang-Langenbeck-Str. 4, 06120 Halle (Saale), Germany

**b** Martin Luther University Halle-Wittenberg, Institute of Pharmacy, Department Biomedical Materials, Heinrich-Damerow-Str. 4, 06120 Halle (Saale), Germany

**c** Department of Pharmaceutics and Biopharmaceutics, University of Marburg, Robert-Koch-Str. 4, 35037, Marburg, Germany

**d** Martin-Luther-University Halle-Wittenberg, Interdisciplinary Center of Materials Science, Heinrich-Damerow-Str. 4, 06120 Halle (Saale), Germany

**e** Martin Luther University Halle-Wittenberg, Institute of Pharmacy, Department of Pharmacology, Wolfgang-Langenbeck-Str. 4, 06120 Halle (Saale), Germany

**f** Laboratory of Biomedical Nanotechnologies, Institute of Bionic Technologies and Engineering, I.M. Sechenov First Moscow State University, 119991, Trubetskaya street 8, Moscow, Russian Federation

**g** Institute of Pharmacy, Pharmaceutical Technology, Faculty of Medicine, Leipzig University, 04317 Leipzig, Germany

corresponding author: Christian Wölk

christian.woelk@pharmazie.uni-halle.de

## Content

1. Additional water contact angle measurements and ellipsometry measurements with PEM films loaded by the Langmuir-Blodgett protocol
2. Results of the DLS measurement of OH4/DOPE 1/1 liposomes
3. Additional images of gel electrophoresis experiment for the determination of the PEM DNA loading efficiency and release.
4. Transfection experiments with DNA embedded without lipids in the PEM

### 1. Additional water contact angle measurements and ellipsometry measurements with PEM films loaded by the Langmuir-Blodgett protocol

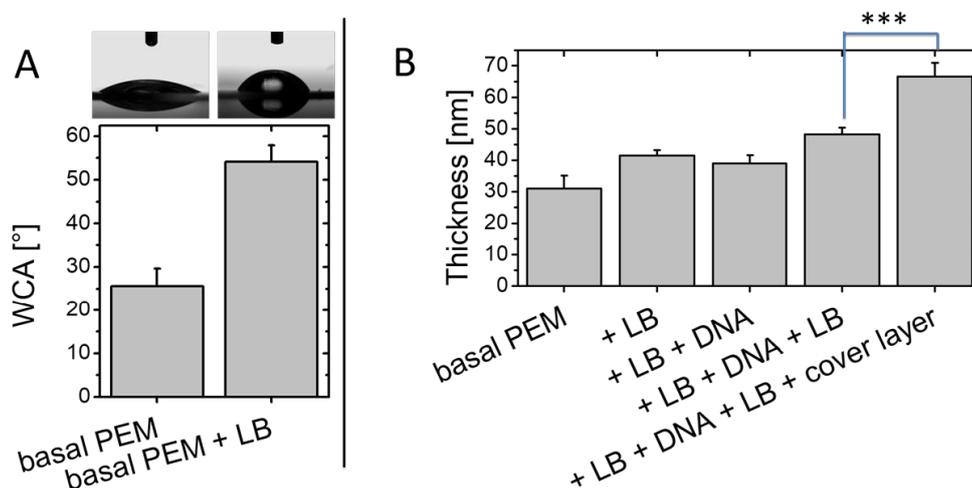


**Figure S1.** A Static water contact angle (WCA) before (basal PEM) and after (basal PEM + LB) the Langmuir Blodgett transfer of a lipid bilayer composed of OH4/DOPE 1/1 (mean  $\pm$  SD,  $n = 6$ ). The images above the corresponding bar show a representative measurement. The WCA increase after Langmuir-Blodgett transfer indicates a successful lipid deposition. B Ellipsometry with hydrated samples: Calculated thickness of the basal PEM [HA,CHI]<sub>2</sub>HA followed by the lipoplex loading processes using the Langmuir-Blodgett protocol studied with ellipsometry: 1. first OH4/DOPE bilayer transfer (+LB), 2. DNA transfe (+LB+DNA), 3. second OH4/DOPE bilayer transfer (+LB+DNA+LB), 4. HA, CHI cover layer (+LB+DNA+LB+cover layer). The values in show mean and corresponding standard deviation (error bars,  $n = 10$ ). The 3 stars (\*\*\*) indicate significant differences in the measured thickness values determined by One-Way ANOVA ( $\alpha = 0.05$ ).

#### Experimental details:

*Water Contact Angle Measurements:* In order to determine the wettability of the surface before and after the first Langmuir Blodgett transfer of a lipid bilayer, static Water Contact Angle Measurements (WCA) measurements were conducted using an OCA15+ device (DataPhysics, Filderstadt, Germany). The experiments were conducted in duplicates with three droplets per sample using a flow rate of  $0.5 \mu\text{L s}^{-1}$ . The software of OCA15+ device for each droplet recorded at least 6 independent measurements.

## 2. Results of the DLS measurement of OH4/DOPE 1/1 liposomes.

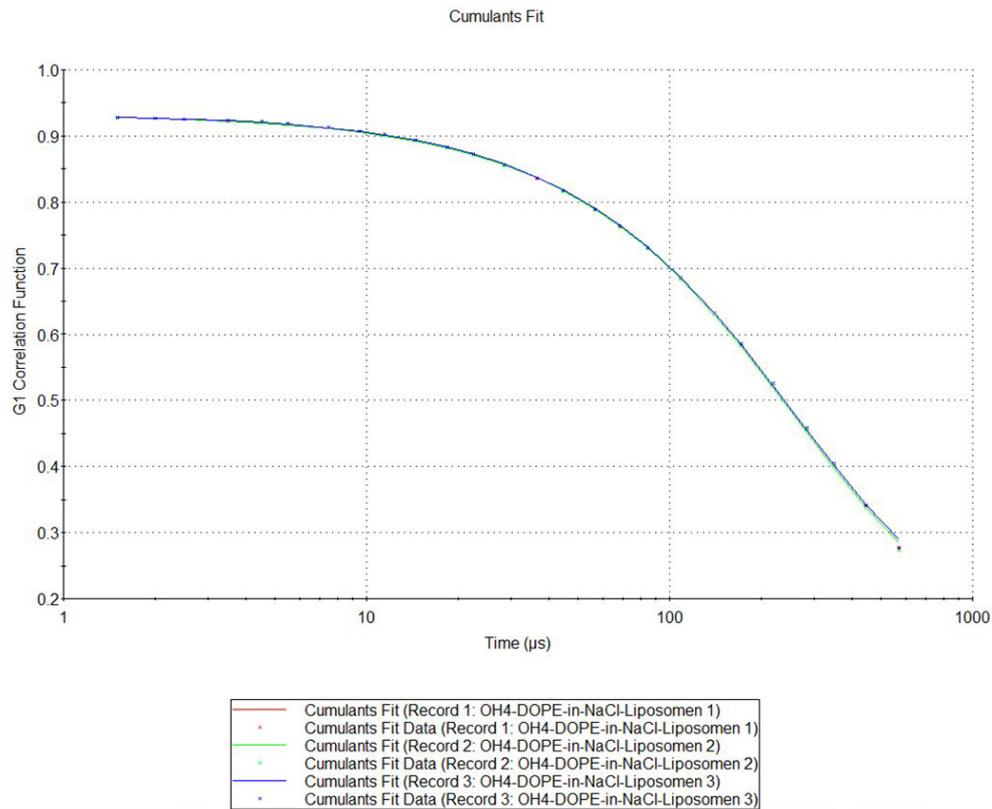


**Figure S2:** Cumulant fit of 3 independent measurements of one OH4/DOPE 1/1 liposome sample. The fit results in z-average diameter and polydispersity index.

**3. Additional images of gel electrophoresis experiment for the determination of the PEM DNA loading efficiency and release.**

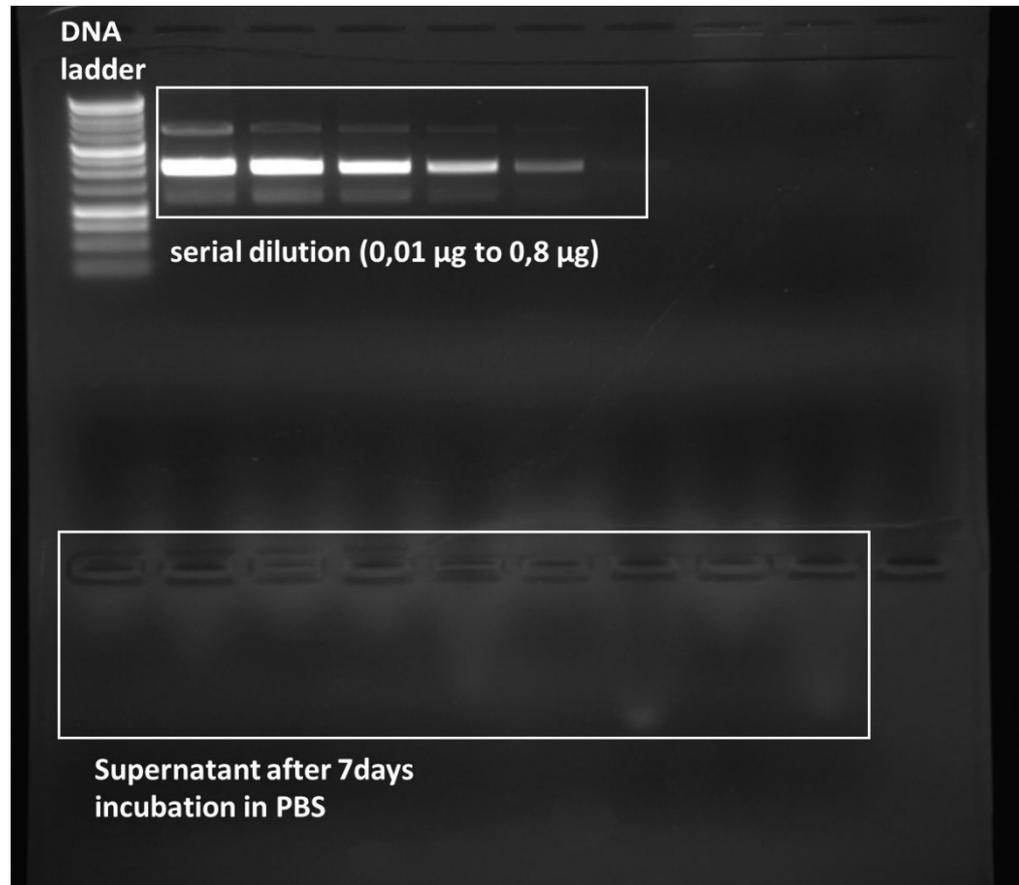


**Figure S3:** Representative Agarose gel for the determination of the DNA release out of  $[\text{HA},\text{CHI}]_5\text{HA-LPX-}[\text{HA},\text{CHI}]_1$  films loaded with  $0.88 \mu\text{g}/\text{cm}^2$  DNA after incubation for 7 days in PBS. No DNA could be detected. SDS was used to release DNA from lipoplexes. Three different amounts of supernatant of three different films were loaded onto the gel.

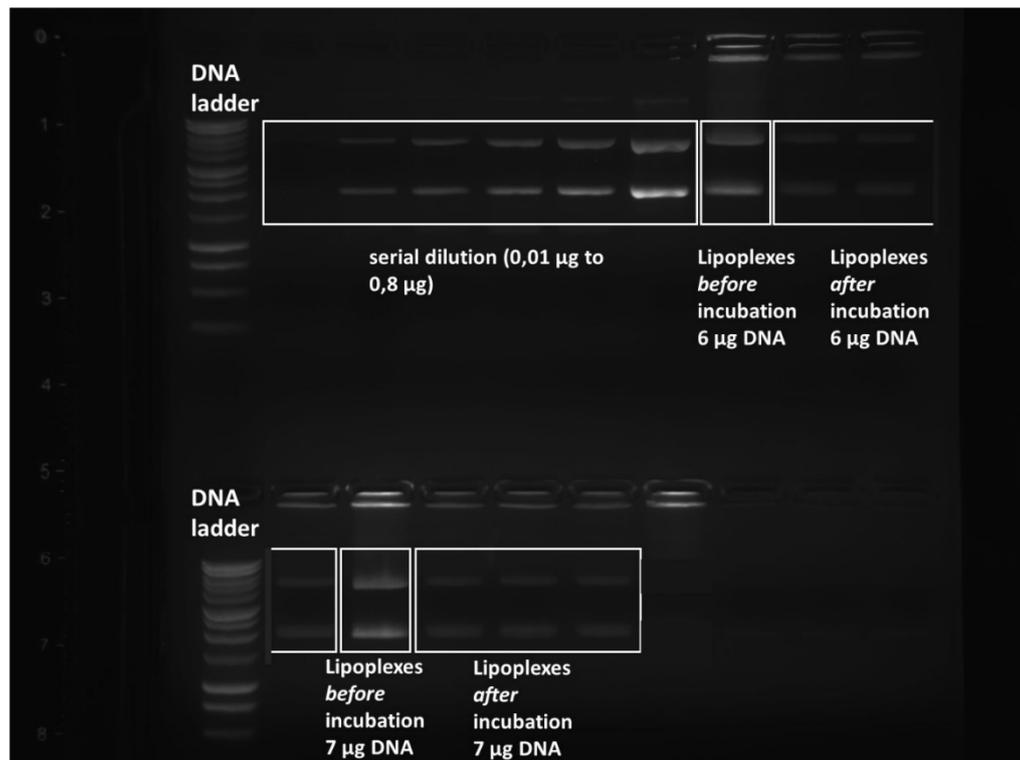


**Figure S4:** Representative Agarose gel for the determination of the loading efficiency of  $[\text{HA},\text{CHI}]_5\text{HA-LPX-}[\text{HA},\text{CHI}]_1$  films after incubation with 6 and 7 µg DNA.

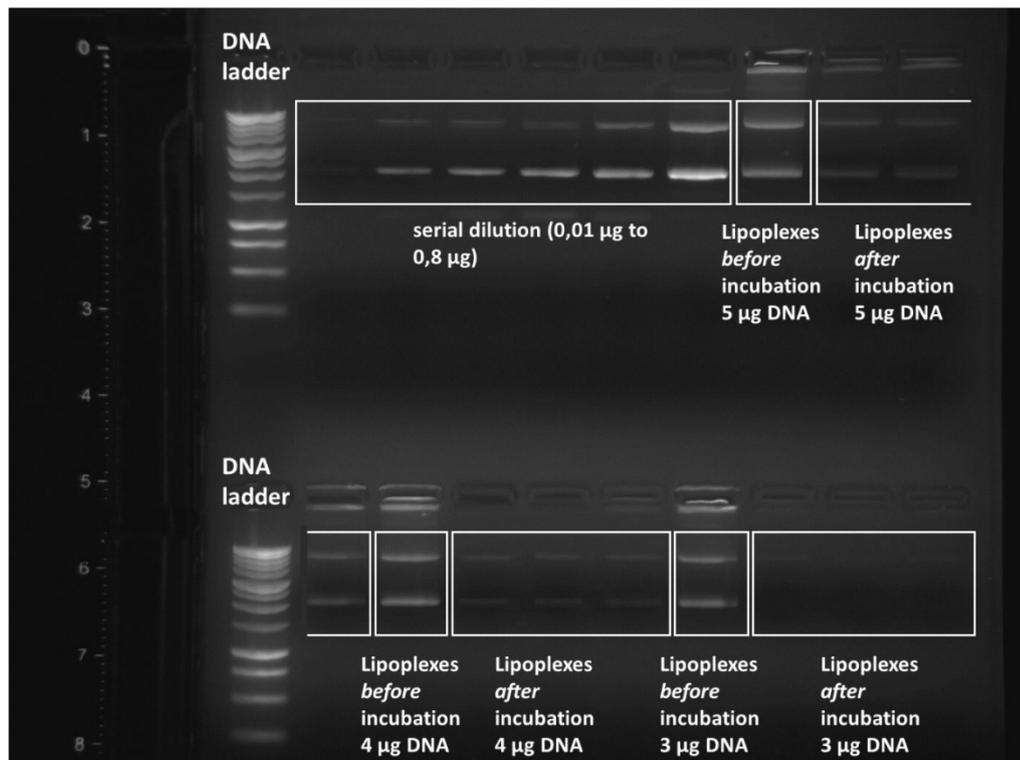


**Figure S5:** Representative Agarose gel for the determination of the loading efficiency of  $[\text{HA},\text{CHI}]_5\text{HA-LPX}-[\text{HA},\text{CHI}]_1$  films after incubation with 5, 4 and 3 µg DNA.



**Figure S6:** Representative Agarose gel for the determination of the loading efficiency of  $[\text{HA,CHI}]_5\text{HA-LPX-}[\text{HA,CHI}]_1$  films after incubation with 2, 1 and 0.5  $\mu\text{g}$  DNA.

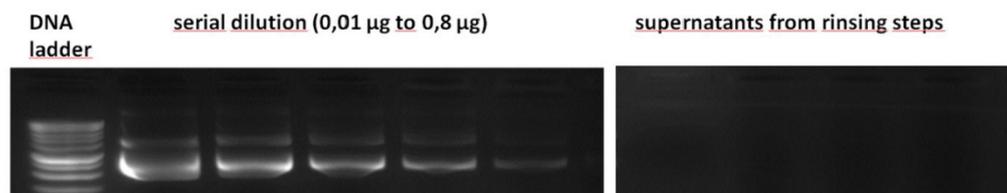


**Figure S7:** Representative Agarose gel bands for the determination of the DNA content in rinsing steps during the loading of  $[\text{HA,CHI}]_5\text{HA-LPX-}[\text{HA,CHI}]_1$  films after incubation with 1  $\mu\text{g}$  DNA.

#### 4. Transfection experiments with DNA embedded without lipids in the PEM

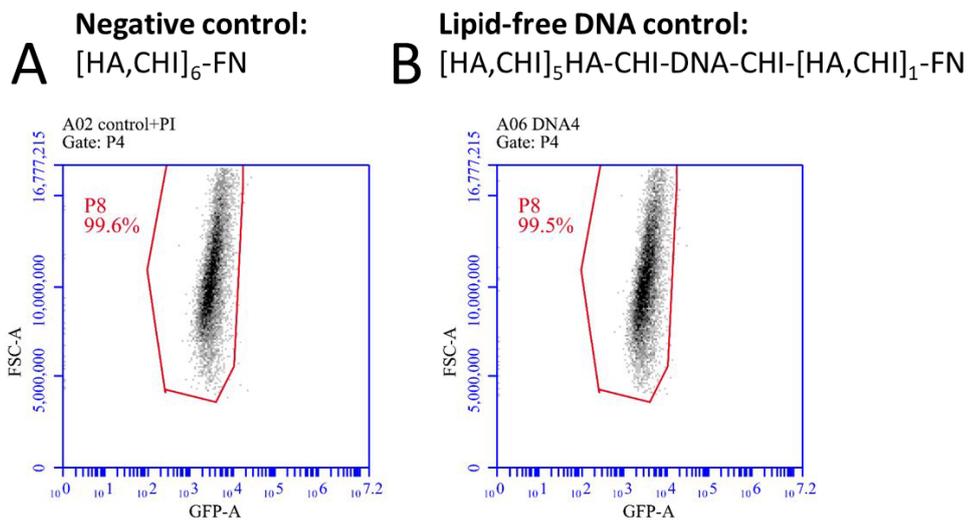


**Figure S8.** Transfection efficiency determined by FACS as % GFP positive cells. The results compare C2C12 cells growing on a DNA-free [HA,CHI]<sub>6</sub>-FN PEM with a PEM where DNA was complexed in absence of the lipid composition OH4/DOPE between two chitosan layers ([HA,CHI]<sub>5</sub>HA-CHI-DNA-CHI-[HA,CHI]<sub>1</sub>-FN, cDNA = 0.4 µg). The measurements were made 24h after seeding the cells on the PEM. The additional CHI layers in the [HA,CHI]<sub>5</sub>HA-CHI-DNA-CHI-[HA,CHI]<sub>1</sub>-FN were necessary to bind the DNA in-between. Successful DNA binding was confirmed by gel electrophoresis.

## Supporting Information Publikation III

**Extracellular matrix-inspired surface coatings functionalized with dexamethasone-loaded liposomes to induce osteo- and chondrogenic differentiation of multipotent stem cells**

Y.A. Brito Barrera, C. Husteden, J. Alherz, B. Fuhrmann, C. Wölk, T. Groth

Materials Science & Engineering C, 2021

*<https://doi.org/10.1016/j.msec.2021.112516>*

## Supplemental information

### Extracellular matrix-inspired surface coatings functionalized with Dexamethasone-loaded liposomes to induce osteo- and chondrogenic differentiation of multipotent stem cells

Yazmin A., Brito Barrera<sup>a</sup>, Catharina Husteden<sup>b</sup>, Jumanah Alherz<sup>a</sup>, Bodo Fuhrmann<sup>c</sup>, Christian Wölk<sup>d</sup>, Thomas Groth<sup>a,c,e\*</sup>,

- a) Department Biomedical Materials, Institute of Pharmacy, Martin Luther University Halle–Wittenberg, Heinrich Damerow Strasse 4, 06120 Halle (Saale), Germany
- b) Medicinal Chemistry Department, Institute of Pharmacy, Martin Luther University Halle-Wittenberg, 06120 Halle (Saale), Germany
- c) Interdisciplinary Center of Materials Science, Martin Luther University Halle-Wittenberg, D-06099 Halle (Saale), Germany
- d) Pharmaceutical Technology, Institute of Pharmacy, Faculty of Medicine, Leipzig University, 04317 Leipzig, Germany
- e) Laboratory of Biomedical Nanotechnologies, Institute of Bionic Technologies and Engineering, I.M. Sechenov First Moscow State University, 119991, Trubetskaya street 8, Moscow, Russian Federation Interdisciplinary

\*Corresponding author:  
Prof. Dr. Thomas Groth  
Department Biomedical Materials  
Institute of Pharmacy  
Martin-Luther-University Halle-Wittenberg  
Heinrich-Damerow-Strasse 4  
06120 Halle (Saale) Germany  
e-mail: thomas.groth@pharmazie.uni-halle.de

**Atomic force microscopy.** Atomic force microscopy (AFM) was performed with a 3D-molecular force probe (MFP-3D-BIO, Asylum Research, Santa Barbara, CA, USA) to investigate the surface roughness and topography. Coated Si substrates were probed in close-contact mode under ambient (air) laboratory conditions. Scans of 5×5mm<sup>2</sup> (512×512 pixel, 1Hz) were analyzed, regarding the polyelectrolyte layer deposition and the presence of liposomes. Roughness analysis was performed using the software Gwyddion (Gwyddion 2.49, 64-bit).

Topography images were used to measure the surface roughness parameters of HA and Col system with and without embedded liposomes. Both the average roughness (R<sub>a</sub>) and the root-mean-square roughness (R<sub>q</sub>) were calculated.

**Table S1.** surface roughness parameters. roughness average (Ra) and root mean square roughness (Rq) of PEM system of [HA/Col]<sub>6</sub>, [HA/Col]<sub>4</sub>HA/Lip, [HA/Col]<sub>4</sub>HA/Lip[HA/Col] measured by AFM.

	[HA/Col] <sub>6</sub>	[HA/Col] <sub>4</sub> HA/Lip	[HA/Col] <sub>4</sub> HA/Lip[HA/Col]
<b>Ra [nm]</b>	1.731 ± 0.721	17.96± 6.219	11.64 ± 2.647
<b>Rq [nm]</b>	2.914 ± 1.698	23.55± 7.66	15.23 ± 3.389

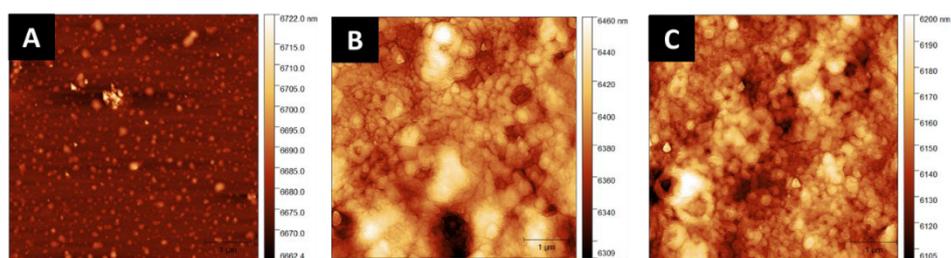


**Figure S1.** Surface topography of (A) liposome-free system sequence [HA/Col]<sub>6</sub>, (B) PEM system of sequence [HA/Col]<sub>4</sub>HA/Lip, (C) PEM system sequence [HA/Col]<sub>4</sub>HA/Lip[HA/Col] by AFM [Scale bar 1μm].

## Supporting Information Publikation IV

### **Lipoplex-functionalized thin-film surface coatings based on extracellular matrix components as local delivery system to control osteogenic stem cell differentiation**

C. Husteden, Y. A. Brito Barrera, S. Tegtmeier, J. Borges, J. Giselbrecht, M. Menzel, A. Langner, J. F. Mano, C.E.H. Schmelzer, C. Wölk, T. Groth

*\* C. Husteden und Y.A. Brito Barrera teilen sich die Erstautorenschaft für diese Publikation*

Advanced Healthcare Materials 2022

<https://doi.org/10.1002/adhm.202201978>

# ADVANCED HEALTHCARE MATERIALS

## Supporting Information

for *Adv. Healthcare Mater.*, DOI 10.1002/adhm.202201978

Lipoplex-Functionalized Thin-Film Surface Coating Based on Extracellular Matrix  
Components as Local Gene Delivery System to Control Osteogenic Stem Cell Differentiation

*Catharina Husteden, Yazmin A. Brito Barrera, Sophia Tegtmeyer, João Borges, Julia Giselbrecht,  
Matthias Menzel, Andreas Langner, João F. Mano, Christian E. H. Schmelzer, Christian Wölk\*  
and Thomas Groth\**

## Supplemental information

### Lipoplex-functionalized thin-film surface coating based on extracellular matrix components as local gene delivery system to control osteogenic stem cell differentiation

Catharina Husteden<sup>a,‡</sup>, Yazmin A. Brito Barrera<sup>b,‡</sup>, Sophia Tegtmeyer<sup>a</sup>, João Borges<sup>c</sup>, Julia Giselbrecht<sup>a</sup>, Matthias Menzel<sup>d</sup>, Andreas Langner<sup>a</sup>, João F. Mano,<sup>c</sup> Christian E.H. Schmelzer<sup>d</sup>, Christian Wölk<sup>e\*</sup>, Thomas Groth<sup>b,f\*</sup>

- a) Martin Luther University Halle-Wittenberg, Institute of Pharmacy, Department of Medicinal Chemistry, Wolfgang-Langenbeck-Str. 4, 06120 Halle (Saale), Germany
- b) Martin Luther University Halle-Wittenberg, Institute of Pharmacy, Department Biomedical Materials, Heinrich-Damerow-Str. 4, 06120 Halle (Saale), Germany
- c) Department of Chemistry, CICECO - Aveiro Institute of Materials, University of Aveiro, Campus Universitário de Santiago, 3810-193 Aveiro, Portugal
- d) Fraunhofer Institute for Microstructure of Materials and Systems (IMWS), Department of Biological and Macromolecular Materials, Walter-Hülse-Str. 1, 06120 Halle (Saale), Germany
- e) Institute of Pharmacy, Pharmaceutical Technology, Faculty of Medicine, Leipzig University, 04317 Leipzig, Germany
- f) Martin-Luther-University Halle-Wittenberg, Interdisciplinary Center of Materials Science, Heinrich-Damerow-Str. 4, 06120 Halle (Saale), Germany

‡ These authors contributed equally to this work.

corresponding author: Thomas Groth & Christian Wölk

\*[thomas.groth@pharmazie.uni-halle.de](mailto:thomas.groth@pharmazie.uni-halle.de)

\*[christian.woelk@medizin.uni-leipzig.de](mailto:christian.woelk@medizin.uni-leipzig.de)

**Schematic illustration and selected images of gel electrophoresis experiment for the determination of the DNA loading efficiency after embedding LPX into PEM using an indirect method of quantifying the fraction of non-adsorbed DNA.**

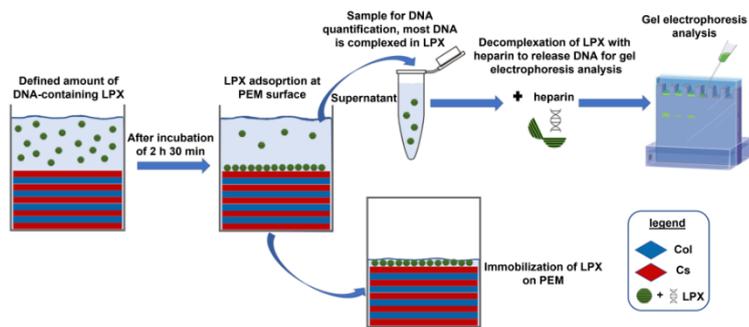


**Figure S1.** Schematic illustration of the indirect quantification of DNA loading of PEMs.

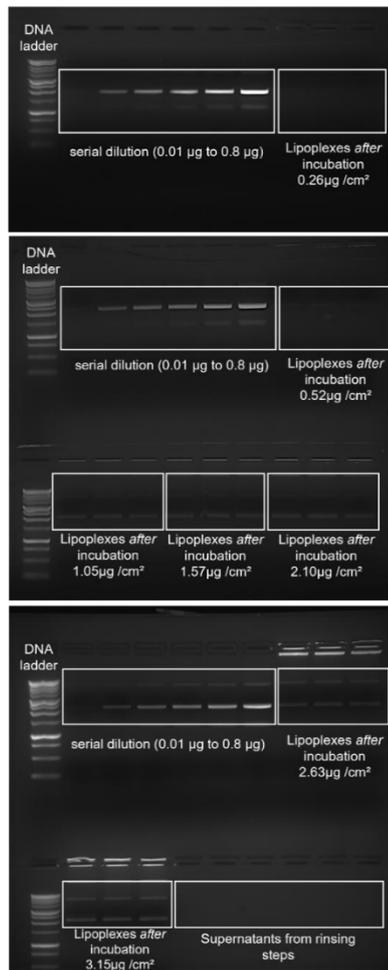


**Figure S2.** Representative agarose gel for the determination of the DNA loading of  $[\text{Cs}/\text{Col}]_4\text{Cs}/\text{LPX}/\text{Cs}/\text{Col}$  films after incubation with different amounts of DNA encapsulated in LPX. The supernatant of the incubation solution was loaded on the gel to determine the adsorbed amount of DNA indirectly.

## Atomic force microscopy

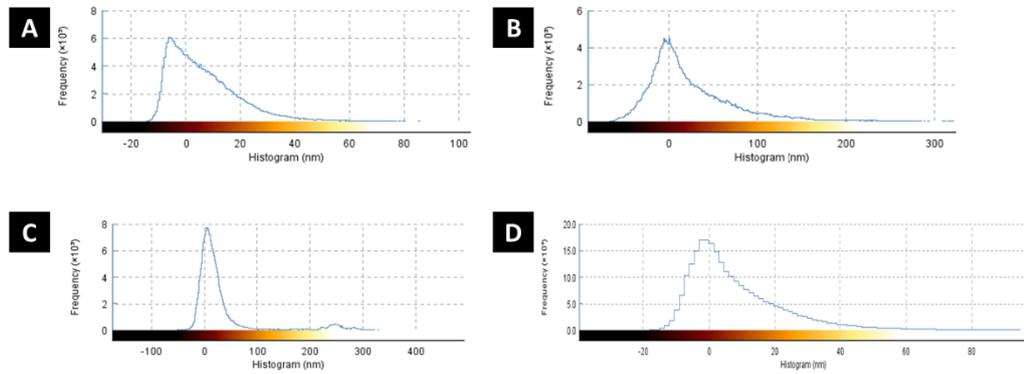


**Figure S3. Figure 4 A-D)** Histograms of height mode **(A)**  $[\text{Cs}/\text{Co}]_4\text{Cs}$ , **(B)**  $[\text{Cs}/\text{Co}]_4\text{Cs}/\text{LPX}$ , **(C)**  $[\text{Cs}/\text{Co}]_4\text{Cs}/\text{LPX}/\text{Cs}$ , and **(D)**  $[\text{Cs}/\text{Co}]_4\text{Cs}/\text{LPX}/\text{Cs}/\text{Col}$  by AFM.

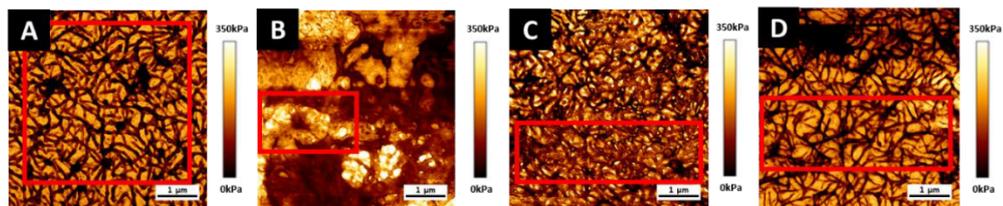


**Figure S4.** Stiffness micrographs of different preparation steps of the PEM system. **(A)**  $[\text{Cs}/\text{Co}]_4\text{Cs}$ , **(B)**  $[\text{Cs}/\text{Co}]_4\text{Cs}/\text{LPX}$ , **(C)**  $[\text{Cs}/\text{Co}]_4\text{Cs}/\text{LPX}/\text{Cs}$ , and **(D)**  $[\text{Cs}/\text{Co}]_4\text{Cs}/\text{LPX}/\text{Cs}/\text{Col}$  by AFM. Red square represents the selected area for the determination of the  $E_0$  modulus. The reduced area of PEMs bearing LPX was necessary due to the inhomogeneity of the PEMs.

**Table S1.** Average third highest peak to third lowest valley height (R3Z ISO), waviness average ( $W_a$ ) and root mean square waviness ( $W_q$ ) distribution of PEM sequences before and after lipoplexes deposition. 1-dimensional roughness analysis, according to ISO 4287, 4288, 3274, mean values calculated from 10 separate lines,  $l_n = 5\mu\text{m}$ ,  $D_c = 1\mu\text{m}$ , cutoff filter: 0.02 measured by AFM

	<i>R3z ISO [nm]</i>	<i>W<sub>a</sub> [nm]</i>	<i>W<sub>q</sub> [nm]</i>
[Cs/Co] <sub>4</sub> Cs	28.5 ±4.7	4.0 ±1.2	5.2 ±1.4
[Cs/Co] <sub>4</sub> Cs/LPX	59.1 ±12.6	31.1 ±8.5	37.3 ±10.6
[Cs/Co] <sub>4</sub> Cs/LPX[C <sub>s</sub> ]	42.3 ±4.9	7.3 ±2.5	9.4 ±3.9
[Cs/Co] <sub>4</sub> Cs/LPX[C <sub>s</sub> /Co]	35.7 ±9.1	5.8 ±1.2	7.2 ±1.5

### Uptake studies of LPX in hADSCs

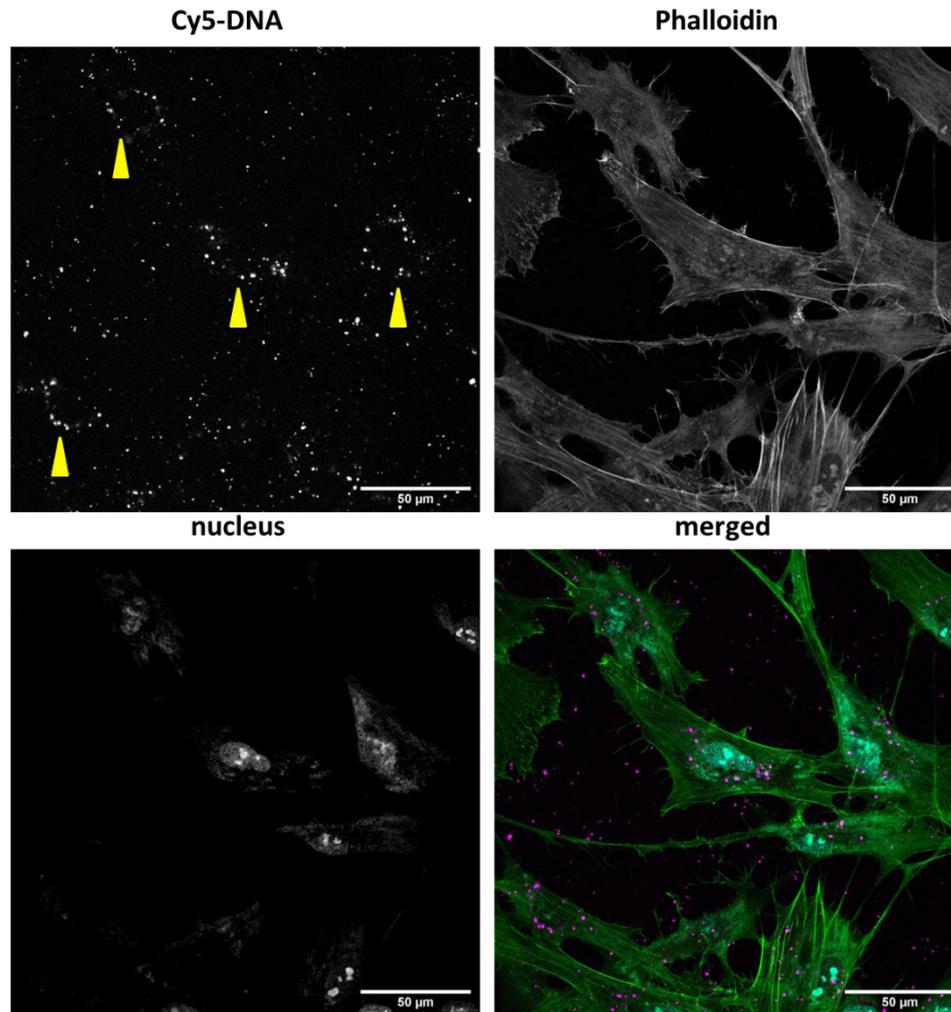


**Figure S5.** CLSM micrograph of transfected hADSCs after 48 h growing on [Cs/Col]<sub>4</sub>Cs/LPX/Cs/Col with Cy-5 LabelIT<sup>®</sup> labelled DNA (merged image magenta). The cells are stained for filamentous actin with Phalloidin-Atto 488 (merged image green) and nuclei with BOBO-1 (merged image cyan). Images were taken at 40x magnification and evaluated with ImageJ. Images are given as single channels and merged. The given image is an optical slight of the basal part taken by CLSM analyses. The bar represents 50 μm.

### Transfection studies with flow cytometry

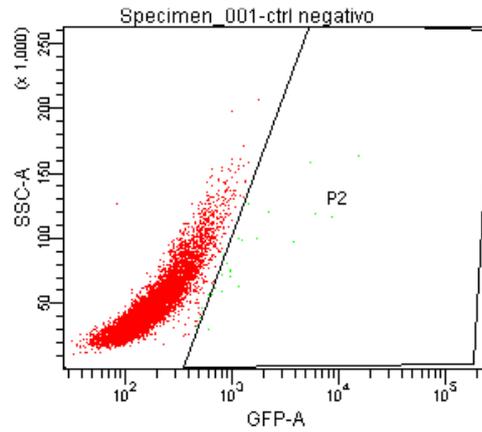


**Figure S6.** Flow cytometry dot plots representing sight scatter of cell light scattering (SSC) and the fluorescence intensity in the GFP-sensitive channel (GFP-A) of hADSC cells seeded on [Cs/Col]<sub>6</sub> in absence of LPX as negative control of the transfection studies.

## **Supporting Information Manuskript I**

### **Osteogenic Stem Cell Differentiation Induced by Contact Triggered In Situ BMP-2 Transfection from DNA lipid Nanoparticle Loaded Multilayer Films**

C. Husteden, S. Tegtmeyer, J. Weber, R. Eckenstaler, F. Erdmann, F. Seifert, R. A. Benndorf, A. Langner, T. Groth, C. Wölk

Osteogenic Stem Cell Differentiation Induced by Contact Triggered In  
Situ BMP-2 Transfection from DNA-lipid Nanoparticle Loaded  
Multilayer Films – Supporting Information

Catharina Husteden<sup>a</sup>, Sophia Tegtmeyer<sup>a</sup>, Juliane Weber<sup>a</sup>, Robert Eckenstaler<sup>b</sup>, Frank Erdmann<sup>c</sup>,  
Franziska Seifert<sup>d</sup>, Ralf A. Benndorf<sup>b</sup>, Andreas Langner<sup>a</sup>, Thomas Groth<sup>e</sup>, Christian Wölk<sup>f\*</sup>

a Martin Luther University Halle-Wittenberg, Institute of Pharmacy, Department of Medicinal  
Chemistry, Wolfgang-Langenbeck-Str. 4, 06120 Halle (Saale), Germany

b Martin Luther University Halle-Wittenberg, Institute of Pharmacy, Department of Clinical  
Pharmacy and Pharmacotherapy, Kurt-Mothes-Str. 3, 06120 Halle (Saale), Germany

c Martin Luther University Halle-Wittenberg, Institute of Pharmacy, Department of Pharmacology,  
Kurt-Mothes-Str. 3, 06120 Halle (Saale), Germany

d Martin Luther University Halle-Wittenberg, Institute of Pharmacy, Chair of Downstream  
Processing, Weinbergweg 22, 06120 Halle (Saale), Germany

e Martin-Luther-University Halle-Wittenberg, Interdisciplinary Center of Materials Science,  
Department of Biomedical Materials, Heinrich-Damerow-Str. 4, 06120 Halle (Saale), Germany

f Institute of Pharmacy, Pharmaceutical Technology, Faculty of Medicine, Leipzig University,  
04317 Leipzig, Germany

\*Corresponding author: Christian Wölk ([christian.woelk@medizin.uni-leipzig.de](mailto:christian.woelk@medizin.uni-leipzig.de))

**S1. Representative illustration of the focal adhesion quantification using CellProfiler™**

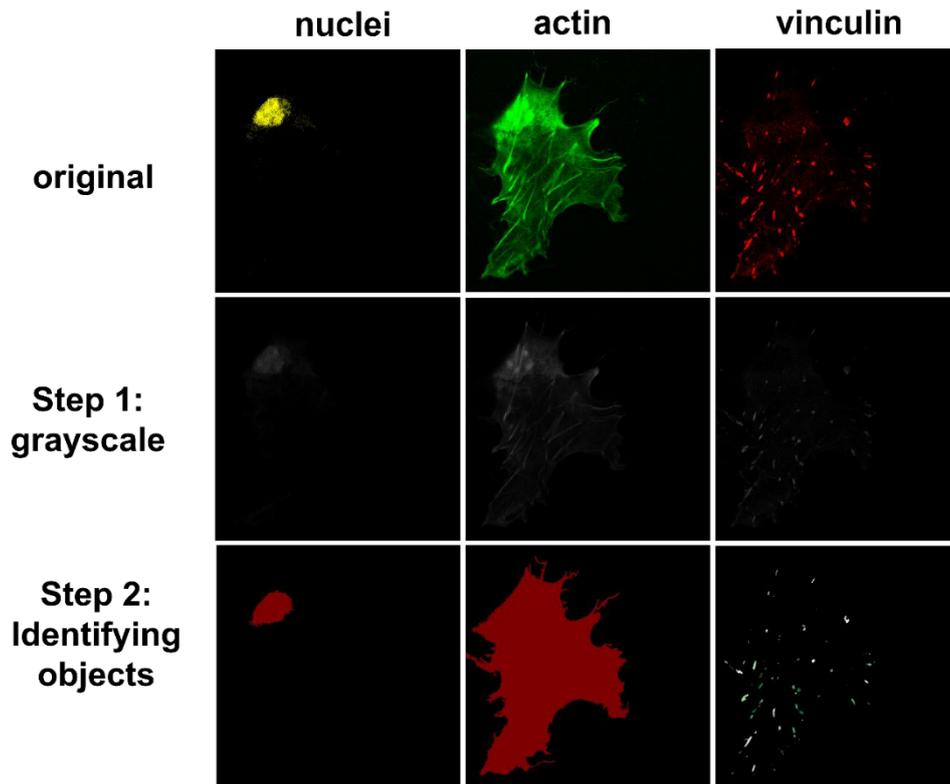


**Figure S1.** Cell morphology was assessed microscopically by staining the cells with fluorescently labelled phalloidin to visualize actin cytoskeleton. Cell nuclei were stained using BOBO-1 and Vinculin using monoclonal Anti-Vinculin Clone hVIN-1 Mouse Acites Fluid Antibody and goat anti-Mouse IgG Secondary Antibody Alexa Fluor 647. Focal adhesion number and cell area were analyzed with CellProfiler™ analysis software using a protocol from the literature [1], based on conversion of the images to grayscale followed by an object identification.

## S2. Cellular uptake of LNP

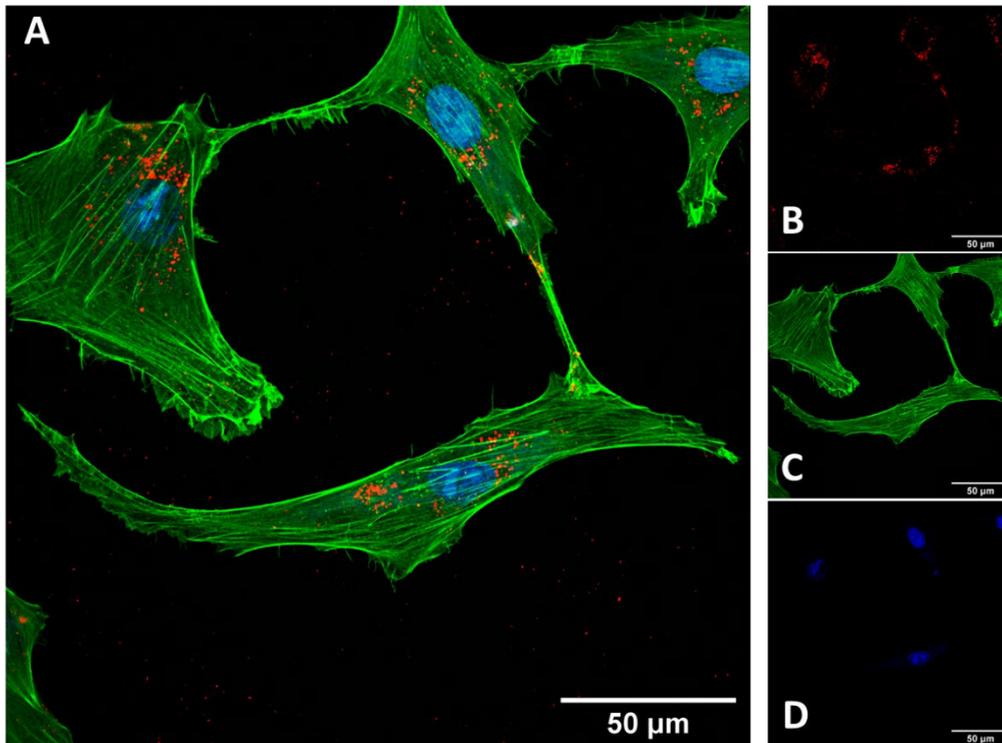


**Figure S2.** CLSM micrograph of transfected hMSCs after 72 h seeded on [HA,CHI]<sub>5</sub>-HA-(DNA-LNP)-[HA,CHI]<sub>1</sub>-VTN with Cy-5 labelled DNA. (A) merged image of fluorescence signals from Cy-5 LabelIT<sup>®</sup> labelled DNA (red) Phalloidin-Atto 488 for staining filamentous actin (green) BOBO-1 for staining the nucleus (blue). (B) single channel of Cy-5 LabelIT<sup>®</sup> labelled DNA (C) single channel Phalloidin-Atto 488 for staining filamentous actin and (D) single channel BOBO-1 for staining the nucleus. The bar represents 50 μm

### S3. OsteoImage™ assay

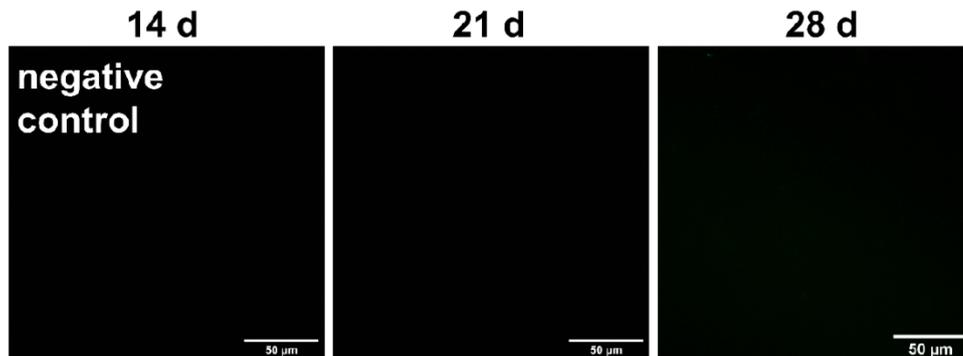


**Figure S3.** Hydroxyapatite content of the negative control, which were hMSCs grown on PEM's without LNPs [HA,CHI]<sub>6</sub>-VTN and treated with BM. The amount of hydroxyapatite was determined using an OsteoImage™ assay (Lonza, Basel, Switzerland). The fluorescent staining reagent (green) binds to the hydroxyapatite portion of the mineralized matrix.

### REFERENCES

1. Carpenter, A.E., et al., CellProfiler: image analysis software for identifying and quantifying cell phenotypes. *Genome Biol*, 2006. 7(10): p. R100.

## Liste der Veröffentlichungen

### Publikationen

---

1. Pinnapireddy, J. Giselbrecht, B. Strehlow, C. Janich, C. Husteden, A. Meister, H. Loppnow, D. Sedding, F. Erdmann, G. Hause, G. Brezesinski, T. Groth, A. Langner, U. Bakowsky, Christian Wölk. *A triple chain polycationic peptide-mimicking amphiphile – efficient DNA-transfer without co-lipids.*  
Biomaterial Science 2020
2. C. Husteden, F. Doberenz, N. Goergen, S. R. Pinnapireddy, C. Janich, A. Langner, F. Syrowatka, A. Repanas, F. Erdmann, J. Jedelská, U. Bakowsky, T. Groth, C. Wölk. *Contact-Triggered Lipofection from Multilayer Films Designed as Surfaces for In Situ Transfection Strategies in Tissue Engineering.*  
ACS Applied Materials & Interfaces 2020
3. C. Husteden, T. Groth, C. Wölk *Implantatüberzüge für die in-situ Transfektion in der regenerativen Medizin.*  
BIOspektrum, Volume 20, Issue 4, 2021
4. Y.A. Brito Barrera, C. Husteden, J. Alherz, B. Fuhrmann, C. Wölk, T. Groth. *Extracellular matrix-inspired surface coatings functionalized with dexamethasone-loaded liposomes to induce osteo- and chondrogenic differentiation of multipotent stem cells.*  
Materials Science & Engineering C 2021
5. C. Husteden, Y. A. Brito Barrera, S. Tegtmeyer, J. Borges, J. Giselbrecht, M. Menzel, A. Langner, J. F. Mano, C.E.H. Schmelzer, C. Wölk, T. Groth. *Lipoplex-functionalized thin-film surface coating based on extracellular matrix components as local gene delivery system to control osteogenic stem cell differentiation.*  
Advanced Healthcare Materials 2022

## Posterbeiträge

1. C. Husteden, T. Groth, C. Wölk. *Development of Methods for Effective DNA Loading of Model Surfaces for in-situ Transfection.* International Conference and Workshop on Biological Barriers 2018 (BioBarriers Saarbrücken)
2. C.Husteden, A. Repanas, T. Groth, C. Wölk. *Surface properties and Cell Adhesions Studies of Lipoplex-Loaded Polyelectrolyte Multilayers.* Symposium Controlled Release Society 2019 (CRS German Chapter Leipzig)
3. C.Husteden, A. Repanas, T. Groth, C. Wölk. *Incorporation of Novel Cationic Lipoplexes in Polyelectrolyte Multilayer Coatings for Controlled Release in the field of Bone Regeneration* International Congress Nanotechnology in Medicine & Biology 2019 (BioNanoMed Graz)
4. C.Husteden, A. Repanas, T. Groth, C. Wölk. *DNA-loaded Polyelectrolyte Multilayer Scaffolds for Local Transfection on Bone Structures.* Annual Meeting of the German Pharmaceutical Society 2019 (DPhG Heidelberg)
5. C. Husteden, F. Doberenz, S.R. Pinapireddy, A. Repanas, T. Groth, C. Wölk. *Functionalized Polyelectrolyte Multilayer Scaffolds as Gene Delivery systems in Tissue Engineering.* 2nd International workshop on advanced materials for healthcare applications 2019 (IWAMHA Madeira)
6. C. Husteden, F. Doberenz, S.R. Pinapireddy, A. Repanas, T. Groth, C. Wölk. *Gene Delivery from new designed Polyelectrolyte Multilayer Scaffolds in Tissue Engineering.* Leipzig Research Festival of Lifescience 2020
7. C. Husteden, F. Doberenz, S.R. Pinapireddy, A. Langner, T. Groth, C. Wölk. *Contact-Triggered Transfection from Multilayer-Systems in Tissue Engineering.* Symposium Controlled Release Society 2020 (CRS German Chapter München)
8. C. Husteden, A. Langner, T. Groth, C. Wölk. *In-situ Lipofection with nanostructured Multilayer Systems to mediate BMP-2 gene delivery for bone regeneration.* 47th European Society for Artificial Organs Congress London (ESAO 2021)

### **Konferenzvorträge**

---

1. C. Husteden, A. Langner, T. Groth, C. Wölk. *Surface-Mediated Gene Delivery from functionalized Polyelectrolyte Multilayer Scaffolds in Tissue Engineering*. 11th World Biomaterials Congress Glasgow (WBC Virtual 2020)

### **Betreute Diplomarbeiten**

---

1. Thema: Untersuchung der DNA-Beladung und des Freisetzungsverhaltens von Polyelektrolyt-Multischichtsystemen zur Transfektion  
Jessica Wiese (11/2018 – 05/2019)  
Die Ergebnisse dieser Arbeit fanden keine Anwendung in der vorliegenden Dissertation

## Lebenslauf

### Persönliche Daten

---

Name	Husteden, Catharina
Geburtsort	Nordhorn
Staatsangehörigkeit	deutsch

### Schulbildung

---

2000 – 2004	Grundschule Kirchsule in Schüttorf
2004 – 2012	Burggymnasium Bad Bentheim
	Abschluss: Allgemeine Hochschulreife

### Akademische Ausbildung

---

2012 – 2016	Studium der Pharmazie an der Martin-Luther-Universität Halle-Wittenberg
04/2015	1. Staatsexamen
11/2016	2. Staatsexamen
11/2016 – 05/2017	Praktisches Jahr, 1. Teil: Diplomstudentin an der Martin-Luther-Universität Halle-Wittenberg Titel: ‚Isolation von Zellkernen zur Quantifizierung eingeschleuster Plasmid-DNA‘
05/2017 – 11/2017	Praktisches Jahr, 2. Teil: Pharmazeutin im Praktikum in der Lipsia Apotheke in Leipzig
11/2017	3. Staatsexamen
12/2017	Verteidigung und Prüfung zur Diplom-Pharmazeutin
12/2017	Approbation zur Apothekerin

## **Eidesstattliche Erklärung**

Hiermit erkläre ich gemäß der Promotionsordnung der Naturwissenschaftlichen Fakultät I (Biowissenschaften) der Martin-Luther-Universität Halle-Wittenberg, dass ich die vorliegende Dissertationsschrift selbstständig und ohne fremde Hilfe angefertigt habe. Weiterhin habe ich keine anderen als die angegebenen Quellen und Hilfsmittel verwendet und die daraus wörtlich und inhaltlich entnommenen Stellen als solche kenntlich gemacht. Die Dissertation wurde ausschließlich der Naturwissenschaftlichen-Fakultät I der Martin-Luther-Universität Halle-Wittenberg vorgelegt und an keiner anderen universitären Einrichtung weder im In- noch im Ausland zur Erlangung des Doktorgrades eingereicht.

Halle (Saale), 19.12.2022